# Quantum information processing with a multimode fibre

Saroch Leedumrongwatthanakun

**THÈSE DE DOCTORAT**
**DE SORBONNE UNIVERSITÉ**

**Spécialité : Physique**

**École doctorale : "Physique en Île-de-France"**

**réalisée au :**

**Laboratoire Kastler Brossel**

**Présentée par**

**Saroch LEEDUMRONGWATTHANAKUN**

**Pour obtenir le grade de**

**DOCTEUR de SORBONNE UNIVERSITÉ**

## Sujet de la thèse :

# Quantum information processing with a multimode fibre

**Soutenue publiquement le 13 décembre 2019**

devant le jury composé de :

| | | | |
|---|---|---|---|
| Prof. | SILBERHORN | Christine | Rapporteur |
| Prof. | MARQUIER | François | Rapporteur |
| Prof. | SAPIENZA | Riccardo | Examinateur |
| Dr. | WALSCHAERS | Mattia | Examinateur (Invité) |
| Prof. | DIAMANTI | Eleni | Examinateur |
| Prof. | GIGAN | Sylvain | Directeur de thèse |

*To mom*

# Contents

# Acronyms

- APD : Avalanche Photodiode Detectors
- CPA : Coherent Perfect Absorption
- DMPK : Dorokhov-Mello-Pereira-Kumar
- EM : ElectroMagnetic
- EMCCD : Electron Multiplying Charge-Coupled Device
- FPGA : Field-Programmable Gate Array
- HOM : Hong-Ou-Mandel
- JSA : Joint Spectral Amplitude
- KLM : Knill-Laflam me-Miburn
- LOQC : Linear Optical Quantum Computing
- LTBS : Lossy phase-Tunable Beam Splitter
- MMF : MultiMode Fibre
- MMI : MultiMode Interference
- MP : Marčhenko-Pastur
- MPLC : Multi-Plane Light Conversion
- MZ : Mach-Zehnder
- PDF : Probability Density Function
- RMT : Random Matrix Theory
- SLD : SuperLuminescent Didode
- SLM : Spatial Light Modulator
- SPDC : Spontaneous Parametric Down-Conversion
- TM : Transmission Matrix

# Preamble

*"Information is physical."*

— R. Landauer, *Physics Today, 1991*

We are in the era where information is processed with nano-scale electronic chips which contain billions of transistors. The density of transistors on a chip keeps double roughly once every two years following *Moore's law*. The prediction has been approximately holding since 1965. Nonetheless, the size of the transistor currently is approaching 10 nm and enters a regime where our technology of photolithography for manufacturing electronic chips is fundamentally challenging, and where electrons transports start to be affected by quantum effects. Some say Moore's law will end soon. While nowadays the need of high-performance and efficient computing is never stopping. Especially this need has been pushed forward by the rise of our trending behaviour of collecting big data and distilling collective patterns of information via machine-learning-based algorithms. This class of algorithms requires a better optimal way for computation.

One of the great route is to step forward onto *quantum computing*; processing of information with a physical system governed by quantum mechanics, rather than classical mechanics. Historically, the idea of bundling quantum computer dates back to around 1981 when our famous physicist, Richard Feynman, said that,

> *"Nature isn't classical, dammit, and if you want to make a simulation of nature, you'd better make it quantum mechanical, and by golly, it's a wonderful problem because it doesn't look so easy."*
>
> – R. Feynman, at a conference co-organized by MIT and IBM, 1981

In essence, quantum computer can provide an efficient speed advantage over in-used classical computers which are built upon the model of computation known as *Turing machine*. One of the famous examples of computational problems, that quantum computer can solve efficiently, is Shor's algorithm [Shor, 1997], the problem of finding the prime factors of an integer. This problem has still had no efficient algorithm on a classical computer and has been widely used nowadays in cryptography. Accordingly, the performance of Shor's algorithm indicates a power of quantum computer beyond a classical computer and attracted a lot of attentions to quantum computer later on. Interestingly, we know quantitatively very little about how powerful quantum computer is in term of computational complexity theory and what kind exactly of physical resources give a quantum computer its efficiency [Nielsen and Chuang, 2010].

To date, Feynman is right, *"it's a wonderful problem because it doesn't look so easy."*. It has been almost four decades since we have a model of quantum-based computation [Deutsch, 1985, Nielsen and Chuang, 2010]. Various physical platforms, namely, superconducting, trapped-ion, nuclear magnetic resonance, linear optics, etc., have been explored for building a quantum computer. Nowadays we are still under the process of research and devel-

opment. The best progress reported so far is the use of programmable 53 superconducting qubits to demonstrate *quantum advantage*[1], in the task of sampling the output of pseudo-random quantum circuit [Arute et al., 2019]. A long debate on which physical platform will be technologically preferable is ongoing, not like in the early development of classical computer when the semiconductor technology for manufacturing transistors distinctly outperforms other physical platforms including optical computing. Linear optical quantum information processing is still considered as one of the most promising candidates for quantum computing [Kok et al., 2007, O'Brien et al., 2009, Wang et al., 2019b]. In this dissertation, we are going to focus on the development of linear optics for quantum applications.

In addition to information processing on electronic chips, communication, i.e., transmitting information via light through optical fibres has been also omnipresent spanning from a short distance in a computer server room to a long-distance communication across oceans. This is thanks to high-speed, high-bandwidth, low attenuation, and low-cost communication provided by optical fibres [Agrawal, 2016]. Likewise to the requirement for high-performance information processing, the requirement in the high capacity of optical communication also rise exponentially at a faster rate than Moore's law (doubling over nine months) due to the use of internet [Agrawal, 2016]. One of the solutions in optical communications that is more and more considered is *space-division multiplexing*, where multiple spatial channels are parallelly utilized using multicore or multimode optical fibre [Richardson et al., 2013]. Unfortunately, the presence of cross-talk between modes and differences in group velocity between modes in multimode fibre (intermodal dispersion) limit the use of this technology. Nowadays, the use of multimode fibre is restricted to a short-distance optical communication and the number of transverse spatial modes cannot be easily scaled up [Agrawal, 2016].

Light transport through a multimode fibre is considered to be too complex such that optical waveguide theory simply fails to accurately describe its scattering behaviour. Thanks to the advances in the technology of optical wavefront control over the last decade [Rotter and Gigan, 2017], a characterization of optical response (transmission matrix) of multimode fibre is now possible using spatial light modulator. This led directly to applications in imaging [Čižmár and Dholakia, 2012, Choi et al., 2012]. For instance, a multimode fibre can used as a compact lensless endoscope: transmitting a high-resolution image from deep brain tissue [Ohayon et al., 2018, Vasquez-Lopez et al., 2018, Turtaev et al., 2018].

Instead of considering as usual light mixing in multimode fibre as a detrimental process, whether for imaging or for communication purposes, we here explore how a multimode fibre provides a useful route for a mixture of information. The objective of this dissertation is to exploit the complex mode mixing of multimode fibre using the technology of optical wavefront control for quantum information processing. In particular, we demonstrate a potential route for implementing a programmable linear optical network for quantum applications. We successfully demonstrate the manipulation of two-photon quantum interferences in various linear optical networks including the implementation of tunable coherent absorption experiments. Furthermore, understanding transport of non-classical states of light through a complex environment is fundamentally interesting. We study statistical properties of scattered lights from various non-classical states including frequency-entangled biphoton states and experimentally show that we can extract infor-

[1] A physical implementation that shows that a device governed on the quantum mechanics outperforms the state-of-the-art classical computer in a specific computation task.

mation about input states and use those information for a purpose of state classification. Our work therefore demonstrate an efficient alternative to integrated circuits for optical quantum information processing and shows a usefulness of a complex-mixing-based optical device for modern quantum optical experiments.

This dissertation is organized as follows:

- In Chapter 1, we introduce the basic tools for understanding nonclassical light and its properties. In particular, we focus on the generation of non-classical state with optical parametric down-conversion process and its quantum interference. We then describe the model of building quantum computing with linear optics. Optical implementations of reconfigurable arbitrary linear transformation are described, and a review on quantum integrated optics is provided.
- In Chapter 2, we present an implementation of programmable optical linear networks across spatial-polarization degrees of freedom. First, we provide description of speckle phenomena, mixing property of a multimode fibre, and wavefront control of light propagating through complex optical systems. Second, an experimental setup and procedure for constructing a programmable optical network is described. Then, two-photon interferences on various programmable optical circuits are experimentally reported. Finally, we provide a theoretical model and numerical and experimental investigations on the scalability and programmability of the proposed architecture for programmable optical linear networks.
- In Chapter 3, the programmable optical linear network is applied to explore two intriguing related phenomena stemming from a non-unitary evolution of a two-photon state on a lossy beamsplitter, which are two-photon absorption and coherent absorption effect in a quantum regime. For each phenomenon, we first introduce the concept and its relevance for applications. We then report theoretical calculations and experimental results.
- In Chapter 4, we use our experimental platform as random projector for quantum state classification. Several ground-truth states were experimentally tested and they demonstrated substantial statistical signatures on photocurrent and second-order intensity correlations which can be used to classify a state and measure its purity and dimensionality, indistinguishability without *a priori* knowing its density matrix.

# 1

# Background

*"All the fifty years of conscious brooding have brought me no closer to the answer to the question: What are light quanta? Of course today every rascal thinks he knows the answer, but he is deluding himself."*

— A. Einstein, *1951*

In the first part of this chapter, we introduce a general background for this dissertation. First, a short introduction to the properties of non-classical light is presented in section 1.1. Next, two essential theoretical aspects that are underlying experiments presented throughout the dissertation are provided: a spontaneous parametric down-conversion source (section 1.2) and quantum interference (section 1.3). In the second part of the chapter, we aim to support a short review in order to emphasize the importance and challenges in modern quantum optic experiments and quantum information processing tasks. We provide in particular the general concept of linear optical quantum computing in section 1.4, of reconfigurable unitary optical networks in section 1.5, of the state-of-the-art integrated quantum optics in section 1.6, and on the boson sampling problem in section 1.7. We finally conclude and state our scientific problem and set the objectives of our study in section 1.8.

## Contents

## 1.1 | Light in a nutshell

Do we understand how light does behave? My honest answer is: more or less. On the history of our understanding, the description of light became more accurate in prediction its behaviours only a couple of hundred years ago. A long development of theory and scientific debates have been interchanging with experimental observations, for example, interference and diffraction, electromagnetic radiation, a black-body radiation, photoelectric effect, absorption, spontaneous and stimulated emissions, and relativistic effects. The accepted theory of light we have nowadays is the quantum electrodynamic [Mandel and Wolf, 1995] and so far there has been no experimental evidence challenging this theory. The mainstream interpretation of light relies on the concept of wave-particle duality [Mandel and Wolf, 1995]. The electromagnetic (EM) field is discretized in quanta, a discrete unit of energy, known as a photon. In this section, we introduce the quantization of the EM field in order to provide notations used in this dissertation and to highlight the key features of light presented in our experiments.

### 1.1.1 Quantized electromagnetic field

We start by considering a quantized EM field. The complex electric field operator is defined as,

$$\begin{aligned}\hat{\mathbf{E}}(\mathbf{r},t) &= \hat{\mathbf{E}}^{(+)}(\mathbf{r},t) + \hat{\mathbf{E}}^{(-)}(\mathbf{r},t) \\ &= i\sum_i \zeta_i \left[\hat{a}_i \mathbf{u}_i(\mathbf{r}) e^{-i\omega_i t} + \hat{a}_i^\dagger \mathbf{u}_i^*(\mathbf{r}) e^{i\omega_i t}\right],\end{aligned} \tag{1.1}$$

where $\zeta_i = \sqrt{\frac{\hbar\omega_i}{2\varepsilon_0}}$ is a constant and $\mathbf{u}_i(\mathbf{r})$ are the mode functions of a propagating electromagnetic wave of angular frequency $\omega_i$, that satisfies, in vacuum:

$$\left(\nabla^2 + \frac{\omega_i^2}{c^2}\right)\mathbf{u}_i(\mathbf{r}) = 0, \quad \nabla\cdot\mathbf{u}_i(\mathbf{r}) = 0, \tag{1.2}$$

where $c$ is the speed of light. One can define the mode functions that form a complete orthonormal set,

$$\int \mathbf{u}_i^*(\mathbf{r})\mathbf{u}_{i'}(\mathbf{r})\mathrm{d}\mathbf{r} = \delta_{ii'}. \tag{1.3}$$

The quantization of the EM field is established by the non-Hermitian operators $\hat{a}_i^\dagger$ and $\hat{a}_i$. They obey the boson commutation relations,

$$\left[\hat{a}_i, \hat{a}_j^\dagger\right] = \delta_{ij}, \quad [\hat{a}_i, \hat{a}_j] = \left[\hat{a}_i^\dagger, \hat{a}_j^\dagger\right] = 0. \tag{1.4}$$

And the Hamiltonian operator of the quantized EM field is

$$\begin{aligned}H &= \sum_i \frac{1}{2}\hbar\omega_i(\hat{a}_i^\dagger\hat{a}_i + \hat{a}_i\hat{a}_i^\dagger), \\ &= \sum_i \hbar\omega_i(\hat{a}_i^\dagger\hat{a}_i + \frac{1}{2}).\end{aligned} \tag{1.5}$$

Light is described by an ensemble of modes which are represented by independent quantum harmonic oscillators. The noncommutativity of $\hat{a}^\dagger$ and $\hat{a}$ indicates a quantum feature of

the EM field. The first important feature is presented in the second term of Eq. 1.5 and known as vacuum fluctuation energy. This means that the energy of the EM field can be non-zero even if there is no photon occupied in the field. The second feature stems from the first term which is quadratic in $\hat{a}^\dagger$ and $\hat{a}$. This means that each mode of the EM field can be identified with photon, a discrete unit of energy occupying the particular mode. Photons obey Bose statistics thus each mode of EM field can be occupied by an arbitrary number of photons. We can measure the number of photons via the photon number operator:

$$\hat{N}_i \equiv \hat{a}_i^\dagger \hat{a}_i. \tag{1.6}$$

A pure quantum state in each mode is described by a state vector $|\psi\rangle$ in the Hilbert space. A pure quantum state of the entire EM field is then defined in a tensor product space of the Hilbert spaces for all of the individual modes. This space includes all possible separable and entangled states. In general, a classical ensemble of pure quantum states is described by the density matrix $\rho$ defined as

$$\rho \equiv \sum_j p_j \left|\psi_j\right\rangle \left\langle\psi_j\right|, \tag{1.7}$$

where $p_j$ is the weight of each pure state $|\psi_j\rangle$. The purity $\mathcal{P}$ of a state is determined via $\mathcal{P} = \operatorname{Tr} \rho^2$, which is 1 if the state is pure and less than 1 if the state is mixed.

### 1.1.2 Relevant states

There are three classes of single-mode states that we would like to introduce here. The first class is composed of photon number Fock states. They are eigenstates of the photon number operator $\hat{N}$, meaning that they have a precise number of photons,

$$\hat{N} \left|N\right\rangle = N \left|N\right\rangle. \tag{1.8}$$

For example, $|0\rangle$ is a vacuum state with property $\hat{a}\,|0\rangle = 0$, $|1\rangle = \hat{a}^\dagger\,|0\rangle$ is a single-photon state, and $|N\rangle = \frac{\hat{a}^{\dagger N}}{\sqrt{N!}}\,|0\rangle$ is a $N$-photon state.

The second class corresponds to the coherent states. These states have a well-defined amplitude and phase and are the eigenstates of annihilation operator $\hat{a}$: $\hat{a}\,|\alpha\rangle = \alpha\,|\alpha\rangle$, where $\alpha$ is a complex number. They were used for a representation of a classical EM field generated by a laser that operate well above a lasing threshold [Glauber, 1963a, Mandel and Wolf, 1995]. They have minimum uncertainty in amplitude and phase allowed by the uncertainty relations. Such state can be represent as a superposition of Fock states,

$$\left|\alpha\right\rangle = e^{-\frac{1}{2}|\alpha|^2} \sum_{N=0}^{\infty} \frac{\alpha^N}{\sqrt{N!}} \left|N\right\rangle. \tag{1.9}$$

The third class is that of squeezed states, which is a generalized class of minimum-uncertainty states. The word *squeezing* refers that noise in one of field quadratures is less than a coherent state while other quadrature is larger. Squeezed states are eigenstates of the squeezed operator $S(\xi)$,

$$S(\xi) = \exp\left(\frac{1}{2}\xi \hat{a}^{\dagger 2} - \frac{1}{2}\xi^* \hat{a}^2\right), \tag{1.10}$$

where $\xi = re^{i\varphi}$ controls the degree and quadrature of squeezing. For the single-mode squeezed-vacuum state, the state reads

$$\begin{aligned}|\xi\rangle &= S(\xi)\,|0\rangle \\ &= \frac{1}{\sqrt{\cosh r}} \exp\left(e^{i\varphi}\tanh r \frac{a^{\dagger 2}}{2}\right)|0\rangle \quad = \frac{1}{\sqrt{\cosh r}} \sum_{N=0}^{\infty} e^{iN\varphi}(\tanh r)^N \frac{\sqrt{(2N)!}}{N!2^N}\,|2N\rangle\,.\end{aligned} \tag{1.11}$$

The state is a superposition of an even number of photons, and can be experimentally produced via spontaneous parametric down-conversion process (SPDC) which we describe in section 1.2.

### 1.1.3 Photodetection theory

In the optical domain, all measurements are done with photodetectors and they respond to EM fields via an absorption process. The probability of absorption is predicted via the interaction of EM fields and matter (a detector) and is related to the normally-ordered correlation of the EM field [Glauber, 1963b, Mandel and Wolf, 1995, Agarwal, 2012]. In general, a set of photodetectors measure a normally-ordered correlation of the EM fields and accordingly provide information of the state of the EM fields. We introduce two types of measurements that will be used throughout the dissertation. Firstly, the intensity of a state at the position $\mathbf{r}_i$ with an integration time $\tau_C$ is related to

$$I_i(\mathbf{r}_i) \propto \int_0^{\tau_C} dt\, \mathrm{Tr}\left[\rho \mathbf{E}^{(-)}(\mathbf{r}_i,t)\mathbf{E}^{(+)}(\mathbf{r}_i,t)\right] \tag{1.12}$$

where $\rho$ is the density matrix of a state that is measured. Secondly, the second-order intensity correlation between two detectors at the position $\mathbf{r}_i$ and $\mathbf{r}_j$ with a coincidence windows $\tau_C$ reads

$$G^{(2)}_{ij}(\mathbf{r}_i,\mathbf{r}_j) \propto \int_0^{\tau_C} dt \int_0^{\tau_C} dt'\, \mathrm{Tr}\left[\rho \mathbf{E}^{(-)}(\mathbf{r}_i,t)\mathbf{E}^{(-)}(\mathbf{r}_j,t')\mathbf{E}^{(+)}(\mathbf{r}_j,t')\mathbf{E}^{(+)}(\mathbf{r}_i,t)\right] \tag{1.13}$$

## 1.2 | Spontaneous parametric down-conversion

The non-classical states used in the dissertation are generated from spontaneous parametric down-conversion process (SPDC). The SPDC is a quantum nonlinear process involving the energy exchanged between three EM fields (three-wave mixing process). The first wave refers to the pump beam $E_p$ which is down-conversed into two generated beams, known as signal $E_s$ and idler $E_i$ beams with the conservation of energy and momentum as depicted in Fig. 1.1. The SPDC occurs in a non-linear crystal lacking inversion symmetry (non-centrosymmetry) [Boyd, 2008]. Such crystals are characterized by the nonlinear susceptibility tensor $\chi^{(2)}_{ijk}$. We consider here the co-linear type-II SPDC process [Bachor and Ralph, 2004] where signal and idler beams are generated in a perpendicular polarization to each other, thereby, the process involve only one scalar element of nonlinear susceptibility, noted as $\chi^{(2)}$. The classical Hamiltonian of the three-wave mixing process can be written as,

$$H(t) \propto \int d^3\mathbf{r}\chi^{(2)}\mathbf{E}^*_p(\mathbf{r},t)\mathbf{E}_s(\mathbf{r},t)\mathbf{E}_i(\mathbf{r},t). \tag{1.14}$$

Replacing the EM fields with the quantized EM operators (Eq. 1.1), the Hamiltonian of the three-wave mixing concerning with the SPDC process is

$$\hat{H}(t) \propto \int d^3\mathbf{r}\chi^{(2)}\hat{\mathbf{E}}_s^{(-)}\hat{\mathbf{E}}_i^{(-)}\hat{\mathbf{E}}_p^{(+)} + h.c., \tag{1.15}$$

where $\hat{\mathbf{E}}_j^{(\pm)}$ is the positive (negative) frequency component of EM operators of a given $j$ beam. The subscripts $j \in \{s, i, p\}$ refers to signal (s), idler (i), and pump (p) beams, respectively. The first term is related to the SPDC process as represented in Fig. 1.1, and the second corresponds to time-reversed process. In the full form, the Hamiltonian of Eq. 1.14, is expressed as

$$\begin{aligned}\hat{H}(t) \propto \int dz\chi^{(2)} \int d\omega_s \sqrt{\frac{\omega_s}{n\left(\omega_s\right)}}\hat{a}_s^{\dagger}\left(\omega_s\right) e^{i\omega_s t - ik_s z} \times \\ \int d\omega_i \sqrt{\frac{\omega_i}{n\left(\omega_i\right)}}\hat{a}_i^{\dagger}\left(\omega_i\right) e^{i\omega_i t - ik_i z} \int d\omega_p \sqrt{\frac{\omega_p}{n\left(\omega_p\right)}}\hat{a}_p\left(\omega_p\right) e^{-i\omega_p t + ik_p z} + h.c.\end{aligned} \tag{1.16}$$

We assume that the refractive indices, $n(\omega_s), n(\omega_i), n(\omega_p)$, and the central frequencies of three waves $\omega_s, \omega_i, \omega_p$ are constant under the integrals over frequencies of interest. By rearranging the terms and integrating over the length $L$ of a non-linear crystal, we obtain

$$\hat{H}(t) \propto \chi^{(2)} L \int d\omega_s d\omega_i d\omega_p \hat{a}_s^{\dagger}\left(\omega_s\right)\hat{a}_i^{\dagger}\left(\omega_i\right)\hat{a}_p\left(\omega_p\right)\Phi\left(\omega_s, \omega_i; \omega_p\right) e^{-i(\omega_p - \omega_s - \omega_i)t} + h.c., \tag{1.17}$$

where $\Phi\left(\omega_s, \omega_i; \omega_p\right)$ is defined as,

$$\Phi\left(\omega_s, \omega_i; \omega_p\right) = \frac{1}{L}\int_0^L dz e^{i(k_p - k_s - k_i)z} = \exp\left(i\frac{\Delta k L}{2}\right)\mathrm{sinc}\left(\frac{\Delta \mathrm{kL}}{2}\right), \tag{1.18}$$

This term corresponds to the phase-matching condition, i.e., the conservation of momentum in the system: $\Delta k = k_p - k_s - k_i$ (Fig. 1.2b). The phase-matching condition depends on the geometry and on the optical properties of the non-linear crystal, for a particular wavelength and the beam profile of the pump field $k_p$. All $k_j$ are implicitly frequency dependent, $k_j = n(\omega_j)\omega_j/c$. The phase-matching condition determines the direction of signal and idler fields. Generally, the down-converted fields can be distributed genuinely over multiple traverse spatial modes depending on the phase-matching condition. In our experiment, we designed the SPDC source in co-linear configuration ($k_p \parallel k_s \parallel k_i$) with a periodically-polled non-linear crystal. Besides, we collect signal and idler beams into single-mode fibres, such that the transverse spatial correlations are not considered here (we refer to a tutorial [Schneeloch and Howell, 2015] regarding transverse spatial correlations of SPDC).

Furthermore, we consider the pump field as an intense coherent state and the down-conversion efficiency as being low. Then it is safe to assume the pump state remains constant during the evolution and can be replaced by the coherent EM field with a spectral profile $\mathtt{P}(\omega_p)$ defined as

$$\mathtt{P} = \int d\omega_p \mathtt{P}(\omega_p). \tag{1.19}$$

Under the low-efficiency SPDC regime, the evolution of a state under the Hamiltonian can be conveniently approximated to the first-order expansion: $U(t) = \exp\left(-\frac{i}{\hbar}H(t)t\right) \approx$

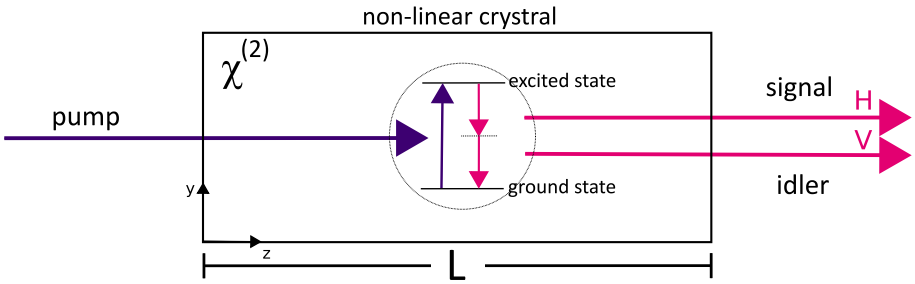


**Figure 1.1 – Spontaneous parametric down-conversion process**: the pump beam propagates through a non-linear crystal which has $\chi^{(2)}$. A photon from the pump beam of a higher energy is probabilistically spontaneously conversed into a pair of photons of lower energy, labelled signal photon (H) and idler photon (V). Energy and momentum are conserved in the process.

$\mathbb{1} - \frac{i}{\hbar}\int \hat{H}(t)dt$. The unitary evolution $U(t)$ reads

$$\begin{aligned} U(t) &\approx 1 - \frac{i}{\hbar}\int dt\hat{H}(t) \\ &= 1 + G\int dt \int d\omega_s d\omega_i d\omega_p \hat{a}_s^\dagger(\omega_s)\,\hat{a}_i^\dagger(\omega_i)\,\mathrm{P}(\omega_p)\Phi(\omega_s,\omega_i;\omega_p)\,e^{-i(\omega_p-\omega_s-\omega_i)t} + h.c. \\ &= 1 + 2\pi G\int d\omega_s d\omega_i \hat{a}_s^\dagger(\omega_s)\,\hat{a}_i^\dagger(\omega_i)\,\mathrm{P}(\omega_s+\omega_i)\Phi(\omega_s,\omega_i;\omega_p) + h.c., \end{aligned} \tag{1.20}$$

where $G$ is a constant. Additionally, we also assume that the Hamiltonian is time-independent. By considering these assumptions, the Hamiltonian in Eq. 1.17 can be written in a simplified form [Agarwal, 2012]:

$$H = i\hbar g(\hat{a}_s^\dagger\hat{a}_i^\dagger + h.c.), \tag{1.21}$$

where $g$ consists coupling constant related to $\chi^{(2)}$, the geometrical and optical parameters of the crystal, and the amplitude of a classical pump beam. The evolution of Hamiltonian has an identical form to the action of the two-mode squeezing operator $S(g)$ [Agarwal, 2012].

$$S(g) = \exp\left(-\frac{i}{\hbar}Ht\right) = \exp\left(g\hat{a}_s^\dagger\hat{a}_i^\dagger + h.c.\right), \tag{1.22}$$

The two-mode squeezing operator can be expressed in a similar form as in the single-mode squeezing operator (Eq. 1.10) [Agarwal, 2012]:

$$S(g) = \exp\Big(\tanh g\hat{a}_s^\dagger\hat{a}_i^\dagger\Big)\exp\Big[-(\ln\cosh g)(\hat{a}_s^\dagger\hat{a}_s + \hat{a}_i^\dagger\hat{a}_i + 1)\Big]\exp(\tanh g\hat{a}_s\hat{a}_i), \tag{1.23}$$

We consider the initial state to be the two-mode vacuum state $|0\rangle_1|0\rangle_2$. The evolution of the initial state via the two-mode squeezing operator is

$$\begin{aligned} |\phi\rangle &= S(\zeta)|0\rangle_s|0\rangle_i \\ &= \frac{1}{\cosh g}\exp\Big(\tanh g\hat{a}_s^\dagger\hat{a}_i^\dagger\Big)|0\rangle_s|0\rangle_i \\ &= \frac{1}{\cosh g}\sum_{N=0}^{\infty}(\tanh g)^N|N,N\rangle. \end{aligned} \tag{1.24}$$

The SPDC thus generates the two-mode squeezed vacuum. In the photon-number basis, we find that the probability $P_{N,M}$ of occupying $N$ photons in the signal mode and $M$ photons in the idler mode is

$$P_{N,M} = \frac{\delta_{NM}}{\cosh^2 g}(\tanh g)^{2N}. \tag{1.25}$$

Therefore we can conclude that the detection of N photons in the signal mode infers the presence of N photons in the idler mode and vice versa. Furthermore, the total number of photons in both modes is always even. Under low-efficiency SPDC regime ($\sinh^2 g \ll 1$), only low-order term, i.e., a vacuum state and a two-photon state, dominates. We can post-select on the two-photon state, which originates from the first-order expansion of the evolution of Hamiltonian. The two-photon state reads

$$\left|\psi^{(1)}\right\rangle \propto \int d\omega_s d\omega_i \mathtt{P}\left(\omega_s+\omega_i\right)\Phi\left(\omega_s,\omega_i;\omega_s+\omega_i\right)\hat{a}_s^{\dagger}\left(\omega_s\right)\hat{a}_i^{\dagger}\left(\omega_i\right)|0\rangle_s|0\rangle_i. \tag{1.26}$$

The state, also called the biphoton state and the photon pairs, describes a superposition of signal and idler frequency modes with the amplitudes weighted by the product of the pump amplitude $\mathtt{P}(\omega_s+\omega_i)$ and the phase-matching condition $\Phi(\omega_s,\omega_i;\omega_p)$. The product is known as the joint spectral amplitude (JSA) and also called the biphoton wavefunction,

$$\Psi\left(\omega_s,\omega_i\right) = \mathtt{P}\left(\omega_s+\omega_i\right)\Phi\left(\omega_s,\omega_i;\omega_s+\omega_i\right). \tag{1.27}$$

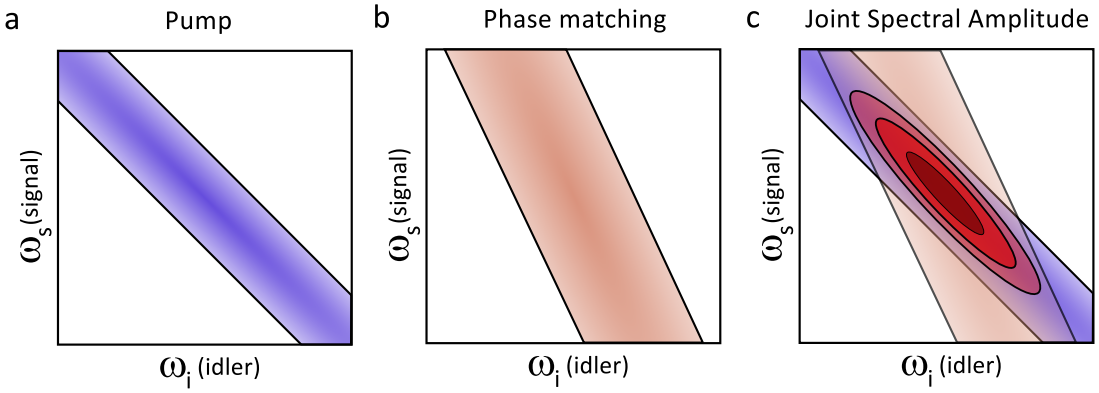


**Figure 1.2 – Joint spectrum amplitude of SPDC**: The spectral correlations of the photons produced in downconversion (c) are a product of the pump profile owing to the conversation of energy (a) and the phase-matching function owing to the conservation of momentum (b). The phase-matching function depends on the optical properties of a non-linear crystal. In our experiment, a non-linear crystal provides the phase-matching condition like sketched in (b). (c) The joint spectral amplitude function $\psi(\omega_i,\omega_s)$ shows the anti-correlation in frequency.

It characterizes the spectral correlation of the two-photon state generated in the SPDC process. In general, the JSA is not separable, $\Psi\left(\omega_s,\omega_i\right) \neq \Psi_s(\omega_s)\Psi_i(\omega_i)$, As a consequence, the photon pairs are entangled in their frequency degree of freedom. An example of JSA is depicted in Fig. 1.2. The first term $\mathtt{P}\left(\omega_s+\omega_i\right)$ related to a pump profile provides the energy conservation to the photon pairs (Fig. 1.2a), while the phase-matching condition contributes to the momentum conservation (Fig. 1.2b). Normally, the downconversed photon pairs show anti-correlation in their frequencies [Grice and Walmsley,

1997] which is also the case of our designed SPDC source. We note that it is possible to engineer the phase-matching condition such that the photon pairs are in separable or correlated state [Grice et al., 2001, Mosley et al., 2008]. A separable biphoton state is required for using a SPDC source as a heralded single-photon source with high purity. One of the simple way to improve the purity is by using spectral filtering, however it also reduce heralding efficiency [Meyer-Scott et al., 2017]. In our experiment, the broadband spectral filter is added only to remove background light from the pump beam, and not to filter the spectrum of photon pairs. The details of our experimental setup are reported in Appendix A.

## 1.3 | Quantum interference

Interference is one of the most basic behaviours of a wave. The phenomenon of interferences can be correctly interpreted for intensities either as the interference of the classical electromagnetic wave or as the interference of probability amplitudes in the quantum theory. The failure of the classical theory happens only in experiments of higher-order interference, involving the correlation of intensities (photoncounts) [Glauber, 1963b, Mandel and Wolf, 1995, Ou, 2007]. For interference phenomena that cannot be explained by the classical theory, we refer to quantum interferences [Pan et al., 2012].

One of the well-known experiment is the Hanbury-Brown and Twiss experiment [Loudon, 1980] where photoncount statistic of an input state of light can be characterised by sending the state to one input port of a beamsplitter and measuring a temporal correlation in photoncounts at both outputs of the beamsplitter. Thermal state, coherent state and single-photon state result in different temporal correlation patterns regarding their photoncount statistics which are sub-Poissonian, Poissonian, and super-Poissonian, respectively [Mandel and Wolf, 1995]. For the single-photon state, the temporal correlation in photoncounts goes to zero, indicating that a photon is detected only at one of the detectors. This is a signature of the single-photon nature of the source. In the following, we focus on quantum interference for a biphoton state, which is a key phenomenon observed in this dissertation.

### 1.3.1 Two-photon interference on a beamsplitter

Let us consider the two separable single-photon states injected on two ports of the beamsplitter as depicted in Fig. 1.3a. In the first input port, the single-photon state with a spectral amplitude function $\Psi_1(\omega)$ is

$$|1_{\Psi_1}\rangle = \int d\omega_1 \Psi_1(\omega_1)\hat{a}_1^\dagger(\omega_1)\,|0\rangle_1\,, \tag{1.28}$$

where $\hat{a}_1^\dagger(\omega)$ is a creation operator acting on a single frequency mode $\omega$ in the first input of the beamsplitter. The state is normalized such that $\int |\Psi_1(\omega)|^2 d\omega = 1$. Similarly, in the second input port, the single-photon state with a spectral amplitude function $\Psi_2(\omega)$ arrives at the beamsplitter with a time delay $\delta$. The state reads

$$|1_{\Psi_2}\rangle = \int d\omega_2 \Psi_2(\omega_2)\hat{a}_2^\dagger(\omega_2)e^{-i\omega_2\delta}\,|0\rangle_2\,. \tag{1.29}$$

The state is normalized such that $\int |\Psi_2(\omega)|^2 d\omega = 1$. Overall, the input state is,

$$\left|\psi^{\text{in}}\right\rangle = \int d\omega_1 \Psi_1(\omega_1)\hat{a}_1^\dagger(\omega_1) \int d\omega_2 \Psi_2(\omega_2)\hat{a}_2^\dagger(\omega_2)e^{-i\omega_2\delta}\,|0\rangle_1\,|0\rangle_2 = |1_{\Psi_1}\rangle\,|1_{\Psi_2}\rangle\,, \tag{1.30}$$

The beamsplitter (BS) can mathematically be modelled as the linear transformation mapping input modes to output modes as follows,

$$\begin{pmatrix} \hat{a}_1 \\ \hat{a}_2 \end{pmatrix} = \mathrm{BS} \begin{pmatrix} \hat{a}_1 \\ \hat{a}_2 \end{pmatrix}, \tag{1.31}$$

where,

$$\mathrm{BS} \equiv \frac{1}{\sqrt{2}} \begin{pmatrix} 1 & 1 \\ 1 & -1 \end{pmatrix}. \tag{1.32}$$

This physically corresponds to the evolution of the state of the form:

$$\begin{aligned} \left|\psi^{\mathrm{out}}\right\rangle &= \mathrm{BS}\left(\left|\psi^{\mathrm{in}}\right\rangle\right) \\ &= \frac{1}{2}\int d\omega_1 \Psi_1(\omega_1)(\hat{a}_1^\dagger(\omega_1) + \hat{a}_2^\dagger(\omega_1)) \int d\omega_2 \Psi_2(\omega_2)(\hat{a}_1^\dagger(\omega_2) - \hat{a}_2^\dagger(\omega_2)) e^{-i\omega_2\delta} \left|0\right\rangle_1 \left|0\right\rangle_2 \\ &= \frac{1}{2}\int d\omega_1 \Psi_1(\omega_1) \int d\omega_2 \Psi_2(\omega_2) e^{-i\omega_2\delta} \times \\ &\quad \left(\hat{a}_1^\dagger(\omega_1)\hat{a}_1^\dagger(\omega_2) + \hat{a}_2^\dagger(\omega_1)\hat{a}_1^\dagger(\omega_2) - \hat{a}_1^\dagger(\omega_1)\hat{a_2}^\dagger(\omega_2) - \hat{a}_2^\dagger(\omega_1)\hat{a}_2^\dagger(\omega_2)\right) \left|0\right\rangle_1 \left|0\right\rangle_2 \end{aligned} \tag{1.33}$$

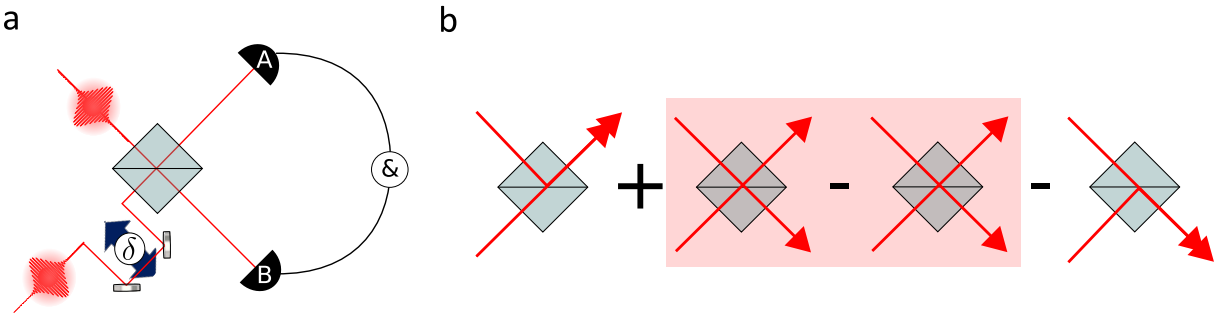


**Figure 1.3 – Two-photon interference**: (a) Experimental scheme: Biphoton states are sent to the beamsplitter with time delay $\delta$ on one of the input arms. A and B detectors measure two-fold coincidence counts with coincidence electronics. (b) Diagrams of four different cases of two photons interference on a beam splitter. The signs correspond to signs in front of terms in Eq. 1.33. The diagrams in a red area cancel each other owing to indistinguishability.

The output state is in a superposition of all four terms in Eq. 1.33. As the time delay $\delta$ is shifted to zero, the two single-photon states arrive at both detectors simultaneously. And in case that the spectral amplitude functions $\Psi_1(\omega)$ and $\Psi_2(\omega)$ are identical, thus the two input single-photon states are completely indistinguishable. The second and third terms of the Eq. 1.33 completely cancels one another. It results in the output state being in the superposition of two possibilites: both photons occupy in one output mode or both in the other. The outcome state is also known as N00N state[1] with N=2,

$$\left|\psi^{\mathrm{out}}\right\rangle = \frac{1}{\sqrt{2}}(|2_1, 0_2\rangle - |0_1, 2_2\rangle). \tag{1.34}$$

One can study the outcome of the interference by measuring the photoncounts (intensity) at each output and the two-fold coincidence counts between two outputs. Interestingly,

[1]The N00N state is also called as a path-entangled state or mode-entangled state.

the photon counts give a constant intensity profile as a function of the time delay [Kim and Grice, 2003]. From the classical interpretation, the effect is similar to the interference of completely incoherent light. In contrast, the effect of interference is presented on the second-order correlation function. Considering the outcome N=2 N00N state in the case of indistinguishability, one finds that the probability of detecting one photon in each output port of the beamsplitter is null. The effect is known as *photon bunching effect* [Fearn and Loudon, 1989] which refers to that two input single-photon states getting bunched into one of the output ports and also known as *quantum destructive interference* [Tichy et al., 2010] which means the destructive interference between two probability amplitudes. By tuning the time delay $\delta$, the second and third terms of the Eq. 1.33 no longer cancel each other, thus the two-fold coincidence counts consequently increase to a classical limit where one has the half of a chance of detecting one photon in each output port simultaneously. This two-photon interference was first observed by Chung Ki Hong, Zhe Yu Ou and Leonard Mandel [Hong et al., 1987] and is now known as the Hong-Ou-Mandel (HOM) interference. The results of original observation is shown in Fig. 1.4.

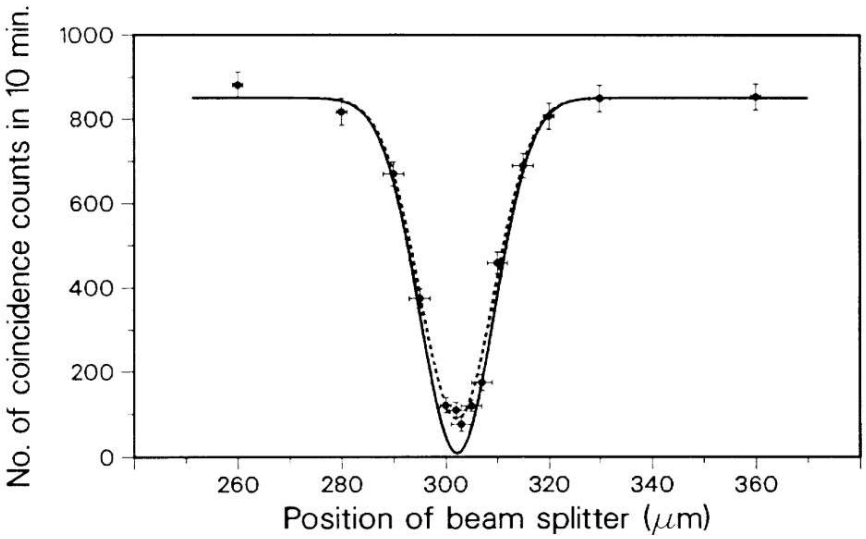


**Figure 1.4 – Hong-Ou-Mandel interference**: By scanning the delay position (*the position of beam splitter* in the figure), two-fold coincidence counts are recorded between two outputs of the beamsplitter. The results is known as the HOM interference where the position of dip is a position where biphoton state are indistinguishable. The width of HOM interference determine the coherence length of the incident biphoton state. Adapted from [Hong et al., 1987]

The concept of indistinguishability in quantum optics is strongly related to the HOM interference. The indistinguishability can be directly characterised by measuring the visibility of the two-photon interference, defined as,

$$V = \frac{P(\delta \to \infty) - P(\delta = 0)}{P(\delta \to \infty)}, \tag{1.35}$$

where $P(\delta)$ is the probability of detecting two-fold coincidences at a given time delay $\delta$. The probability, $P(\delta \to \infty)$ is detected at a certain delay that is longer that the coherence length $l_c$ of the input state ($\delta > l_c$). The complete indistinguishability of a two-photon input state corresponds to the visibility of one. In general, the HOM interference also occurs with a frequency-entangled biphoton state (Eq. 1.26). The indistinguishability of

a biphoton state refers to the spectral overlap integral $I(\delta)$, that is

$$V(\delta) = I(\delta) = \int_0^\infty d\omega_1 \int_0^\infty d\omega_2 \Psi(\omega_1, \omega_2) \Psi^*(\omega_2, \omega_1) \exp[-i(\omega_1 - \omega_2)\delta]. \tag{1.36}$$

Distinguishability of a biphoton state therefore can originate from the asymmetric exchange in the JSA function: $\Psi(\omega_1, \omega_2) \neq \Psi(\omega_2, \omega_1)$. Furthermore, additional degrees of freedom such as, polarization, transverse spatial mode, that label differently a state during the evolution, also degrade the indistinguishability of the state; thereby the visibility of the HOM interference. Likewise, a mixed input state also results in the degradation of visibility. The HOM effect can be mimicked using interference of classical EM wave, however, the maximal value that the visibility can attain has been shown to be at most 0.5 [Mandel, 1983, Ou, 1988, Rarity et al., 2005]. A visibility greater than 0.5 is thus considered to be a sign of non-classical phenomenon.

The HOM interference has been observed in different photonic degrees of freedom, for example, transverse spatial mode [Zhang et al., 2016], radial degree of freedom [Karimi et al., 2014b] and structured mode (a transverse spatial mode where polarization varies across beam profile) [D'Ambrosio et al., 2019]. Moreover, the HOM effect has been observed with light in a microwave frequency [Lang et al., 2013], with plasmons [Heeres et al., 2013], and with a matter wave [Lopes et al., 2015, Kaufman et al., 2018]. In term of applications, in addition to the fundamental test of indistinguishability, the HOM effect plays an important role in the optical quantum information processing, basically, it is the underlying phenomenon for linear entangling gates [Nielsen, 2004]. Moreover, the HOM effect has been also applied to optical coherence tomography [Abouraddy et al., 2002] and metrology [Lyons et al., 2018].

### 1.3.2 Two-photon interference in a Mach-Zehnder interferometer

Let us consider the indistinguishable biphoton state incident on two input ports of the Mach-Zehnder (MZ) interferometer as depicted in Fig. 1.5. After the evolution of the input state through the first beamsplitter and the acquisition of a phase shift $\phi$, one obtains the general N00N state with N=2 that reads,

$$\frac{1}{\sqrt{2}}(|2_1, 0_2\rangle + e^{i2\phi}\,|0_1, 2_2\rangle). \tag{1.37}$$

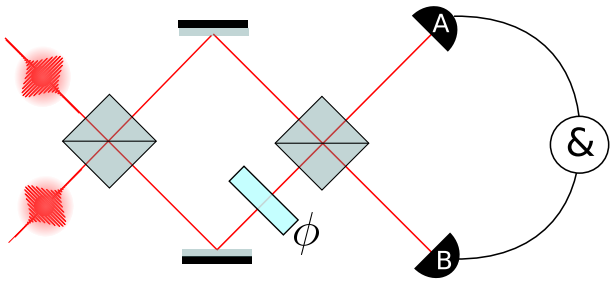


**Figure 1.5 – Scheme of two-photon Mach-Zehnder interferometer**: a biphoton state evolves through the MZ interferometer and experiences phase shift $\phi$ in one arm. The detections A and B measure the two-fold coincidence counts at the outputs.

Then N00N state evolves through the second beam splitter and is then measured at detectors A and B. The probability of detecting two-fold coincidence counts between both detectors is

$$P\,(1_A, 1_B) = \frac{1 - \cos 2\phi}{2}. \tag{1.38}$$

The two-photon interference of a N00N state with N=2 shows a phase super-resolution that reveals the effect of De Broglie wavelength of the multi-photon state [Campos et al., 1990]. In fact, the photonic De Broglie wavelength is $1/N$ shorter than the wavelength of the single-photon state [Campos et al., 1990, Pan et al., 2012]. The interference of a N00N state have been observed [Rarity et al., 1990, Shih et al., 1994, Nagata et al., 2007] and applied in quantum metrology. The phenomenon is related to the experimental results presented in chapter 3.

As explained in the general introduction, in this dissertation, our objective is to demonstrate the use of a multimode fibre, (and in general complex scattering medium), for quantum information processing. Before motivating why a multimode fibre is useful in quantum applications, we provide first a concise review to describe the technological challenges in modern quantum optics experiments. We introduce the general concept of linear optical quantum computing in section 1.4, of reconfigurable unitary optical networks in section 1.5, of the state-of-the-art integrated quantum optics in section 1.6, and on the boson sampling problem in section 1.7 before concluding.

## 1.4 | Linear optical quantum computing

Information can be stored in a state of a quantum system; it is encoded in the probability amplitudes of a state. A well-known case is a qubit, a state that belongs to a two-dimensional Hibert space. Quantum mechanics allows information to be processed via unitary evolutions (referred as operations) which lead to *interference* effects which cannot be mimicked by classical means [Nielsen and Chuang, 2010]. By exploiting such operations, a physical quantum system (referred as a qauntum machine) can process certain solvable computational tasks via a procedure called quantum algorithms, using fewer resource than a classical machine [Nielsen and Chuang, 2010]. The general-purpose quantum machines can encode information, reprogramme an evolution to implement any quantum algorithm and measure outcome information. The machines can practically work below a certain error threshold [Knill et al., 2002, Nielsen and Chuang, 2010].

Linear optics is considered as one of the most promising candidates for quantum computing. However, the optical system is similar to other physical quantum systems in the sense that they always present some drawback compared with each other. In the following, we discuss features, schemes, and main physical components of linear optical quantum computing (LOQC). The LOQC pass all five DiVincenzo criteria for building a quantum computer [DiVincenzo, 2000]:

- ☑ **A scalable physical system with well characterized qubits** Single qubit can encode coherently quantum superposition of information. In linear optics, an information is encoded in probability amplitudes of a photon in a discrete-variable fashion. Experimental resources should scale at most polynomially with the total number of qubits.
- ☑ **The ability to initialize the state of the qubits to a simple fiducial state** The initial state need to be pure.
- ☑ **Long decoherence times compared to the gate operation time** Optics satisfy well this criteria.
- ☑ **A universal set of quantum gates** Small and discrete sets of elementary operations on qubits can be combined to implement any quantum algorithm [Nielsen and Chuang, 2010]. One famous example of a universal gate set consists of two-qubit controlled-not (CNOT) gate and arbitrary single-qubit gates [DiVincenzo, 1995]. All universal gate sets contain at least one entangling operation [Nielsen and Chuang, 2010]. In linear optics, arbitrary single-qubit gates can be easily performed with high fidelity [Nielsen and Chuang, 2010]. This is not the case for two-qubit entangling gates (see below).
- ☑ **A qubit-specific measurement capability** Single-qubit measurement can be preformed to evaluate any possible observable on the system of qubit.

One of the critical problems in linear optics is that there is not easy to implement two-qubit entangling gates since the efficient implementation of two-qubit gates requires the interaction between photons. This means that an optical quantum information processing would rather need a non-linear effect to couple different input EM fields [Milburn, 1989, Myers and Laflamme, 2006]. Furthermore, a non-linear interaction at the single-photon level normally is extremely weak. Over the last 20 years, many LOQC schemes have been proposed and developed as an alternative route for implementing quantum

computing [Myers and Laflamme, 2006, Kok et al., 2007, Rudolph, 2017, Takeda and Furusawa, 2019].

One of the famous solutions is to implement two-qubit entangling gates with linear optics; therefore, one has a universal set of quantum gates. However, this comes at a cost. Two-qubit operations require the ability to control a $\pi$-phase shift rotation on the logical qubit via a controlling qubit. The same kind of requirement is requested for general entangling operations in a higher dimension. These operations can be mimicked via linear optics and measurement and this is the origin of a probabilistic gate [Knill et al., 2001] used in the LOQC. The probabilistic gates will work correctly if and only if a post-selection has been appropriately applied. The LOQC schemes are generally based on probabilistic quantum operations or measurement-based approach. Two well-known schemes are the Knill-Laflamme-Milburn (KLM) model [Gottesman and Chuang, 1999, Knill et al., 2001] and one-way quantum computing [Raussendorf and Briegel, 2001, Raussendorf et al., 2003, Nielsen, 2004].

In the KLM scheme, the LOQC is based on three basic components: single-photon sources, reconfigurable linear optical network, and photon-number resolving detectors. It requires adaptive measurement known as classical feed-forward [Knill et al., 2001]. In essence, non-linear interaction is represented by quantum interference (Sec. 1.3), which is considered as the *"interaction"*[2] of single photons. The quantum interference can be used to implement a two-qubit entangling operation probabilistically (Fig. 1.6b). All other operations are built upon the probabilistic gates [Myers and Laflamme, 2006]. The success probability of such operations is a fundamental problem in the implementation because the success rate falls exponentially with size of operations. The KLM model proposes the key solution to such a problem by using auxiliary photons together with measurement and feed-forward technique [Knill et al., 2001]. The key is to use quantum teleportation to implement gates. In details, the operations run in a feed-forward mode. This means that they will repeat an operation until they have succeeded. Successful implementation of gate operations is thus conditional upon a certain post-selection at detectors. The detection events registered at the output provide the information on the success or failure of the gate. The successful operation of the gate is then teleported onto the logical qubits, the protocol of teleportation is explained in Fig. 1.6a. The KLM scheme provides a way to build a universal quantum computer, although it requires a huge number of ancilla photons and of probabilistic two-qubit gates. The scalability of KLM implementation requires with at most a polynomial resource overhead [Myers and Laflamme, 2006, Kok et al., 2007, Nielsen and Chuang, 2010].

[2]Strictly speaking, this is not the interaction.

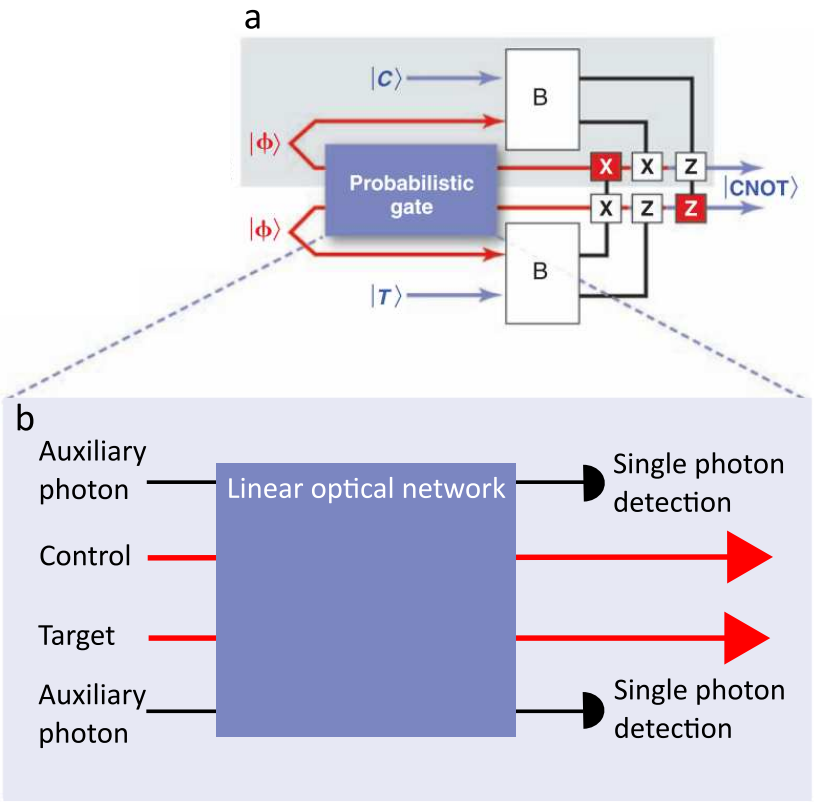


**Figure 1.6 – CNOT gate**: (a) Using the probabilistic CNOT gate (blue box descried in (b)) the probabilistic CNOT gate repeatedly performs on the two parties of two maximally entangled states $|\Phi\rangle$, and only when the CNOT gate works (using ancillary photons together with measurement and feed-forward technique) would one proceeds with the protocol for teleportation. It starts with a qubit in an unknown state $|C\rangle$ and one of two photons prepared in maximally entangled state $|\Phi\rangle$. Both are projected via Bell measurement (B box). The measurement leaves the outcome qubit in three possibilities: the state $|C\rangle$, or the bit (X), and/or phase (Z) flipped version of $|C\rangle$, depending on which of the four maximally Bell states is measured. An unwanted X and/or Z flip can be later corrected by implementing X and/or Z gate as required. The unknown input state of the control $|C\rangle$ and target $|T\rangle$ qubits can be teleported and the CNOT gate performed on the output. (b) A diagram of a probabilistic CNOT gate implemented via quantum interference using two ancillary photons and measurement. Adapted from [O'Brien, 2007]

In the second scheme, known as one-way quantum computing and cluster-state quantum computing, R.Raussendorf and H.Breigel propose the measurement-based protocol for quantum computing [Raussendorf and Briegel, 2001, Raussendorf et al., 2003, Nielsen, 2004]. From the experimental point of view, the key idea is to move all difficulty (*entanglement*) to the generation of an initial state. As shown in Fig. 1.7, the protocol starts with an initially entangled state of a specific form (called a cluster state). Then via only a sequence of single-qubit measurements followed by consequent single-qubit unitary transformations, one can determine the subset of the qubits in a specific required state. The required state will be equivalent to the output of the gate-based quantum computing [Nielsen and Chuang, 2010].

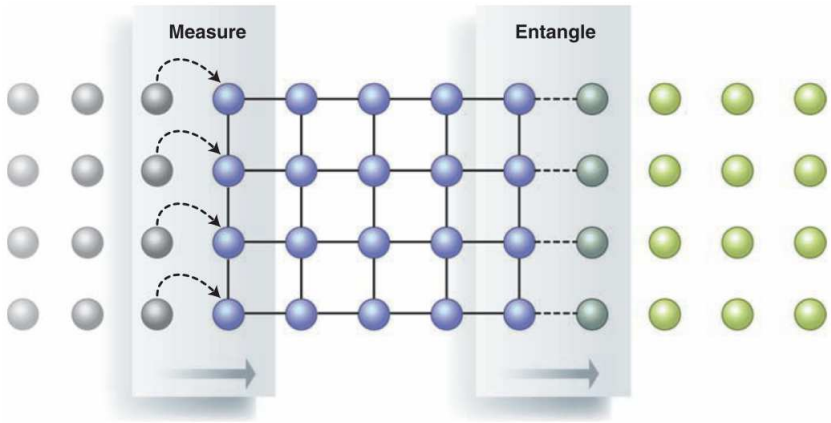


**Figure 1.7 – Cluster-state quantum computing**: Cluster state is represented by a network, where the blue nodes represent qbits in a cluster state, and the links (black lines) represent the entanglement between qubits. The protocol start to measure the qubits (Measure box), while the cluster is still being grown (Entangle box) by adding additional qubits (green circles) to the cluster state. The measurement disentangle the blue qubits to grey qubits and the outcome from measurement determines a projective measurement for the next qubit. Adapted from [O'Brien, 2007]

## 1.5 | Universal reconfigurable unitary transformation

A reconfigurable linear operator is one of the important components required in quantum information processing for implementing several protocols on the same platform [O'Brien, 2007, O'Brien et al., 2009]. Besides, a reconfigurable linear transformation is a useful tool also in many fields, for instance, classical signal processing, mode multiplexing/demultiplexing [Miller, 2015b, Annoni et al., 2017, Tang et al., 2017, Shen et al., 2017, Zhou et al., 2018], radio-frequency photonics [Zhuang et al., 2015, Capmany et al., 2016]. To implement a $k$-dimensional unitary transformation $U(k)$, one typically needs to decompose a $k$-dimensional unitary transformation into a large number of two-dimensional unitary transformations [Reck et al., 1994]. The reconfigurability of two-dimensional unitary transformation is provided by Mach-Zehnder (MZ) interferometer. Each MZ interferometer consists of two beamsplitters and two tunable phase shifters, as shown in Fig. 1.8d. The corresponding transformation of the MZ interferometer is expressed as

$$T(\phi,\theta) = \begin{pmatrix} e^{i\theta}\sin\frac{\phi}{2} & \cos\frac{\phi}{2} \\ e^{i\theta}\cos\frac{\phi}{2} & -\sin\frac{\phi}{2} \end{pmatrix}, \tag{1.39}$$

where the reflectivity of the MZ interferometer is parametrized by $\phi \in [0, \pi/2]$ and a phase shift $\theta \in [0, 2\pi]$. In general, a k-dimensional unitary transformation $U(k)$ requires $k(k-1)/2 \approx \mathcal{O}(k^2)$ MZ interferometers [Reck et al., 1994]. A few decomposition techniques have been proposed. Each technique leads to different arrangement of a cascade of MZ interferometers. The most well-known decomposition is proposed by M. Reck *et al.* in 1994 [Reck et al., 1994], and is known as the triangular architecture (Reck-Zeilinger design) as depicted in Fig 1.8b. Another decomposition is proposed by [Clements et al., 2016], as depicted in Fig. 1.8c, and we called it the rectangular decomposition (Clements design).

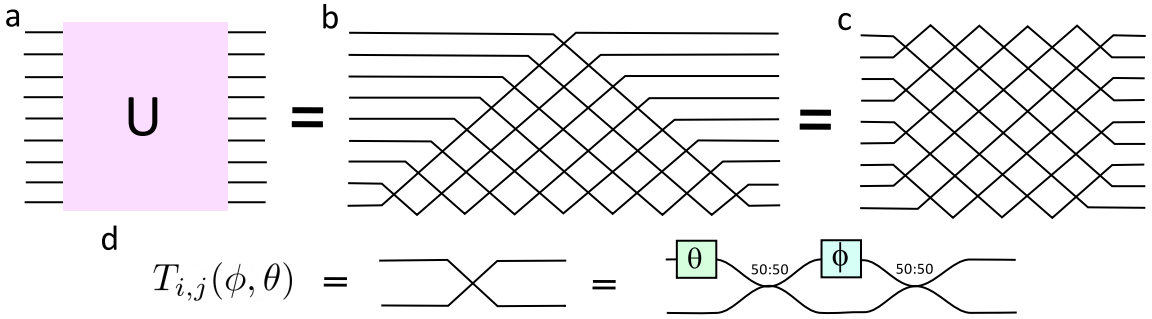


**Figure 1.8 – Universal reconfigurable unitary transformation**: (a) Unitary transformation $U$ can be decomposed into (b) triangular architecture (Reck-Zeilinger design) or (c) rectangular architecture (Clements design). (d) $2 \times 2$ reconfigurable unitary transformation is implemented with the MZ interferometer.

In general, the decomposition techniques can be described in the following manner. First, we define a 2-dimensional unitary transformation $T_{i,j}(\phi, \theta)$ of the MZ interferometer between $i$ and $j$ port, where $j = i + 1$, on the $k$-dimensional space,

$$T_{i,j}(\phi,\theta) = \begin{bmatrix} 1 & 0 & \cdots & \cdots & \cdots & 0 \\ 0 & 1 & & & & \vdots \\ \vdots & \ddots & & & & \vdots \\ \vdots & & e^{i\theta}\sin\frac{\phi}{2} & \cos\frac{\phi}{2} & & \vdots \\ \vdots & & e^{i\theta}\cos\frac{\phi}{2} & -\sin\frac{\phi}{2} & & \vdots \\ \vdots & & & & \ddots & \vdots \\ \vdots & & & & 1 & 0 \\ 0 & \cdots & \cdots & \cdots & 0 & 1 \end{bmatrix} \tag{1.40}$$

All decomposition techniques rely on the analytical method of decomposing the $U(k)$ into a product of $T$ [Reck et al., 1994, Clements et al., 2016] as follows,

$$U = D\left(\prod_{(i,j)\in \mathsf{O}} T_{i,j}\right), \tag{1.41}$$

where $\mathsf{O}$ defines a specific sequence of $T_{i,j}$ and $D$ is a diagonal matrix. Each diagonal element of $D$ is a complex amplitude with a modulus of one and corresponds to a global phase shift for each output mode. All decomposition techniques (Eq. 1.41) rely the same facts:

1. Any target matrix element in row $i$ or $j$ of $U$ can be set to zero by controlling specific values of $\phi$ and $\theta$ of $T_{i,j}$ so that it modulates the target element of matrix $T_{i,j}U$ to zero. Similarly, any target element in column $i$ or $j$ of $U$ can be set to zero by setting specific values of $\phi$ and $\theta$, that leads $UT_{i,j}^{-1}$ to be zero.
2. The multiplicative sequence of $T_{i,j}$ and $T_{i,j}^{-1}$ matrices do not affect the resultant zero elements.

Depending on a specific ordering $\mathsf{O}$ of $T_{i,j}$ and $T_{i,j}^{-1}$, the physical architecture will be different.

In the following we will demonstrate the construction of the rectangular architecture. Elements of $U$ are sequentially set to zeros following the alternating multiplication sequence of $T_{i,j}$ and $T_{i,j}^{-1}$ on $U$ in the following order,

$$\begin{bmatrix} & & & & & \mathsf{U} \\ \vdots & & & & & \\ 15 & & & & & \\ (7) & 14 & & & & \\ 6 & (8) & 13 & & & \\ (2) & 5 & (9) & 12 & & \\ 1 & (3) & 4 & (10) & 11 & \cdots \end{bmatrix}$$

As presented above, a number, located at a position of each element of matrix $U$, represents the ordering sequence of multiplication of $T_{i,j}$ and $T_{i,j}^{-1}$ on $U$. The first element of $U$ to be set to zero is at the bottom left of the matrix, labelled by ordered number 1, following by the consecutive diagonal, which contains ordered number (2) and (3). A corresponding element of $U$ at an ordered number without a parenthesis in column $i$ is set to zero via $T_{i,i+1}^{-1}$ and a corresponding element of $U$ at an ordered number with a parenthesis in row $i$ is set to zero via $T_{i-1,i}$. For example, we give an example in the case of $U(5)$ as illustrated in Fig. 1.9.

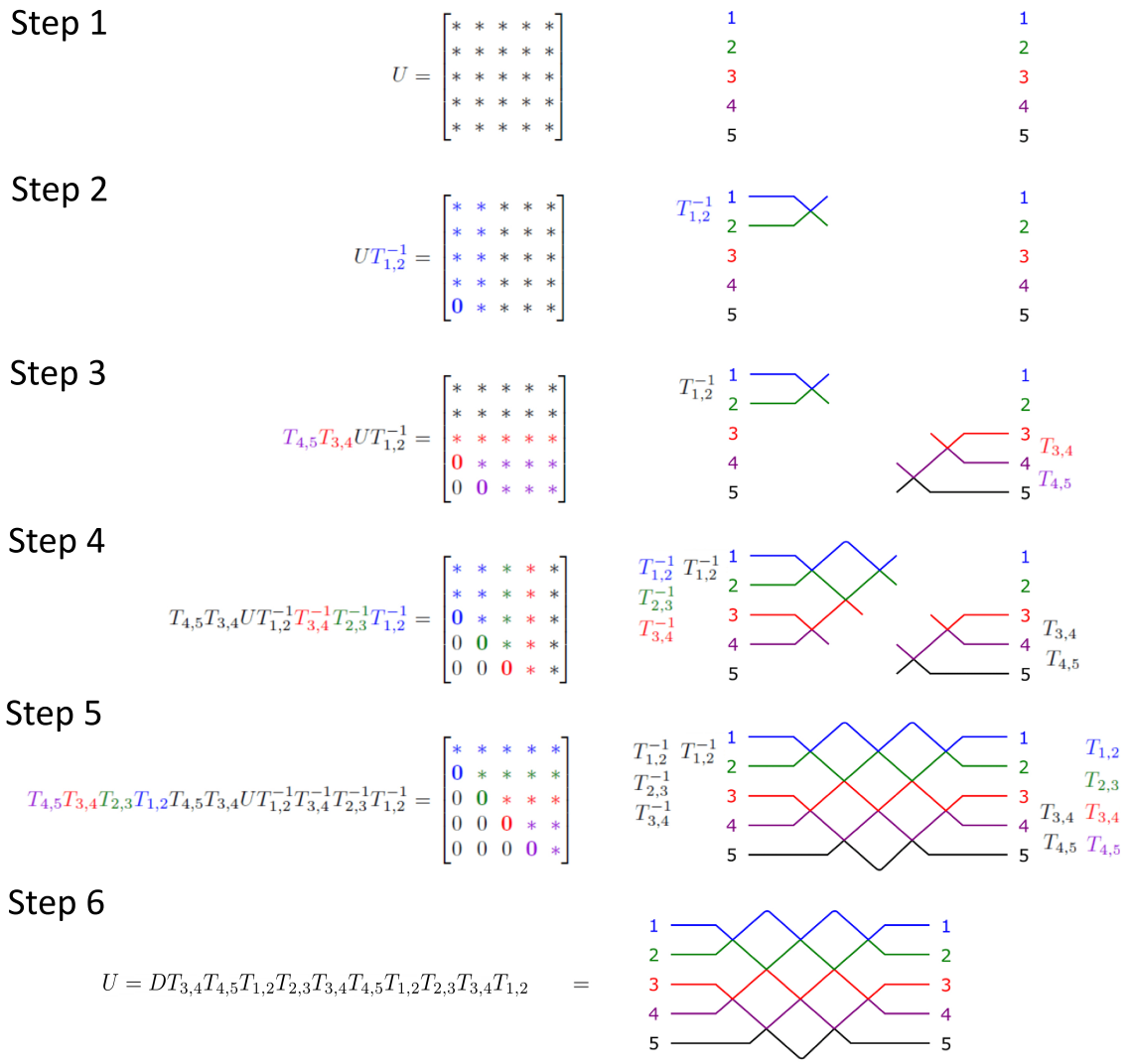


**Figure 1.9 – Decomposition technique for rectangular architecture**: (left panel) decomposition procedure. (right panel) the corresponding interferometer. **Step (1)**: a desired unitary matrix of dimension 5 is given. **Step (2)**: The bottom-left element of $U$ is suppressed with $T_{1,2}^{-1}$ resulting in the mixing of first two columns. This corresponds to adding the top-left MZ interferometer into the circuit. **Step (3)**: The next two elements on the consecutive diagonal of $U$ are sequentially set to zeros with $T_{3,4}$ and $T_{4,5}$. This corresponds to adding the two MZ interferometers at bottom-right in the circuit. The (1,5) and (1,4) elements of the resultant matrix do not change values from zeros when $T_{4,5}$ is implemented in order to set the (2,5) element to zero. **Step (4) and (5)**: are repeated the suppression process on the consecutive diagonal of the resultant matrix by alternating between $T_{i,j}^{-1}$ in the step (4) and $T_{i,j}$ in the step (5). Each corresponds to adding a diagonal line of MZ interferometers on each side of the circuit. The resultant matrix of $U$ is a lower triangular matrix after the step (5). **Step (6)** By rearranging the form of the resultant matrix, an implemented $U$ can be decomposed to the rectangular architecture. The output phase shift corresponding to $D$ is implemented at the output ports. Adapted from [Clements et al., 2016]

After the decomposition explained in Fig. 1.9, we have

$$T_{4,5}T_{3,4}T_{2,3}T_{1,2}T_{4,5}T_{3,4}UT_{1,2}^{-1}T_{3,4}^{-1}T_{2,3}^{-1}T_{1,2}^{-1} = D', \tag{1.42}$$

where $D'$ is a diagonal matrix whose diagonal elements are complex elements with a modulus of one corresponding to a global phase shift for each mode in the middle of the interferometer. The equation 1.42 can be reformulated as

$$U = T_{3,4}^{-1}T_{4,5}^{-1}T_{1,2}^{-1}T_{2,3}^{-1}T_{3,4}^{-1}T_{4,5}^{-1}D'T_{1,2}T_{2,3}T_{3,4}T_{1,2}. \tag{1.43}$$

By using the fact that $T_{i,j}^{-1}D' = DT_{i,j}$, we end up with

$$U = DT_{3,4}T_{4,5}T_{1,2}T_{2,3}T_{3,4}T_{4,5}T_{1,2}T_{2,3}T_{3,4}T_{1,2}, \tag{1.44}$$

which is consistent with Eq. 1.41. The parametrized reflectivity $\phi$ and phase shift $\theta$ of each MZ interferometer $T_{i,j}$ is determined. In general for $k$-dimensional unitary transformation, Eq. 1.42 and 1.43 can be generalised to

$$\left(\prod_{(i,j)\in\mathsf{O}_L} T_{i,j}\right) U \left(\prod_{(i,j)\in\mathsf{O}_R} T_{i,j}^{-1}\right) = D', \tag{1.45a}$$

$$U = \left(\prod_{(i,j)\in\mathsf{O}_L^T} T_{i,j}^{-1}\right) D' \left(\prod_{(i,j)\in\mathsf{O}_R^T} T_{i,j}\right), \tag{1.45b}$$

where $\mathsf{O}_L$ and $\mathsf{O}_R$ are the specific sequence of multiplication of $T_{i,j}$ and $T_{i,j}^{-1}$, on left and right hand of $U$ respectively. Again, by using the same fact that $T_{i,j}^{-1}D' = DT_{i,j}$, we arrive at the final decomposition of $U$ (Eq. 1.44) with the overall sequence of multiplication: $\mathsf{O} = [\mathsf{O}_L^T, \mathsf{O}_R^T]$ of $T_{i,j}$. This result corresponds directly to the physical implementation of MZ interferometers in the rectangular architecture [Clements et al., 2016] where specific values of $\phi$ and $\theta$ for each MZ interferometer were determined during the decomposition procedure. We note that this is an implementation of $U(k)$ up to global input or output phases diag($D$) which can be additionally implemented at the final stage by using phase shifter at each input port or each output port as preferred.

In addition to the implementation of $k \times k$ unitary transformation $U(k)$, the implementation of arbitrary $k \times m$ linear transformation $\mathcal{L}$ can be completed by using the singular value decomposition. $\mathcal{L}$ is decomposed into

$$\mathcal{L} = U\Sigma V^\dagger, \tag{1.46}$$

where $U$ is an $k \times k$ unitary matrix, $\Sigma$ is an $k \times m$ diagonal rectangular matrix whose diagonal elements are nonnegative real numbers, and $V$ is an $m \times m$ unitary matrix. The physical implementation is illustrated in Fig. 1.10, $U$ and $V^\dagger$ are implemented by applying the unitary decomposition techniques explained above. Two unitary networks, $U$ and $V^\dagger$, are then connected via $\Sigma$ which is implemented by coupling each link of the interconnected network ($U$ and $V^\dagger$) with one arm of an additional MZ interferometer, while another arm of the added MZ is used to couple light into an unmonitored mode. The added MZ thus acts as an attenuator inducing loss corresponding to one diagonal value of $\Sigma$ at a given mode. This technique is proposed in [Miller, 2013b]. Implementations of arbitrary linear networks in the quantum domain have been pointed out, for example, in [He et al., 2007, Tischler et al., 2018].

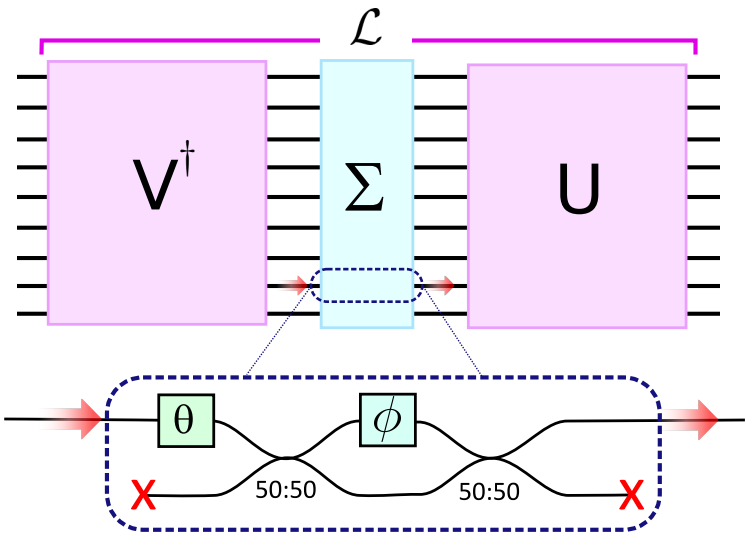


**Figure 1.10 – Universal reconfigurable linear transformation**: A linear transformation $\mathcal{L}$ is composed of two universal unitary transformations, $V^\dagger$ and $U$, and additional column of MZ interferometers coupling into unmonitored modes $\Sigma$.

## 1.6 | Review on integrated quantum optics

The implementation of a reconfigurable unitary transformation on an optical platform is crucial for a large-scale quantum information processing. A linear optical network such as one relying on Reck's decomposition needs a large number of connected MZ interferometers [Matthews et al., 2009, Smith et al., 2009, Metcalf et al., 2013, Carolan et al., 2015]. Optical instability, misalignment, losses thus quickly grow as the dimension of circuits increases [Flamini et al., 2019, Harris et al., 2018, Slussarenko and Pryde, 2019]. The problems can be alleviated by the use of integrated photonics technology, since it provides a possibility for implementing linear optics on a chip platform, as for example depicted in Fig. 1.11. The implementation provides interferometric stability, miniaturisation, and additionally, it allows reconfigurability via tunable phase shifters in each unit of the MZ interferometers. Many researchers have been developing materials, fabrication techniques, design of different optical elements in order to archive requirements for the quantum applications. In this section, we introduce those requirements and discuss technological challenges and point out successful quantum applications implemented on such an integrated photonics platform. Our objective for this part of introduction is to present the challenges that can be tackled via our approach for programmable linear optical networks presented in the following chapters.

### 1.6.1 Integrated photonics and technological challenges

Over the last two decades, requirements for many optical communication devices such as switch, modulator, wavelength division multiplexer have advanced our integrated photonics technology towards a mature stage where many reliable applications are utilized in real life thanks to high bandwidth, compactness, high stability and ability to reconfigure a functionality. Still, there are plenty of room for improvements and advancing the technology for widespread applications [Minzioni et al., 2019]. Nowadays, there are mainly two classes of materials that have been employed as a platform for on-chip optical networks [Bogdanov et al., 2017]: The first is based on a silica glass ($SiO_2$) and the second is

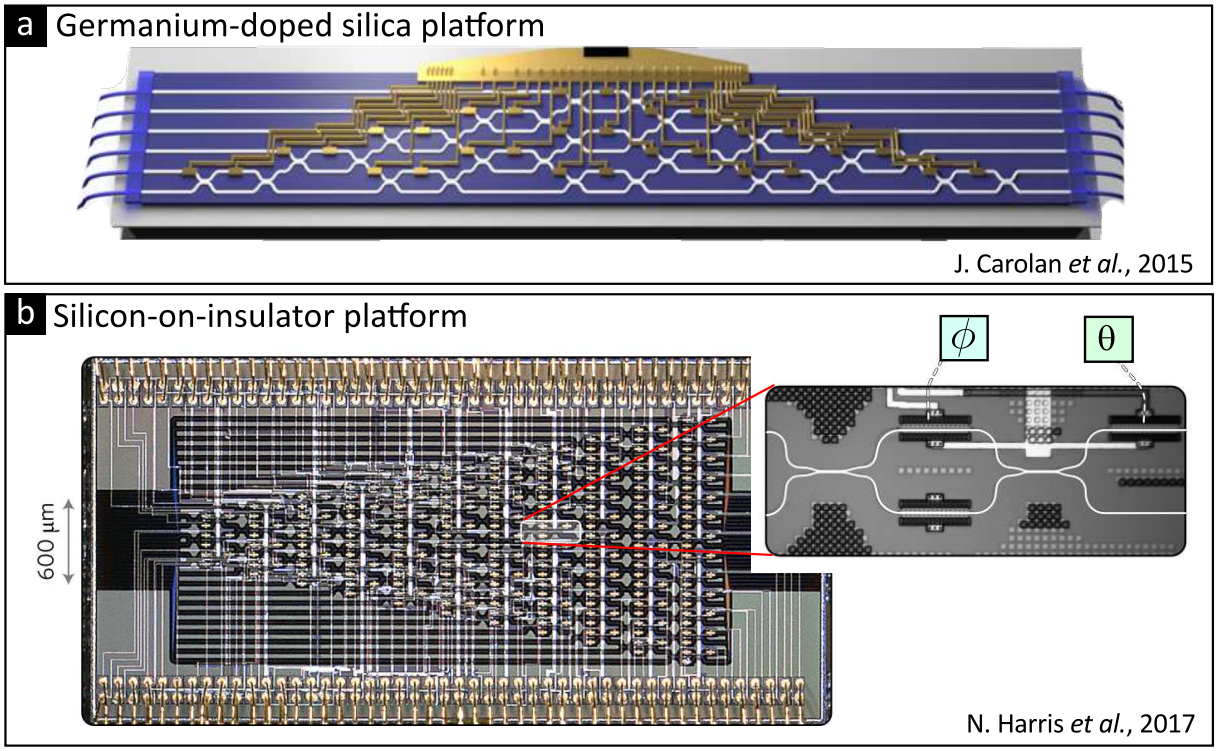


**Figure 1.11 – Physical implementations of reconfigurable linear optical network on integrated photonic on-chip**: (a) Germanium-doped silica platform with thermal phase shifters. Adapted from [Carolan et al., 2015] (b) Silicon-on-insulator platform. Adapted from [Harris et al., 2017]

silicon-on-insulator (SOI) platform, including silicon nitride ($Si_3N_4$), silicon carbide (SiC), indium phosphide (InP), gallium arsenide (GaAs), lithium niobate ($LiNbO_3$).

**Manufacturing process and loss**: In the first class of silica-based optical platform, fabrication techniques utilize either laser-writing technique on a silica [Osellame et al., 2012] or photolithography and etching technique on a doped silica-on-silicon wafer [Politi et al., 2009a]. The optical loss is low, at about $< 0.1$ to 0.8 dB/cm, depending on a manufacturing technique [Politi et al., 2009a, Sansoni et al., 2010, Dyakonov et al., 2018]. However, the silica platform has a low contrasts of refractive index, typically about $\Delta n \approx 0.5\%$. The silica-based platform thus cannot have a high optical component density since a waveguide is sensitive to bending which induces radiation losses. The standard limit of bends radius of waveguides is of 15-40 mm [Osellame et al., 2012] and the typical size of an optical network is thus about a few centimetres to 10 cm. On the other hand, the silicon-on-insulator platform provides a high refractive index contrast ($\Delta n \approx 40\%$), thus very high compact chip can be achieved since small waveguides, and small bending can be implemented without inducing additional loss. The size of a chip is typically a few mm [Silverstone et al., 2016]. Manufacturing optical network on the silicon-on-insulator platform requires a mature fabrication technique. Nowadays, it can provide low cost, high production yields and complementary metal-oxide-semiconductor (CMOS) compatibility [Silverstone et al., 2016, Harris et al., 2017]. However, surface scattering, crystallinity, high refractive index contrast results seriously in optical losses at a level of several dB/cm [Harris et al., 2017]. In addition to these two optical platforms, an intermediate solution for loss and compact design has been proposed based on silicon nitride $Si_3N_4$ [Bauters et al., 2011]. It provides the low propagation loss of about 0.2dB/cm

while having a refractive index contrast of $\Delta n \approx 18\%$. Recently, two-photon quantum interference has been demonstrated on such platform [Taballione et al., 2019].

**Technology of phase modulation and issue of scalability**: Reconfigurability of the optical networks is provided by a phase shifter, typically implemented by a thermo-optic effect[3]. On the silicon-on-insulator platform, the thermal phase-shifter can be applied without inducing an additional loss. However, the modulation speed is low and can reach a few hundred kHz [Harris et al., 2014], and it requires typically a large power consumption of a few mW to 10 mW per phase shifter. This, therefore, generates heat on the platform. It induces thermal crosstalk between MZ interferometers, one of the limitations in scaling-up this optical platform [Milanizadeh et al., 2019, Jacques et al., 2019, Chung et al., 2019]. Several alternative techniques of phase modulation have been proposed and developed. They are based on mechanical effect (∼MHz bandwidth) [Humphreys et al., 2014, Poot and Tang, 2014, Han et al., 2015], or direct-current Kerr effect (∼GHz bandwidth) [Timurdogan et al., 2017]. Recently, the phase modulation using InGaAsP/Si hybrid metal-oxide-semiconductor provides a route to low-loss, high speed and lower power consumption [Takenaka et al., 2018]. It provides $\pi$-phase shift using a gate voltage of 0.8 V which is 5-folds lower than that of state-of-the-art Si optical modulator while having a loss at 0.25 dB which is also 10 times lower than that of Si modulator but still higher than thermo-optic phase modulator [Takenaka et al., 2018]. On the silica platform, the thermal-optic effect is also used for phase modulation. Typically it requires a high power consumption of about 0.8 W for modulating $2\pi$ phase shift [Matthews et al., 2009, Smith et al., 2009, Flamini et al., 2015, Carolan et al., 2015]. Recently the low power consumption of 0.2 W has been demonstrated by using a new design of micro-heater [Ceccarelli et al., 2019].

Coherent control of optical networks has been hitherto demonstrated up to tens of optical modes on silicon-on-insulator [Harris et al., 2017, Harris et al., 2018, Wang et al., 2018b], up to six modes on silica platform [Carolan et al., 2015], and eight modes on silicon nitride platform [Taballione et al., 2019]. Interestingly, there have been a few studies showing that a nearly perfect linear transformation is still achievable in sufficiently large reconfigurable network [Miller, 2015a, Mower et al., 2015, Burgwal et al., 2017, Pai et al., 2018].

**Manipulation of light across photonic degrees of freedom**: Manipulation of light across different photonic degrees of freedom provides a different route towards encoding and processing information in high dimensions [Lanyon et al., 2009, Su et al., 2019, Takeda and Furusawa, 2019]. In bulk optics, polarization is the most obvious photonic degree of freedom for encoding and manipulating information using waveplates. Transforming polarization-encoding information to a path-encoding one can naturally be archived by using a polarizing beamsplitter. In integrated optics, the standard design is, on the other hand, based practically on a coupling between many single-mode waveguides (a cascade of MZ interferometers). Coupling the spatial modes with other degrees of freedom, such as time [Humphreys et al., 2013], frequency [Kues et al., 2016, Kues et al., 2017, Imany et al., 2019] and polarization [Xu et al., 2014], remains an engineering challenge in integrated optics. Here we list examples of development on encoding and manipulating light in each photonic degree of freedom:

- **Polarization**: Full control of polarization on the silicon-on-insulator platform has been demonstrated, for example, by using polarization rotators (waveplates) based

[3]Change in refractive index is induced by temperature.

on electrically-controlled thermal-optic effect [Sarmiento-Merenguel et al., 2015], or by using an out-of-plane waveguide to induce Berry's phase [Xu et al., 2014].

- **Temporal degree**: Time-bin encoding has been demonstrated on silicon nitride platform by using Franson interferometer where a 14-cm long path is embedded in a spiral form [Xiong et al., 2015]. Moreover, the programmable two-photon interference with a tunable time delay on-chip has been recently introduced by harnessing birefringent electro-optic effect on lithium niobate platform [Luo et al., 2019].
- **Transverse spatial degree**: A few optical elements for manipulating transverse spatial degree on chip have been demonstrated and there are still passive. Regarding transport, single laser-written doughnut waveguide shows an ability to transmit single-photon state with a few transverse spatial modes with minimal crosstalk (the demonstrated reachable length is of 19 mm) [Chen et al., 2018]. In term of beam splitter, two-photon quantum interference has been observed across different two transverse spatial modes via a nanoscale grating and tapper as mode conversion [Mohanty et al., 2017].

To sum up, programmable on-chip optical elements which are beamsplitter, waveplate, temporal delay line, strongly rely on the phase-shifter technologies. Demonstrated manipulation of light on-chip across photonic degrees of freedom is nowadays mainly passive. Hitherto, passive mode conversion of a photonic quantum state between path, polarization, and transverse waveguide-mode degrees on a single integrated photonic chip has been demonstrated [Feng et al., 2016, Mohanty et al., 2017]. To date, the quest for a programmable high-dimensional optical network offering arbitrary connectivity is ongoing.

**Integration of light source and detection on chip**: In addition to the challenge for a programmable optical network that relates to our research question in the dissertation, we would like to note that there have been numerous endeavours to integrate non-classical light sources and single-photon detectors on a chip platform. Non-classical light sources can be embedded on-chip platform principally due to wide spectral transparency of the waveguide and the presence of non-linearity of materials [Silverstone et al., 2016, Taballione et al., 2019]. Different types of sources have been demonstrated, for instance, parametric down-conversion [Sansoni et al., 2017, Lenzini et al., 2018], four-wave mixing [Spring et al., 2013b, Paesani et al., 2019, Feng et al., 2019, Adcock et al., 2019, Lu et al., 2019, Wang et al., 2018b] and quantum dots [Lodahl et al., 2015, Davanco et al., 2017, Kiršanskė et al., 2017, Ellis et al., 2018]. Similarly, integration of single-photon detectors have been reported [Sprengers et al., 2011, Pernice et al., 2012, Najafi et al., 2015, Schuck et al., 2016a, Korneev et al., 2018].

### 1.6.2 Alternative designs

In order to give a complete overview, we present several alternatives designs that have been demonstrated for implementing optical elements to overcome these technical challenges in an optical experiment. We categorise them into four groups:

- **Inverse photonic design**: This technique is applied for designing an optical element on a chip. It is based on a computational approach to discover a non-trivial optical structure for a given desired functional characteristics by means of an optimization problem [Molesky et al., 2018]. The space of optimized parameters is normally a large area of refractive index on a silicon wafer. For example, as shown

in Fig. 1.12a, the wavelength demultiplexer is inversely designed to split 1,300 nm and 1,500 nm input lights into two output waveguides [Piggott et al., 2015]. Another example, a broadband on-chip polarization beamsplitter is designed by using genetic algorithm [Shen et al., 2015]. The devices are passive and have not been used for quantum applications.

- **Dielectric metasurfaces**: The optical element is designed by manipulating Mie resonances in dielectric and semiconductor nanoparticles with high refractive indices on a flat surface (typically silicon-on-insulator) [Kuznetsov et al., 2016]. Recently, mode conversion between polarization and orbital angular momentum [Stav et al., 2018] and two-photon state reconstruction across path-polarization degrees of freedom, as depicted in Fig. 1.12b, have been demonstrated on all-dielectric metasurfaces [Paniagua-Diaz et al., 2019a]. Quantum weak measurements have also been reported [Chen et al., 2017]. The metasurfaces are often passive, but, can be reconfigurable by using the technologies of phase-shifting presented in the silicon-on-insulator platform or liquid crystal modulation [Wu et al., 2019].

- **Spatial Light Modulator (SLM)**: SLM is a device for phase or amplitude manipulation on a two-dimensional plane. The present technologies of SLMs offer control of up to million pixels based either mostly on a liquid crystal or microelectromechanical systems. Liquid-crystal-based SLM is omnipresent in quantum optic experiments used as a regular optical device for a high-dimensional encode and projection of a transverse spatial degree of freedom, i.e., azimuthal degree [Krenn et al., 2017] and radial degree [Karimi et al., 2014a, Plick and Krenn, 2015]. The relevant review on using SLM for mode generation and detection can be seen, for example, in [Forbes et al., 2016].

- **Multi-Plane Light Conversion (MPLC)**: MPLC device was first proposed to provide an arbitrary unitary programmable spatial mode converter [Morizur et al., 2010, Labroille et al., 2014]. It is composed of a succession of designed phase plates. As depicted in Fig. 1.12c, a spatial basis on the Cartesian grid of 210 identical Gaussian spots is transformed into spatially-overlapped Hermite-Gaussian mode basis by using seven phase plates [Fontaine et al., 2019]. The algorithm for designing phase plates relies on an optimization approach, such as, wavefront matching (WFM) [Fontaine et al., 2017] which is also used in the inverse design for a waveguide in integrated optics [Sakamaki et al., 2007]. The theory shows that a number of phase plates can be reduced to two per mode for some certain transform [Morizur et al., 2010]. MPLC implementation with fewer phase planes has been studied [Wang et al., 2017b, Zhao et al., 2019]. Recently, two-plane MPLC has been used in jointly azimuthal-radial mode sorting for a high-dimensional quantum cryptography [Fickler et al., 2020]. Key quantum gates have also been demonstrated in both azimuthal and radial degrees of freedom [Brandt et al., 2019]. Moreover, the idea of MPLC can be implemented on a waveguide-based platform [Tang et al., 2017, Zhou et al., 2018] which links back to a general idea of inverse photonic design that one explores a large degree of parameters for building an optical element.

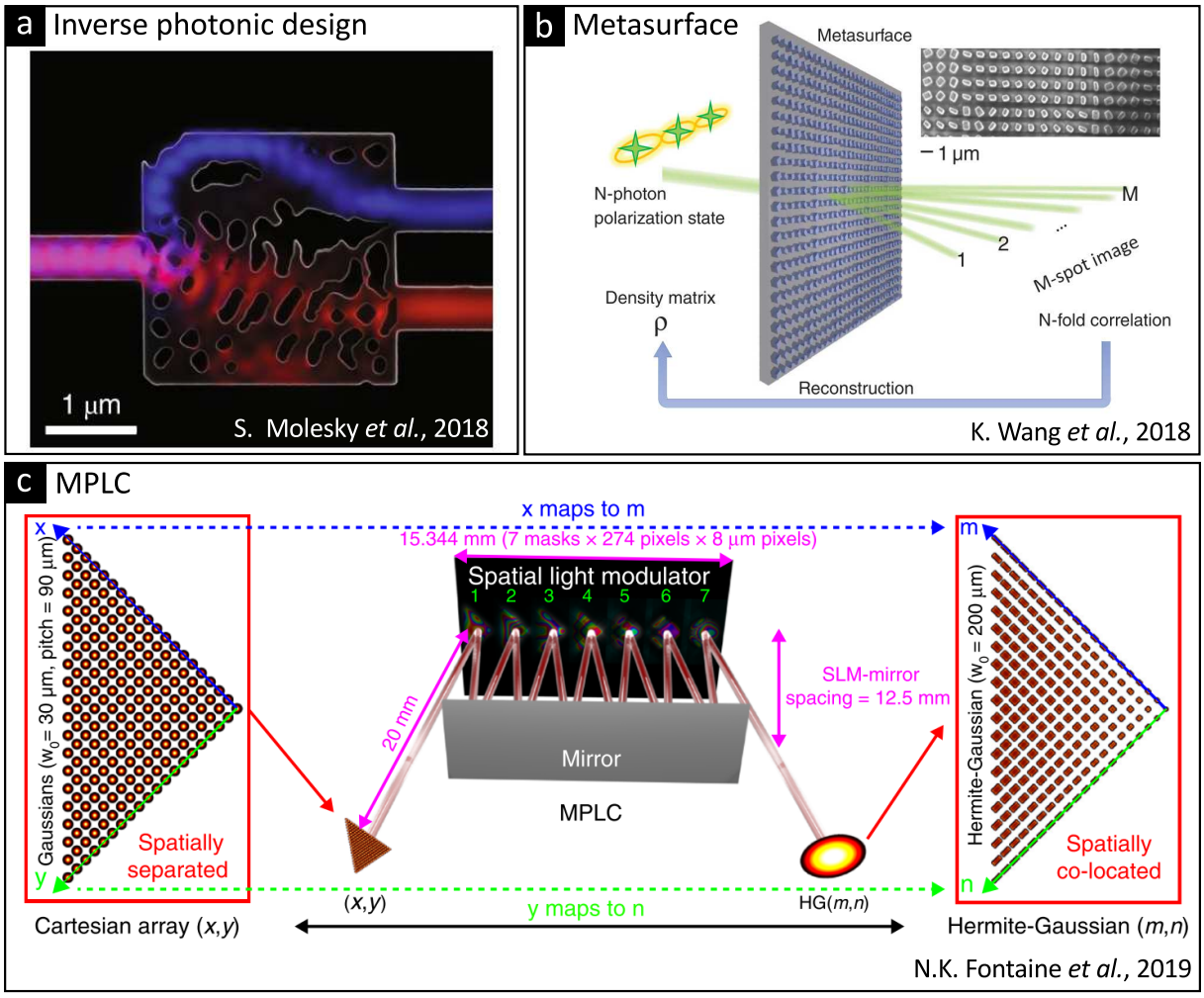


**Figure 1.12 – Alternative implementations of desired optical elements**: (a) Inverse photonic design for demultiplexing of two wavelengths. The figure displays a overlaid structure of the chip and corresponding field profiles at two wavelengths (red and blue). Adapted from [Molesky et al., 2018] (b) Metasurface designed for projecting polarizations of input light into $M$ output spots. The platform is used for quantum state tomography. Adapted from [Paniagua-Diaz et al., 2019a], (c) Multi-plane light conversion (MPLC) is used as mode conversion that maps a Cartesian grid of identical Gaussian spots into Hermite-Gaussian modes. Adapted from [Fontaine et al., 2019]

### 1.6.3 Quantum applications

Linear optical networks enable many implementations of quantum experiments spanning from fundamental experiments, information processing, simulation, metrology, communication [Aspuru-Guzik and Walther, 2012, Orieux and Diamanti, 2016, Harris et al., 2018, Flamini et al., 2019, Wang et al., 2019b]. We review here a few landmarks of quantum optic experiments on integrated platforms. We focus on works related to linear optical networks and their quantum applications. Our intention here is to reveal potential applications of the linear optical networks in the quantum domain while showing technological development and challenges. The review is presented in the timeline format in order to clearly perceive the development of the field.

- In 2008, two-photon interference was first realised on a passive silica-on-silicon platform [Politi et al., 2008]. One year later, thermally phase-controlled MZ interferometer was successfully used to manipulate two-photon and four-photon N00N interference on the silica platform [Matthews et al., 2009, Smith et al., 2009, Marshall et al., 2009]. The first integrated quantum metrology experiments is reported. In the same year, Shor's algorithm for factoring 15 was implemented on a photonic chip [Politi et al., 2009b].

- In 2010, the quantum interference of polarization-entangled Bell states was performed on a laser-written platform [Sansoni et al., 2010]. This shows the ability to encode any polarization state on an integrated waveguide on silica platform. Evolution of two-photon interference across arrays of coupled waveguides, known as quantum walks (see review [Gräfe et al., 2016]), has been demonstrated [Peruzzo et al., 2010]. It indicates a generalization of the HOM effect on a large linear network.

- In 2011, linear CNOT gate was demonstrated on laser-written platforms [Crespi et al., 2011, Li et al., 2011] and interestingly in the same year in bulk optics [Okamoto et al., 2011]. In the context of metrology, four-photon N00N state has been demonstrated on silica platform [Matthews et al., 2011].

- In 2012, generation of four Bell states, state tomography and test of Bell inequality were performed on a silicon platform [Shadbolt et al., 2012b, Shadbolt et al., 2012a]. This was possible due to the reconfiguration of eight phase shifters on the same chip. Quantum delayed-choice experiment, which tests the concept of complementary (wave-particle duality), has been demonstrated [Peruzzo et al., 2012]. In term of design of optical networks, a laser-writing technique has shown a capability to implement a network of waveguides in the three-dimensional geometry that allows the implementation of beam tritter (three-port splitter) and quarter (four-port splitter) [Spagnolo et al., 2012].

- In 2013, it was a year of *boson sampling*, a generalization of the HOM effect on many single-photons on multimode interferometer [Spring et al., 2013a, Crespi et al., 2013a, Broome et al., 2013, Tillmann et al., 2013, Metcalf et al., 2013]. We will discuss this paradigm in the following section. In parallel, the quantum walk of Bell entangled states have been demonstrated showing an interesting behaviour of quantum transport [Crespi et al., 2013b].

- In 2014, a protocol for quantum teleportation was demonstrated on chip [Metcalf et al., 2014]. In term of boson sampling, the verification of up to five-photon inter-

ferences on both an array of coupled waveguides and random unitary interferometer was reported [Carolan et al., 2014, Spagnolo et al., 2014]. Moreover, an eigenvalue of ground-state molecular energy was estimated with the help of two-photon interference on a photonic chip [Peruzzo et al., 2014].

- In 2015, a fully reprogrammable silica-on-silicon platform implemented several quantum protocols such as conditional gate, entangling gate, state tomography, boson sampling on a single chip [Carolan et al., 2015]. Moreover, basic operations for continuous-variable quantum optics which are the generation, characterization, and verification of entanglement of Einstien-Podolsky-Rosen (EPR) state were demonstrated on a chip [Masada et al., 2015] and a nine-dimensional entangled quantum system (entangled two-qutrit) was characterized on a chip [Schaeff et al., 2015].
- In 2016, one-way quantum computing with a four-qubit linear cluster state was used for Grover's algorithm [Ciampini et al., 2016]. In the context of communication, transfer of quantum information between photonic chips demonstrated the feasibility of entanglement distribution [Ang et al., 2016]. Furthermore, state preparations of polarization-encoded and time-bin-encoded BB84 protocols were implemented on a silicon chip providing the high-speed low-error quantum key distribution. This is thanks to fast phase modulation (10 GHz bandwidth) [Sibson et al., 2017b, Sibson et al., 2017a, Bunandar et al., 2018].
- From 2017 to presents, a full programmable two-qubit operation has been demonstrated on a silicon platform [Santagati et al., 2017, Qiang et al., 2018]. The silicon platform has been expanded to a larger dimension and applied to implement many protocols, state tomography, testing multi-dimensional Bell correlation [Qiang et al., 2018, Wang et al., 2018b]. In the context of quantum simulation, different approaches for estimating of eigenvalues of ground and excited states of Hydrogen molecules [Paesani et al., 2017, Santagati et al., 2018] and dynamic simulation of vibrational states of a few molecules [Sparrow et al., 2018] have been reported. In the context of quantum transport, the simulation of static versus dynamic disordered wave transports was simulated the presence of environment-assisted transport on a silicon chip [Harris et al., 2017].

## 1.7 | Boson sampling

As pointed out in the previous section, several quantum applications of linear optical networks have been developed towards a large-scale implementation. However, the practical large-scale universal quantum computer seems to be far from our current technology and development. Towards this long-term effort, harnessing the computational potential of quantum systems for a specific computing task is an intermediate achievement. One of an important milestone towards this direction is revealing quantum computation advantage: an experimental demonstration of a device governed on the quantum mechanics capable of performing a specific computing task more efficient than current classical computers [Arute et al., 2019]. One famous model of computation for testing such quantum advantage is *boson sampling problem* [Brod et al., 2019], which was formulated by Aaronson and Arkhipov [Aaronson and Arkhipov, 2011, Aaronson, 2011]. In particular, a number of indistinguishable photons are propagated through a linear optical network, then are measured at the outputs. The resultant distribution of number of photons at the outputs forms a pattern that is difficult to predict as the number of photons and

the dimensionality of optical network grow. The boson sampling problem is physically equivalent to a quantum many-particle interference, which is a generalization of the HOM effect discussed in section 1.3.

Mathematically the many-particle interference is equivalent to a calculation of the permanent of matrix governed an evolution of a linear optical network [Tichy, 2014]. The statement of the boson sampling problem starts by defining an input Fock state of N photons in n modes,

$$|S\rangle = |s_1 s_2 \dots s_n\rangle = \prod_{p=1}^{n} \frac{(\hat{a}_p^\dagger)^{s_p}}{\sqrt{s_p!}} |0\rangle \,, \tag{1.47}$$

where $s_p$ is the number of photons occupying in the $p$-th input mode and the total number of photons is $\sum_p s_p = N$. The input state $|S\rangle$ is then evolved through a linear transformation $\mathcal{L}$ in which the element $l_{qp}$ relates input $p$ and output $q$. The transition probability of detecting the targeted output state $|T\rangle = |t_1 t_2 \dots t_n\rangle$ is expressed as

$$P(S \to T) = \frac{|\mathrm{Per}(L_{S,T})|^2}{s_1! \dots s_n! t_1! \dots t_n!}, \tag{1.48}$$

where Per is the permanent of the sub-matrix $L_{S,T}$ which is constructed by taking $s_p$ copies of the $p$-th column of $\mathcal{L}$ and $t_q$ copies of the $q$-th row of $\mathcal{L}$. The permanent is defined as

$$\mathrm{Per}(L_{S,T}) = \sum_{\sigma \in S_n} \prod_{q=1}^{n} l_{q,\sigma(q)}, \tag{1.49}$$

where $S_n$ is the set of all permutations of $n$ elements. For example, the permanent of $2 \times 2$ matrix $\mathrm{BS} = \left[\begin{smallmatrix} a & b \\ c & d \end{smallmatrix}\right]$ is $\mathrm{Per}(\mathrm{BS}) = ad + bc$. Let us consider the HOM interference, in which case one sends $|S\rangle = |1_1 1_2\rangle$ input state evolving through the beamsplitter (Eq. 1.31). The transition probability of detecting the targeted output state $|T\rangle = |1_1 1_2\rangle$ reads

$$P(S \to T) = \left| \mathrm{Per}\left( \frac{1}{\sqrt{2}} \begin{bmatrix} 1 & 1 \\ 1 & -1 \end{bmatrix} \right) \right|^2 = 0, \tag{1.50}$$

This corresponds to the zero probability of detecting two-fold coincidence count (Sec. 1.3.1).

The evaluation of the permanent is believed to be hard on a classical computer if the matrix $L_{S,T}$ presents sufficient complexity. In order to guarantee the complexity, three conditions need to be satisfied [Aaronson and Arkhipov, 2011]:

1. Initialisation of the input state with $s_p \in \{0, 1\}$, in order to avoid repeated columns in the calculation.

2. A linear transformation is drawn from $n$-dimensional Haar-random unitary transformation with $n = O(N^2)$ [Aaronson and Arkhipov, 2011, Życzkowski and Kuś, 1994, Russell et al., 2017, Pai et al., 2018]. First, this is to avoid a special symmetry that a classical algorithm could exploit. Second, a Harr-random unitary does not provide dominantly bunching events, also known as collision events, which are events when two or more photons are in the same output mode. This results from the photon bunching effect in which there is highly probable to have an outcome probability of more-than-one photons occupying in a mode if $n = O(N^2)$. This is known as the bosonic birthday paradox [Aaronson and Arkhipov, 2011, Arkhipov

and Kuperberg, 2012]. Otherwise, if $n \gg N^2$, the probability of two or more photons occupying in the same mode is not too large [Aaronson and Arkhipov, 2011, Arkhipov and Kuperberg, 2012, Urbina et al., 2016]. The event is known as a collision-free event.

3. Due to the bosonic birthday paradox [Arkhipov and Kuperberg, 2012], outcome probabilities are dominated by collision-free events that is $t_i \in \{0, 1\}$; therefore, it is sufficient to use photon detectors in Geiger mode which recognize only vacuum and non-vacuum states.

The computational complexity of the boson sampling problem belongs to the $\#P$-hard class [Valiant, 1979]. The best known classical algorithm for calculating the permanent is Ryser's algorithm, which takes $O(2^{n+1}n)$ arithmetic operations for an $n \times n$ matrix [van Lint et al., 2001].

A few alternative schemes of the boson sampling have been proposed and experimentally demonstrated. They use different input states and detectors. The first alternative model is *scattershot boson sampling*. In this case, the input states are randomly excited by many probabilistic heralded single-photon sources [Lund et al., 2014, Bentivegna et al., 2015], which is experimentally handy using heralded single-photon sources from probabilistic SPDC. This scheme improves exponentially a generation rate of the photons and provides uniformly sampling input at random. The second choice is *gaussian boson sampling* [Hamilton et al., 2017, Kruse et al., 2019], where the input states are replaced by a number of single-mode squeezed states and the detectors are single-photon detectors. In this case, the output distributions are governed by hafnian calculation of a matrix, which is also in $\#P$-hard complexity class [Hamilton et al., 2017].

The scalability of boson sampling has been experimentally challenging in all three components: the number of single-photon sources, the dimensionality of linear optical network, and the number of detectors. Last year, up to five-photon interferences were experimentally demonstrated [Wang et al., 2017a, Wang et al., 2018a, Zhong et al., 2018]. Very recently, boson sampling with twenty input single-photon sources has been reported [Wang et al., 2019a].

## 1.8 | Summary

In this chapter, necessary notations and tools needed for understanding the underlying physics presented in the dissertation were introduced: spontaneous parametric down-conversion source and two-photon interference. Both are used widespread not only in fundamental quantum optics experiments but also in many quantum applications spanning from quantum simulation, metrology, communication, including both famous protocols for linear optical quantum computing, and testing quantum computation advantage via boson sampling problem [Harris et al., 2018, Flamini et al., 2019, Wang et al., 2019b].

Programmable linear optical network is the heart of these implementations. It allows implementing different experiments, simulations and information processing tasks on the same optical platform. The famous architecture of the programmable linear optical network is a cascade of the MZ interferometers that consists of many beamsplitters and tunable phase shifters. Nowadays, the state of the art for physical implementation of optical networks usually relies on integrated optics. They provide many advantages thanks to high stability, compactness, and ability to reprogramme a functionality of many linear transformations, beyond a bulk optics experiments.

Nevertheless, integrated optics meets many technological challenges in term of fabrications, cross-talk, optical loss, power consumption in phase shifters and a capability to encoding and manipulating information in many photonic degrees of freedom [Wang et al., 2019b]. These issues result in one major problem, which is the scalability of the integrated photonic platform for practical use. To date, many researchers and developers have been pursuing and tackling the problems with either direct or alternative ways. Alternative implementations of optical networks that one can think of are, for example, inverse photonic design [Molesky et al., 2018] and MPLC [Morizur et al., 2010].

In this dissertation, we aim at proposing another potential architecture for implementing a programmable linear optical network and experimentally implementing it for quantum applications. It relies on a complex mixing of modes, a.k.a. multiple scattering process. In the following chapters, we are going to introduce a concept of the architecture and present a use of the platform for quantum experiments.

# 2

# Programming linear quantum networks

*"Good design is as little design as possible."*

— Dieter Rams

This chapter introduces our technique to harness a complex mixing property of a dielectric medium, here a multi-mode fibre, for constructing a programmable optical network. We start with providing a literature review in Section 2.1 concerning the framework for scattering theory, the complex mixing property of fibre, and the control of light propagation through scattering medium. Those are the tools used for implementing a programmable *complex mixing-based optical network*. We detail the general concept and give the key ingredients for programming such an optical network in subsection 2.1.4. We then give details on our experiment in Section 2.2; the setup, the acquisition of transmission matrix, and the construction of the optical network. In Section 2.3, the reliability and versatility of our experimental implementation are presented through a series of controlling two-photon interferences of various networks. Finally, the reliability and scalability of our optical-network architecture are explored both theoretically and numerically, and are validated through a characterization of experimentally implemented optical networks in Section 2.4.

## Contents

## 2.1 | Complex mixing-based optical networks

In this section, the relevant physics and concepts used for programming optical network by harnessing the complex mixing property of a medium are introduced.

### 2.1.1 Speckle phenomena and mesoscopic effects

#### Scattering theory

Light propagating through a complex scattering medium forms a complex interference pattern, known as a speckle pattern (Fig. 2.1a) [Goodman, 2005b, Beenakker, 2018]. The speckle carries information both on the coherence properties of the light and on mesoscopic and microscopic details of the scattering medium. To introduce the properties of speckled light, we use an inhomogeneous dielectric medium in a waveguide illustrated in Fig. 2.1b as the model of interest.

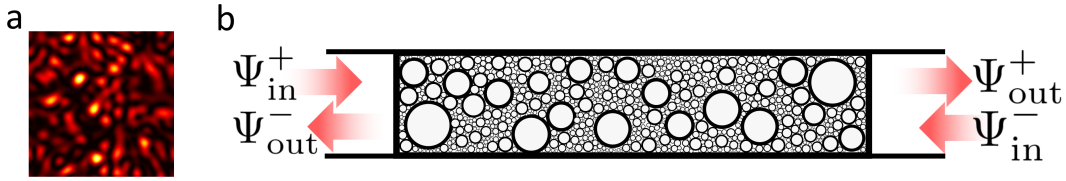


**Figure 2.1 – Scattering system**: (a) Speckle pattern (b) Model of light scattering from an inhomogeneous medium in a waveguide geometry

In the asymptotic scattering region, at the given wavelength $\lambda$ the total number of propagating modes of the waveguide is given by $n$ proportional to the width of the waveguide. Light transport through the linear diffusive waveguide can be described by the scattering matrix $\mathbf{S}$ that relates incoming $\Psi_{\text{in}}$ and outgoing $\Psi_{\text{out}}$ optical fields as explained in Eq. 2.1,

$$\begin{pmatrix} \Psi^-_{\text{out}} \\ \Psi^+_{\text{out}} \end{pmatrix} = \mathbf{S} \begin{pmatrix} \Psi^+_{\text{in}} \\ \Psi^-_{\text{in}} \end{pmatrix}, \tag{2.1}$$

where +(-) are right(left)-moving waves, respectively. The $2n \times 2n$ scattering matrix is subdivided into four block matrices,

$$\mathbf{S} = \begin{pmatrix} \mathbf{R} & \mathbf{T}' \\ \mathbf{T} & \mathbf{R}' \end{pmatrix}, \tag{2.2}$$

where the blocks on the diagonal contain the reflection matrices for incoming modes from left $\mathbf{R}$ and from the right $\mathbf{R}'$, respectively. The off-diagonal blocks contain the transmission matrices (TM) for scattering from left-to-right $\mathbf{T}$ and from right-to-left $\mathbf{T}'$, respectively. Considering a scattering process without loss and gain, the main properties of scattering process can be deduced. Firstly, the flux of optical field is conserved, the scattering matrix thus is unitary $\mathbf{S}^\dagger\mathbf{S} = \mathbf{1}$. The second important property is reciprocity: $\mathbf{S} = \mathbf{S}^{\mathrm{T}}$ meaning that the scattering amplitude from a mode $i$ to another mode $j$ is the same as that from $j$ to $i$. The reciprocity can be inferred to the presence of time-reversal

symmetry in the static system without loss and gain [Rotter and Gigan, 2017]. We note that **T** - the *transmission matrix* (TM) - is the matrix of our main interest for further discussion, and it can be measured experientially (see subsection 2.2.2 for the method).

To further understand the statistical properties of scattering matrix **S** and transmission matrix **T**, random matrix theory (RMT) is used as a convenient tool since the statistical properties of a sufficiently chaotic or disordered system can be obtained from a suitably chosen ensemble of random matrices. The interned goal of the RMT is to calculate the statistical properties of the eigenvalues and eigenvectors of a random matrix. The RMT was first introduced by Wishart in 1928 [Wishart, 1928] and then used by Wigner to explain the statistics of energy levels in complex nuclei [Wigner, 1951]. RMT has been successfully used in many applications and are nowadays omnipresent in physics [Brouwer, 1971, Beenakker, 1997, Tao, 2012, Akemann et al., 2018]. Relevant classes of a random matrix for explaining the model of disordered waveguide are presented in order to give an overview of underlying physics related to our problem of interest.

### Speckle: Indicator of complex mixing

Like many statistical frameworks, we start by sampling the transmission matrix **T** from the space containing random matrices with a same statistical feature. In the first case, the elements $t_{ij}$ of **T** are represented by a randomly generated complex numbers from Gaussian ensemble where real $\mathcal{R} = \mathrm{Re}(t_{ij})$ and imaginary $\mathcal{I} = \mathrm{Im}(t_{ij})$ parts are sampled independently. The join probability distribution on the complex plane is $P(\mathcal{R},\mathcal{I}) = (2\pi\sigma^2)^{-1}\exp[-(\mathcal{R}^2+\mathcal{I}^2)/(2\sigma^2)]$. Transforming the distribution via the Jacobian [Goodman, 2005b], three key statistical features of the speckled light can be extracted, which are the distribution of amplitude $A = \sqrt{\mathcal{R}^2+\mathcal{I}^2}$, phase $\theta = \arctan(\mathcal{I}/\mathcal{R})$, and intensity $I = |A|^2$,

$$P(A) = \frac{A}{\sigma^2}\exp\left(-\frac{A^2}{2\sigma^2}\right) \qquad ,A \geq 0 \tag{2.3a}$$

$$P(\theta) = \frac{1}{2\pi} \qquad , -\pi < \theta \leq \pi \tag{2.3b}$$

$$P(I) = \frac{1}{\bar{I}}\exp\left(-\frac{I}{\bar{I}}\right) \qquad ,I \geq 0. \tag{2.3c}$$

The distribution of amplitude follows the Rayleigh density function, the phase has a uniform distribution and the intensity has the exponential decay [Goodman, 2005b]. The mean intensity ($\bar{I}$) is equal to the standard deviation of intensity ($\sigma_I$). Speckle pattern (Fig. 2.1a) with these features is normally referred to as *fully developed speckle*. This is the first key feature of complex-mixing property required for programming optical networks since it shows coherence superposition and complete randomization of partial contributed waves with randomly varying phases and amplitudes. We note that in practical situations, correlations can be presented in speckle patterns, we provide the related information about the correlations in Appendix C.2.

### Properties of time-reversal operator

In this section, we aim at introducing properties of $\mathbf{TT}^\dagger$ from the RMT frameworks. The $\mathbf{TT}^\dagger$ operator, which is known as time-reversal operator [Prada and Fink, 1994, Popoff

et al., 2010b], plays an important role in the implementation of our programmable optical network. It is used to map designed linear optical networks onto an experimentally implemented one (see Sec. 2.4.1 for the mapping relation). In an ideal case, we would want, $\mathbf{T}\mathbf{T}^\dagger = \mathbb{1}$, meaning that our experimental implementation of a linear optical network is perfectly identical to what we intend to design. The properties of $\mathbf{T}\mathbf{T}^\dagger$ depend on the model used to describe the transmission matrix $\mathbf{T}$. Here we introduce the properties of $\mathbf{T}\mathbf{T}^\dagger$ from a few models developed from the RMT frameworks.

The properties of interest are related to $\mathbf{T}\mathbf{T}^\dagger$ or $\mathbf{T}^\dagger\mathbf{T}$. Both operators share the same non-zero transmission eigenvalues $\tau_i, i \in [1, n]$ which provides the information of flux transmission on each channel (each eigenvector). We note that $\tau$ is equal to the square of singular values of $\mathbf{T}$ and the total transmission through a scattering medium is defined as $T = \sum_i \tau_i$.

In the first simplest model, the elements of $\mathbf{T}$ are again sampled from independent and identically distributed (i.i.d.) complex Gaussian random variables. For the sake of generality $\mathbf{T}$ is here considered to be a rectangular matrix linking $d$ input modes to $n$ output modes, thus the size of $\mathbf{T}$ is $n \times d$. A square matrix $\mathbf{W} = \mathbf{T}\mathbf{T}^\dagger$ is also known as Wishart matrix [Wishart, 1928] that has been applied in many areas including multivariate statistical analysis, data compression techniques, the communication theory [Tulino and Verdú, 2004, Couillet and Debbah, 2011]. The Wishart matrix is related to a covariance matrix, thus $\mathbf{T}\mathbf{T}^\dagger$ is nearly close to the identity, which is good for our implementation of a linear optical network. But interestingly, the eigenvalue distribution of transmission eigenvalues is not located in the peak at 1 as one may be tempted to expect. The distribution of transmission eigenvalues, on the other hand, converges to the Marčhenko-Pastur (MP) law in the limit $n, d \to \infty$ with $r = n/d \in (0, \infty)$ [Marčenko and Pastur, 1967, Janik and Nowak, 2003]. The MP distribution, shown in Fig. 2.2, is defined as follows,

$$P_{\mathrm{MP}}(\tau) = \left(1 - \frac{1}{r}\right)^+ \delta(\tau) + \frac{1}{2\pi r\tau}\sqrt{(\tau_+ - \tau)^+(\tau - \tau_-)^+}, \tag{2.4}$$

where $\tau_\pm = (1 \pm \sqrt{r})^2$ and $(\cdot)^+$ is considered only positive values [Couillet and Debbah, 2011].[1] In 2010, the Marčhenko-Pastur law was experimentally observed in optics by measuring a small portion of the transmission matrix of a slab of disordered medium where related correlations are not significantly presented in the experimental condition [Popoff et al., 2010b, Popoff et al., 2011]. Noticeably, when $r = 1$, Eq. 2.4 can be simplified to the form, $P_{\mathrm{MP}}(\sqrt{\tau}) = \pi^{-1}\sqrt{(4 - \sqrt{\tau}^2)^+}$, which is known as *quarter circle law* since the distribution of eigenvalues $\sqrt{\tau}$ of $\mathbf{T}$ has a quarter circle profile [Marčenko and Pastur, 1967, Tulino and Verdú, 2004].

To better take into account a realistic system, one needs to take into account the unitarity of the scattering system, this means that real system are not described by a i.i.d Gaussian random transmission matrix. Several models have been introduced to describe the statistical properties of such a scattering medium.

In the second interesting class of RMT, the scattering matrix is sampled from Dyson's circular ensemble [Dyson, 1962a, Dyson, 1962b].[2] It is so-called circular unitary ensemble (CUE), the scattering matrix has to respect the unitarity. Imposing such symmetric

[1] The MP distribution get broader as $n > m$ because of the repulsion of eigenvalues

[2] These ensembles are called circular because their eigenvalues are relied on the unit circle in the complex plane.

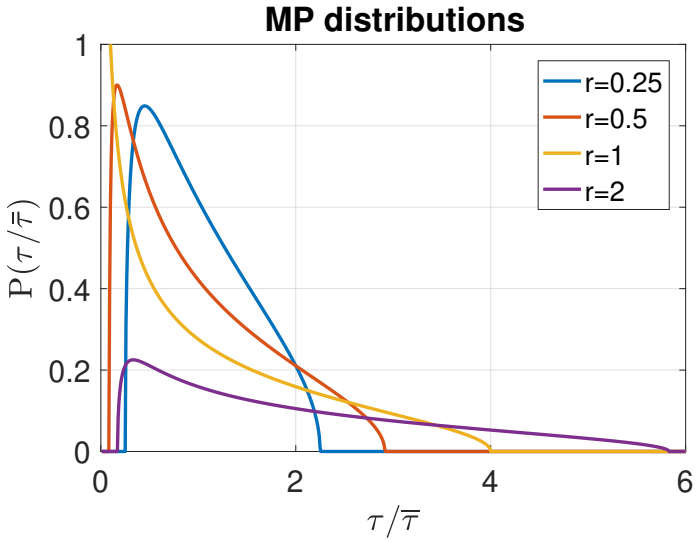


**Figure 2.2 – Marčhenko-Pastur (MP) law**: Probability density function of transmission eigenvalues $\tau$ (Eq. 2.4) at different $r = n/d$.

constraints results in correlation in a scattering phase shifts [Akbulut et al., 2016a], and thus, leads to the interesting statistical distribution of transmission eigenvalues $\tau$. Under the limit of a large $n$, the distribution for the case of CUE presents bimodal and symmetric profile at $\tau = 1/2$ [Baranger and Mello, 1994, Jalabert et al., 1994] (Fig. 2.3a),

$$P_{\text{Bimodal}}(\tau) = \frac{n}{\pi} \frac{1}{\sqrt{\tau(1-\tau)}}. \tag{2.5}$$

In the context of electronic transport, the bimodal distribution Eq. 2.5 can explain well the transmission through a chaotic quantum dot (chaotic cavity)[3] without any requirement or information about a specific geometry of scattering object (Fig. 2.3a). On the other hand, it cannot describe well the electron transports through a diffusive wire and also light transports through a diffusive waveguide since the RMT does not take the geometry of the scattering object into consideration. The geometry controls how the input field experiences the scattering process. For instance, as the length of the diffusive waveguide $L$ is longer than the transport mean free path $\ell^\star$, which is the characteristic length over which the direction of propagating field is randomized [Rotter and Gigan, 2017], the overall transmission usually decreases linearly with length $L$ following the Ohm's law [Dragoman and Dragoman, 2004, Wiersma et al., 1997].

In general, a more realistic model considering the length of a diffusive waveguide is clearly needed to understand transmission and reflection properties of the scattering object. Dorokhov, Mello, Pereira, and Kumar have proposed such model, known as the DMPK model which is the third model presented in this introduction. In DMPK model, they subdivide the scattering system into a series of weakly scattering segments with isotropically connection between each segment [Dorokhov, 1982, Mello et al., 1988a]. This results

[3] A quantum dot (electron billiard) is a small metal/semiconductor heterostructure island with high mobility, the current flows from source to drain reservoirs by point contacts which are small compared to the overall size of the scattering domain.

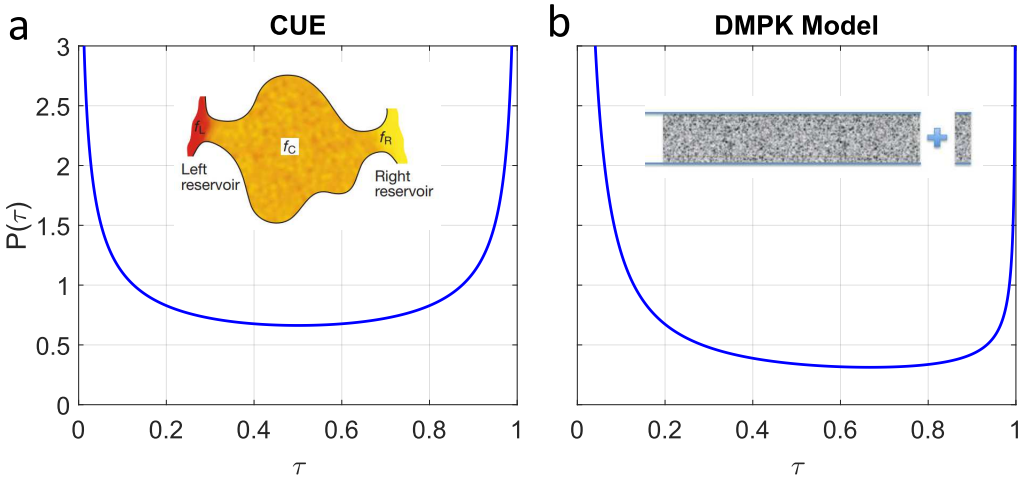


**Figure 2.3 – Distribution of transmission eigenvalues $\tau$ for two independent situations**: (a) Bimodal distribution predicted by the RMT with circular unitary ensemble describes the electron transport in a chaotic cavity (insert). Adapted from [Oberholzer et al., 2002] (b) Dorokhov-Mello-Pereira-Kumar model for a diffusive wire (insert). The normalization is such that $\int_{\tau_0}^{1} P(\tau)d\tau = 1$. Adapted from [Rotter and Gigan, 2017].

in the DMPK equation describing an evolution of the distribution of transmission eigenvalues $\tau_i$ as a function of the length of disordered waveguide covering different transport regimes: ballistic, diffusive, localized. In diffusive regime, there are $g \simeq n\ell^\star/L$ transmission channels having a finite transmission with $\tau > \tau_0$, where $\tau_0 = 4\exp(-2L/\ell^\star)$. The $g$ is known as the dimensionless conductance which is equal to the total transmission, $g = \overline{\mathrm{Tr}\,\mathbf{T}^\dagger\mathbf{T}}$ [Imry, 1986]. The remaining $n(1-\ell^\star/L)$ channels are closed, $\tau \approx 0$. Accordingly, wave cannot transport through a medium. The DMPK equation gives back bimodal but asymmetric distribution of transmission eigenvalues [Dorokhov, 1984],

$$P_{\mathrm{DMPK}}(\tau) = \frac{n\ell^\star}{2L}\frac{1}{\tau\sqrt{1-\tau}}. \tag{2.6}$$

As shown in Fig. 2.3, both CUE and DMPK distributions of transmission eigenvalues present a nontrivial bimodal profile indicating high probabilities of having transmission channels that are almost closed $\tau \approx 0$ or open $\tau \approx 1$, which are known as close channels and open channels, respectively. The phenomenon is known as *maximum fluctuation* [Pendry et al., 1990] and was theoretically discovered by [Dorokhov, 1984] in context of electron transports. Experimentally, the bimodal distribution was observed using disordered waveguides in acoustics [Gérardin et al., 2014]. In optics, the direct observation of the bimodal distribution of transmission eigenvalues have not been reported so far. Nevertheless, the presence of close and open channels in optics influences the control of light transports through or reflected from a diffusive scattering medium. We provides relevant information in Appendix C.1. The most advanced experimental results regarding the bimodal distribution were demonstrated in context of electron transports [Beenakker, 2018]. Even though, the direct observation of the bimodal distribution has not been reported since the coherent control of electrons transport through a proper transmission channel is still impossible for a scattering system larger that electronic wavelength. The open transmission eigenchannels, however, create indirect effect on *electric shot noise*[4]

[4]The electric shot noise is referred to a temporal current fluctuations, originates only from the transport, not from an emission process of the source.

which has been experimentally observed [Beenakker, 2018]. In a condition where electrons behave as matter waves, the transports through different geometries, i.e, chaotic cavity and diffusive wire, generate distinct reductions of the electric shot noise by a value of 2/3 for DMPK distribution and of 3/4 for CUE distribution. These reductions are independent of the thickness $L$ and the means free path $\ell^\star$ (see reviews [Beenakker, 1997, sec.III.E.] and [Rotter and Gigan, 2017, sec.II.B.]). These evidence strongly support the validity of RMT and the DMPK models. Therefore, they show the distinct influences of the geometry of the scattering object on the physics of transport.

#### Conclusion

A realistic model of the transmission matrix $\mathbf{T}$ for a particular scattering medium is necessary not only for understanding a transport properties but also for exploiting their properties in applications as we are going to present. Statistical properties of the scattered light deduced from the model of the diffusive waveguide were introduced. Two key information from this section are:

- The presence of fully developed speckle indicates the isotropic (*equally-weight*) mixing of information from all inputs to all outputs. We would like to refer to such a scattering object as an ideal optical mixer.
- The properties of $\mathbf{T}\mathbf{T}^\dagger$ play an important role in our programmable optical network.

In the next section, we are going to introduce our optical mixer which is a multimode fibre and its mixing properties in practice. The model of the diffusive waveguide presented above does not describe all of the physical aspects of light transports through the multimode fibre. Since the reflection of the multimode fibre is negligible, this imposes new constraints on the scattering process.

### 2.1.2 Multimode waveguide and its mixing property

#### Introduction

Multimode fibres (MMF) are cylindrical waveguides transporting a high number of propagating modes, composed of a core and a cladding. The core of the fibre has a diameter, noted $D$, and is made of a dielectric medium with a high value of refractive index profile $n_1(r)$, where $r$ is radial coordinate defined from the optical axis to the cladding boundary $D/2$. The cladding covers the core and is made of a medium with a lower refractive index: $n_0 < n_1(r)$. Here we focus on graded-index multimode fibres, which we use. They have a parabolic refractive index profile: $n_1^2(r) = n_1^2[1 - 8\Delta(r/D)^2]$, where $\Delta = (n_1^2 - n_0^2)/(2n_1^2)$ is the refractive index contrast. The number of propagating modes $n$ scales with the diameter $D$ of the core and the refractive index contrast $\Delta$, which typically vary from a few modes to a few thousands. In principle, a well-defined mode basis, typically linear polarized (LP), can describe eigenmodes of an ideal MMF under weak guidance approximation[5] [Snitzer, 1961, Gloge, 1971, Snyder and Love, 1984]. The basis of propagating modes of MMF is described in Appendix B.1.

Nowadays, MMFs are more and more considered to be used for high bit-rate optical communication, i.e., space-division multiplexing, where many spatial modes are utilized to

[5]The weak guidance approximates a small refractive index difference between core and cladding.

increase the capacity of data transmission [Richardson et al., 2013]. While time, wavelength, and polarization multiplexing have been commercially used in a single-mode communication fibre, spatial degree of freedom remains a technical challenge of increasing the capacity in MMFs due to the presence of cross-talk and differences in group velocity between modes [Berdagué and Facq, 1982, Richardson et al., 2013, Agrawal, 2016]. As a result, the transmitted light at the output of MMF also presents speckle pattern. To date, space-division multiplexing has relied on a multi-core fibre (7-19 cores) [Agrawal, 2016], a few-mode fibre (∼3-6 spatial modes) [Richardson et al., 2013] or on a few mode groups (9 mode groups with 45 spatial modes) of a multimode fibre [Sillard et al., 2016, Fontaine et al., 2018]. The complex nature of mode coupling in MMFs depends on inhomogeneities of a refractive index profile of a waveguide along propagation [Ho and Kahn, 2013] and can arise from several reasons. Notably, the inhomogeneities can be categorized into Rayleigh scattering and Mie scattering from impurities, refractive index variations over the length in graded-index fibres, impurities at the core-cladding interface, strains or bubbles in the fibre, diameter fluctuations, bending, twisting, elliptical core deformation, and eccentricity [Ho and Kahn, 2013].

### Mode mixing in multimode fibres

In essence, mode mixing can be described by field coupling models [Marcuse, 1991, Rowe, 1999], or by the cascade of RMT [Ho and Kahn, 2011b, Goetschy and Stone, 2013, Chiarawongse et al., 2018, Li et al., 2019b]. It has been shown that most of the inhomogeneities can be considered a low-pass perturbation that couple strongly modes having a small difference in propagation constant $\Delta\beta$, while weakly couple modes having large $\Delta\beta$ [Ho and Kahn, 2013]. Therefore, modes in a same mode group with the same mode index $l$ of orbital angular momentum are strongly coupled. Typically, an intentional and strong perturbation is required to couple different mode groups. Mode mixing can be classified into different regimes from no coupling, weakly coupling to strong coupling with different characteristic lengths depending on the properties of interest, e.g., polarization-mode dispersion [Shemirani et al., 2009], modal dispersion [Shemirani and Kahn, 2009], group velocity dispersion [Ho and Kahn, 2011b], and mode-dependent loss [Mickelson and Eriksrud, 1983, Olshansky, 1975, Ho and Kahn, 2011a, Carpenter et al., 2014]. In communications, most of the works are more interested in the dispersion effect since it results in a low bit-rate transmission [Shemirani et al., 2009, Shemirani, 2010]. The statistical distribution of group delays in the strong coupling regime has been shown to approach the semicircle law of the RMT with Gaussian unitary ensemble [Ho and Kahn, 2011b].

Characterisation of mode mixing and phase delay depends in practice on the type of fibres and on the experimental setting [Di Leonardo and Bianchi, 2011, Čižmár and Dholakia, 2011, Carpenter et al., 2014, Plöschner et al., 2015b, Boonzajer Flaes et al., 2018]. Recently, multimode fibres have been studied in detail via the measurement of their transmission matrices in different settings (see 2.2.2). In 2015, Martin Plöschner, Tomáš Tyc and Tomáš Čižmár showed that light propagation within straight or even significantly deformed segments of step-index fibres may be predicted with a sufficiently accurate theoretical model up to distances of hundreds of millimetres [Plöschner et al., 2015b]. Nonetheless, a step-index fibre still presents weakly a polarization mixing at a few-cm length [Plöschner et al., 2015b]. In 2018, Dirk E. Boonzajer Flaes, *et al.*, showed that the multimode waveguide with perfectly parabolic refractive index profile is significantly more

robust to bending, and conserving the propagation-invariant modes (PIMs)[6] much better than step-index fibre under the same conditions [Boonzajer Flaes et al., 2018]. Interestingly, the properties of a graded-index MMF used in this dissertation (Thorlabs, GIF50C) were also studied and present a mode coupling for length longer than 20 mm [Boonzajer Flaes et al., 2018]. With their calibration procedure, the optical power preserved in PIMs increases from 5.4% to 53%, significantly less than the analogous modal analysis in the step-index fibre showed over 95% conservation in PIMs [Plöschner et al., 2015b]. Dirk E. Boonzajer Flaes, *et al.* suspected that the modal coupling is caused by imperfections in the refractive index profile of the graded-index MMF. The inhomogeneities allows transmitted lights propagating through MMF to be scattered a sufficient number of times. With a sufficient long fibre, power in each input mode is distributed to different spatial and polarization modes isotropically. As a consequence, the speckle has a complex polarization state at any outputs [Shemirani et al., 2009, McMichael et al., 1987, Kiesewetter, 2010, Fridman et al., 2012, Xiong et al., 2018]. Intuitively, a completely mixed spatial and polarization modes of a fibre are guaranteed when intensity distribution at the output of the fibre is statistically independent of the launch condition of incoming light. For example, the input light injected to fibre will result in an unpolarized speckle, which is the sum of two orthogonally polarized speckles that are uncorrelated to each other, irrespectively of the input polarized states. The mixing property of the graded-index multimode fibres (Thorlabs, GIF50C) used in this dissertation is presented in Appendix B, which indicates the appearance of highly isotropic mixing across spatial and polarization modes.

### Multimode waveguides for quantum information processing

Instead of considering mode mixing in MMFs as the problem in communication, we consider it as an advantage for quantum applications in this dissertation. Mixing of modes is an underlying process for the interference. The observation of two-photon interference in an optical fibre coupler dates back to 1996 [Weihs et al., 1996]. The mode mixing in the fibre coupler is based on a directional coupler (DC) in which two waveguides are brought close together such that the guided modes are coupled by the evanescent field [Lifante, 2003]. The directional coupler is a common method for inducing a mode mixing on an integrated quantum photonic chip, where $2 \times 2$ reconfigurable Mach-Zehnder interferometer is built upon for implementing large unitary transformation, on various platforms using different materials and fabrication techniques [Carolan et al., 2015, Harris et al., 2018] as discussed in section 1.6.

Alternatively, the mode mixing can also rely on multimode interference (MMI) couplers [Peruzzo et al., 2011, Bonneau et al., 2012, Poulios et al., 2013], where the self-imaging principle[7] replicates input fields at different outputs [Soldano and Pennings, 1995]. The MMI coupler can provide a higher-dimensional transform with better performances since it allows low tolerance to wavelength and polarization variations, and alleviates fabrication requirement due to a larger size of waveguide compared to DC [Soldano and Pennings, 1995]. The two-photon interferences have hitherto been observed in $2 \times 2$ [Bonneau et al., 2012, Poulios et al., 2013], $4 \times 4$ integrated MMI waveguides [Peruzzo et al., 2011, Barrett et al., 2019] and up to $5 \times 5$ multimode waveguide made of two parallel metallic mirrors [Poem et al., 2012]. MMI devices are, however, still mainly

[6] Eigenmodes of the system

[7] The self-imaging principle is a property of multimode waveguides by which an input field profile is reproduced by interference into single or multiple images at periodic intervals along the propagation direction.

passive, a reconfigurability has been recently realized by local modulation of the spatial refractive index profile of MMI devices [Bruck et al., 2016, van Niekerk et al., 2019]. Noticeably, one may envisage that a graded-index fibre might also present such self-imaging principle. Due to the inhomogeneities along propagation as discussed above, we do not, however, observe the effect in the graded-index fibre. This fact can be understood from the destruction of the stable periodicity of self-imaging due to wave chaos [Doya et al., 2002, Joseph et al., 2015, Cao and Wiersig, 2015].

### 2.1.3 Control of light propagation through complex media

#### Introduction

The speckle phenomena do also occur in a multimode fibre. The presence of speckle has been considered, from a traditional viewpoint, as the main challenge for imaging applications and signal transmission through a fibre since input information is getting mixed as discussed in subsection 2.1.2.

In 2007, the seminal experiment by Ivo Vellekoop and Allard Mosk from University of Twente proposed a paradigm shift. They reported focusing of coherent light through opaque scattering material by control of incident wavefront using a spatial light modulator (SLM) [Vellekoop and Mosk, 2007]. An iterative optimization technique was proposed to obtain the optimal incident wavefront that would enhance the intensity at a targeted diffraction-limited spot on another side of the medium. To understand how it works in the context of linear optics, the speckle on an observation plane corresponds to the coherent sum of all speckle contributions from all input channels as illustrated in Fig. 2.4a. By considering at one targeted output speckle gain, the corresponding electric field results mathematically from a sum of phasors (complex electric fields) with uncorrelated and evenly distributed phases. When optimizing the phase of $n$ input channels, $n$ input contributions with initially uncorrelated phases are updated to $n$ contributions all adding up in phase, resulting in an enhancement of electric field at the targeted output of the order of $\sqrt{n}$, and accordingly to an enhancement of the intensity of the order of $n$ (Fig. 2.4b). In the first experimental realization, a 2000-fold enhancement in focus light intensity than the average intensity of the unoptimized speckle was observed. The result showed a high degree of wavefront control through disordered media well beyond aberration correction in adaptive optics [Tyson, 1991, Vellekoop, 2015].

Alternatively, by ruminating the time-reversal symmetry of the optical system in Fig. 2.4, one understands that a phase solution displayed on the SLM is a phase conjugation of a speckle monochromatic field generated from a single-mode light source placed at the targeted output (white circle) in the time-reversed version. This is the concept of optical phase conjugation [Goodman, 2005a] (Fig. 2.5). Light propagates from the phase-conjugated SLM solution, undos the multiple scattering process, and focuses onto the target. For this purpose, one needs to know the optical transfer response of a medium that links many inputs to the targeted output. In 2010, Sébastien M. Popoff, *et al.* reported the first experimental measurement of the transmission matrix (TM) of a disordered medium [Popoff et al., 2010b]. Focusing light on any desired outgoing mode can be straightforwardly done using the acquired TM. Since 2007, the corresponding technique, so-called *wavefront shaping through complex media* or in short *wavefront shaping*, has been widely applied in many contexts ranging from extending many imaging techniques deep in a sample [Horstmeyer et al., 2015] to various observation of important mesoscopic effects

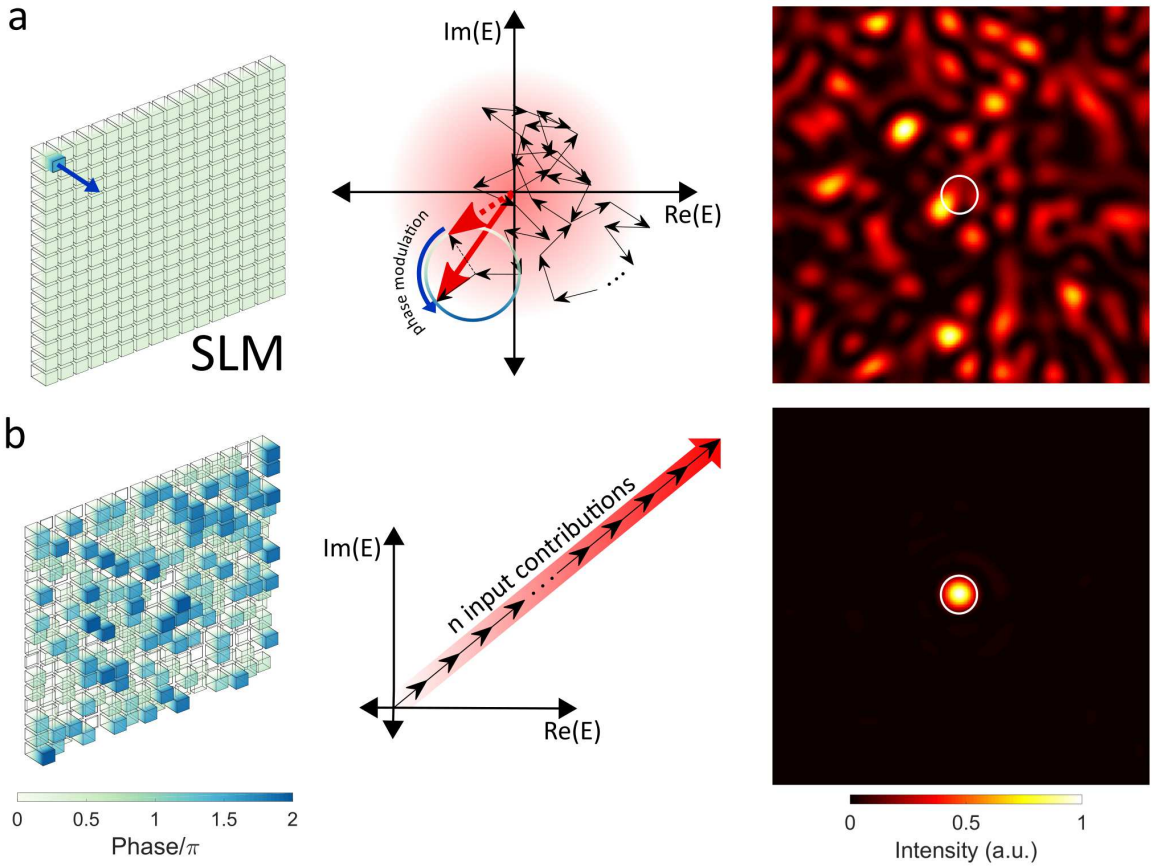


**Figure 2.4 – Concept of wavefront shaping through complex media**: (a) Incident light is coupled into a disordered optical system resulting in a speckle pattern in the first place. Considering one targeted output (white ring), the corresponding optical field $E_{\text{out}}$ is a superposition of many input fields represented on the phase space. By modulating the incident phase of light at one SLM pixel from 0 to $2\pi$ (blue arrow), one can control the corresponding input contribution to the overall interference at the targeted output. For example, with a goal to enhance intensity at the targeted output, one can set a certain phase at that input in order to form a constructive interference. (b) By doing the same for all $n$ input contributions, one thus obtains an enhancement of the intensity at the targeted output of the order of $n$. Intensity scales of (a) and (b) outputs are on different scales for visualization.

in optical systems [Vellekoop and Mosk, 2008, Mosk et al., 2012, Rotter and Gigan, 2017].

In addition to a wide range of wavefront-shaping-based applications, others that are based on strong, deterministic and optimal mixing can be applied in, for instance, cryptography and security [Pappu et al., 2002, Horstmeyer et al., 2013, Goorden et al., 2014, Bromberg et al., 2019], communication [Skipetrov, 2003], and compressive sensing [Donoho, 2006, Candes and Tao, 2006, Liutkus et al., 2014]. For more information, please refer to the review [Rotter and Gigan, 2017].

### Applications: Concept of opaque lens

The spatial light modulator in conjugation with a complex medium becomes an optical system that acts as so-called *opaque lens* [Jon Cartwright, 2007, Vellekoop et al., 2010].

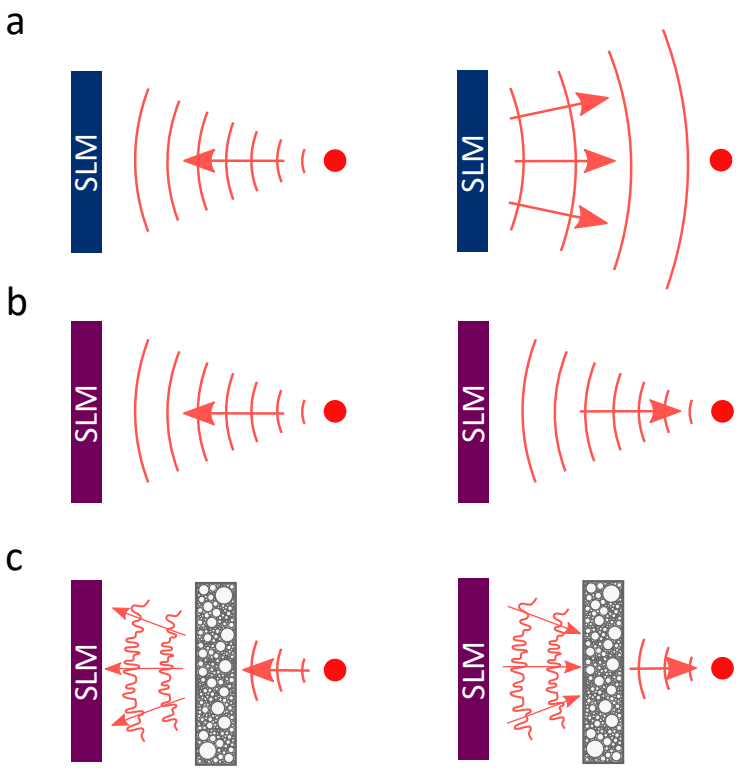


**Figure 2.5 – Optical phase conjugation**: (a) Time-reversed version of a simplified experiement in Fig. 2.4 without scattering medium. Light emits from point source then reflect by a flat phase on the SLM (b) By displaying the phase-conjugated of the propagating wavefront from the emitter on the SLM, Light is controlled to transport back in the same way. This is the concept of optical phase conjugation. (c) The same concept also apply to a case with the presence of a scattering medium.

The system can also enhance lights to focus on many output spots [Vellekoop and Mosk, 2007, Popoff et al., 2010b], therefore, behaving as a beam splitter [Huisman et al., 2015]. By exploiting the presence of fully mixed polarization in a transmitted speckle of a complex medium, an arbitrary polarization state at the focus can be controlled [Small et al., 2012a, Tripathi et al., 2012, Tripathi and Toussaint, 2014]. Similarly, the presence of complex mixing between the spatial degree of freedom and other photonic degrees of freedom in a medium allows the wavefront shaping technique to manipulate light onto a targeted output allocated on different photonic degrees of freedom, i.e., (1) polarization [Small et al., 2012a, Xiong et al., 2018], (2) spectral [Small et al., 2012b, Paudel et al., 2013, Andreoli et al., 2015] and (3) temporal [McCabe et al., 2011, Choi et al., 2013, Kang et al., 2015, Mounaix et al., 2016a, Mounaix et al., 2016b].

Consequently, the concept of opaque lens, i.e., the combination of SLM and complex medium, has been nowadays applied to various tunable optical devices as illustrated in Fig. 2.6, for instance, a beam splitter, a waveplate [Small et al., 2012a], a diffraction grating [Andreoli et al., 2015], a spectral filter and spectrometer [Small et al., 2012b, Redding and Cao, 2012, Bruce et al., 2019], a pulse shaper [Mounaix et al., 2016b], a point-spread-function engineering system [Čižmár and Dholakia, 2012, Boniface et al., 2017], or a mode sorter [Fickler et al., 2017].

Over the last decade, the concept of opaque lens has also been actively applied to a mul-

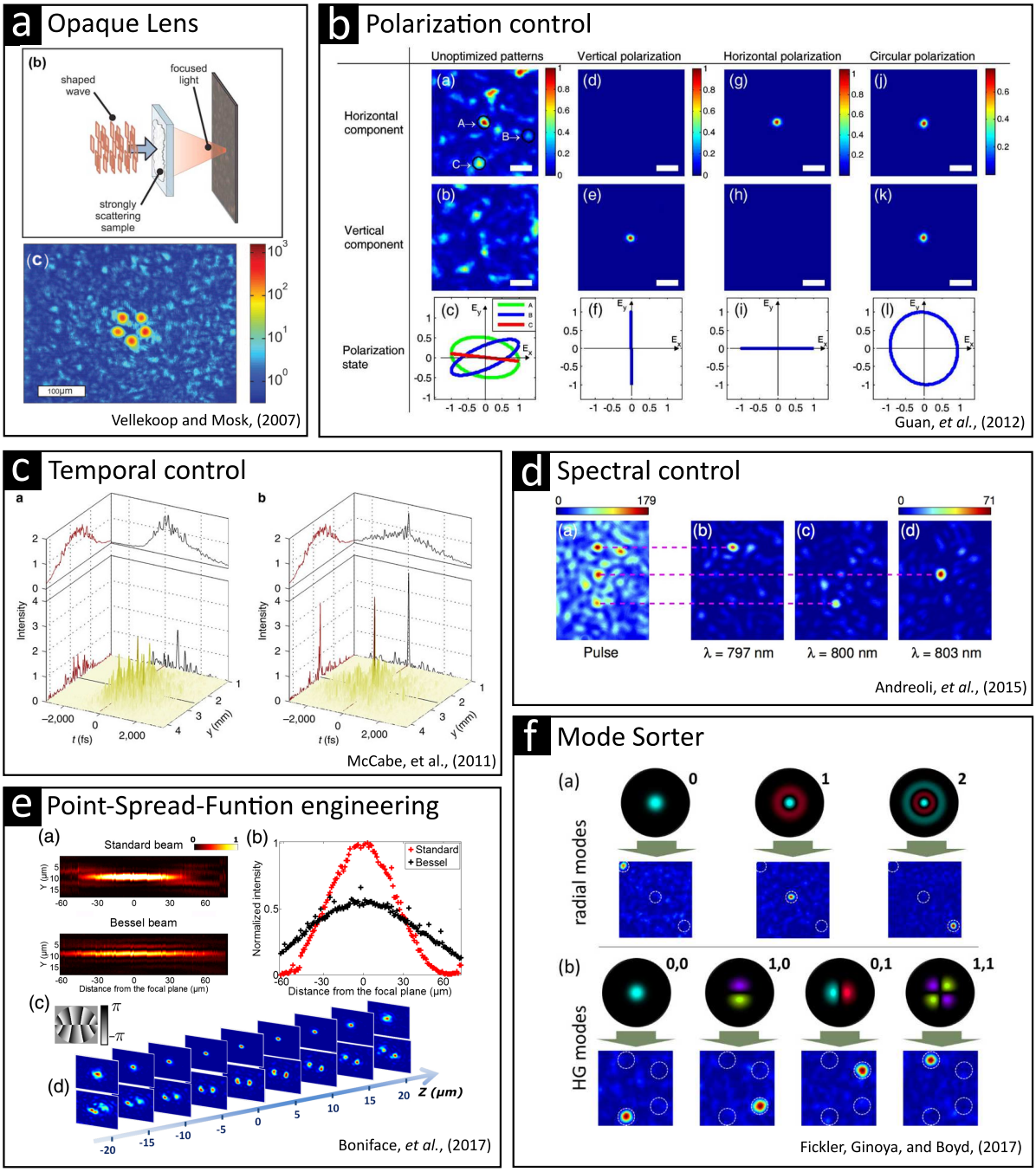


**Figure 2.6 – Applications of wavefront shaping through complex medium**: (a) Opaque lens: a combination of SLM and disordered medium (top) is applied to focusing light into multiple foci (below). Adapted from [Vellekoop and Mosk, 2007]. (b) Control of polarization states at the output focus. Adapted from [Small et al., 2012a]. (c) Control of focusing light on both spatial-temporal domains before (left) and after (right) wavefront shaping. Adapted from [McCabe et al., 2011]. (d) Opaque lens as a grating splitting different wavelengths to focusing onto different outputs. Adapted from [Andreoli et al., 2015]. (e) Opaque lens as a point-spread-function engineering system for generating Bessel-like beam (top) and double helix beam (below). Adapted from [Boniface et al., 2017]. (f) Opaque lens as a mode sorter for radial mode and Hermite-Gaussian (HG) modes. Adapted from [Fickler et al., 2017].

timode fibre with a wide range of applications [Di Leonardo and Bianchi, 2011, Čižmár and Dholakia, 2011]. The main research area aims at exploiting a multimode fibre in conjugation with the SLM as a compact endoscope for imaging applications and optical manipulations [Čižmár and Dholakia, 2011]. This is because a long multimode fibre (> few millimetres) can bypass a scattering biological tissue and provides a good and high-resolution image while keeping minimal invasiveness. This has been a very active field and applied to many image techniques. Pioneering works demonstrated optical manipulation [Di Leonardo and Bianchi, 2011, Čižmár and Dholakia, 2011, Čižmár and Dholakia, 2012, Bianchi and Di Leonardo, 2012], bright- and dark-field imaging [Čižmár and Dholakia, 2012], TM-based imaging [Choi et al., 2012], fluorescence imaging through a fibre [Čižmár and Dholakia, 2012, Papadopoulos et al., 2013, Loterie et al., 2015], and point-spread-function engineering at the distal end of a fibre for light-sheet microscopy [Plöschner et al., 2015a]. Many works have studied and improved imaging techniques, for example, the study of focusing quality and image resolution [Mahalati et al., 2012, Papadopoulos et al., 2012, Mahalati et al., 2013, Descloux et al., 2016], and the development of fast and efficient wavefront shaping techniques [Plöschner et al., 2014, Plöschner and Čižmár, 2015, Caravaca-Aguirre and Piestun, 2017, Gordon et al., 2019]. Furthermore, important issues concerning dynamical bending of a fibre, which will occur in a real imaging situation, have been addressed [Caravaca-Aguirre et al., 2013, Farahi et al., 2013, Gu et al., 2015, Caravaca-Aguirre and Piestun, 2017, Plöschner et al., 2015b, Boonzajer Flaes et al., 2018]. These researches have put forward imaging techniques in realistic applications e.g., deep-brain fluorescence imaging [Ohayon et al., 2018, Vasquez-Lopez et al., 2018, Turtaev et al., 2018]. Non-linear fluorescence and Raman imaging have been demonstrated through a fibre [Morales-Delgado et al., 2015b, Rosen et al., 2015, Sivankutty et al., 2016, Gusachenko et al., 2017].

Moreover, machine-learning-based approaches have also been applied to tackle the imaging problem through fibres with high reliability [Aisawa et al., 1991, Marusarz and Sayeh, 2001, Takagi et al., 2017, Caramazza et al., 2019]. Most techniques use artificial neural networks e.g., convolutional neural network, to predict input images from the intensity-only output speckle pattern, for example, reconstructing handwritten digits from the MNIST database [Borhani et al., 2018, Rahmani et al., 2018, Turpin et al., 2018, Li et al., 2018, Fan et al., 2019].

In the context of wavefront control of light propagating through a fibre, complete control on a polarization state of an output field by modulating only the spatial profile in a graded-index fibre has been recently achieved [Xiong et al., 2018]. Likewise, many demonstrations for a control of pulse delivery through a MMF have been reported [Morales-Delgado et al., 2015a, Mounaix and Carpenter, 2019].

### Applications in quantum domain

In the context of quantum optics, wavefront shaping techniques were first applied in 2014 to control the propagation of a he ralded single-photon Fock state through opaque scattering medium (ZnO) [Huisman et al., 2014b]. The concept of the demonstration is analogous to the pioneering work by [Vellekoop and Mosk, 2007]. After the wavefront optimisation, the input light source was replaced by the single-photon source that was prepared exactly in the same optical mode. As shown in Fig. 2.7a, phase pattern displayed on the SLM is optimised to focus a single-photon state onto a single output speckle grain. The heralded single-photon rate shows the 30-fold enhancement compared to the

average heralded rate where random phase patterns are displayed on the SLM. In the same year, wavefront shaping was applied to engineer a heralded single-photon state that is allocated between two output foci reflected from the opaque scattering media ($TiO_2$) [Defienne et al., 2014] (Fig. 2.7b). The optimal wavefront was obtained via the scattering-matrix approach [Popoff et al., 2010b]. The engineered single-photon states are in the superposition of two output modes and the coherence property of the state was investigated via the single-photon interference. The reported visibility of interference is $0.78 \pm 0.04$ and the reduced density matrix was deduced [Defienne et al., 2014] and depicted in Fig. 2.7b. The results indicate a high degree of coherent wavefront control of the single-photon state.

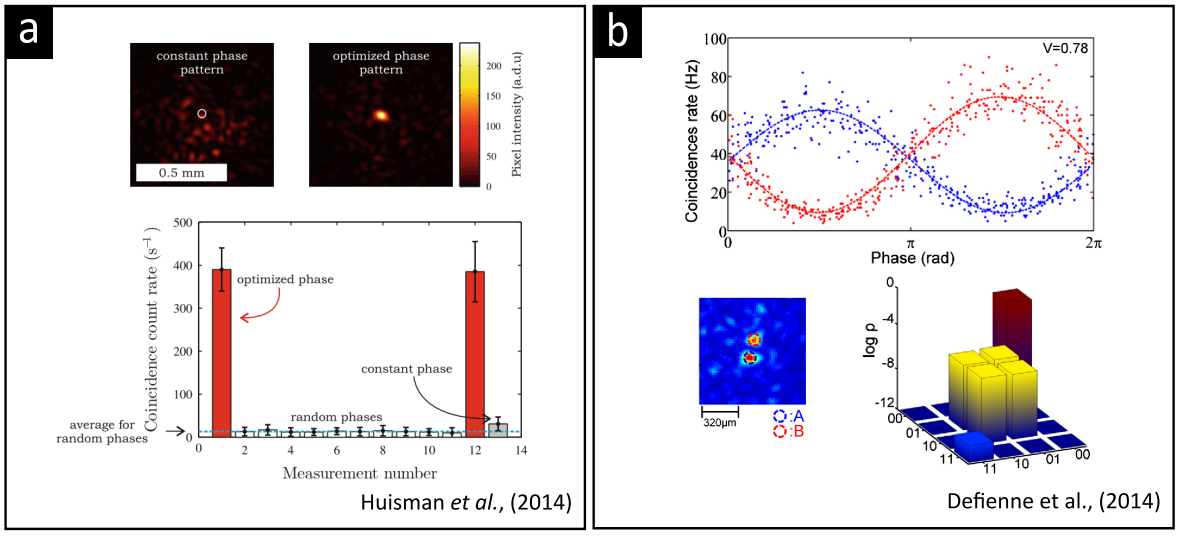


**Figure 2.7 – Manipulation of single-photon states through disordered media**: Wavefront shaping of single-photon states through disordered media: (a) Focussing of a single-photon state Adapted from [Huisman et al., 2014b] and (b) Single-photon state engineering Adapted from [Defienne et al., 2014]

In 2016, the wavefront shaping technique was extended to control a two-photon state using a diffusive medium (500-$\mu m$-thick polytetrafluoroethylene, PTFE, Teflon) [Wolterink et al., 2015] as well as a multimode fibre [Defienne et al., 2016]. The SLM and a complex medium together acts as a programmable beamsplitter used for manipulating two-photon interferences. As depicted in Fig. 2.8, the profile of the two-photon interference can be manipulated from the conventional dip feature (a well-known HOM two-photon interference [Hong et al., 1987]) to an inverted dip, i.e, a peak feature. In the case of a transport through the diffusive medium [Wolterink et al., 2015], the maximum visibility of two-photon interference is reduced from 0.86 of the SPDC source to 0.59 after propagating through the PTFE medium. We expect that result from temporal distinguishability of photon pairs. Moreover, the coincidence count is of the order of a few tens per hour. On the other hand, the control of two-photon interference with the multimode fibre [Defienne et al., 2016] provides the maximum visibility of 0.81 after propagating through the MMF, which is close to the visibiltiy of the light source of 0.86, while the coincidence count is much higher than that of the PTFE medium [Defienne, 2015, Defienne et al., 2016].

In fact, the idea of using the opaque lens as the beamsplitter can be generalized to a multimode interferometer, a.k.a, a linear optical network. For this purpose, the control

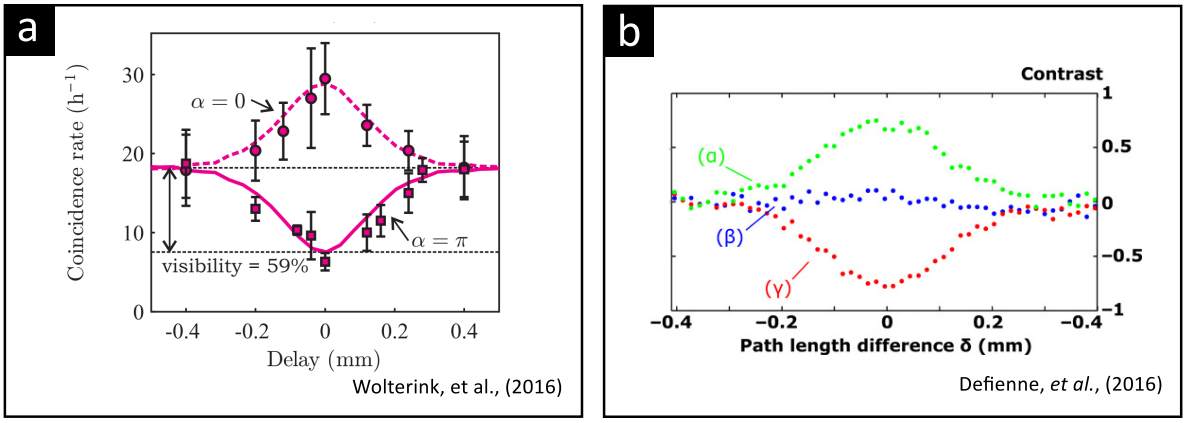


**Figure 2.8 – Control of two-photon interferences with complex media**: Two-photon interference with (a) a diffusive medium Adapted from [Wolterink et al., 2015] and (b) wtih a MMF. Adapted from [Defienne et al., 2016]

of not only amplitude but also phase of each element of a desired linear transformation is required. The initial idea has been proposed in 2014 by Simon R. Huisman *et al.* [Huisman et al., 2014a, Huisman et al., 2015] where programmable 2-input to 2- or 3-output balanced beamsplitters were classically implemented in opaque scattering medium using iterative optimization. Hitherto, there has been only one experimental work reported by Maxime W. Matthès, *et al.* showing scalability of this idea on a spatial degree of freedom with a step-index fibre via an optimization-based approach [Matthès et al., 2019]. As shown in Fig. 2.9, the procedure of optimizations consists of two steps: In step 1 (calibration), the transmission matrix of a medium is obtained via phase retrieval algorithm. Then, in step 2 (projection calculation), the set of SLM phase patterns for a given target optical network is estimated via the convex optimization. The results present an implementation of up to a 16-dimensional reconfigurable linear transformation. One could mention that this approach to wavefront control is very lossy since the SLM is implemented by means of amplitude modulation with a digital micro-mirror devices (DMD). We note that, more generally, the ability to design a linear transformation based on the complex mixing of wave fields finds use also in the context of radio-frequency in a controllable indoor environment [del Hougne and Lerosey, 2018]. Furthermore, the wavefront shaping technique has recently been applied to control a second-order spatial coherence of spatially-entangled photon pairs through a thin diffusive medium (parafilm) [Defienne et al., 2018a].

### 2.1.4 Conclusive remarks and objectives

To conclude, two key ingredients for programming optical networks were introduced, which are (1) the spatio-polarization complex mixing property of the multimode fibre (Sec. 2.1.2) and (2) the technique of wavefront shaping (Sec. 2.1.3). As for practical linear circuits, there are still many open questions to answer and requirements to satisfy for quantum applications, in particular, loss, scalability, and programmability. In this chapter, our objective is to answer those questions and also to demonstrate experimentally the accuracy and reliability of our arbitrary programmable linear optical networks for controlling two-photon interference in a high-dimensional linear transform across different degrees of freedom. In the next section (Sec. 2.2), the method for constructing a linear network is presented, and the quantum experimental results (Sec. 2.3) and the theoretical model of the implementing optical networks (Sec. 2.4.1) are discussed accordingly.

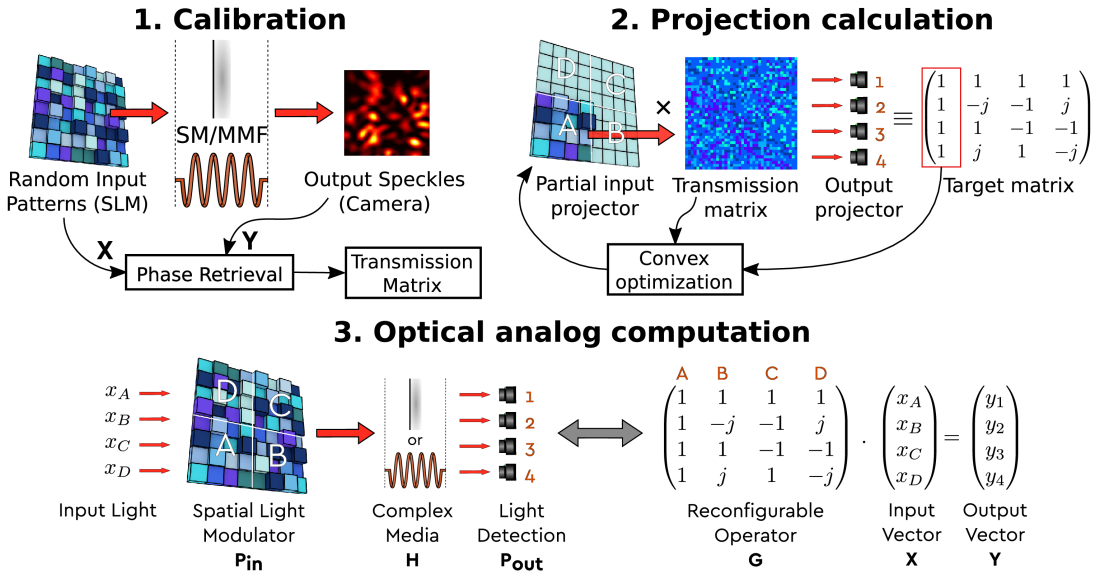


**Figure 2.9 – Complex media as reconfigurable linear optical network**: (1) Calibration step, (2) Calculation of projection, and (3) Implementation. Adapted from [Matthès et al., 2019]

## 2.2 | Experimental methods

The complex spatial and polarization mixing occurring in the multimode fibre is the key ingredient that enables the design of a reconfigurable linear transformation $\mathcal{L}_i$. In the next section, we present the main components of the experimental setup which are used in every experiments described in this dissertation. The details of minor change for each specific experiment are pointed out in the method section of each experiment.

### 2.2.1 Experimental setup

The experimental setup is conceptually illustrated in Fig. 2.10. The setup is composed of three main parts: a light source, a programmable linear optical network, and a detection part.

- **Source**: Two-photon state is generated by a spontaneous parametric down-conversion (SPDC) process (see details in Appendix A). In this chapter, the prepared photon pairs are frequency-degenerate polarization-separable biphoton state.
- **Programmable linear optical network**: It consists of a liquid-crystal-on-silicon-based SLM (LCOS-SLM) and MMF. The LCOS-SLM is a reflective type of a pure phase modulation technique (Hamamatsu, X10468-02). The MMF used in this chapter is a graded-index fibre supporting $\sim$ 400 propagating modes at $\lambda = 810$ nm. (Thorlabs, GIF50C of length 55.3±0.1 cm, core diameter 50±2.5 $\mu$m, and numerical aperture 0.200±0.015)
- **Detection**: There are two detection pathways. In the first pathway, four targeted output ports which correspond to two spatial modes and two polarizations labelled as (H1, V1, H2, V2) are detected by four avalanche photodiode detectors (APDs). The photocurrents are sent to the coincidence electronics where the photocount and two-fold coincidences are registered. In this chapter, we set the coincidence time window to 2.5 ns. The accidental coincidences are subtracted from the two-fold

coincidence counts. In the second pathway, outputs among spatial and polarization are imaged simultaneously by an electron multiplying charge-coupled device (EMCCD) camera.

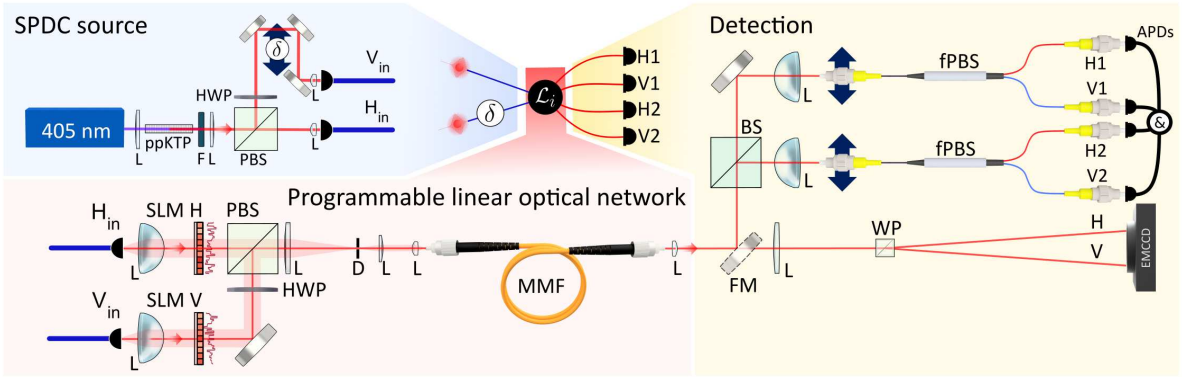


**Figure 2.10 – Multimode fibre-based programmable optical network**: Conceptual schematics of the apparatus. Photon pairs produced by spontaneous parametric down-conversion (SPDC) are injected into a multimode fibre (MMF) along orthogonal polarizations using spatial light modulators (SLM). We use commercial MMF (Thorlabs, GIF50C) as a tool to achieve mode mixing. The transmission matrix (TM) is measured across spatial and polarization modes of the MMF. The wavefront corresponding to a desired linear transformation $\mathcal{L}_i$ is calculated and displayed on the SLMs. Output ports of interest are selected by two single-mode fibre-based polarization beamsplitters (fPBS) mounted on translation stages. These correspond to two spatial modes and two polarizations labeled as (H1, V1, H2, V2). Light is detected by four Si-based avalanche photodiode single photon detectors (APDs) connected to the field-programmable gate array (FPGA) for counting photons and coincidences. The output plane of the MMF is imaged onto an electron multiplying charge-coupled device (EMCCD) camera along both polarizations (H and V). (L: lens, F: filter, HWP: half-wave plate, PBS: polarizing beamsplitter, D: iris diaphragm, FM: flip mirror, WP: Wollaston prism, BS: beamsplitter.)

There are two main techniques to construct a linear optical network: the first is based on an optimization approach and the second technique uses the knowledge of the transmission matrix (TM). In essence, both techniques should yield ideally almost the same results (see discussion in Sec. 2.4.3). In practice, the optimization-based techniques [Huisman et al., 2015, Spagnolo et al., 2017, Matthès et al., 2019] need typically to perform an optimization procedure for each implementation of an optical network; consequently they are extremely time consuming. On the other hand, the techniques based on the acquisition of TM can implement essentially any optical networks on arbitrary outputs since the complete TM is measured. In the following, we are going to present our methods for constructing a linear optical network. The technique is based fundamentally on the acquisition of TM and only apply an optimization approach on the last step in order to finely tune an accurate implementation.

### 2.2.2 Acquisition of transmission matrix

To obtain the TM, which relates optical input and output fields, direct and indirect measurements can be considered. The indirect TM measurement relies generally on phase retrieval techniques on measured intensity-only dataset [Drémeau et al., 2015, N'Gom et al., 2018, Matthès et al., 2019, Caramazza et al., 2019]. It has the advantage of using less number of measurements but can be computationally expensive. Noises might be present in the reconstructed TM. A large number of measurements are typically required before obtaining a sufficiently accurate TM. On the other hand, the direct measurement [Popoff et al., 2010b, Čižmár and Dholakia, 2011] relies on interferometry with the coherent light source. Consequently, the main issue is stability, which can be alleviated by the use of a co-propagating reference. The direct measurement has been a widespread method for characterizing an optical system, e.g, integrated photonic chips, scattering media and multimode fibres [Popoff et al., 2010b, Čižmár and Dholakia, 2011, Rahimi-Keshari et al., 2013, Dhand et al., 2016, Florentin et al., 2018]. In our experiment, we use the direct TM measurement with a few improvements that we have developed in order to acquire a complete and low-noise TM. In the following, the techniques we used are presented with their underlying justifications while introducing the acquisition of TM in detail.

In our experiment, the input basis is defined as a set of focus spots on an isometric grid on the input facet of the MMF, as shown in Fig. 2.12. This input basis corresponds to a set of grating patterns on the Fourier plane where the SLM is placed on (Fig. 2.10). The centre of the optical axis of the MMF is set apart from the zero-th diffraction order by 50 $\mu$m both horizontally and vertically. By doing this, we can avoid any unmodulated light from the zero-th order entering the MMF and we can, therefore, modulate an optical field at the input facet of the MMF more accurately and efficiently. The output basis is also chosen to be an array of diffraction-limited spots on the distal facet of the MMF, which is convenient for coupling the light into a single photon counting module. In the setup, one can measure all output modes simultaneously with an EMCCD camera or measure the targeted outputs of interest on desired positions using APDs. In our experiment, we separate the full completed TM for two desired input ports on different polarizations $p \in \{\mathrm{H_{in}}, \mathrm{V_{in}}\}$. Each input port corresponds to approximately 200 spatial modes.

The TM of the graded-index MMF is acquired using a co-propagating reference [Popoff et al., 2010b, Čižmár and Dholakia, 2011]. As illustrated in Fig. 2.12, for each $p$-th input port (each polarization), an over-complete spatial basis set of input wavefronts is sequentially sent through the MMF. By shifting the phase $\theta$ of each $i$-th input mode relative

to the co-propagating reference[8], the amplitude and phase of all targeted outputs are retrieved simultaneously from photon counts using APDs or EMCCD. The technique for reconstructing the optical field from an intensity is the so-called phase-shifting interferometry [Yamaguchi and Zhang, 1997]. In detail, for each $p$-th input port, the photocurrent at a given input mode $i$-th and the $j$-th output mode is related via:

$$\begin{aligned} I_{ji}^{(p,\theta)} &= |\tilde{R}_j^{(p)} + \tilde{E}_{ji} e^{i\theta}|^2 \\ &= |\tilde{R}_j^{(p)}|^2 + |\tilde{E}_{ji}|^2 + 2|\tilde{R}_j^{(p)}||\tilde{E}_{ji}| \cos\Big(\phi_j^{R^{(p)}} - \phi_{ji} - \theta\Big), \end{aligned} \tag{2.7}$$

where $\tilde{R}_j^{(p)} = |\tilde{R}_j^{(p)}| e^{i\phi_j^{R^{(p)}}}$ denotes the complex reference field for $p$ input port, $\tilde{E}_{ji} = |\tilde{E}_{ji}| e^{i\phi_{ji}}$ is the complex field at the $j^{\text{th}}$ output mode for a given $i^{\text{th}}$ input mode, i.e., the element of the TM. By shifting the phase $\theta$ for $N_\theta$ steps, one can retrieve a transmission matrix element $M_{ji}$:

$$\begin{aligned} M_{ji}^{(p)} &= \frac{1}{N_\theta} [I_{ji}^{(p,\boldsymbol{\theta})} \cdot \cos(\boldsymbol{\theta}) - i I_{ji}^{(p,\boldsymbol{\theta})} \cdot \sin(\boldsymbol{\theta})] \\ &= \tilde{E}_{ji} \tilde{R}_j^{(p)*} \\ &= |\tilde{E}_{ji}||\tilde{R}_j^{(p)}| e^{i(\phi_{ji} - \phi_j^{R^{(p)}})}, \end{aligned} \tag{2.8}$$

where $\boldsymbol{\theta}$ is the vector contained $N_\theta$ number of shifted phases, and $I_{ji}^{(p,\boldsymbol{\theta})}$ is the corresponding vector of measured photocurrents. The transmission matrix element $M_{ji}^{(p)}$ contains both optical output field and the reference field. After measuring the whole set of $i$-th inputs, all elements of $\mathbf{M}^{(p)}$ are obtained. Then, the amplitude of reference can be eliminated from $\mathbf{M}^{(p)}$ by sending only the reference light through the fibre, and measuring the intensity pattern of the output reference $I_j^{R^{(p)}} = |\tilde{R}_j^{(p)}|^2$. The transmission matrix $\mathbf{T}^{(p)}$ linking the relevant input modes for each $p$-th input port to the targeted output modes is acquired:

$$\begin{aligned} T_{ji}^{(p)} &= \frac{M_{ji}^{(p)}}{\sqrt{I^{R_j^{(p)}}}} \\ &= |\tilde{E}_{ji}| e^{i(\phi_{ji} - \phi_j^{R^{(p)}})}. \end{aligned} \tag{2.9}$$

Via this method, the TM for each $p$-th input port $(\mathrm{H_{in}}, \mathrm{V_{in}})$ is independently acquired. Thus the relative amplitudes and phases of the co-propagating references between both input ports remain unknown and need to be calibrated.

To do so, we program a given designed linear transformation $\mathcal{L}$ by using the pre-calibrated TM in Eq. 2.9 (see network programming in subsection 2.2.3 for a method). For example, we choose $\mathcal{L} \propto \left[\begin{smallmatrix} 1 & 1 & 1 & 1 \\ 1 & 1 & 1 & 1 \end{smallmatrix}\right]^{\mathsf{T}}$ for 2-input $\times$ 4-output optical network in this experiment. Then we use the corresponding measured photon counts and two-photon interferences (section 1.3) to obtain a complex amplitude of the relative co-propagating reference fields (see the calculation in [Laing and O'Brien, 2012]).

In practice, the presence of experimental noises and instability results in a low-intensity enhancement and therefore poor fidelity of a desired linear network. By combining the

[8]The use of co-propagating reference improves the stability of the interferometric measurement [Popoff et al., 2010b].

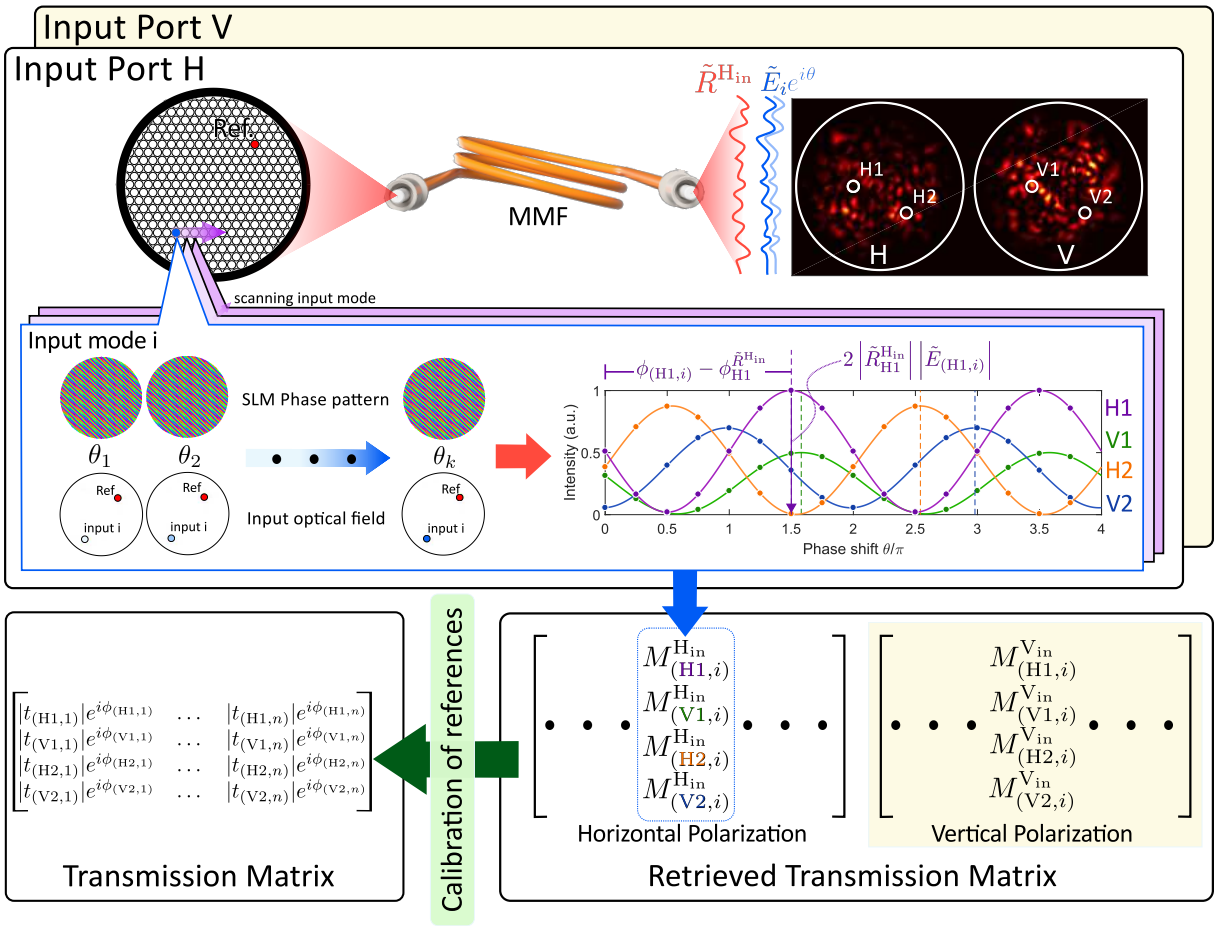


**Figure 2.11** – **Acquisition of transmission matrix**: The TM of a graded-index MMF is acquired using a phase-shifting holographic technique with a co-propagating reference. The TM for two input ports (H and V) are measured independently. For each input port, an over-complete spatial basis set of input wavefronts is sequentially sent through the MMF (blue). By shifting the phase $\theta$ of each $i$-th input mode $\tilde{E}_i e^{i\theta}$ relative to the co-propagating reference $\bar{R}$ (red), the complex amplitude of the targeted outputs, labelled H1, V1, H2, V2, are retrieved simultaneously from photon counts using APDs. When the process is done for all input modes and two input ports (H and V), the relative amplitudes and phases of the co-propagating references are then calibrated to obtain the TM.

information from two-photon interferences, the relative phases of reference are therefore obtained with high stability, compared to the measurement of classical interference between two input ports as reported in [Defienne, 2015]. The calibration via the two-photon interference is moreover independent of loss at input and output ports, which can be present in the amplitude calibration (Eq. 2.9). To further get rid of noises in the TM acquisition, one acquires multiple phase-shifting steps $\theta$, while the acquisition time is increased to get rid of noises from the light source. Due to the speckle statistics (see Eq. 2.3), a low-intensity co-propagating speckle reference is more likely to result in a low-intensity enhancement [Čižmár and Dholakia, 2011, Hofer and Brasselet, 2019]. In order to tackle this problem, we perfect the measurement by coupling the co-propagating reference field to different inputs of the MMF, or by using a focusing co-propagating reference field generated from the previous TM acquisition.

In particular for the quantum experiment reported in this chapter, we use the SPDC light source in the TM measurement, set the APD acquisition time of 0.2 s, and set the number of phase-shifting $N_\theta$ to 16 steps over $4\pi$ phase shift. We solve the low-intensity co-propagating reference by using the focusing co-propagating reference field calculated from the previous acquired TM.

### 2.2.3 Construction of linear optical network

Once the TM has been measured, the information can be used to control light propagation through a system of interest. Typically, the TM is used for focusing light in a given output mode; therefore, only an intensity enhancement is needed. For this purpose, the pre-calibration TM is sufficient (Eq. 2.8). To construct a linear optical network, on the other hand, both amplitude and phase of each element of a programmed linear transformation $\mathcal{L}$ needs to be accurately controlled; hence one need the calibrated TM. The concept of programming network relies on an inverse scattering problem (phase conjugation) [Rotter and Gigan, 2017], similar to focusing applications. For each $p$-th input port of the desired network $\mathcal{L}^{(p)}$, the input optical fields $\tilde{E}_{\text{in}}^{(p)}$ is calculated by,

$$\tilde{E}_{\text{in}}^{(p)} = \mathbf{T}^{(p)\dagger}\mathcal{L}^{(p)}, \tag{2.10}$$

where $\mathbf{T}^{(p)}$ is the sub-part of the measured TM linking the relevant input modes for each $p$-th input port of the optical network to the targeted output modes. In our experiment, the inverse operator is achieved by the conjugate transpose (Hermitian transpose, †). Fidelity of the desired optical networks is introduced by the imperfection in the inverse process (see related discussion presented in section 2.4). The corresponding phase pattern on the SLM is then calculated by means of Fourier transform. In detail, the calculated optical field on the SLM is a weighted summation of blazed gratings obtained by combining amplitudes and phases from Eq. 2.10. The phase solution of the calculated optical field is displayed on the SLM for each input port so that the linear network is programmed as illustrated in Fig. 2.12.

Imperfections in generating the optical input fields $\tilde{E}_{\text{in}}$ with the SLM lead to errors in the TM estimation, and accordingly result in errors in the coefficients of the linear transformation $\mathcal{L}$. In addition, we can further adjust the relative amplitude of the co-propagating reference field of each $p$-th input port independently by minimizing $\sum_q \left(|\mathcal{L}_{qp}^{\text{exp}}| - |\mathcal{L}_{qp}^{\text{th}}|\right)^2$, where $\mathcal{L}_{qp}^{\text{exp(th)}}$ is the element of implemented (desired) linear transformation at $q^{\text{th}}$ output port and $p^{\text{th}}$ input port. Then, we can accurately calibrate the relative phases of

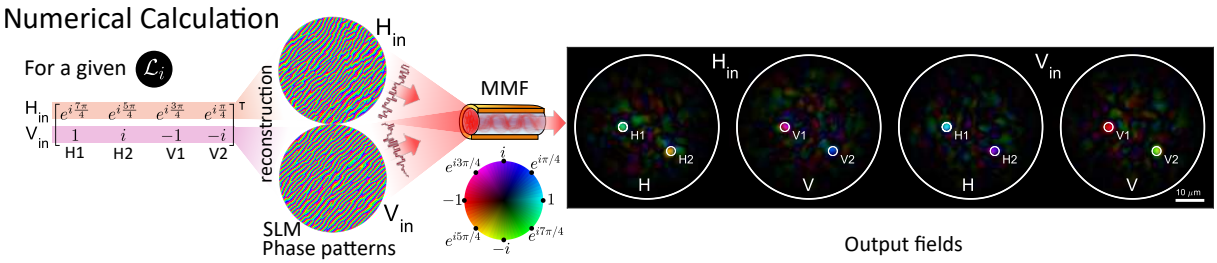


**Figure 2.12 – Construction of programmable linear optical network** An arbitrary $4 \times 2$ linear network $\mathcal{L}$ is implemented by shaping the spatial phases of each input port $H_{in}$ and $V_{in}$. For each input, the predicted numerical output fields after propagation through the MMF are shown. We observe that light is focused on the four targeted output ports with the desired amplitudes and phases. The TM used in the calculation is obtained from the experiment.

the reference field by minimizing the distance $\Delta\mathbb{V}$, where $\Delta\mathbb{V} = \sum_{(i,j)} |V^{\text{exp}}_{(i,j)} - V^{\text{th}}_{(i,j)}|$ and $V^{\text{exp(th)}}_{(i,j)}$ is the experimental (theoretical) visibility of two-photon interference at the $(i,j)$ pair of detectors. We refer to the optimizations in this paragraph as the procedure of fine calibrations. It is an optional step for perfect implementation of a linear optical network.

For the experimental results presented in this chapter, after the TM has been measured and calibrated via the information from the two-photon interference, we performed first the procedure of fine calibrations for amplitude and phase of the co-propagating reference fields using the designed linear transformation $\mathcal{L} \propto \left[\begin{smallmatrix} 1 & 1 & 1 & 1 \\ 1 & 1 & 1 & 1 \end{smallmatrix}\right]^{\mathsf{T}}$. Then, for each new linear transformation $\mathcal{L}$ implemented later on, we additionally readjust only the amplitudes by minimizing $\sum_q \left(|\mathcal{L}^{\text{exp}}_{qp}| - |\mathcal{L}^{\text{th}}_{qp}|\right)^2$ before using the implemented optical network $\mathcal{L}$ in the quantum experiments[9].

## 2.3 | Experimental results

The complex mixing together with the near-unitary of the MMF are exploited to program linear optical transformations $\mathcal{L}$. The experimental setup, as shown Fig. 2.10, was designed such that one can program linear optical network between two input ports on orthogonal polarizations $H_{in}, V_{in}$ into arbitrary targeted output ports across spatial and polarization degrees of freedom on the EMCCD camera. In term of technical challenge, we aim at demonstrating programmable arbitrary $2-$input $\times\, k-$output optical circuits across photonic degrees of freedom. To demonstrate so, we sent SPDC light through the optical setup where the four output ports of interest are allocated across spatial and polarization degrees of freedom, labelled H1, V1, H2, V2 (Fig. 2.10). First, the transmission matrix linking to these 4 outputs is measured (Sec. 2.2.2), then a designed linear optical network $\mathcal{L}$ is programmed using the SLM (Sec. 2.2.3).

### 2.3.1 Two-photon interference on multi-mode interferometer

By letting the indistinguishable two-photon state evolve through an optical interferometer, the two-photon interference occurs. We use this phenomenon to demonstrate the deterministic manipulation of quantum interference through a designed optical network

[9] The amplitude correction is for a perfect implementation of network programming.

$\mathcal{L}_i$, thereby showing the potential of the technique for quantum information processing. To demonstrate this, we implement programmable optical 2-input × 4-output networks simulating the action of three interesting interferometers in a four-dimensional Hilbert space defined across spatial and polarization degrees of freedom. They consist of four-dimensional Fourier [Schuck et al., 2016b], Sylvester [Viggianiello et al., 2018], and a non-unitary interferometer. We generalise the non-unitary interferometer from the tensor product of the 2-dimensional non-unitary interferometer proposed in [Barnett et al., 1998]. The Fourier and Sylvester interferometers have been used for certifying indistinguishability between input photons via verifying a suppression criteria [Tichy, 2014, Dittel et al., 2018a, Dittel et al., 2018b]. We verify these criteria for a specific two-photon input state by measuring the full set of output two-fold coincidence counts. Each type of interferometer consists of six optical networks of which each corresponds to one input combination pairs. Practically, the experiments demonstrate 18 balanced optical networks with fully controllable phase relations. In the following, the definitions of these interferometers and the experimental two-photon interferences are provided.

### Fourier interferometer

The $k$-dimensional Fourier transformation is defined element-wise as $e^{i2\pi(j-1)(p-1)/k}/\sqrt{k}$. In the four-dimensional case it reads

$$\mathcal{L}_{\mathrm{F}} = \frac{1}{2}\begin{bmatrix} 1 & 1 & 1 & 1 \\ 1 & i & -1 & -i \\ 1 & -1 & 1 & -1 \\ 1 & -i & -1 & i \end{bmatrix}, \tag{2.11}$$

The Fourier interferometer (F), also known as Discrete Fourier transform (DFT) or quantum Fourier transform (QFT), have been applied for phase estimation, prime factorization, and many quantum algorithms [Shor, 1997, Motes et al., 2015, Su et al., 2017]. The Fourier transform presents a symmetry which allows one to implement it with the least number of optical elements required in an implementation of a general unitary transform (section 1.5). Typically one needs $(\log_2 k)k/2$ optical elements instead of $k(k-1)/2$ used in the standard Fourier transform of dimension $k$ [Barak and Ben-Aryeh, 2007]. We note that this fact directly links to the digital implementation known as fast-Fourier transform [Cooley and Tukey, 1965]. Quantum interference on the Fourier interferometer has been implemented on an integrated photonic chip with fully reconfigurable silica-based planar waveguide circuit [Carolan et al., 2015] and with static laser-written silica-based circuit [Schuck et al., 2016b]. Our experimental two-photon interference on the Fourier interferometer is presented in Fig. 2.13.

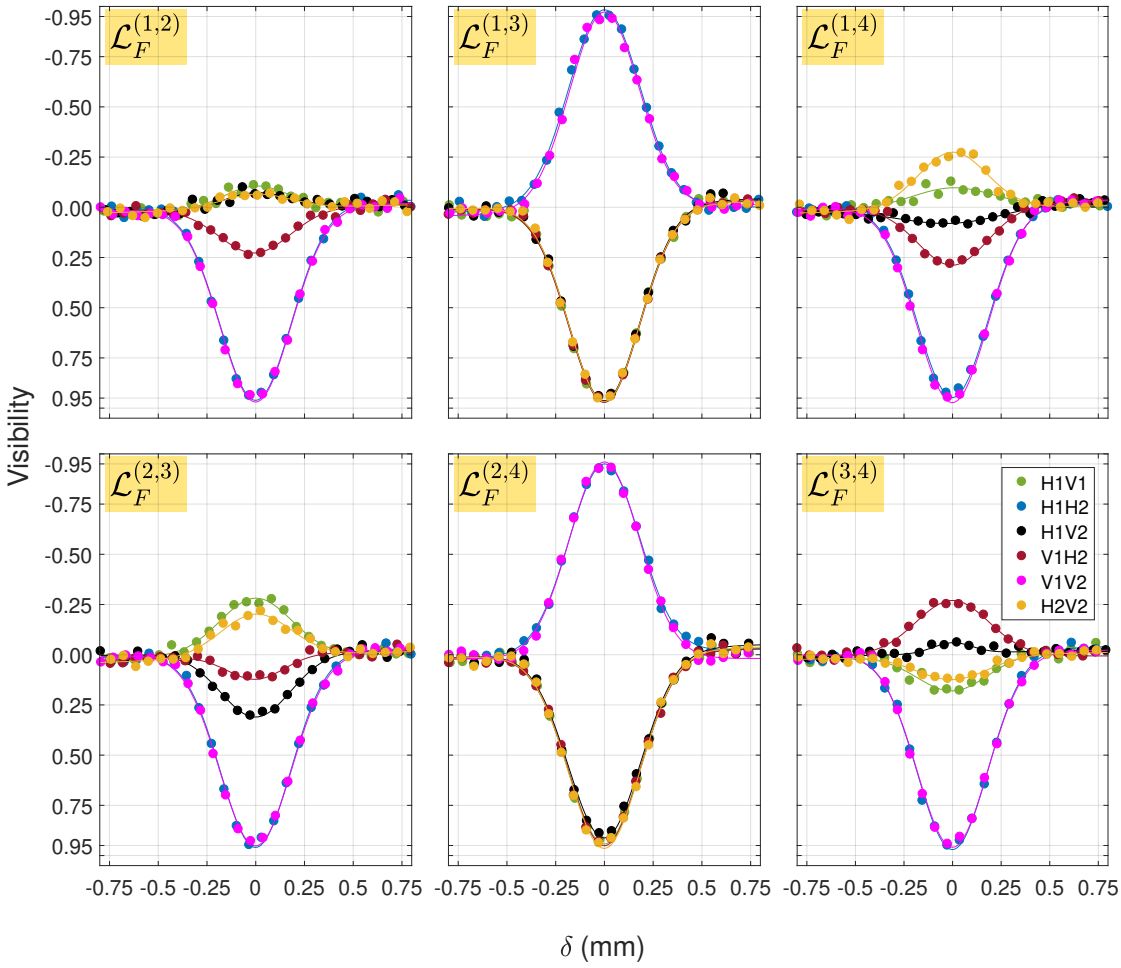


**Figure 2.13 – Visibility of two-photon interference on Fourier transformation $\mathcal{L}_\mathbf{F}$**: fitting (solid lines) and experiment (dots). In each panel the two-photon state is coupled to the different (i,j) input pairs $\mathcal{L}_\mathsf{F}^{(i,j)}$.

### Sylvester interferometer

The $k$-dimensional Sylvester transformation is a particular class of Hadamard matrices[10], where $k = 2^w$. The $2^w$-dimensional Sylvester transformation can be recursively constructed by

$$H(2^w) = \begin{bmatrix} H(2^{w-1}) & H(2^{w-1}) \\ H(2^{w-1}) & -H(2^{w-1}) \end{bmatrix}, \tag{2.12}$$

where $H(1) = [1]$. The definition equivalently corresponds to an element-wise expression where $[H(2^w)_{i,j}] = (-1)^{i_B \odot j_B}$ represents a value of element in each $i$ and $j$. $i$ and $j$ starts counting from zero. $i_B$ and $j_B$ represents in binary form and $\odot$ is the bitwise dot product defined as the sum modulo 2 of the product of bits. A simple case of the Sylvester interferometer in dimension of 2 is the balance beam splitter ($w = 1$) where the well-known Hong-Ou-Mandel effect is observed [Hong et al., 1987]. In our experiment, we implement the action of a 4-dimensional Sylvester transformation, which is expressed as,

$$\mathcal{L}_{\text{Sy}} = \frac{1}{2} \begin{bmatrix} 1 & 1 & 1 & 1 \\ 1 & -1 & 1 & -1 \\ 1 & 1 & -1 & -1 \\ 1 & -1 & -1 & 1 \end{bmatrix}, \tag{2.13}$$

As shown on Fig. 2.13, the experimental two-photon interferences on the Sylvester interferometer present photon bunching occurring in some input-output combinations (the two-photon visibility goes to 1) and photon anti-bunching occurred in other combinations (the two-photon visibility goes to $-1$). The theoretical prediction for the Sylvester interferometer [Crespi, 2015] shows that the number of output combinations, where photon bunching is presented, is the same for arbitrary two-photon coupling into different input ports. This number, which is known as the number of suppressed configurations (HOM dip), is equal to four in the 4-dimensional Sylvester transformation, as shown on Fig. 2.13. The results of suppression on the Sylvester interferometer have been reported on the integrated photonic platform with three-photon interference [Viggianiello et al., 2018].

[10] Hadamard matrices are orthogonal matrices with unnormalized elements equal to $\pm 1$.

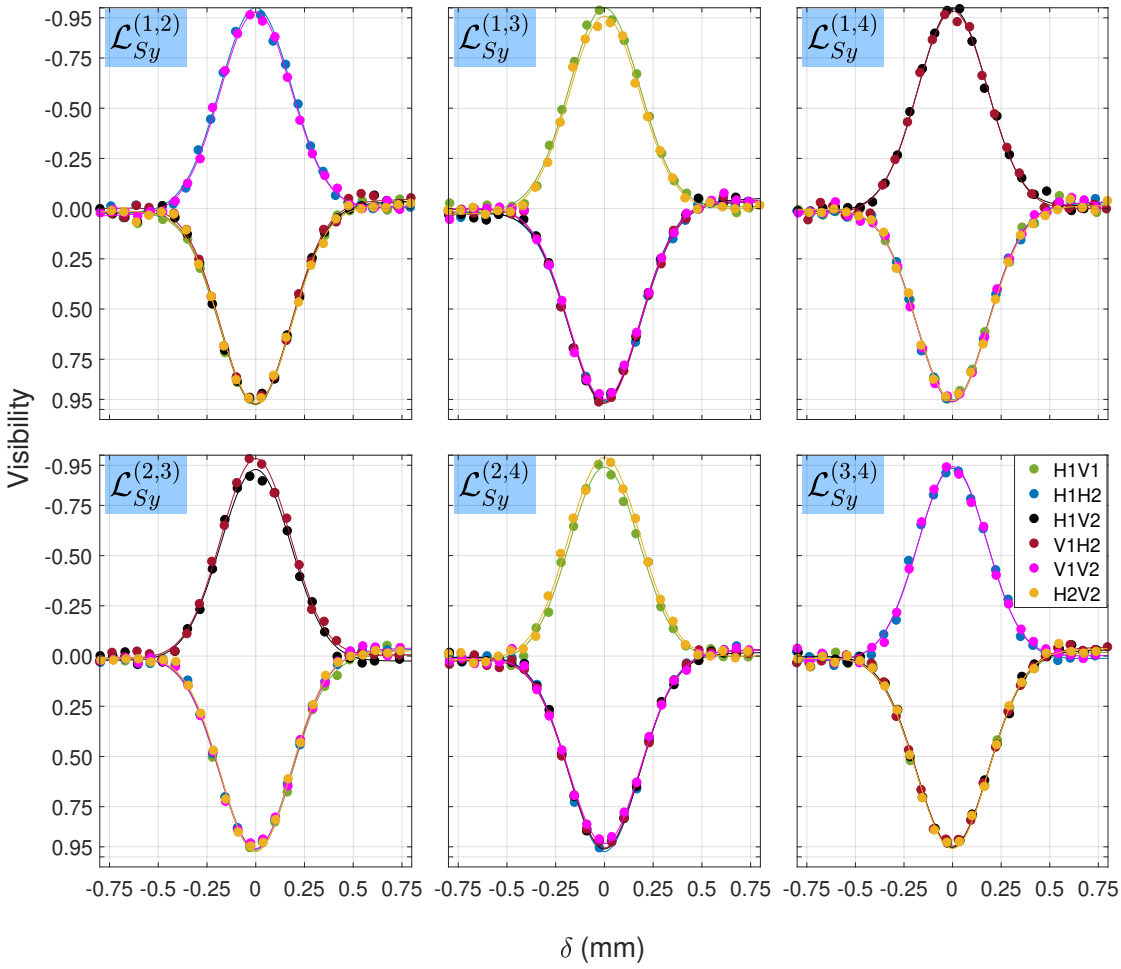


**Figure 2.14 – Visibility of two-photon interference on Sylvester transformation $\mathcal{L}_{\mathsf{Sy}}$**: fitting (solid lines) and experiment (dots). In each panel the two-photon state is coupled to the different (i,j) input pairs $\mathcal{L}_{\mathsf{Sy}}^{(i,j)}$.

### Non-unitary interferometer

Our platform can also implement an arbitrary linear network, which means an independent manipulation of phase and amplitude of each element in an optical network. To demonstrate this ability, we implement a non-unitary transformation $\mathcal{L}_{\mathrm{N}}$, defined as $\begin{bmatrix} 1 & -1 \\ -1 & 1 \end{bmatrix}^{\otimes 2}$, which reads

$$\mathcal{L}_{\mathrm{N}} \propto \begin{bmatrix} 1 & -1 & -1 & 1 \\ -1 & 1 & 1 & -1 \\ -1 & 1 & 1 & -1 \\ 1 & -1 & -1 & 1 \end{bmatrix}, \tag{2.14}$$

As shown in Fig. 2.15, all two-photon interferences across input-output combinations are mapped into photon anti-coalescence. This is the most interesting feature of the non-unitary transformation. We believe that this result has not been reported in literatures since the bulk of research has been focusing on unitary evolutions. We discuss and explore

this property in chapter 3. We note that the result purely stems from non-Hermitian physics of two-photon interference, and is not related to anti-bunching typically observed from two-photon interference of a singlet Bell entangled state on a unitary non-polarizing beamsplitter.

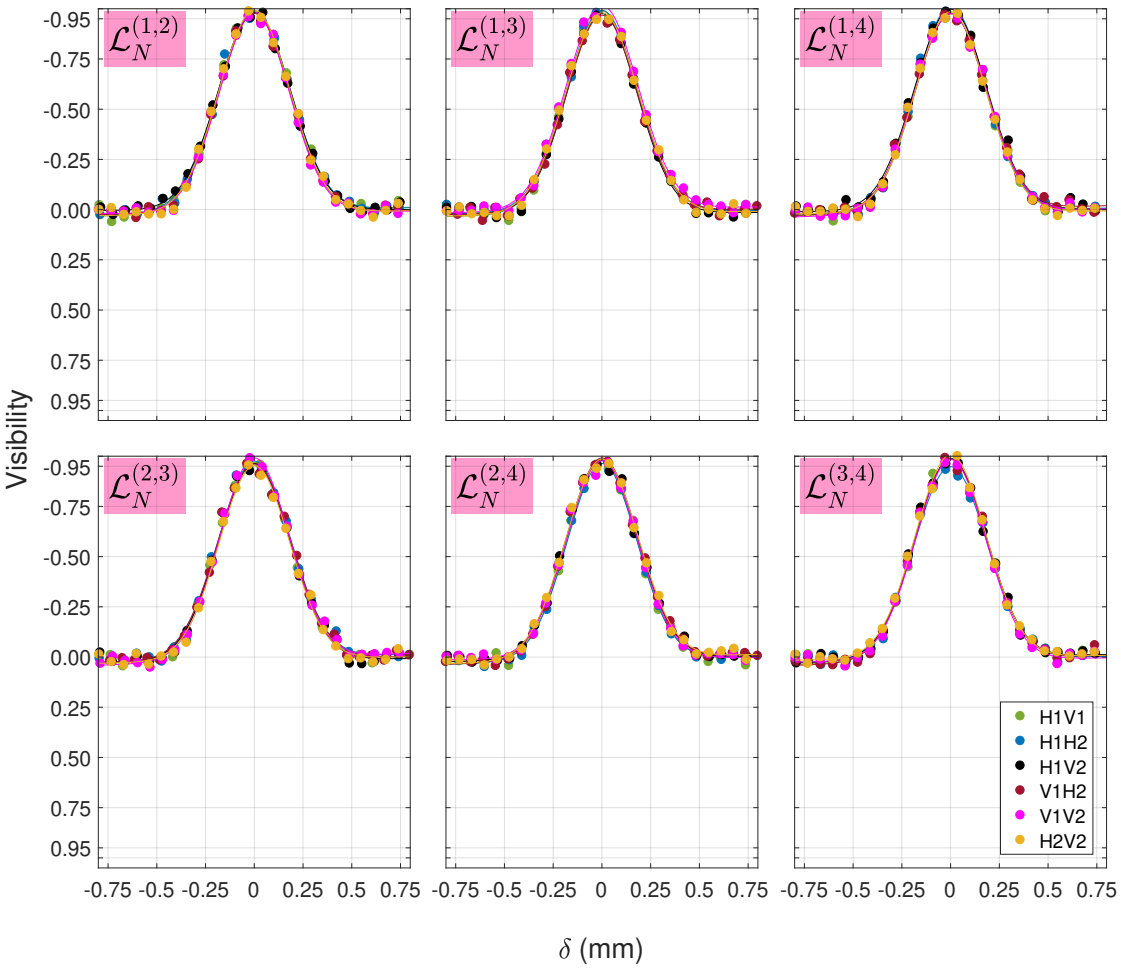


**Figure 2.15 – Visibility of two-photon interference on non-unitary transformation $\mathcal{L}_N$**: fitting (solid lines) and experiment (dots). In each panel the two-photon state is coupled to the different (i,j) input pairs $\mathcal{L}_N^{(i,j)}$.

### 2.3.2 Discussion

The results of two-photon interferences presented in Figs. 2.13, 2.14, and 2.15 can be summarized into a pattern of two-photon visibility depicted in Fig. 2.16 which presents the patterns of two-photon visibility as predicted by the theory (section 1.7). Importantly, maximum two-photon visibility values measured after propagation through the combination of SLM and MMF, which is $0.96 \pm 0.01$ averaged over the HOM dip configurations, are the same as those directly measured at the SPDC source ($0.95 \pm 0.03$). This indicates that the optical platform does not introduce significant temporal distinguishability between photon pairs.

#### Fidelity of linear optical networks

To quantitatively estimate the reliability of our platform, we provide a statistical analysis of the experiment on the control of two-photon interference. First, we compare the difference of predicted and measured visibility $V$ of the two-photon interference, (see definition in Eq. 1.35), as shown in Fig. 2.16. The error of two-photon interference between the experimentally synthesized transformation and the theoretically desired one is then determined by $\Delta\mathbb{V} = \sum_{(i,j)} |V^{\text{exp}}_{(i,j)} - V^{\text{th}}_{(i,j)}|/6$, where $V^{\text{exp(th)}}_{(i,j)}$ is the experimental (theoretical) visibility at the $(i,j)$ output ports. The values of $\Delta\mathbb{V}$ for the implemented optical networks are presented in the Table 2.1.

**Table 2.1** – The error of two-photon interference between the experimentally implemented and the theoretically desired transformations.

| Input pair | Fourier (F) | Sylvester (Sy) | Non-unitary (N) |
|---|---|---|---|
| (1,2) | 0.05 | 0.04 | 0.06 |
| (1,3) | 0.03 | 0.02 | 0.06 |
| (1,4) | 0.13 | 0.02 | 0.06 |
| (2,3) | 0.16 | 0.02 | 0.04 |
| (2,4) | 0.02 | 0.02 | 0.05 |
| (3,4) | 0.11 | 0.01 | 0.06 |

We measure $\Delta\mathbb{V} = 0.05 \pm 0.04$ on average over all transformations. The error presented in two-photon interference originates from the permanent of the corresponding linear transformation. The main contribution to the error originates from a case where the visibility of two-photon interference is zero (flat coincidence pattern), which exists only in the Fourier transformation. This is due to the fact that the phase sensitivity of two-photon interference is the highest at $V = 0$, the result implies the presence of a incorrect phase setting of implemented linear transformations.

To measure the fidelity of implemented linear transformations, an experimental linear transformation $\tilde{\mathcal{L}}$ is reconstructed with the measured two-photon visibility $V^{\text{exp}}$ by minimizing $\sum_{(i,j)} |V^{\text{th}}_{(i,j)} - V^{\text{exp}}_{(i,j)}|$, over the $(i,j)$ pair of detectors. The Monte Carlo technique is used to obtain statistics with 200 different initial conditions of an estimated linear transformation. Both experimental and desired linear operators are set to have the same setting of global input and output phases in order to avoid minima. This is because the equivalent class of a linear transformation up to a global input and output phases results in an identical two-photon interference patterns. We quantify the difference between the

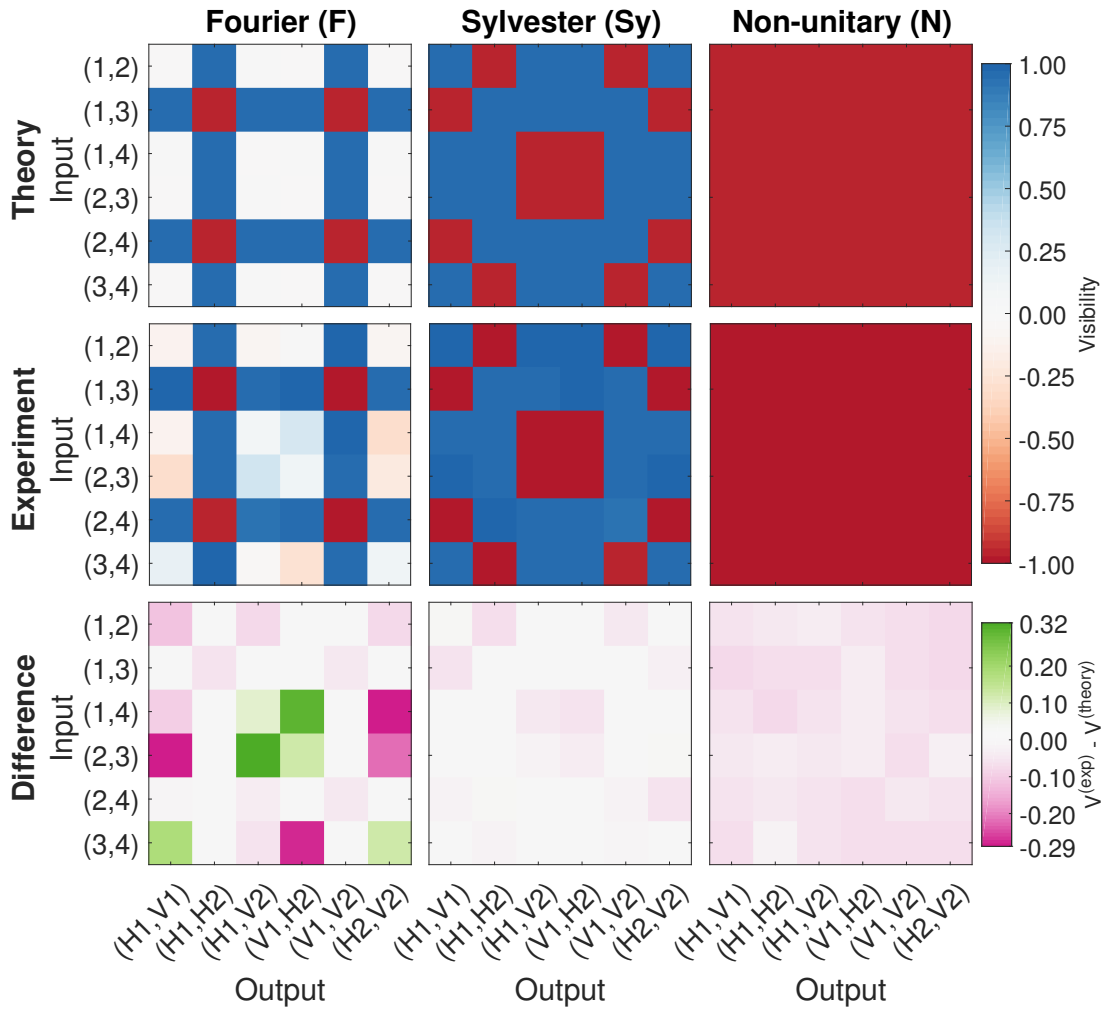


**Figure 2.16 – Control of two-photon interference among spatial-polarization degrees of freedom**: Visibility pattern of four-dimensional Fourier (F), Sylvester (Sy) and non-unitary (N) transformations for all input-output combinations. Theoretical perdition (the first row), experimental results (the second row), and difference between the experimental and theoretical visibility of two-photon interference (the third row). We obtained $\Delta\mathbb{V}_{\mathsf{F}} = 0.08 \pm 0.06$, $\Delta\mathbb{V}_{\mathsf{Sy}} = 0.02 \pm 0.01$, and $\Delta\mathbb{V}_{\mathsf{N}} = 0.06 \pm 0.01$ for Fourier, Sylvester, and non-unitary transformation, respectively.

implemented optical network $\tilde{\mathcal{L}}$ and the desired one $\mathcal{L}$ using the quantity $\mathcal{F}$, defined as

$$\mathcal{F}(\tilde{\mathcal{L}}, \mathcal{L}) = 1 - \|\mathcal{L} - \tilde{\mathcal{L}}\|_1, \tag{2.15}$$

where $\|\cdot\|_1$ is defined as $\|A\|_1 \equiv \sum_{i=1}^{k}\sum_{j=1}^{m}|a_{ij}|/mk$. The last term in Eq. 2.15 measures an average element-wise distance between $\mathcal{L}$ and $\tilde{\mathcal{L}}$. In the following, we refer to $\mathcal{F}$ as the figure of merit (fidelity) to characterise the performance of our implementation.

The obtained fidelities are presented in Table 2.2. For each type of transformation, we have the quantity $\mathcal{F}$ (Eq. 2.15) of $0.95 \pm 0.03$ (Fourier), $0.98 \pm 0.01$ (Sylvester), and $0.97 \pm 0.02$ (Non-unitary), respectively. Consequently, the experimental results clearly demonstrate the accurate control of two-photon interference over a $4 \times 2$ linear transformations across spatial-polarization degrees of freedom. In section 2.4, a theoretical explanation on how programming linear network works and related issues about fidelity, scalability, and programmability are discussed.

**Table 2.2** – Fidelity of linear optical networks

| Input pair | Fourier (F) | Sylvester (Sy) | Non-unitary (N) |
|---|---|---|---|
| (1,2) | 0.987±0.007 | 0.985±0.001 | 0.957±0.004 |
| (1,3) | 0.976±0.005 | 0.973±0.005 | 0.983±0.006 |
| (1,4) | 0.9498±0.0003 | 0.98±0.01 | 0.987±0.006 |
| (2,3) | 0.9136±0.0005 | 0.983±0.008 | 0.979±0.002 |
| (2,4) | 0.938±0.001 | 0.9730±0.0008 | 0.987±0.007 |
| (3,4) | 0.9608±0.0003 | 0.985±0.003 | 0.938±0.003 |

### Suppression phenomenon

A suppression phenomenon originates from symmetry in a many-particle interference resulting in a zero probability of occupation particles in specific input-output combinations of a given interferometer. The specific input-output combinations are known as the suppressed or forbidden configurations. The phenomenon is also known as *zero-transmission law* [Tichy et al., 2010].

To test the validity of the zero-transmission law, we measured the number of coincidences at all forbidden output combinations $N_{\text{forbidden}}$ while sending two indistinguishable photons into cyclic pair of inputs [Tichy et al., 2010]. The quantity is related to the *degree of violation* $\mathcal{D}$ which measures the probability of detecting two-photon states in all suppressed configurations ($N_{\text{forbidden}}/N_{\text{events}}$), where $N_{\text{events}}$ is the total number of events [Schuck et al., 2016b, Viggianiello et al., 2018]. The degree of violation $\mathcal{D}$ is defined as,

$$\mathcal{D} = \frac{N_{\text{forbidden}}}{N_{\text{events}}} = \sum_{(i,j)_{\text{forbidden}}} P^{\text{I}}_{(i,j)} = \sum_{(i,j)_{\text{forbidden}}} P^{\text{D}}_{(i,j)}(1 - V_{(i,j)}), \tag{2.16}$$

where $P^{\text{I(D)}}_{(i,j)}$ are the probabilties of having photons in the output $(i,j)$ in the case of indistinguishability (distinguishability). Note that $P^{\text{D}}_{(i,j)}$ is determined from single-particle probability.

In the perfectly indistinguishable case, the value of $\mathcal{D}$ goes zero, that is, no possibility of detecting particles in all suppressed configurations. In our experiment, the values of

$\mathcal{D}$ are presented in Table 2.3, on average they are as small as $0.022 \pm 0.009$ for Fourier interferometer averaged over $(1,3)$ and $(2,4)$ input pairs and $0.014 \pm 0.008$ for Sylvester interferometer averaged over all input pairs. The results show clear quantum distinctive feature where the probability amplitudes of the biphoton field related to all suppressed configurations interfere destructively.

**Table 2.3** – Degree of violation $\mathcal{D}$ for Fourier and Sylvester interferometers

| Input pair | Fourier (F) | Sylvester (Sy) |
|---|---|---|
| (1,2) | - | 0.0138 |
| (1,3) | 0.0158 | 0.0198 |
| (1,4) | - | 0.0206 |
| (2,3) | - | 0.0168 |
| (2,4) | 0.0284 | 0.0219 |
| (3,4) | - | 0.0233 |

## 2.4 | Reliability of complex mixing-based optical networks

The experimental results presented in the previous section indicate the realization of reconfigurable and accurate complex mixing-based optical networks. To provide a comprehensive insight into how our platform works and how reliable it is, the theoretical model is provided below. Through the end of the section, scalability of implemented optical networks is experimentally tested using the EMCCD camera.

### 2.4.1 Theoretical model

Recalling from Fig. 2.10, our programmable optical network is the linear system which is composed of two main elements, a programmable SLM followed by an optical mixer, the multimode fibre supporting the $n$ number of propagation modes. We here want to study the usability of our method to faithfully generate a given target linear transformation $\mathcal{L}$, modelled as a $k \times m$ matrix. Here $m$ is the number of input ports and $k$ of output modes of the associated optical network. We assume that the SLM provides complete control over all $n$ propagating modes of the MMF. Thus, the number of tunable elements in the setup is also $n$ and for each of the $m$ input ports of the target optical network, we can control and inject $d = n/m$ input physical modes of the MMF. For instance, we have $m = 2$ input ports of an optical network in the experiment, each input port can thus inject to $(n \approx 400)/(m = 2) \approx 200$ spatial modes in orthogonal polarizations. It is important to note that here with $p$-th input port we mean a set of $d$ physical modes controlled by a given SLM, which are used collectively to reproduce the action of the target linear transformation $\mathcal{L}$ on the $p$-th input port. The corresponding column of $\mathcal{L}$ is thus denoted as $\mathcal{L}^{(p)}$.

First, we quantify the ability to theoretically program a linear transformation $\mathcal{L}$. Let us first denote with $\mathbf{T}^{(p)}$ the part of transmission matrix linking the $p$-th input port to the $k$ output ports of interest, which is thus a $k \times d$ matrix. The input optical field $\tilde{E}_{\text{in}}^{(p)}$ that reproduces the target evolution $\mathcal{L}^{(p)}$ is determined by solving the relation $\tilde{E}_{\text{in}}^{(p)} =$

$\mathbf{T}^{(p)\dagger}\mathcal{L}^{(p)}$. With this notation, $\tilde{E}_{\text{in}}^{(p)}$ is thus a vector of length $d$, which represents the set of amplitudes of the input wavefront that, when displayed on the SLM, results in an effective implemented set of output amplitudes, here denoted as $\tilde{\mathcal{L}}^{(p)}$. Then, the corresponding phase patterns for all input ports are displayed on the SLM and light propagates through the fibre. MMF and SLMs thus work together to implement an effective linear optical network, which we describe with the matrix $\tilde{\mathcal{L}}$, that corresponds to desired $\mathcal{L}$ up to a global amplitude and phase factor. For each $p$-th input port, $\tilde{\mathcal{L}}^{(p)}$ and $\mathcal{L}^{(p)}$ are related via

$$\tilde{\mathcal{L}}^{(p)} = \mathbf{T}^{(p)}\mathbf{T}^{(p)\dagger}\mathcal{L}^{(p)}. \tag{2.17}$$

The overall fidelity of the optical network can, therefore, be related to the so-called time-reversal operator $\mathbf{T}^{(p)}\mathbf{T}^{(p)\dagger}$, which in general is an operator close to the identity operator [Popoff et al., 2010b]. To get an insight into the programming of a complex-mixing-based optical network, one needs to know or be able to model a transmission matrix $\mathbf{T}$ of the optical mixer.

For a straightforward model, the transmission matrix of the MMF is simply represented with a random matrix (RM), i.e., a matrix composed of i.i.d. complex Gaussian coefficients. $\mathbf{T}\mathbf{T}^\dagger$ is explicitly estimated [Derode et al., 2001, Aubry and Derode, 2010] and was shown that it converges to $\mathbf{T}\mathbf{T}^\dagger = \mathbb{1} + \mathbf{H}/\sqrt{n}$, where $\mathbf{H}$ is a complex Hermitian noise matrix. $\mathbf{T}\mathbf{T}^\dagger$ clearly converges to the identity operator $\mathbb{1}$ with $1/\sqrt{n}$. Similarly, when only $n/m$ input modes are controlled for each input port, the corresponding time reversal operator $\mathbf{T}^{(p)}\mathbf{T}^{(p)\dagger}$ which is constructed from the rectangular matrix $\mathbf{T}^{(p)}$ converges to the identity operator with $\sqrt{m/n}$:

$$\mathbf{T}^{(p)}\mathbf{T}^{(p)\dagger} = \mathbb{1} + \sqrt{\frac{m}{n}}\mathbf{H}. \tag{2.18}$$

Considering the distance between the desired linear transformation $\mathcal{L}$ and implemented linear transformation $\tilde{\mathcal{L}}$ as calculated in Appendix D, one obtains the fidelity scales as

$$\mathcal{F}(\tilde{\mathcal{L}}, \mathcal{L}) = 1 - \mathcal{O}\left(\sqrt{\frac{mk}{n}}\right). \tag{2.19}$$

This RM model, albeit a simple one, provides strong evidence in support of the statement that arbitrary desired transformations can be implemented with high performance, even when the dimension of optical networks is scaled up.

### 2.4.2 Numerical investigation

To compare our theoretical model with more practical cases close to real MMF, we numerically evaluate the fidelity $\mathcal{F}$ achieved for implementation of arbitrary optical networks using 3 different models of transmission matrices, which are a random matrix (RM), a random unitary matrix (RUM) obtained by the orthogonal triangular decomposition of a RM (see [Mezzadri, 2006] for the calculation routine), and an experimentally measured TM of the fibre (MMF). To take into account the ability to implement an arbitrary linear transformation $\mathcal{L}$, a set of $k \times m$ desired linear transformation $\mathcal{L}$ are sampled from random $k \times m$ matrices in our numerical model. Furthermore, in order to account for the

noise on the other unmonitored output modes, we define $\mathcal{L}$ on a complete output space of dimension $n$ where the $(n-k)$ rows of $\mathcal{L}$ corresponding to unassigned output modes are set to zeros.

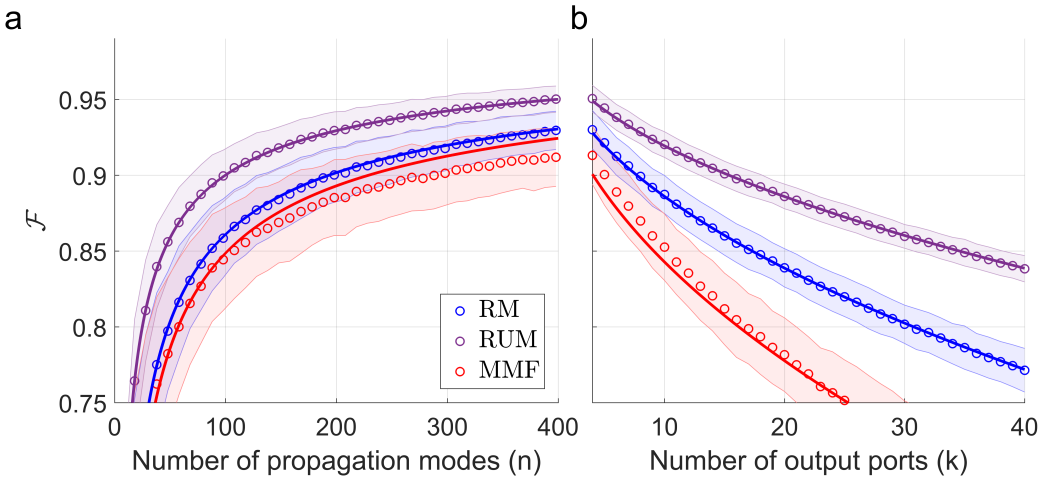


**Figure 2.17** – (a) Fidelity $\mathcal{F}$ of an optical network as a function of the number $n$ of propagating modes supported by a medium. We set $m$=2, $k$=4. (b) Fidelity $\mathcal{F}$ as a function of the number $k$ of the targeted outputs. We set $m$=2, $n$=398. The mean (circle) and standard deviation (shaded area) of the fidelity are calculated from simulating 1000 desired linear networks arbitrarily defined on different targeted outputs of a high-dimensional $n \times n$ random matrices (RM, RUM or MMF). The desired linear networks are generated randomly, i.e., elements are i.i.d. complex Gaussian coefficients. The high-dimensional $n \times n$ random matrix are generated from a random matrix (RM, blue circle), a random unitary matrix (RUM, purple circle), and the experimentally measured transmission matrix (MMF, red circle). In the case of MMF, we reduce the number of the propagating modes $n$ by randomly selecting $n$ columns and rows of the measured full TM. All curves show the predicted $1-\mathcal{O}\left(\sqrt{mk/n}\right)$ behaviour.

As shown in Fig. 2.17a, for optical networks of dimension $4 \times 2$ which simulates our experimental implementation, the fidelity $\mathcal{F}$ scales as expected as $1-\mathcal{O}(1/\sqrt{n})$ when we increase the number of propagation modes of the complex highly-mixing medium. For a fixed $n$, the fidelity decreases when increasing the number of targeted output ports $k$, following $1-\mathcal{O}(\sqrt{k})$ (Fig. 2.17b). For both graphs, the RUM provides the highest fidelity since it ensures energy conservation[11], while the fidelity with the MMF model is slightly below the RM one. This could be attributed to mesoscopic correlations [Rotter and Gigan, 2017], the variation of the enhancement at different targeted outputs due to the co-propagating speckle reference [Čižmár and Dholakia, 2011], and to mode-dependent losses [Carpenter et al., 2014, Chiarawongse et al., 2018].

We note that a similar simulation was reported in Simon R. Huisman's dissertation [Huisman, 2013, in Appendix C] where he designed 2×2 balanced beamsplitter using an optimization approach, $\mathcal{L} \propto \left[\begin{smallmatrix} 1 & -1 \\ 1 & 1 \end{smallmatrix}\right]$. The reported error in the relative phase $\pi$ of the beamsplitter in [Huisman, 2013, Fig.C.2] shows a decreasing trend as the degree of wavefront control $n/m$ increases. We expect that this result present similarly a square-root trend of improvement, which appears to be consistent with the proposed theoretical model.

[11] RUM provides the highest fidelity when the number of input ports $m$ is low. As $m$ increases, the fidelity converges to the value provided by the RM because the unitary condition of $\mathbf{T}^{(p)}$ relaxes.

### 2.4.3 Discussion

Our architecture for programming optical network relies on the high dimensional complex mixing of a multimode fibre; the high fidelity of implemented network is achieved when $m, k \ll n$ as presented Eq. 2.19. Three points of the reliability of our programmable optical network need to be discussed.

#### Programmability

The programmability of our optical network architecture originates from how well the SLMs controls lights interference through a high-dimensional fixed intermodal coupling provided by the fibre. Two key properties are required for this propose:

- **Complex mixing across modes and degrees of freedom**: This property of the multimode fibre allows one to assign k targeted output ports on arbitrary position and polarization with a corresponding desired complex coefficient of $\mathcal{L}$. We experimentally verified this property by checking feasibility to focus on any position and polarization state across the output plane with high efficiency, while keeping a low unstructured background on the other modes.
- **Degree of wavefront control**: It is proportional to $n/(mk)$ as suggested by Eq. 2.19. For each input (each column of $\mathcal{L}$), one has high $d = n/m$ number of programmable SLM elements and the same $d$ number of a corresponding complex intermodal coupling coefficients provided by the MMF for programming each desired coefficient of $\mathcal{L}$ allocated on the target outputs. Increasing number of targeted outputs $k$, on the other hand, reduces the degree of SLM control. This effect physically corresponds to a cross-talk between targeted outputs due to an overlap of speckle background fields with other targeted outputs.

In the following we compare our programmable platform to the conventional architecture, in which a large number of phase shifters in cascaded Mach-Zehnder interferometers has to be controlled [Reck et al., 1994]. While the conventional architecture follows a bottom-up approach, where a large desired transformation is constructed from a series of small $2 \times 2$ ones, our platform can be considered to follow a top-down approach, in that the desired transformation is obtained directly, without the need to decompose it in terms of simpler components. In other word, in our implementation a small programmable optical network is encoded on a large fixed highly-mixing linear transformation. In a conventional architecture, to have a fully reconfigurable $k \times k$ unitary transformation $\mathcal{O}(k^2)$ tunable optical elements are required [Reck et al., 1994, Miller, 2013b, Clements et al., 2016, Tillmann et al., 2016, Tischler et al., 2018]. In our setup, since we have $n$ tunable elements at the input of the complex medium, we expect to be able to program unitaries of dimension up to $m = k = \sqrt{n}$. For a given network, scaling to a larger complex medium (larger $n$, which could be realised for instance by increasing the diameter or the numerical aperture of the multimode fibre) allows increasing the fidelity to values close to unity.

#### Imperfect wavefront control

One of the interesting features of our technique is that the overall enhancement of the photon counts does not depend significantly on the number of targeted output modes $k$. This is well-known from the first article on wavefront shaping through complex me-

dia [Vellekoop and Mosk, 2007], where it was noted that focusing on $k$ target points, instead of on a single one resulted in a k-fold reduction of the intensity per target, but the overall intensity remained the same. For an optimal input, the maximal fraction of total energy that can theoretically be transmitted on a target output mode $i$ is equal to $\sum_{j=1}^{d} |t_{ij}|^2$, where the $t_{ij}$ are the elements of the TM and $d$ is the number of modes that are controlled, this is approximately equal to $n/m$ [Vellekoop, 2015]. Increasing $k$ is equivalent to a change of basis and does not significantly modify the total transmitted intensity.

On the other hand, increasing number $m$ of input ports reduces the degree of wavefront control, which results in an uncontrolled light scattered from a desired optical network. To quantify the overall energy transmittance through a desired optical network, $\gamma$ is defined as the ratio of the photon flux carried by the targeted outputs of interest to the total photon flux transmitted through the MMF[12]. When all input modes of an optical system are controlled both in amplitude and phase, the overall energy transmittance through a desired optical network $\gamma$ is unity. From a mathematical perspective, this is because the time-reversal operator is the identity matrix: $\mathbf{T}\mathbf{T}^{\dagger} = \mathbb{1}$. As the number of input ports $m$ increases, $\gamma$ is reduced follows: $\gamma = 1/m$. This effect is called imperfect wavefront control.

We measured $\gamma$ across all possible target outputs; we found that the enhancement $\gamma$ has a speckle-like feature. This well-known imperfection results from using a co-propagating speckle reference in the measurement of TM [Čižmár and Dholakia, 2011, Tao et al., 2015, Hofer and Brasselet, 2019], and can be unravelled by using an external reference field [Čižmár and Dholakia, 2011], phase retrieval techniques [Drémeau et al., 2015]. To avoid this inhomogeneity, we acquired the TM with a co-propagating focusing reference as described in the Section 2.2.2. In our experiment, $\gamma$ can reach 0.45 for each input port, which is consistent with the fact that we control only half of the number of propagating modes on each polarization. The state-of-the-art $\gamma$ of 0.6 has been experimentally reported in a step-index MMF using one of circular input polarizations. This is owing to the fact that the polarization is conserved in the step-index fibre [Plöschner et al., 2015b]. And, the $\gamma$ of 0.8 has also been reported in a step-index MMF when controlling both linear polarization channels [Čižmár and Dholakia, 2011, Turtaev et al., 2017].

### Inverse scattering process

In our experiment, the inverse operator that is used in Eq. 2.10 is achieved by the conjugate transpose (Hermitian transpose, †) $(\mathbf{T}^{(p)})^{\dagger}$, instead of the inverse operator $(\mathbf{T}^{(p)})^{-1}$. This is because the conjugate transpose is very robust to noise present in the measured TM, unlike the inverse one $(\mathbf{T}^{(p)})^{-1}$ which is unstable in the presence of noise. The noise results in a low fidelity in the implementation of the optical networks. The unsuitability of $(\mathbf{T}^{(p)})^{-1}$ is because high-value components of singular values of $(\mathbf{T}^{(p)})^{-1}$ originate from small singular values from the noise of the transmission matrix $(\mathbf{T}^{(p)})$ [Popoff et al., 2010a]. In our experiment, the conjugate transpose works efficiently since the conjugate transpose maximizes the energy at the target outputs [Tanter et al., 2000, Derode et al., 2001] and the background noise $\mathbf{H}$ in Eq. 2.18 keeps very low. In case that one wants to scale the dimension of implemented linear optical networks $k \times m$ without increasing of the dimension of multimode fibre $n$, one thus has a low fidelity in the implementation of the networks with the conjugate transpose. To have better implementation of a linear

[12]We note that the total photon flux transmitted through our optical system is nearly lossless, because of a high transmission of the multi-mode fibre and a high reflectivity of the SLM.

network in such a case, alternative inverse process could be applied, for instance, pseudo-inverse method [Campbell and Meyer, 2009], mean square optimized operator [Popoff et al., 2010a].

### 2.4.4 Scalability of optical networks

The dimensionality of our programmable optical networks can in principle be scaled up, as the main limiting factor in our experimental implementation is given by the number of APD detections (Fig. 2.10). A significantly larger network can be managed, for instance, by replacing our detection apparatus with an array of coincidence detectors [Jost et al., 1998, Basden et al., 2003, Edgar et al., 2012, Peřina et al., 2012, Tasca et al., 2013, Fickler et al., 2013, Chrapkiewicz et al., 2014, Jachura and Chrapkiewicz, 2015, Bolduc et al., 2017, Reichert et al., 2018, Defienne et al., 2018b, Bruschini et al., 2019]. As a proof-of-principle, we experimentally verify the scalability of our platform classically by implementing a larger optical network on the EMCCD camera using the superluminescent diode (Superlum) as a light source. The transmission matrix is acquired as explained in Section 2.2.2 and the relation of co-propagating focusing references between two input ports are calibrated by the phase-shifting interferometry [Popoff et al., 2010a, Plöschner et al., 2015b]. In order to study the scalability, we implement desired linear optical networks (Section 2.2.3) at different number of targeted output ports $k$. The output ports of desired linear optical networks are arbitrary allocated on 18 positions where the co-propagating focusing references are defined as depicted in Fig. 2.18. The amplitudes of linear elements $|\mathcal{L}_{qp}|$ are sampled from the uniform distribution in the interval $[0.5, 1]$ and the phases of linear elements $\arg(\mathcal{L}_{qp})$ are sampled from the uniform distribution in the interval $(-\pi, \pi]$.

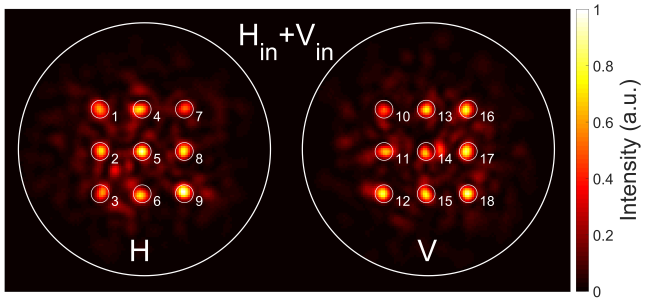


**Figure 2.18** – Intensity image of a high-dimensional balanced linear-optical network on the EMCCD. The SPDC light from both inputs is simultaneously distributed into 18 targeted outputs, 9 in each polarization (H: Horizontal; V: Vertical). The implementation of a small optical network in the experiment on the scalability are randomly allocated on the 18 targeted outputs.

In Fig. 2.19, we show one example of optical networks with the number of targeted outputs ($k = 18$). The results illustrate the implemented settings of phase and amplitude on targeted outputs of interest compared the desired elements of $\mathcal{L}$.

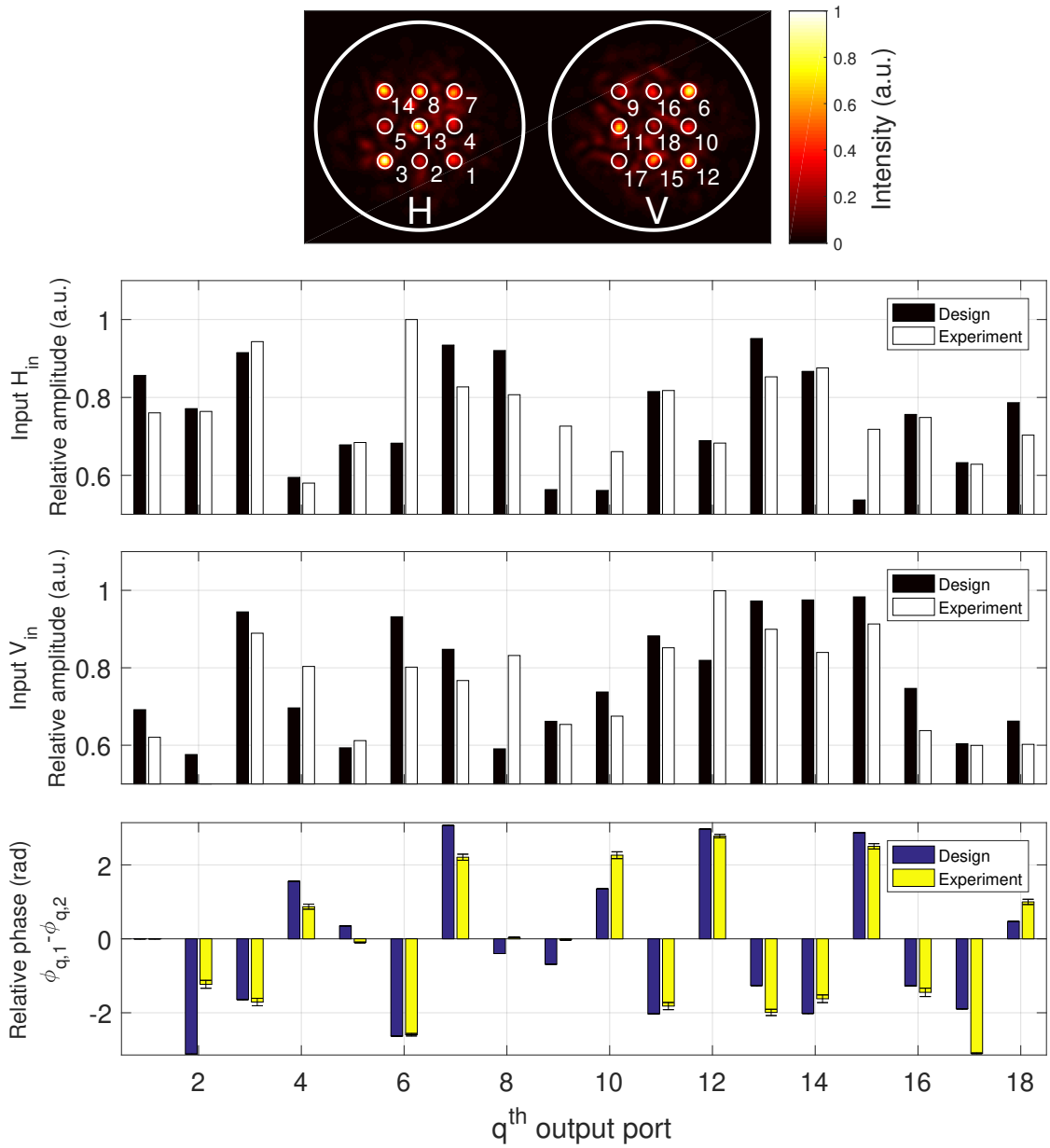


**Figure 2.19 – Example of implemented optical network (k=18)**: The location of targeted outputs on the EMCCD camera for both input ports, H: Horizontal; V: Vertical, (Top). Experimental amplitudes are compared to the designed one (Middle). Experimental relative phases are compared to the designed one (Below).

By plotting the averaged fidelity over many implemented optical networks as a function of the number of targeted outputs, we observe a decrease in fidelity following the $1 - O(\sqrt{k})$ curve as shown in Fig. 2.20. This result is consistent with the theoretical model and it supports the scalability of our platform. Furthermore, the experimental curve of fidelity also matches with the numerical curve that was simulated with the measured TM of the MMF, in the case where amplitudes of linear elements $|\mathcal{L}_{qp}|$ are uniformly sampled as in

the experimental case. Consequently, these results indicate the good consistency between in the experimental implementation and the numerical study.

In addition, we observe the decrease of fidelity in this case of uniformly sampling as compared to the numerical results where optical networks are i.i.d random matrix. This is due to that fact that the defined fidelity $\mathcal{F}$ measures the averaged distance between the linear elements of optical networks. Change of normalization factor and/or variance of linear elements $\mathcal{L}_{qp}$ results in a different prefactor in $\mathcal{O}(mk/n)$. This purely results from the statistical properties of optical networks and the property of the fidelity as explained in Appendix D.2 and does not originate from the limitation of our technique.

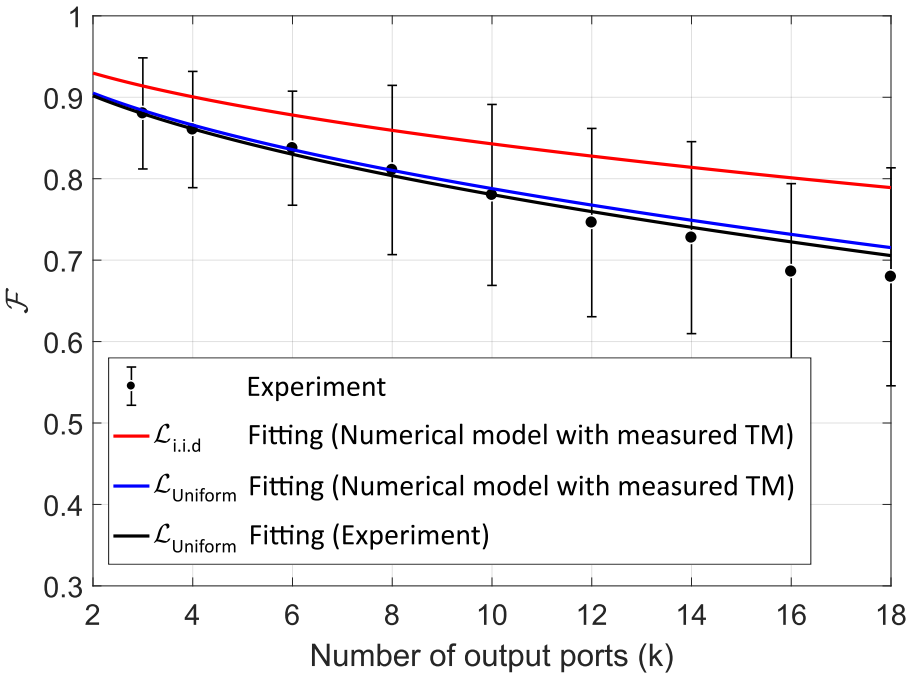


**Figure 2.20** – Experimental fidelity $\mathcal{F}$ of optical networks as a function of the number $k$ of the targeted outputs. The mean (dot) and standard deviation (bar) of the fidelity are measured from 48 experimental $k \times 2$ desired linear networks. The desired linear networks are generated from a random matrix where the amplitudes of linear elements $|\mathcal{L}_{qp}|$ are sampled from the uniform distribution in the interval $[0.5, 1]$ and the phases of linear elements $\arg(\mathcal{L}_{qp})$ are sampled from the uniform distribution in the interval $(-\pi, \pi]$. The fitting experimental curve (black curve) is consistent with the numerical prediction curve (blue curve) $1-\mathcal{O}\left(\sqrt{mk/n}\right)$ where optical network are sampled from the same random ensemble as descried above. The red line is represented the fitting curve of the numerical result presented in Fig. 2.17 which models optical networks with the i.i.d Gaussian random matrix using the measured TM of the MMF.

To conclude, the scalability of the optical networks have been verified numerically and experimentally. The results demonstrate the potential to implement a large optical network following the theoretical model in Eq. 2.19. Scaling to a large dimension of optical network $(k \times m)$, one needs to scale linearly the dimension of optical mixer, MMF and SLM, $(n)$ in order to keep a constant performance.

## 2.5 | Summary and perspectives

In this chapter, we have presented the use of a multimode fibre to implement fully programmable linear optical networks across spatial and polarization degrees of freedom. This platform harnesses the highly complex coupling between a large number of modes of the MMF and the ability to spatially control the input light wavefront.

We successfully programmed this platform to implement circuits able to manipulate two-photon quantum interferences in various interferometers which can be used to tackle certification tasks of indistinguishability (suppression phenomenon). We have thus demonstrated the versatility and full reconfigurability of our approach, including the management of different degrees of freedom of the propagating light. It is also worth highlighting the outlooks offered by our work. Linear complex mixing occurring in an optical mixer can go beyond path and polarization. Spectral, temporal and spatial (radial and orbital angular momentum) degrees of freedom can also be manipulated with an SLM in combination with a scattering medium. We believe that our alternative implementation of programming a linear transformation can be extended all the way up to those degrees of freedom. In essence, our method significantly simplifies the design and avoids entirely the need to further decompose such transformations in terms of simpler optical components which can be sensitive to a fabrication and alignment processes.

We have also highlight its scaling potential by providing the theoretical model and the numerical simulations. Furthermore, we have demonstrated the experiential implementation of the optical networks over up to 18 output ports. Our architecture provides an efficient and scalable alternative to integrated circuits for linear quantum networks.

# 3

# Coherent absorption effect

*"The most important questions in life are, for the most part, really only problem of probability."*

— Pierre-Simon Laplace

In this chapter, the scheme of programmable optical network presented in the previous chapter is used to explore the interesting phenomenon of non-unitary evolution of a two-photon state. In particular, the theory of a two-photon state evolving through a lossy beamsplitter is presented in section 3.1. Then, an intriguing phenomenon related to non-unitary systems, known as *coherent absorption* is introduced in section 3.2. The two experimental results related to the two-photon interference with a lossy beamsplitter and the emulation of the coherent absorption with a N00N state are presented and discussed in each section accordingly.

## Contents

# 3.1 | Two-photon interference on a lossy beamsplitter

## 3.1.1 Why a lossy beamsplitter is interesting?

Losses are usually considered to be deleterious for quantum systems and are difficult to eliminate in an optical experiment. In quantum optics, losses tend to suppress non-classical properties of light [Kok et al., 2007]. A well-known effect of loss is the degradation of the squeezing property of light [Bandilla, 1989, Patra and Beenakker, 2000]. Besides, losses also tend to be a limitation in the scalability of boson sampling [Rohde and Ralph, 2012, Rudolph, 2017, Oszmaniec and Brod, 2018, Wang et al., 2018a, García-Patrón et al., 2019]. An emerging research topic is related to the effect of mode-dependent loss[1] on a reduction of the computational complexity of boson sampling problem [Oszmaniec and Brod, 2018].

In contrast to their typical undesirable effects, losses can bring about an intriguing quantum interference phenomenon thanks to the relaxation of unitarity condition. It leads to the appearance of non-linear absorption at a low photon-counting regime, using solely a linear beamsplitter [Barnett et al., 1998]. The relevant theory, explanation and complete experimental results of the effect implemented with our setup are presented in the following sections.

## 3.1.2 Theory

The lossy beamsplitter has been studied theoretically since the 1990s [Gruner and Welsch, 1996, Barnett et al., 1998], but only few experimental studies have been reported so far. This is understandable since lossless beamsplitters are omnipresent in optics, whereas, lossy beamsplitters are not. Most experiement thus consider the beamsplitter to be lossless and reciprocal; therefore, the input and output operators are related by a unitary transform which imposes phase constraint on the scattering matrix of the beamsplitter. In the case of well-known symmetric[2] and balanced[3] beamsplitter, the scattering matrix is $\frac{1}{\sqrt{2}}\begin{bmatrix} 1 & i \\ i & 1 \end{bmatrix}$.

### Model of lossy beamsplitter

The presence of losses can relax the relative phase constraint of a beamsplitter [Barnett et al., 1998, Huisman et al., 2014a, Uppu et al., 2016]. For the sake of simplicity, the lossy balanced beamsplitter can be modelled by,

$$\text{LTBS} = t \begin{pmatrix} 1 & 1 \\ 1 & e^{i\alpha} \end{pmatrix}, \tag{3.1}$$

where $\alpha$ is a tunable phase and the amplitude of all linear elements are assumed to be equal and denoted as the transmission coefficient $t$. The tunable range of $\alpha$ depends on the transmission coefficient [Huisman et al., 2014a] and can be expressed as,

$$\left|\cos\frac{\alpha}{2}\right| \leq \frac{1}{2t^2} - 1. \tag{3.2}$$

[1] Mode-dependent loss means that different propagation paths in an optical network encounter different amounts of losses depending on the length of propagation paths.

[2] The symmetric means the equality of reflected and transmitted amplitudes for both inputs.

[3] The balance means the equality of reflected and transmitted amplitudes in each input.

The tunable range, determined by Eq. 3.2, is depicted in Fig. 3.1. The black region indicates the possible setting of $\alpha$, while the white region is forbidden due to the conservation of energy. At $t = 1/\sqrt{2}$ which corresponds to a lossless case, only $\alpha = \pi$ is valid. Moreover, $\alpha$ is fully tunable range for $t \leq 1/2$. The tunability can be exploited as a parameter revealing interesting effects on quantum interference.

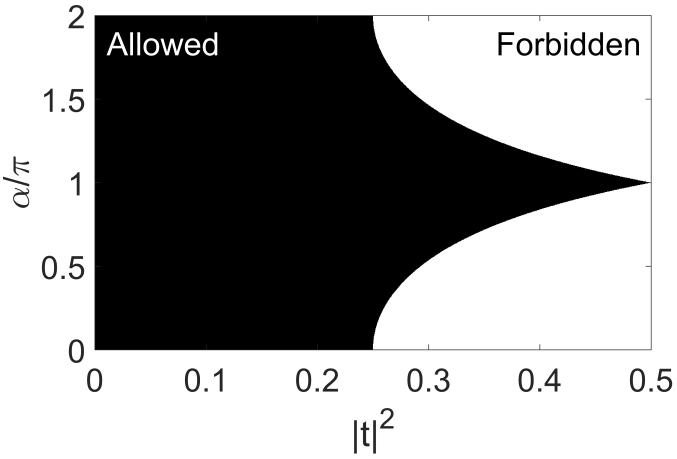


**Figure 3.1** – The tunable range of $\alpha$ as a function of transmittance $|t|^2$. The black area is allowed for control of $\alpha$.

In the most general case, a beamsplitter is used to superpose, or mix, two incoming fields to two outgoing fields. The scattering matrix of beamsplitter must satisfy the commutation relations between the outgoing creation and annihilation operators ($\hat{a}_1$ and $\hat{a}_2$) as they represent a property of the free-space quantized electromagnetic fields [Blow et al., 1990, Huttner and Barnett, 1992, Matloob et al., 1995, Matloob and Loudon, 1996]:

$$[\hat{a}_i(\omega), \hat{a}_j(\omega')] = 0 \qquad ,i,j \in \{1,2\} \tag{3.3a}$$

$$\left[\hat{a}_i(\omega), \hat{a}_j^\dagger(\omega')\right] = \delta_{ij}\delta(\omega - \omega') \qquad ,i,j \in \{1,2\}, \tag{3.3b}$$

where $\omega$ represents an angular frequency of the quantized electromagnetic fields. These commutation relations guarantee the conservation of energy and the orthogonality of the two outgoing modes. In the presence of loss, these properties of the outgoing modes can be modulated. In order to maintain the commutation relations, a Langevin noise operators $\hat{F}_i$, $i \in \{1,2\}$ has to be added [Barnett et al., 1996, Barnett et al., 1998] into the relationships between the input and output operators via the lossy beamsplitter as follows,

$$\begin{pmatrix} \hat{a}_1 \\ \hat{a}_2 \end{pmatrix} = \mathrm{LTBS} \begin{pmatrix} \hat{a}_1 \\ \hat{a}_2 \end{pmatrix} + \begin{pmatrix} \hat{F}_1 \\ \hat{F}_2 \end{pmatrix}. \tag{3.4}$$

The losses represented by the Langevin noise operators in the model can be theoretically associated with fluctuating currents within the medium forming the beamsplitter [Barnett et al., 1998]. In reality, losses can originate from different physical sources regarding the construction of beamsplitter. For example, a mechanism of losses in a dielectric medium can arise not only from absorption [Matloob et al., 1995, Matloob and Loudon, 1996]

but also from scattering into a large number of unmonitored modes. The Langevin noise operators include a general effect of loss which takes place in the lossy beamsplitter. In other words, the losses can be considered as an influence of the environment into the system of interest (the beamsplitter) in context of the open quantum system. Owing to the mechanism of loss, we can assume that the noise operators do not contribute to output photon counts [Barnett et al., 1998]. Moreover, the two incoming and outgoing fields are independent of the noise sources. Under these hypothesis, the input operators commute with the Langevin noise operators,

$$\left[\hat{a}_i(\omega), \hat{F}_j^{\dagger}(\omega')\right] = \left[\hat{a}_i(\omega), \hat{F}_j(\omega')\right] = 0 \quad , i, j \in \{1, 2\}. \tag{3.5}$$

### Two-photon interference

As introduced in chapter 1, the two-photon state $|\Psi\rangle$ incident in two different input ports of the lossy beamsplitter is expressed as

$$|\Psi\rangle = \int_0^{\infty} \int_0^{\infty} \Psi(\omega_1, \omega_2)\, \hat{a}_1^{\dagger}(\omega_1)\, \hat{a}_2^{\dagger}(\omega_2)\, d\omega_1 d\omega_2 |0\rangle, \tag{3.6}$$

where the biphoton wavefunction $\psi(\omega_1, \omega_2)$ is normalized as $\int_0^{\infty} \int_0^{\infty} |\psi(\omega_1, \omega_2)|^2 \, d\omega_1 d\omega_2 = 1$ so that the state vector $|\Psi\rangle$ is normalized too [Fearn and Loudon, 1989].

One can determine the probabilities of obtaining a given number of photons in the outputs of the lossy beamsplitter via the Kelley-Kleiner counting formula [Kelley and Kleiner, 1964]. In the following consideration, the quantum efficiency of the detectors is assumed to be unity and the detecting time is set to infinite[4]. We define $\hat{N}_i$ the photon number operator at the $i$ output port [Barnett and Radmore, 2002] defined as,

$$\hat{N}_i(\omega) = \int_0^{\infty} d\omega \hat{a}_i^{\dagger}(\omega) \hat{a}_i(\omega), \quad i \in \{1, 2\}. \tag{3.7}$$

The outcome probabilities of the lossy beamsplitter consist of six distinct cases which can be categorized into three groups [Barnett et al., 1998]. The first group is the probabilities of having two-photon at the output ports. They are composed of the two cases that have two-photon detected in either output port and one case that has single-photon detected in each of the two output ports,

$$P(2_1, 0_2) = \frac{1}{2} \left\langle \hat{N}_1 \left( \hat{N}_1 - 1 \right) \right\rangle, \tag{3.8a}$$

$$P(0_1, 2_2) = \frac{1}{2} \left\langle \hat{N}_2 \left( \hat{N}_2 - 1 \right) \right\rangle, \tag{3.8b}$$

$$P(1_1, 1_2) = \left\langle \hat{N}_1 \hat{N}_2 \right\rangle. \tag{3.8c}$$

The second group corresponds to the two cases having a single-photon loss,

$$P(1_1, 0_2) = \left\langle \hat{N}_1 \right\rangle - \left\langle \hat{N}_1 \left( \hat{N}_1 - 1 \right) \right\rangle - \left\langle \hat{N}_1 \hat{N}_2 \right\rangle, \tag{3.9a}$$

$$P(0_1, 1_2) = \left\langle \hat{N}_2 \right\rangle - \left\langle \hat{N}_2 \left( \hat{N}_2 - 1 \right) \right\rangle - \left\langle \hat{N}_1 \hat{N}_2 \right\rangle. \tag{3.9b}$$

[4]The detection time is considered to be very long compared to the coherence time of the biphoton state which is consistent with the experiment.

The third group has the one case where all photons are lost,

$$P\left(0_1,0_2\right)=1-\left\langle\hat{N}_1\right\rangle-\left\langle\hat{N}_2\right\rangle+\left\langle\hat{N}_1\hat{N}_2\right\rangle+\frac{1}{2}\left\langle\hat{N}_1\left(\hat{N}_1-1\right)\right\rangle+\frac{1}{2}\left\langle\hat{N}_2\left(\hat{N}_2-1\right)\right\rangle \quad (3.10)$$

In the case of a frequency-independent lossy beamsplitter, these probabilities can be straightforwardly calculated by substituting the input photon number operators from the linear relation of the lossy beamsplitter (Eq. 3.4) into the output photon number operators (Eq. 3.7) and then applying the commutation relations (Eq. 3.3 and 3.5). One obtains,

$$P(1_1,1_2)=2t^4(1+I(\delta)\cos\alpha), \quad (3.11a)$$
$$P(2_1,0_2)=P(0_1,2_2)=t^4(1+I(\delta)), \quad (3.11b)$$
$$P(1_1,0_2)=P(0_1,1_2)=2t^2-2t^4\left(2+I(\delta)[1+\cos\alpha]\right), \quad (3.11c)$$
$$P(0_1,0_2)=1-4t^2+2t^4\left(2+I(\delta)[1+\cos\alpha]\right), \quad (3.11d)$$

where $I(\delta)$ is the spectral overlap integral of the biphoton state as a function of a temporal delay $\delta$, as expressed in Eq. 1.36.

The probabilities in Eq. 3.11 depend on the indistinguishability of the biphoton state, related to Eq. 1.36. For distinguishable photons ($I=0$), the probabilities reduce to the case of two independent particles with the single-particle probability $2\left|t\right|^2$ for scattering (both transmission and reflection) and $1-2\left|t\right|^2$ for absorption. The interesting effect appears at the complete indistinguishable case ($I=1$) where quantum interference plays a role. The probability of interest is $P(1_1,1_2)$ for detecting one photon in each of the two output ports. The probability oscillates sinusoidally with the phase $\alpha$. At $\alpha=\pi$, the lossy beamsplitter behaves similarly as a lossless beamsplitter. The well-known Hong-Ou-Mandel (HOM) interference effect [Hong et al., 1987] survives with the two-photon visibility $V=1$ (HOM dip). As $\alpha$ is tuned to zero, the two-photon interference is modulated to the peak profile behaviour, with two-photon visibility of $V=-1$; this means that one detects a two-fold enhancement of coincidence counts at pair of outputs of the lossy beamsplitter as compared to the case of distinguishable input photons, i.e., a peak. The effect is known as the photon anti-coalescence.

Considering $t=1/2$ and $\alpha=0$, the probabilities from Eq. 3.11 reduce the form to,

$$P\left(2_1,0_2\right)=P\left(0_1,2_2\right)=\frac{1}{8}, \quad (3.12a)$$
$$P\left(1_1,1_2\right)=\frac{1}{4}, \quad (3.12b)$$
$$P\left(1_1,0_2\right)=P\left(0_1,1_2\right)=0, \quad (3.12c)$$
$$P\left(0_1,0_2\right)=\frac{1}{2}, \quad (3.12d)$$

which is the maximal condition of transmitting two photons through the lossy beamsplitter. The quantum interference at the lossy beamsplitter generally affects absorbing probabilities. We consider the probabilities for no, single, or two photons survival at the output of the lossy beamsplitter, which are expressed as follows:

$$P_{\text{no-photons survival}}=P(0_1,0_2), \quad (3.13a)$$
$$P_{\text{one-photons survival}}=P(1_1,0_2)+P(0_1,1_2), \quad (3.13b)$$
$$P_{\text{two-photons survival}}=P(1_1,1_2)+P(2_1,0_2)+P(0_1,2_2). \quad (3.13c)$$

The probability that single photons survive is zero under the maximal condition. Only the cases where either both photons are absorbed or transmitted occur with the same probability of 1/2. The result thus presents a non-linear two-photon absorption on the linear lossy beamsplitter [Barnett et al., 1998]. In the next section, the experimental demonstration of the effect of the lossy beamsplitter, using the programmable optical network is presented.

### 3.1.3 Experiment

#### Method

We implement the 2×2 lossy phase-tunable beamsplitters on the programmable optical network by means of the procedure presented in section 2.2. The lossy phase-tunable beamsplitter ($\mathrm{LTBS}_1$) is now defined as follows,

$$\mathrm{LTBS}_1 = t \begin{pmatrix} 1 & i \\ e^{i\alpha} & 1 \end{pmatrix}, \tag{3.14}$$

In short, in the first part of experiment, we characterise the TM of the MMF on the two targeted output modes of interest (subsection 2.2.2). The selected outputs are in this experiment allocated on the same spatial spot at the output of the fibre but are the orthogonal polarizations, labelled H1 and V1, as shown in Fig. 3.2. In the second part of the experiment, the SLM is programmed to design the lossy beamsplitters as defined in Eq. 3.14 for different $\alpha$ phase setting. The photon pairs from the SPDC source are then sent to the implemented lossy beamsplitter. The two-photon interference is acquired for different delay times $\delta$. The acquisition time was set to 5 s in each measurement. In order to analyse the output probabilities of the lossy beamsplitter, we insert the fibre-based beamsplitter (fBS) at each of the targeted output ports. The corresponding two-photon interferences of the lossy beamsplitter are acquired at the four outputs of the fBSs, labelled A, B, C, D, as depicted in Fig. 3.2. The probability of detecting two photons in the V1 output of the beamsplitter $P(2_{V1}, 0_{H1})$ is twice the two-fold coincidence count $2C_{AB}$ between the A and B output ports, and similarly the probability of detecting two photons in the H1 output $P(0_{V1}, 2_{H1})$ is related to $2C_{CD}$. The multiplication factor of 2 comes from the probability of photon bunching that occurs at the analysed fBS. The probability of one photons detected on each output port of the lossy beamsplitter $P(1_{V1}, 1_{H1})$ is then related to $C_{AC} + C_{AD} + C_{BC} + C_{BD}$.

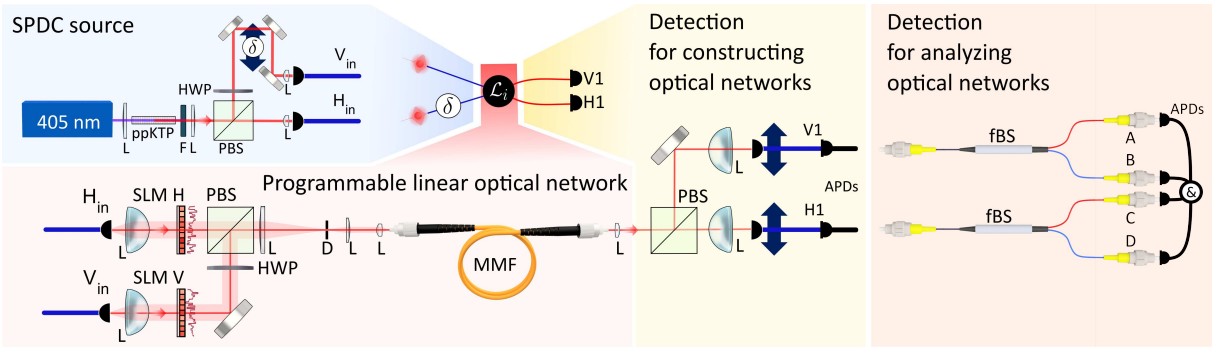


**Figure 3.2 – Experimental setup for two-photon interference on a lossy beamsplitter**: Photon pairs produced by spontaneous parametric down-conversion (SPDC) using ppKTP crystal are injected into a multimode fibre (MMF) along orthogonal polarizations using spatial light modulators (SLM). In the first part of the experiment (construction of the optical networks), the transmission matrix (TM) is measured across spatial and polarization input modes of the MMF. Two output ports of interest are selected by two single-mode fibres mounted on translation stages labelled as (H1, V1). In the second part, a designed lossy beamsplitter is programmed by calculating and displaying the corresponding wavefront on the SLMs. In order to analyse the outcome probabilities of the implemented lossy beamsplitters, the fibre-based beamsplitter (fBS) is placed at each of the targeted output ports. Light is detected by four Si-based avalanche photodiode detectors (APDs) connected to the field-programmable gate array (FPGA) for counting photons and coincidences. (L: lens, F: filter, HWP: half-wave plate, PBS: polarizing beamsplitter, D: iris diaphragm, FM: flip mirror, WP: Wollaston prism, BS: beamsplitter.)

### Results and discussion

The experimental probabilities of two-photon survival at the outputs of our implemented lossy phase-tunable beamsplitters are shown in Fig. 3.3. We observe the full control of two-photon interference over the tunable phase $\alpha$ of the lossy beamsplitter. The experimental results are consistent with the theory [Barnett et al., 1998] as presented in subsection 3.1.2. The two interesting features are displayed in Fig. 3.3. The first is the oscillation of the probability of detecting single photons in each of the two output ports $P(1_{V1}, 1_{H1})$: The well-known HOM dip of two-photon interference is observed at $\alpha = \pi/2$, whereas the characteristic peak of the two-photon interference is presented at $\alpha = 3\pi/2$ for the lossy beamsplitter owing to the photon anti-coalescence. Two-fold coincidences at the output ports of the lossy beamsplitter have been recently measured in optic and plasmonic platforms on the spatial output ports [Defienne et al., 2016, Wolterink et al., 2015, Vest et al., 2017, Taballione et al., 2019]. We here demonstrate that the oscillation can be also observed on polarization degree of freedom and shows full programmability of our platform[5]. The second feature of interest is the probability of detecting two photons in each of the outputs ($P(2_{V1}, 0_{H1})$ and $P(0_{V1}, 2_{H1})$). The results presented in Fig. 3.3(a and c) indicate the independence of the probability on phase $\alpha$ as predicated by Eq. 3.11. To the best of our knowledge, this is the first demonstration of two-photon interference measured for all events of two-photon survival at the lossy beamsplitter. The probability of two-photon survival is measured: $P(1_{V1}, 1_{H1}) + P(2_{V1}, 0_{H1}) + P(2_{V1}, 0_{H1})$ and is shown in Fig. 3.3d. At $\alpha = \pi/2$, the probability is constant at 0.25 across the delay;

[5]The same results have been observed for arbitrary spatial positions (by moving the transition stage) and polarization states (by adding wave plates with arbitrary rotation at input and output of the MMF).

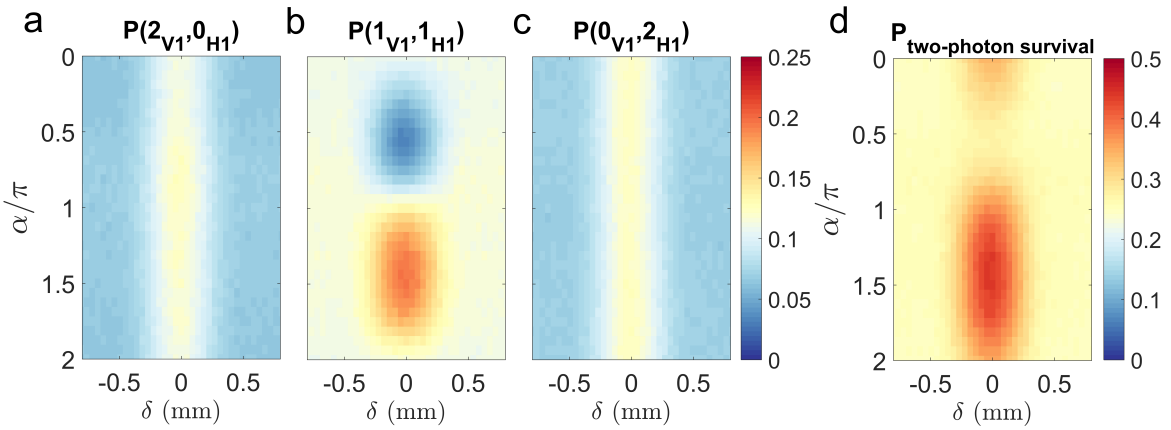


**Figure 3.3 – Probability of detecting two photons at the output ports of the lossy beamsplitter** as a function of relative phase $\alpha$ of the lossy beamsplitter and delay $\delta$. (a) Detection of two photons in the V1 output of the lossy beamsplitter $P(2_{V1}, 0_{H1})$, (b) Detection of single photons in each of the two output ports $P(1_{V1}, 1_{H1})$, (c) Detection of two photons in the H1 output of the lossy beamsplitter $P(0_{V1}, 2_{H1})$, (d) Probability of two-photon survival.

the result indicates the independence of the probability of two-photon survival from the distinguishability of biphotons. Interestingly, at $\alpha = 3\pi/2$, the probability of two-photon survival increases to 0.5 in the case of indistinguishability ($\delta = 0$). This reveals the two-fold enhancement of the probability of two-photon survival as compared to the case of distinguishability. The result thus shows the manifestation of the effect of quantum interference on the loss process; the probability of non-linear two-photon absorption can be controlled by the relative phase of a linear lossy beamsplitter [Barnett et al., 1998]. In the next section, a more in depth study of the phenomenon known as coherent absorption is presented and experimentally demonstrated.

## 3.2 | Coherent absorption

### 3.2.1 Introduction

Coherent absorption is an interference-assisted absorption process. It is a phenomenon by which one can manipulate the outcome of a mechanism of absorption (loss) via the control of phases of incident light. In particular, a famous classical case of coherent absorption is coherent perfect absorption (CPA) in which the complete absorption is achieved by controlling the interference of incoming light. As depicted in Fig. 3.4, the simple example of CPA is a linear system represented by an absorbing planar slab. In general, many materials have been reported to the appearance of CPA, for instance, composites of metal dielectric, metasurfaces, graphene, plasmonic waveguides [Wan et al., 2011, Baranov et al., 2017]. Light incidents on each input port can be partially reflected, transmitted, or absorbed into the medium, as illustrated in Fig. 3.4a. In the simplest case, the CPA takes place when two coherent beams are propagating to the opposite sides of the absorbing slab with a suitable relative phase. As a result, the reflected part of one of incoming beam interferes destructively with the transmitted part of the other beam and vice versa [Dutta Gupta, 2007, Chong et al., 2010, Gmachl, 2010, Baranov et al., 2017]. The interference generates a perfect channel where all energy is transferred to the process of absorption. The rigorous classical explanation of the phenomenon can be provided by the scattering

theory [Chong et al., 2010]: The optical input fields $\Psi_{\text{CPA}}$ that generate the coherent perfect absorption must satisfy,

$$\mathbf{S}\Psi_{\text{CPA}} = 0, \tag{3.15}$$

where $\mathbf{S}$ is the scattering matrix of the absorbing planar slab. This refers to the fact that $\Psi_{\text{CPA}}$ is a non-zero eigenvector of $\mathbf{S}$ whose corresponding eigenvalue is zero. The presence of zero eigenvalues is physically realizable and requires a certain amount of loss in a medium at a given frequency $\omega$. The condition allows the zero eigenvalues to have a propagating wave solution. The CPA phenomenon can be understood as the time-reversal version of the lasing process at the lasing threshold [Chong et al., 2010] in which the linear approximation of scattering process is valid.

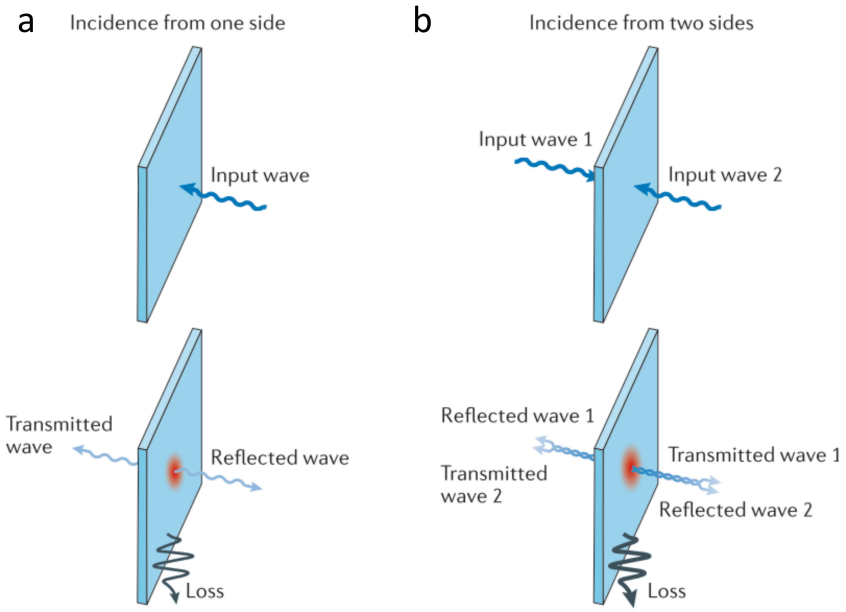


**Figure 3.4 – Concept of coherent perfect absorption**: (a) Light incident on one of part of an absorbing planar slab is partially reflected, transmitted, and absorbed by the medium. (b) Two incoming coherent beams travel onto the opposite sides of absorbing slab with a suitable relative phase. The coherent perfect absorption takes place, resulting in the perfect absorption. Adapted from [Baranov et al., 2017]

For more complex structures where many scattering modes are involved, the CPA process is achievable if the corresponding scattering matrix still presents a CPA mode and complete control of incident wavefront is realizable. Recently, the CPA process in a disordered waveguide has been demonstrated in microwave domain [Pichler et al., 2019]. The random matrix theory can predict the presence of coherent absorption in a disordered medium, and it has been theoretically shown that very strong enhancement of the coherent absorption is possible in a weakly absorbing but strongly scattering medium by the control of incident optical fields at any frequency in a strongly scattering regime [Chong and Stone, 2011, Li et al., 2017].

Coherent absorption has recently aroused widespread applications in optics, ranging from improved photovoltaic devices to all-optical data processing. In the context of the photocurrent generation, a two-fold enhancement of the generated photocurrent has been observed in a dye-sensitized solar cell when the incident wavefront is optimally shaped [Liew et al., 2016]. The interference allows lights to be concentrated close to the interface of

electrodes where electrons are most efficiently generated and collected [Liew et al., 2016]. In the context of data processing, the coherent absorption provides control of optical signal by another optical signal without the need for material non-linearity. Therefore, it can be exploited for processing tasks and provide a novel route towards the implementation of switches, modulators, filters, and logic gates at any intensity level [Zhang et al., 2012, Fang et al., 2015, Papaioannou et al., 2016b, Papaioannou et al., 2016a, Xomalis et al., 2018]. Different boolean operations (AND, OR, XOR, NOT) have been realized by using the coherent absorption process exploiting various relative phases between the two input beams as depicted in Fig. 3.5.

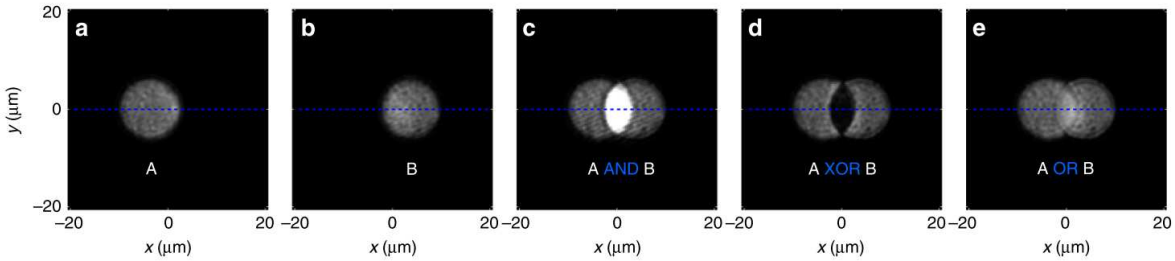


**Figure 3.5 – CPA applications for logic operators**:(a) beam A only presents, (b) beam B only presents, (c) A AND B, (d) A XOR B, and (e) A OR B. Adapted form [Papaioannou et al., 2016a]

In quantum optics, the coherent absorption has been theoretically investigated using the model of a lossy beamsplitter long before the well-known establishment of classical CPA [Barnett et al., 1998, Jeffers, 2000, Chong et al., 2010].

The CPA of a single-photon state in a superposition form $1/\sqrt{2}(|1_1, 0_2\rangle + e^{i\phi}|0_1, 1_2\rangle)$ has been experimentally demonstrated recently on a plasmonic metasurface and on a multilayer graphene film [Roger et al., 2015]. The effect occurs in the same manner as the CPA with the coherent state and implies the perfect coupling of a single photon to the plasmonic mode of the absorber [Roger et al., 2015]. The presence of the effect is clearly due to the self-interference of single photons [Huang and Agarwal, 2014]. The interference is the key feature that redistributes the energy flow between inputs, outputs and the absorption channel. Moreover, the CPA effect has been demonstrated in the context of quantum eraser experiment with the polarization-entangled biphoton state where only one party of the state interacts with the plasmonic absorbing metasurface [Altuzarra et al., 2017]. Owing to the entanglement of the state, the presence of CPA effect can be controlled by the projective measurement on the non-local party of the state that never interacts with the absorbing metasurface [Altuzarra et al., 2017]. The theoretical prediction of the CPA effect with squeezed coherent states has been recently reported [Hardal and Wubs, 2019]. Very recently, non-local coherent absorption has been predicted [Jeffers, 2019]. An effect of Bell states on a non-polarizing lossy beamsplitter and the corresponding calculation is presented in Appendix E.

In general, the coherent absorption is an emergent phenomenon arising from an interplay of interference of input light and dissipation process. One of an interesting situation of the coherent absorption occurs when an input state is a N00N state with N=2 since the interference appears on the second-order intensity correlation, but not on the intensity level [Hong et al., 1987, Jeffers, 2000]. In the following section, the theory of the coherent absorption of a N00N state with N=2 is presented and then our experimental demonstration is reported.

### 3.2.2 Theory of coherent absorption

We refer to the theory of coherent absorption developed in [Jeffers, 2000, Barnett et al., 1998] for the original calculation. An input state of interest is a N00N state with N=2, which is generated from the Hong-On-Mandel interference on a balanced lossless beamsplitter. The N00N state with N=2 ($|2_{e^{i2\phi}}\rangle$) is defined as,

$$|2_{e^{i2\phi}}\rangle \equiv \frac{1}{\sqrt{2}}(|2_1, 0_2\rangle + e^{i2\phi}\,|0_1, 2_2\rangle), \tag{3.16}$$

where $\phi$ is the relative phase between two output ports of the lossless beamsplitter. The state then impinges on the lossy beamsplitter ($\mathrm{LTBS}_2$) which here is redefined to be symmetric as follows,

$$\mathrm{LTBS}_2 = t\begin{pmatrix} 1 & e^{i\alpha} \\ e^{i\alpha} & 1 \end{pmatrix}, \tag{3.17}$$

where $t$ is the transmission coefficient, and $\alpha$ is the tunable phase. Considering the linear relation of the lossy beamsplitter from Eq. 3.4, we calculate how specific two-photon input states Eq. 3.16 result in the coherent absorption effect. The evolution of light from two input modes ($\hat{a}_1$ and $\hat{a}_2$) of the LTBS to the outputs is modelled as,

$$\hat{a}_1^\dagger \to t(\hat{a}_1^\dagger + e^{i\alpha}\hat{a}_2^\dagger) + \hat{F}_1^\dagger, \tag{3.18a}$$

$$\hat{a}_2^\dagger \to t(e^{i\alpha}\hat{a}_1^\dagger + \hat{a}_2^\dagger) + \hat{F}_2^\dagger. \tag{3.18b}$$

In order to highlight one of the maximum conditions of coherent absorption, we set $\alpha = 0$ and $t = 1/2$ throughout the presented calculations. Owing to the commutation relation in Eq. 3.5, the noise operators are not independent and obey the commutation relations,

$$\left[\hat{F}_1, \hat{F}_1^\dagger\right] = \left[\hat{F}_2, \hat{F}_2^\dagger\right] = 1 - 2|t|^2 = \frac{1}{2}, \tag{3.19a}$$

$$\left[\hat{F}_1, \hat{F}_2^\dagger\right] = \left[\hat{F}_2, \hat{F}_1^\dagger\right] = -2|t|^2 = -\frac{1}{2}. \tag{3.19b}$$

We consider the evolution in Eq. 3.18 to be unitary and the model of noise is represented by a simplified model of loss:

$$\hat{F}_1 = -\hat{F}_2 = \frac{1}{\sqrt{2}}\hat{a}_3, \tag{3.20}$$

where $\hat{a}_3$ is used to represent a lossy channel into which the light is dissipated. The provided noise operators satisfy the commutation relations (Eq. 3.19) and the energy conservation of the whole system. Introducing the operator $\hat{a}_+ \equiv (\hat{a}_1 + \hat{a}_2)/\sqrt{2}$, we can rearrange Eq. 3.18 as

$$\hat{a}_1^\dagger \to \frac{1}{\sqrt{2}}(\hat{a}_+^\dagger + \hat{a}_3^\dagger), \quad \hat{a}_2^\dagger \to \frac{1}{\sqrt{2}}(\hat{a}_+^\dagger - \hat{a}_3^\dagger). \tag{3.21}$$

We now consider the transformation of the N00N state with the lossy beamsplitter. A straightforward calculation then leads to

$$a_1^{\dagger 2} + (e^{i\phi}a_2^\dagger)^2 \to \frac{1}{2}(1 + e^{i2\phi})(a_+^{\dagger 2} + \hat{a}_3^{\dagger 2}) + (1 - e^{i2\phi})a_+^\dagger \hat{a}_3^\dagger. \tag{3.22}$$

In the case $\phi = q\pi + \pi/2, q \in \mathbb{Z}$ we have

$$a_1^{\dagger 2} - a_2^{\dagger 2} \rightarrow 2a_+^\dagger a_3^\dagger. \tag{3.23}$$

By introducing the states $|n_j\rangle$, which are Fock states of $n$ excitations in mode $j = 1, 2, 3$, we have

$$|2_-\rangle \equiv \frac{(|2_1, 0_2\rangle - |0_1, 2_2\rangle)}{\sqrt{2}} |0_3\rangle \rightarrow \frac{(|1_1, 0_2\rangle + |0_1, 1_2\rangle)}{\sqrt{2}} |1_3\rangle , \tag{3.24}$$

This means that single photons are deterministically absorbed while the other evolves into a balanced superposition of the two output modes.

In contrast, for $\phi = q\pi, q \in \mathbb{Z}$, the state becomes

$$a_1^{\dagger 2} + a_2^{\dagger 2} \rightarrow a_+^{\dagger 2} + a_3^{\dagger 2}, \tag{3.25}$$

which corresponds to the state,

$$\begin{aligned} |2_+\rangle \equiv \frac{|2_1, 0_2\rangle + |0_1, 2_2\rangle}{\sqrt{2}} |0_3\rangle \rightarrow & \frac{1}{\sqrt{2}} \left( \frac{(|2_1, 0_2\rangle + |0_1, 2_2\rangle)}{\sqrt{2}} + |1_1, 1_2\rangle \right) |0_3\rangle \\ & + \frac{1}{\sqrt{2}} |0_1, 0_2, 2_3\rangle . \end{aligned} \tag{3.26}$$

The state clearly shows that no single-photon absorption occurs in this case. On the other hand, two-photon absorption takes place with the probability of 0.5, and the other half of the probability is associated with the two-photon survival probability, which distributes the superposition of two-photon state on three output combinations. These terms in Eq. 3.26 correspond to the probabilities of two photons being in mode 1, being in mode 2, or of single photons being in either mode, respectively. As the relative phase $\phi$ of the input state is modulated, the combination of one-photon absorption and two-photon absorption are controlled following Eq. 3.22. The calculation denotes the coherent absorption effect of a N00N state with N=2. The experimental demonstrations of coherent absorption with the N00N state have been recently reported with a bulk-optics setup in which a lossy beamsplitter was implemented by multilayer absorbing graphene film, plasmonic chip, or plasmonic metasurface [Roger et al., 2016, Vest et al., 2018, Lyons et al., 2019]. In the next section, we experimentally demonstrate the coherent absorption effect with a full control range of relative phase $\alpha$ of the lossy beamsplitter by using our programmable optical network presented in chapter 2.

### 3.2.3 Experiment

#### Method

We illustrate the use of our experimental programmable optical network to simulate coherent absorption. We model to the interaction of a N00N state with N=2, $(|2, 0\rangle + e^{i2\phi} |0, 2\rangle)/\sqrt{2}$, on the LTBS. The interaction between the N00N state and the LTBS produces an intriguing $\phi$-phase dependence of outcome probabilities of one- and two-photon survival at the targeted outputs as discussed in subsection 3.2.2. We use our programmable optical network to simulate the coherent absorption experiment (Fig. 3.6a). In detail, the experimental setup used in this experiment is the same as the one illustrated in subsection 2.2.1. The four targeted output ports of interest are allocated on two arbitrary output positions and two polarization modes of the MMF as labelled H1, V1,

H2, and V2. We first measure the transmission matrix of the multimode fibre, then calibrate the relative phases and amplitudes of co-propagating reference fields as thoroughly explained in section 2.2. The programmable linear network $\mathcal{L}(\phi, \alpha)$ of the whole coherent absorption experiment (Fig. 3.6a) for different $\phi, \alpha$ phase settings are then programmed on the SLM[6].

The linear transformation $\mathcal{L}(\phi, \alpha)$ used as the representative of the coherent absorption experiment can be seen as a succession of three linear operations: (i) indistinguishable photons from the SPDC source are split by a beamsplitter to generate a NOON state with N=2 with a controllable output phase $\phi$; (ii) the NOON state interacts with a lossy beamsplitter (LTBS). The LTBS is here defined to be the symmetric form as in Eq. 3.17; (iii) photons are distributed into four output ports by two lossless beamsplitters in order to measure the probability of two-photon survival, defined as a sum of probabilities of detecting two photons in all possible output combinations of the LTBS, i.e., both photons on either output ports ($P(2_1, 0_2)$ and $P(0_1, 2_2)$) or single photons at each port ($P(1_1, 1_2)$).

The probabilities correspond to the two-fold coincidence counts at the four outputs of the linear network. For each phase setting of $\mathcal{L}(\phi, \alpha)$, the two-fold coincidence counts were integrated over 10 s. The probability of detecting two photons in the first output of the lossy beamsplitter $P(2_1, 0_2)$ corresponds to the double probability of detecting two-fold coincidence $2P_{H1V1}$ between the H1 and V1 output ports, and similarly the probability of detecting two photons in the second output $P(0_1, 2_2)$ is related to $2P_{H2V2}$. The double of the probability takes the probability of photon bunching that occurs at the analysed beamsplitter (BS) into account. The probability of single photons detected on each output port of the lossy beamsplitter $P(1_1, 1_2)$ are then related to the summation of probabilities of detecting two-fold coincidence, $P_{H1H2} + P_{H1V2} + P_{V1H2} + P_{V1V2}$. All measured probabilities are normalized with the probability of two-photon survival in a case of mimicking the lossless Mach–Zehnder interferometer with $\alpha = \pi/2$.

### Results and discussion

As shown in Fig. 3.6b, the effect of coherent absorption is maximized for $\alpha = p\pi, p \in \mathbb{Z}$ (red line). In the case where the relative phase $\phi = q\pi, q \in \mathbb{Z}$, which corresponds to a state $(|2, 0\rangle + |0, 2\rangle)/\sqrt{2}$ as an input, the output state is a superposition of vacuum- and two-photon state and the probability of one-photon being transmitted into the targeted outputs is null as in Eq. 3.26. This result hence exhibits the non-linear behaviour of the two-photon absorption in the quantum regime. On the other hand, when $\phi = q\pi + \pi/2$, which corresponds to a state $(|2, 0\rangle - |0, 2\rangle)/\sqrt{2}$, only single-photon loss occurs as explained in Eq. 3.24. Owing to our ability of fully control the relative phase $\alpha$ (Fig. 3.6c), which was not possible in previous works [Roger et al., 2016, Vest et al., 2018, Lyons et al., 2019], we observe a transition of the coherent absorption phenomenon from unitary for $\alpha = \pi/2$ (blue dots) to the maximal coherent absorption situation for $\alpha = \pi$ (red dots).

As presented in Fig. 3.7, the two-photon survival probability is composed of three contributions which are the probability of occupying two photons on the first output of the lossy beamsplitter $\mathrm{P}(2_1, 0_2)$, and the probability of occupying two photons on the second output of the lossy beamsplitter $\mathrm{P}(0_1, 2_1)$ and the probability of occupying one photon of photon pairs on each of output modes $\mathrm{P}(1_1, 1_2)$. At $\alpha = p\pi, p \in \mathbb{Z}$ which corresponds the maximally lossy case, we observe in-phase oscillations of these contributions. It shows

[6]We note that here we do not implement the procedure of the fine amplitude calibration, as described in subsection 2.2.3, when we program a different optical network, varying the phase parameter $\alpha$.

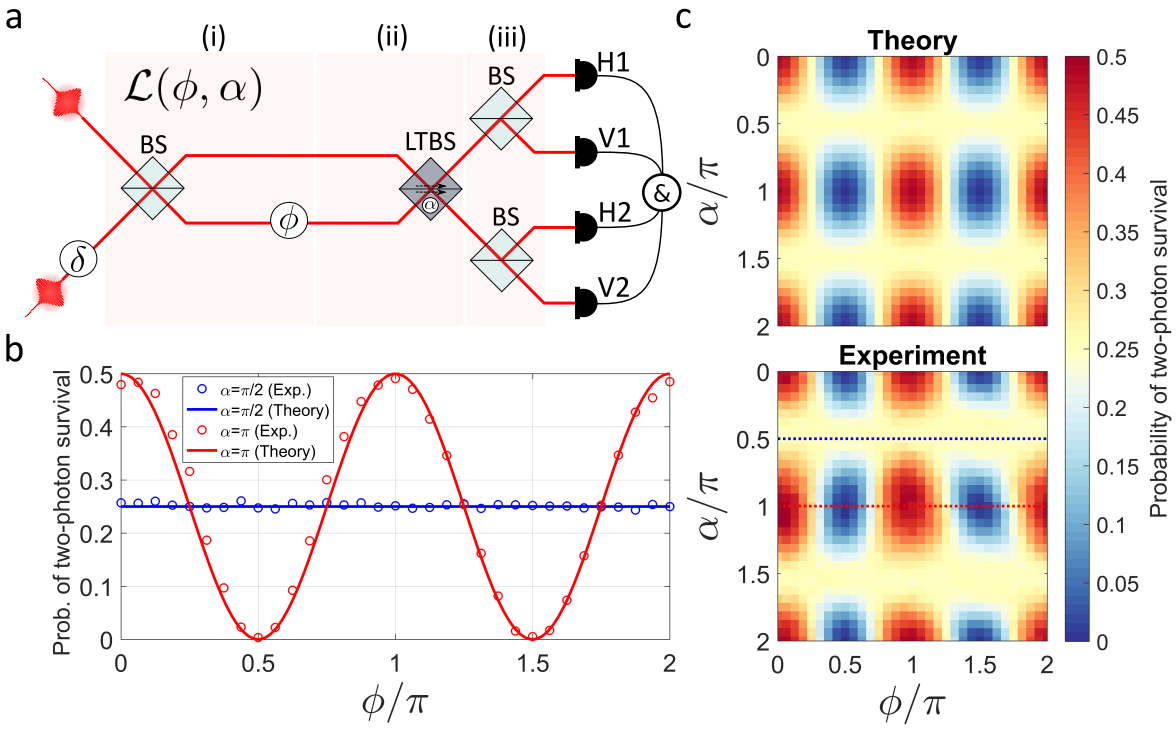


**Figure 3.6 – Experimental emulation of controlled coherent absorption**: (a) The linear network $\mathcal{L}(\phi,\alpha)$ programmed in the MMF emulates the following circuit: (i) Photon pair enters a Mach–Zehnder interferometer composed of a balanced beamsplitter and (ii) a lossy symmetric phase-tunable beamsplitter (LTBS). Both the phase $\phi$ between the two arms and the phase $\alpha$ of the LTBS can be tuned independently. (iii) Light in each output port of the MZ interferometer is analysed via two balanced beamsplitters preceding an array of four photon counters to measure the probability of two-photon survival at the targeted output ports. (b) Probability of two-photon survival at the targeted outputs: theory (solid lines) and experiment (dots). The blue dots are for $\alpha = \pi/2$, corresponding to an emulated lossless MZ interferometer. The corresponding probability of two-photon survival is independent of $\phi$. The red dots are for $\alpha = \pi$, corresponding to a lossy beamsplitter in which the probability of two-photon survival depends on the relative phase $\phi$. (c) Probability of two-photon survival as a function of $\phi$ and $\alpha$, showing a transition from emulated lossless to lossy LTBS.

the maximum two-photon survival probability of 0.5 when the two-photon N00N state is $1/\sqrt{2}(|2_1, 0_2\rangle + |0_1, 2_2\rangle)$. In contrast, zero probability of two-photon survival is observed when $\phi = q\pi + \pi/2, q \in \mathbb{Z}$. At $\alpha = \pi/2$ which mimics the relative phase of lossless beamsplitter, the probabilities of having two photons in either path of the MZ interferometer are out-of-phase to the probability of having exactly one photon on each path. The presence of out-of-phase component results in a constant two-photon survival probability for $\alpha = \pi/2$ as depicted in Fig. 3.6 which is a signature of a lossless beamsplitter.

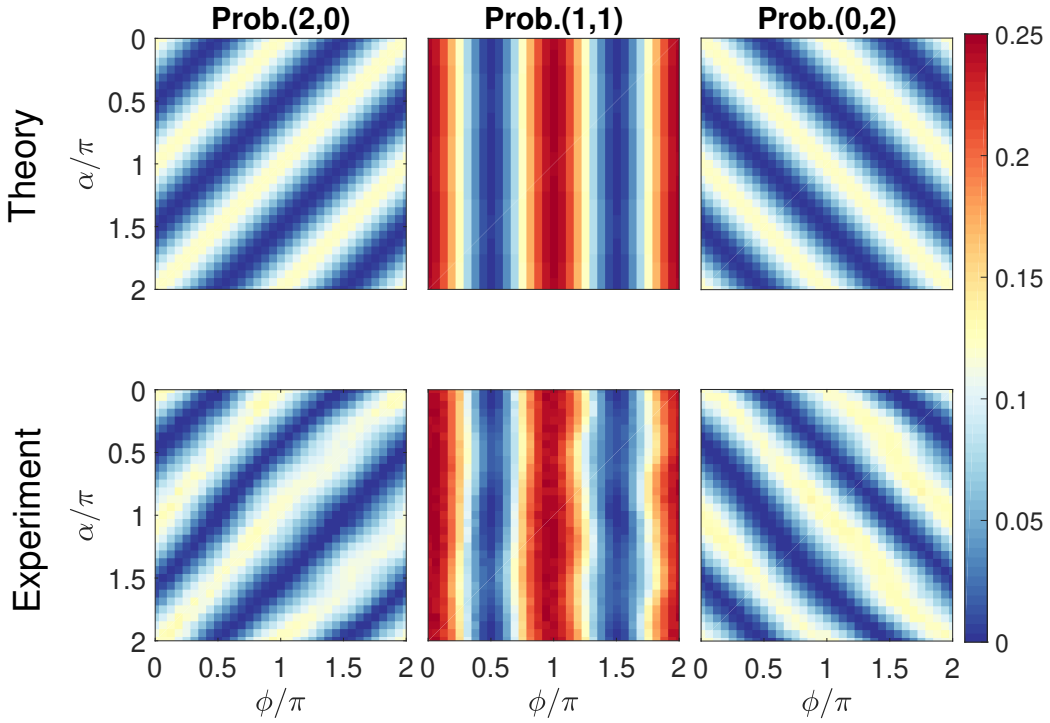


**Figure 3.7 – Contributions to the probability of two-photon survival**: (Theory) top panel and (Experiment) bottom panel. Decomposition of the two-photon survival probability into its three contributions, $\mathrm{P}(2_1, 0_2)$, $\mathrm{P}(0_1, 2_2)$, and $\mathrm{P}(1_1, 1_2)$, corresponding to two photons detected on the first output, on the second output of the lossy beamsplitter and one of photon pairs detected on each of outputs of the lossy beamsplitter, respectively. All probabilities are normalized with the probability of two-photon survival in a case of mimicking the lossless MZ interferometer with $\alpha = \pi/2$.

We want to note that the losses addressed in this chapter do not originate from the optical system. Indeed, our optical system is nearly lossless. The multimode fibre is a practically lossless waveguide[7], which transports light from the input to output with nearly perfect efficiency. The experimental transmission of the MMF was $\sim 0.95$. The SLM efficiency of light utilization[8] is 0.97 at 785 nm (Hamamatsu LCOS-SLM X10468-02). The loss utilized in our experiment for implementing non-unitary transforms, on

[7]The propagation loss of the MMF is <2.3 dB/km at 850 nm.

[8]Light utilization efficiency is defined as a ratio of the zero-th order diffraction light level to input light level.

the other hand, stems from the fact that we control only half of the propagating modes of the MMF in each input port of an optical network, which is known as the imperfect wavefront control (section 2.4.3). The part of the light from an input port is dissipated to the unmonitored output modes owing to the partial wavefront control. The unmonitored modes thus embody an environmental bath where information about the desired optical network leaks, resulting in effective open system dynamics of the latter.

The total energy transmittance $2|t|^2$ to all targeted outputs of the implemented optical networks $\mathcal{L}$ reaches 0.45(0.5) experimentally[9] (theoretically). This transmittance allows us to use this platform to emulate the coherent absorption effect close to the critical transmission of 0.5, while still allowing full control on the relative $\alpha$ of the lossy beamsplitter. In fact, the partial wavefront control allows us to generate arbitrary linear optical networks on the platform without being constrained by unitarity. The experimental scheme is thus handy for implementing non-unitary evolution. For example, one can implement a $k \times m$ non-unitary transformation embedded on the large dimension of the multimode fibre instead of doing this on a large-dimensional unitary transformation implemented via the well-known decomposition techniques [Reck et al., 1994, Clements et al., 2016, Miller, 2013b, Miller, 2013a].

## 3.3 | Summary and perspectives

In this chapter, two related phenomena resulting from a non-unitary evolution of two-photon states have been explored by the use of the programmable optical networks. In particular, the two-photon interference on the lossy beamsplitter and the coherent absorption of a path-entangled N00N state with N=2 have been demonstrated experimentally.

In the first experiment, two indistinguishable input photons interfere on the lossy beamsplitter. The results show the non-linear behaviour of the dissipation process in which only a two-photon state has a probability of being absorbed or transmitted with 50% chance, while no probability of single-photon being absorbed and transmitted. The phenomenon is known as two-photon absorption on a linear lossy beamsplitter, which clearly occurs in a low photon count level [Barnett et al., 1998]. In the second experiment, a N00N state with N=2 is sent through the lossy beamsplitter, the relative phase $\phi$ of the path-entangled N00N state with N=2 allows for the control of the probabilities of single- and two-photon absorption. The phenomenon is known as coherent absorption [Jeffers, 2000]. The results indicate the two intriguing effects, which are non-linear and coherent absorptions, of a non-unitary evolution of the two-photon interference.

Losses of control are usually deleterious for a quantum system. In our experiment, partial wavefront control provides the ability to coherently and arbitrary implement linear transforms beyond the unitary constraint, inducing a useful non-linearity and coherent absorption. The classical analogue of the coherent absorption phenomenon has been widely exploited for several processing tasks [Zhang et al., 2012, Fang et al., 2015, Papaioannou et al., 2016b, Papaioannou et al., 2016a, Xomalis et al., 2018, Baranov et al., 2017]. We anticipate that both related effects, non-linear and coherent absorption, pave an alternative route for quantum information processing without the need of a conventional non-linear optics. For instance, one might perspectively employ the coherent absorption of two photons as a route to induce the interaction between two qubits [Kok et al., 2007]

[9]The experimental transmittance is defined as the ratio of the photon flux carried by all targeted outputs of interest to the total photon flux transmitted through the MMF.

which could apply as a protocol for a quantum logic gate. Furthermore, the reconfigurable nature and viability of our experiment also point a prospective towards the implementation of high-dimensional non-unitary linear circuits. The optical platform can be used not only to study a fundamental non-Hermitian physics but also to apply to a quantum information task such as dissipative quantum state engineering which is enabled by the explicit presence of noise.

# 4

# State classifier

*"The Milky Way is nothing else but a mass of innumerable stars planted together in clusters."*

— Galileo Galilei

In this chapter, we exploit the complex mixing characteristics of the multimode fibre to randomly projecting unknown states of light onto the high-dimensional output space. By measuring statistical properties of intensity, second-order correlation, and a normalized second-order correlation between two outputs over many realizations of random projection, we can distil information on the unknown states such as the purity, dimensionality, indistinguishability. This information allows us to classify a certain set of unknown light states without performing state tomography.

## Contents

## 4.1 | Introduction

Classical speckles can be used to reveal characteristics of light forming it. Statistical properties of intensity speckles provide information about the first-order degree of coherence. In case of classical fully-mixing of coherent states, i.e., equally-weighted incoherent summation of coherent light source, the probability density function (PDF) of intensity speckle is

$$P_1(\frac{I}{\bar{I}}) = \frac{d^d}{\Gamma(d)} \left(\frac{I}{\bar{I}}\right)^{d-1} \exp\left(-d\frac{I}{\bar{I}}\right), \tag{4.1}$$

where $d$ represents a number of coherent sources, $\Gamma$ is the gamma function, and $\bar{I}$ is an average intensity. This PDF is known as a gamma density function of order $d$ or $\chi^2$-distribution [Réfrégier, 2004, Goodman, 2005b]. In case of fully developed speckle ($d = 1$), the PDF reduces to the exponential decay shown in Eq. 2.3.

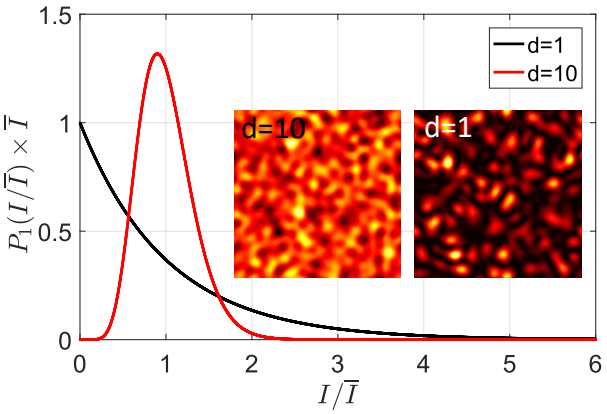


**Figure 4.1 – Probability density distributions of intensity**: (black line) $d = 1$ and (red line) $d = 10$. Insets show intensity speckle patterns in which one easily distinguishes the coherent light $d = 1$ and the partially-coherent light $d = 10$.

As shown in the insets of Fig. 4.1, speckle patterns of coherent light and partially-coherent light are clearly distinct. By fitting the statistical distribution or estimating statistical moments, a number of modes of an unknown light source can be predicted, typically via the calculation of visibility of intensity speckle[1],

$$\mathcal{V}_I = \frac{\mathrm{Var}\,(I)}{\bar{I}^2} = \frac{1}{d}, \tag{4.2}$$

In general, one could ask a question about what kind of possible information of an input non-classical light can be predicted from statistical properties of its corresponding scattered light also at higher-order correlations. This is the initial motivation of research that we are going to explore in this chapter. As depicted in Fig. 4.2, our general statement of research problem is summarized in the following question:

"How much information about an input state $\rho$ one can distil by measuring statistical properties of the first-order intensity as well as a certain number of high-order correlations, when the input state is randomly projected into a high-dimensional space?".

In the following section, a literature review regarding the problem is provided.

[1]The visibility is a square of the contrast of the speckles.

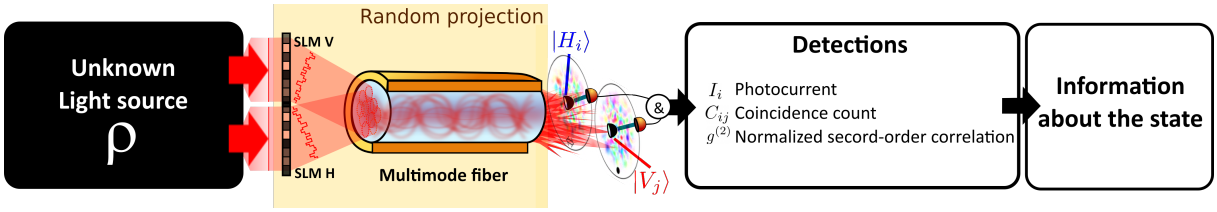


**Figure 4.2 – Research problem**: An unknown light source is randomly projected to a high-dimensional output space via the SLM and multimode fibre (MMF). We probe the state on two-output mode subspaces, labelled $H_i$ and $V_j$. Photocurrents ($I_i$), two-fold coincidence counts ($C_{ij}$), and normalized second-order correlation $g^{(2)}$ are measured and used to extract information about an input state.

### 4.1.1 Quantum optics in multiple scattering process

#### Overview

Quantum optics in multiple scattering process have been explored as a small sub-field since the last 1990s [Patra, 2000, Beenakker, 2018]. One of early work is a study of the process of thermal radiation and amplified spontaneous emission from a scattering medium [Beenakker, 1998, Beenakker and Patra, 1999]. Over the last two decades, substantial theoretical endeavours have been devoted to understanding how non-classical lights behave during multiple scattering. A wide range of topics has been investigated, for instance, the degradation of entanglement [Aiello and Woerdman, 2004, Van Velsen and Beenakker, 2004, Puentes et al., 2007, Candé et al., 2014], the transport of quantum noise [Patra and Beenakker, 2000, Lodahl and Lagendijk, 2005, Lodahl, 2006b, Lodahl, 2006a, Skipetrov, 2007], and dynamics of photon statistics in disordered or structured lattices [Bromberg et al., 2009, Lahini et al., 2010, Esat Kondakci et al., 2016, Kondakci et al., 2017].

One of the relevant phenomena is the presence of spatial correlation averaged over an ensemble of realizations of the scattering medium [Lodahl et al., 2005, Smolka et al., 2009, Smolka et al., 2011, Ott et al., 2010]. The phenomenon results from both classical and quantum origins [Candé and Skipetrov, 2013, Starshynov et al., 2016]. The disorder-averaged spatial correlation varies depending on scattering properties of a medium and the input state of light, e.g., squeezed state [Smolka et al., 2009, Smolka et al., 2012], a photon-number state [Ott et al., 2010, Ott, 2012, Li et al., 2019a], thermal state [Lodahl et al., 2005, Starshynov et al., 2016] or frequency-entangled biphoton states [Cherroret and Buchleitner, 2011]. In consequence, the averaged spatial correlation can be potentially applied to extract information about an incident state of light [Ott et al., 2010, Cherroret and Buchleitner, 2011].

#### Statistical property of two-photon speckles

The speckle pattern of two-fold coincidences generated from a biphoton state is known as two-photon speckle [Beenakker et al., 2009]. In 2009, C.W.J Beenakker, J.W.F. Vederbos, and M.P. Exter calculated a statistical property of two-photon speckles produced by a pure state of spatially-entangled photon pairs of dimension $d$. They found a one-to-one mapping between the probability density functions of intensity speckle $P_1(I)$ and of two-photon speckle $P_2(C)$. In case of a pure spatially and maximally-entangled biphoton state, the PDF of the intensity speckle $P_1(I)$ has the same form as in the case of a classical fully-

mixture of coherent states (Eq. 4.1) [Beenakker et al., 2009]. Consequently, the PDF of two-photon speckle $P_2(C)$ reads,

$$P_2(\frac{C}{\overline{C}}) = \frac{2d}{\Gamma(d)} \left(d\frac{C}{\overline{C}}\right)^{\frac{d-1}{2}} \mathcal{K}_{d-1}\left(2\sqrt{d\frac{C}{\overline{C}}}\right), \tag{4.3}$$

where $\mathcal{K}_{d-1}$ is a modified Bessel function of the second kind. This distribution is known as K-distribution [Réfrégier, 2004, Andrews and Phillips, 2005] and has a classical analogy with an intensity speckle, and appears, for example, in linear optical rogue waves [Arecchi et al., 2011].

For a pure biphoton state, the PDF of two-photon speckle is fixed via the PDF of intensity speckle owing to this one-to-one mapping [Beenakker et al., 2009]. Therefore, it does not provide additional information about a given pure biphoton state [Beenakker et al., 2009]. Nevertheless, the PDF of two-photon speckles can be used to distinguish a pure biphoton state from other states. For example, in case of a single-photon state, no genuine two-fold quantum coincidences exist. Furthermore, in case of a mixed biphoton state, no such one-to-one mapping between $P_1(I)$ and $P_2(C)$ exists [Beenakker et al., 2009].

Furthermore, C.W.J Beenakker, J.W.F. Vederbos, and M.P. Exter have also shown that the purity $\mathcal{P}$ of a biphoton density matrix $\rho$ can be directly obtained from the first two statistical moments of intensity speckle and two-fold coincidence speckle [Beenakker et al., 2009, van Enk and Beenakker, 2012] as follows:

$$\mathcal{P} = \mathrm{Tr}\,\rho^2 = \mathcal{V}_C - 2\mathcal{V}_I. \tag{4.4}$$

where $\mathcal{V}_I$ is the visibility of intensity speckles (Eq. 4.2) and $\mathcal{V}_C$ is the visibility of two-fold coincidence speckles defined as,

$$\mathcal{V}_C = \frac{\mathrm{Var}(C)}{\overline{C}^2}. \tag{4.5}$$

The dimensionality[2] $d$ of a pure spatially maximally-entangled biphoton state can be obtained from both visibilities,

$$\mathcal{V}_I^{\mathrm{pure}} = \frac{1}{d}, \tag{4.6a}$$

$$\mathcal{V}_C^{\mathrm{pure}} = 1 + \frac{2}{d}. \tag{4.6b}$$

On the other hand, one can consider the case of a fully-mixed biphoton state, defined as

$$\rho^{\mathrm{mixed}} = \frac{1}{D}\sum_{i=1}^{D} |\Psi_i\rangle \langle\Psi_i|, \tag{4.7}$$

where $|\Psi_i\rangle \equiv |1\rangle_a \otimes |1\rangle_b$ is a pure separable biphoton state. Its purity is determined by a number of classical mixtures $D$ in the fully-mixed state. According to Eq. 4.4, the purity and visibility of two-fold coincidences are

$$\mathcal{P}^{\mathrm{mixed}} = \frac{1}{D} = \frac{2}{d} \tag{4.8a}$$

$$\mathcal{V}_C^{\mathrm{mixed}} = \frac{2}{D} = \frac{4}{d} \tag{4.8b}$$

[2]We define here the dimensionality $d$ as twice the Schmidt rank $D$, that quantifies the dimensionality of entanglement: $d = 2D$. Our underlying reason is that it provides an analogy with a classical source.

As $d \to \infty$, the corresponding statistical distribution of two-fold coincidences $P_2(C)$ tends to a narrow Gaussian profile and is completely different from the case of a pure maximally-entangled biphoton state, as shown in Fig. 4.3. The PDF of a pure maximally-entangled biphoton state is K-distribution and it converges to the exponential decay behaviour as $d \to \infty$. The K-distribution shows a non-exponential long decay at low $d$ [Abraham and Lyons, 2010].

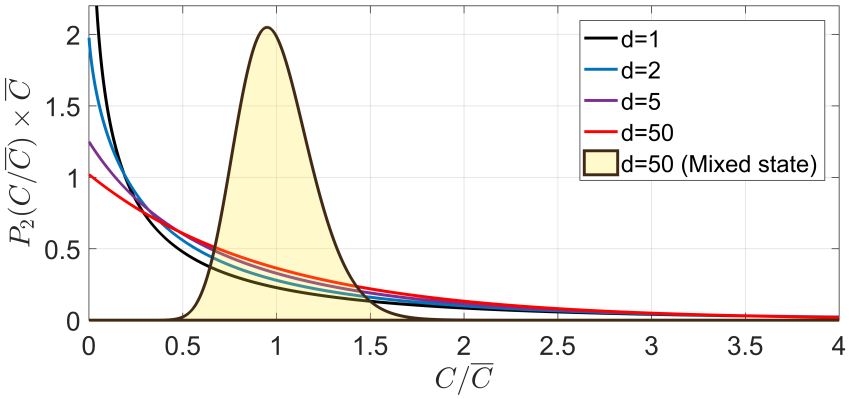


**Figure 4.3 – Probability density distributions of two-fold coincidences**: (lines) for a pure maximally-entangled biphoton state of various dimension $d$ and (yellow area) for fully-mixed biphoton state ($d = 50$).

### Experimental observations

A considerable number of experiments have been carried out in the context of non-classical light propagating through a complex scattering medium [Lodahl et al., 2005, Puentes et al., 2007, Smolka et al., 2009, Peeters et al., 2010, Van Exter et al., 2012, Di Lorenzo Pires et al., 2012]. Two related experiments are mentioned here. In 2010, W. H. Peeters, J. J. D. Moerman, and M.P. van Exter observed a two-photon speckle. As shown in Fig. 4.4, the intensity speckle appears to be like a speckle of incoherent source, while a high-contrast two-photon speckle is observed. This is clearly the feature of a high-dimensional spatially-entangled biphoton state. In 2012, the statistical distributions of speckles generated from pure entangled biphoton states of different dimensions $d$ have been demonstrated by using the scattering system made of two rotated diffusers [Di Lorenzo Pires et al., 2012]. As shown in Fig. 4.5, the PDFs of two pure spatially-entangled biphoton states for $d = 1.4$ and $d = 80$ is consistent with the theory, explained in the previous section [Beenakker et al., 2009, Di Lorenzo Pires et al., 2012].

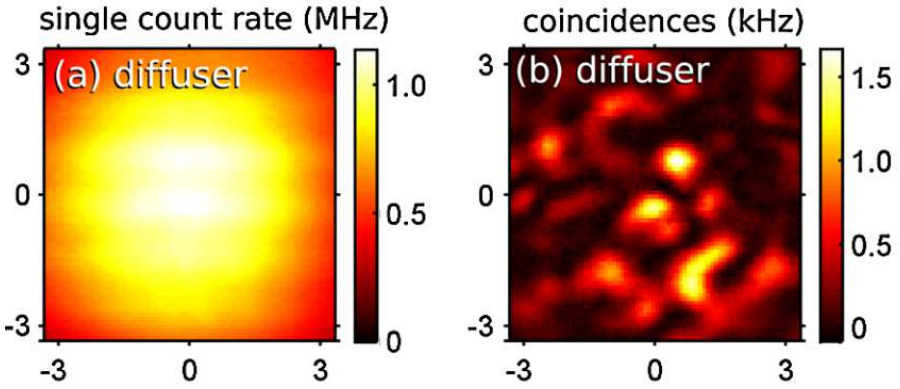


**Figure 4.4 – Intensity and two-photon speckles**: (a) Measured single count rate scanning across the image plane and (b) Corresponding measured two-fold coincidence counts scanning across the image place with the first detection while keep the position of second detector fixed. Adapted from [Peeters et al., 2010]

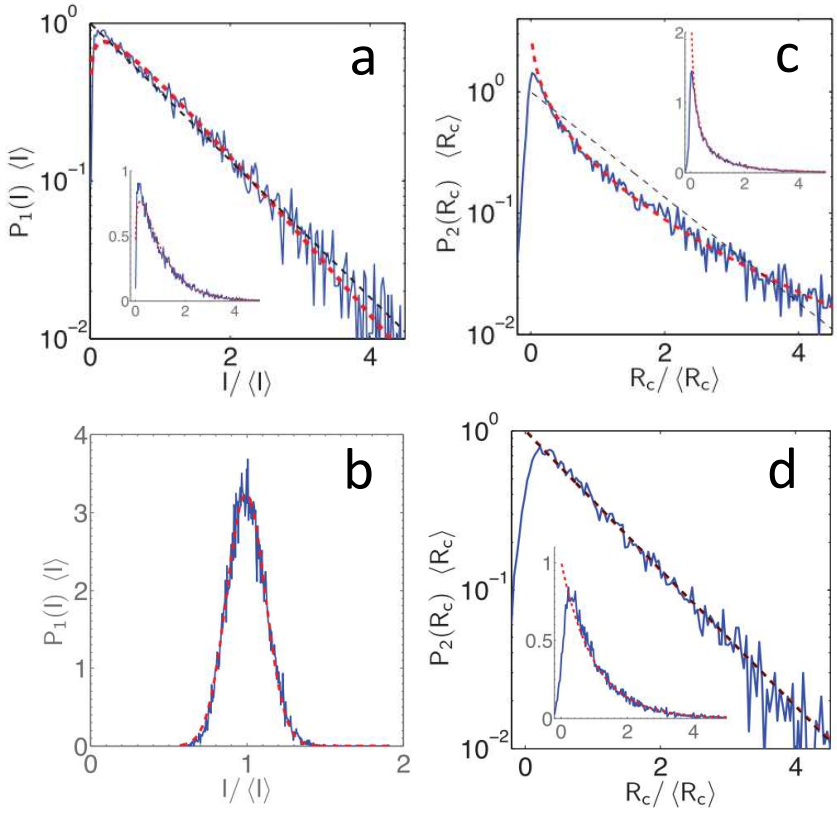


**Figure 4.5 – Probability density distributions for pure biphoton states**: (a and b) PDF of intensity speckles for two pure entangled biphoton states of dimension $d = 1.4$ (a) and $d = 80$ (b). (c and d) PDF of two-photon speckles for two pure entangled biphoton states of dimension $d = 1.4$ (c) and $d = 80$ (d). Adapted from [Di Lorenzo Pires et al., 2012]

**Statistical verification for boson sampling**

In the context of boson sampling, many protocols have been proposed to certify the presence of genuine many-particle quantum interference on an optical device [Brod et al., 2019], for example, likelihood ratio tests [Spagnolo et al., 2014], zero transmission laws [Tichy et al., 2010], and pattern recognition techniques [Agresti et al., 2019]. One of the promising techniques is based on statistical signatures of low-order spatial correlation of many-particle quantum interference. M. Walschaers *et al.* have proposed to certify the degree of indistinguishability of an input state by using the first three statistical moments of *two-mode truncated correlation* [Walschaers et al., 2016b, Walschaers et al., 2016a]. The *two-mode truncated correlation* or *two-point photon-number correlation* is defined as

$$\mathtt{C}_{ij} = \left\langle \hat{N}_i \hat{N}_j \right\rangle - \left\langle \hat{N}_i \right\rangle \left\langle \hat{N}_j \right\rangle, \tag{4.9}$$

where $\hat{N}$ is the photon number operator. It measures all possible two-particle interferences that contribute to mode $i$ and $j$. The statistical technique has been extended to certify temporal indistinguishability [Walschaers et al., 2016b] and Gaussian boson sampling [Phillips et al., 2019]. D.S.Phillips *et al.* has theoretically shown that squeezing of Gaussian input states provide statistical signatures in the first three statistical moments of two-point correlation that is not observable in a photon number Fock state [Phillips et al., 2019]. Experimentally, this statistical technique has been recently applied to classify the indistinguishability of three-photon interference on seven-mode integrated photonic chip [Giordani et al., 2018].

### 4.1.2 Conclusive remarks and objectives

Many theoretical works have been exploring statistical properties of second-order correlation to measure purity, dimensionality and indistinguishability of a state. A few experiments have been reported the use of those techniques. In this chapter, our objective is to study the statistical properties of two-photon speckles for different input states in order to extend the techniques for a more general class including frequency-entangled biphoton states. In particular, we are going to experimentally show the feasibility of the technique for state classification. In the following, we provide the experimental details and describe various input states used in our study.

## 4.2 | Experimental details

For our experiment, the optical setup is the same as described previously in Fig. 3.2. As conceptually shown in Fig. 4.2, the combination of SLM and MMF (Thorlabs, GIF50C) is used as an optical mixer for random projection [Mahoney, 2010]. An unknown state of light is randomly projected via the optical mixer onto many output modes ($n \approx 400$). We measure statistical properties using two fixed output modes which are randomly selected on two different spatial modes and are in orthogonal polarizations. We assume that the optical mixer is unitary and sufficiently random. This means that the correlation presented in a sub-part transmission matrix of the multimode fibre linking to two measured outputs is negligible and can be efficiently represented by an i.i.d. complex Gaussian random matrix [Aaronson and Arkhipov, 2011]. Many realizations are set via a different phase pattern displayed on the SLM, which controls light coupling through the MMF with random phases and amplitudes. Photocurrents and two-fold coincidence counts are

acquired by single-photon counting module and coincidence electronics for many realizations of the optical mixer. We tested several input ground-truth states as listed in the following.

### 4.2.1 Ground-truth input states

Our ground-truth input states can be divided into two main categories regarding emission process. The first category is quantum, generated from the frequency-degenerate polarization-separable type-II SPDC process (the details of the source are explained in Appendix A). The second is classical, generated by the amplified spontaneous emission (ASE) process from the superluminescent diode light source (SLD, Superlum).

Furthermore, we study the effect of temporal mixing on the statistical properties of scattered lights by changing the length of the fibre. We prepared the spectral bandwidth of the SLD source to be approximately the same as the SPDC source. The spectral full width at half maximum is $\Delta\lambda_{\text{SPDC}} = 1.56 \pm 0.05$ nm for the SPDC source and $\Delta\lambda_{\text{SLD}} = 2.33 \pm 0.05$ nm for the SLD source. We split ground-truth light states into two categories: monochromatic case and polychromatic case. In the monochromatic case, we use a short fibre with a length of 55 cm in order to control the spectral correlation bandwidth of the medium to be broader than the spectral bandwidth of all ground-truth light sources, i.e., non-dispersive. In contrast, we use the fibre with a length of 25 m for the polychromatic case as a highly dispersive medium. The indistinguishability of the SPDC source and the coherence property of the SLD source are controlled by the delay line $\delta$ between two inputs. We provide details of state preparation for each ground-truth state:

- **Monochromatic case**: 55-cm long MMF (GIF50C, Thorlab).
    1. **Indistinguishable monochromatic biphoton state**: The delay between two input modes is set to zero ($\delta = 0$). The state can be appropriately written as $|1_{H_{\text{in}}} 1_{V_{\text{in}}}\rangle$.
    2. **Distinguishable monochromatic biphoton state**: The same as before but the delay between two input modes is set to be longer than the coherence length $l_c$ of the biphoton state ($\delta > l_c$). The state can be appropriately written as $|1_{H_{\text{in}}}\rangle_{\delta=0} |1_{V_{\text{in}}}\rangle_{\delta>l_c}$.
    3. **Indistinguishable N00N state with N=2**: The N00N state is prepared via HOM interference with a balanced fibre-based beamsplitter just after the SPDC source. The measured two-photon visibility is 0.98. Initially, we test the indistinguishability of the NOON state after propagating through the MMF by programming an optical network to act as the balanced beamsplitter (see subsection 2.2.3 for details). We observe the N00N-state interference (subsection 1.3.2) and ensured that the visibility of interference is observed at the same visibility as the HOM interference before propagating through the fibre. The state can be written as in Eq. 1.37.
    4. **Heralded single-photon state**: We use the SPDC source as heralded single-photon source by sending only a vertical-polarization photon of the biphoton state through the fibre. We post-select the single-photon state via heralding process.
    5. **Two-photon Fock state**: We post-select one output of the N00N state generated by the fibre-based beamsplitter as explained in (3).

6. **Incoherent source**: The spectral-filtered and polarized SLD source is distributed by the beamsplitter into the two input modes and the delay between two inputs is set to be longer than the coherence length of the source ($\delta > l_c$).

- **Polychromatic case**: We use the 25-m long MMF (GIF50C, Thorlab) with the spectral correlation bandwidth of the fibre $\Delta\lambda_{\text{fibre}} = 0.222 \pm 0.004$ nm.

1. **Indistinguishable frequency-entangled biphoton state**: The same source as in the case of indistinguishable monochromatic biphoton state ($\delta = 0$). The anti-correlation in frequency need to be taken into account. The state can be written as in Eq. 1.26.

2. **Distinguishable frequency-entangled biphoton state**: The same as above with the delay ($\delta > l_c$). The state can be appropriately written as in Eq. 1.30.

3. **Incoherent source**: It is the same as the incoherent source, but propagating through the 25-m long MMF. The number of spectral channels of the state is $\Delta\lambda_{\text{SLD}}/\Delta\lambda_{\text{fibre}} \approx 10.6$.

### 4.2.2 Detection and data analysis

For a given input state at each realization, on each random projection, we record photocurrents $(I_1, I_2)$ and two-fold coincidence counts $(C)$ between two outputs using two APD detectors and coincidence electronic circuit. The coincidence window $(\tau_C)$ is set to 2.5 ns. We define the normalized second-order correlation $(g^{(2)})$ as the ratio between two-fold coincidence counts $C$ and the expected accidental coincidences $R$ as follows, $g^{(2)} = C/R$, where the accidental coincidences are defined as $R = \tau_C I_1 I_2$. The accidental coincidences are not subtracted from the raw two-fold coincidences $C$ in all cases; therefore, measured two-fold coincidence counts contain the contributions both from classical and non-classical origins.

In order to take into account the contribution of accidental coincidences, we provide a more detailed data analysis of $R$. According to the fact that photocurrents $I_1$ and $I_2$ are two independent random variables[3] with a gamma density function of order $d$ (Eq. 4.1), we calculate the probability density function of accidental coincidences $R$, and it reads,

$$P_2(\frac{R}{\overline{R}}) = \frac{2}{\Gamma(d)^2} d^{2d} \left(\frac{R}{\overline{R}}\right)^{d-1} \mathcal{K}_0\left(2d\sqrt{\frac{R}{\overline{R}}}\right), \tag{4.10}$$

The integration time of each realization of the optical mixer is set such that the averaged integrated intensity of all ground-truth light states are in the same range of a value, and two-fold coincidences are detected in the range of a few tens per second. The number of realizations that we acquired is about 10000 realizations. The information about experimental details is provided in Appendix F. The overall measurement time was a few days per ground-truth state.

To verify the stability of the sources and of the optical setup, we keep tracking every hour the mean intensities at the two outputs and the mean and variance of the normalized second-order correlation. Furthermore, in cases of SPDC source, the visibility of HOM interference is measured before starting and after finishing the experiment in order to ensure the stability of the source. In the following, the results are presented and discussed.

[3] We assume no correlations in the subpart of TM of MMF.

## 4.3 | Results and discussion

We first present raw measured data on the scatter plot of intensity $I_1/\overline{I_1}$ and normalized second-order correlation $g^{(2)}/\overline{g^{(2)}}$ for all ground-truth states in Fig. 4.6a. The statistical distributions of all ground-truth states plotted in intensity and second-order correlation indicate highly uncorrelated feature. We can thus extract information about the states from the marginal probability distributions on the intensity and normalized second-order correlation independently.

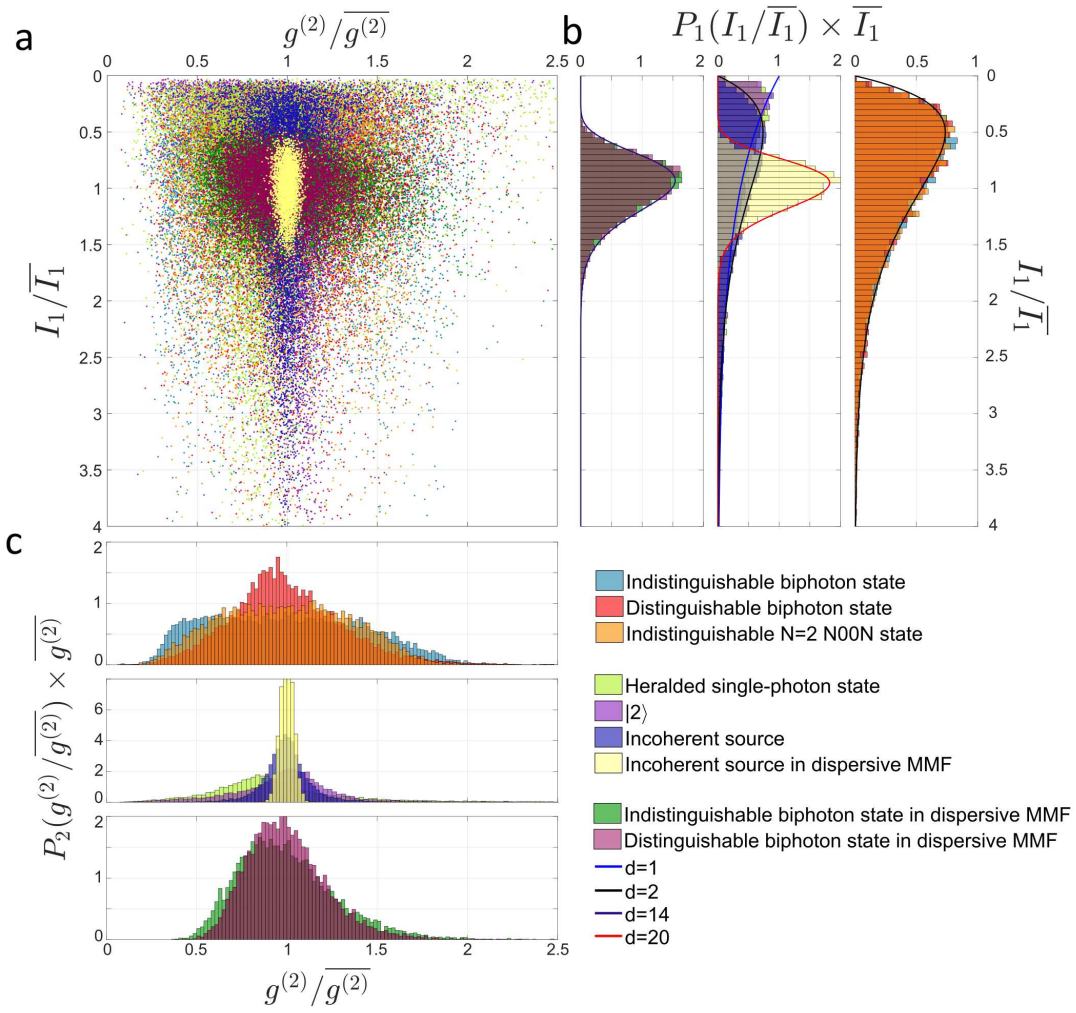


**Figure 4.6 – Statistical distributions of intensity $I_1/\overline{I_1}$ and normalized second-order correlation $g^{(2)}/\overline{g^{(2)}}$:** (a) Scatter plot of intensity $I_1/\overline{I_1}$ and normalized second-order correlation $g^{(2)}/\overline{g^{(2)}}$. Each point represents measurement obtained from one realization of the optical mixer. (b) Marginal probability density function of intensity $P_1(I_1/\overline{I_1})$ provides information of a number of modes $d$. (c) Marginal probability density function of normalized second-order correlation $P_2(g^{(2)}/\overline{g^{(2)}})$ can be applied to further classify states. Ground-truth states are labelled as indicated in the figure.

At the intensity level, the statistical properties of intensity speckle $P_1$ (Fig. 4.6b) cannot be used to distinguish a classical state apart from a non-classical state; it provides only information about the number of modes ($d$) that a state occupies as described by

Eq. 4.1. The additional information of an unknown state can be extracted by measuring statistical properties of a second-order correlation such as the purity [Beenakker et al., 2009] and degree of indistinguishability [Walschaers et al., 2016b]. We propose here that the statistical property of normalized second-order correlation $g^{(2)}$ (Fig. 4.6c) is a most useful indicator, that can be applied for state classification. In the following, we report our experimental observations and supporting evidence for this proposal.

### 4.3.1 Purity and dimensionality of biphoton states

The statistical distribution of two-fold coincidences for each ground-truth state is shown in Fig. 4.7. We observe that the contribution of accidental coincidences in the experiment potentially degrades the statistical distribution from the expected genuine two-fold coincidences. In the case of monochromatic biphoton states, the distributions are better described by the statistical distribution of accidental coincidences (Eq. 4.10), rather than by the PDF of two-fold coincidences (Eq. 4.3). This effect of accidental coincidences also occurs in the case in which the expected accidental coincidences are subtracted from the measured two-fold coincidences as presented in Fig. F.3. Due to this effect, for example for $d = 2$, one cannot easily distinguish the incoherent light source (dark blue) from the indistinguishable biphoton state (blue), distinguishable biphoton state (red), and N00N state with N=2 (orange).

This influence of the effect is fewer at a high value of $d$ in the long MMF. We observe a sizeable deviation of statistical distributions of dispersive indistinguishable (green) and distinguishable (light magenta) biphoton states from the predicted distribution of accidental coincidences (dashed magenta line with $d \approx 14$, estimated by measuring the statistics of intensity). The experimental distributions of both dispersed biphoton states tend to shift towards zero and have a higher skewness compared to the distribution of accidental coincidences, which may be a feature originating from a quantum effect[4]. Unfortunately, both distributions have a feature similar to the distribution of accidental coincidences around $d \approx 10$. Consequently, classifying the state with two-fold coincidences in the presence of accidental coincidences is a challenging task.

We estimate the purity of ground-truth monochromatic biphoton states from the visibilities of intensity, and two-fold coincidences using the theoretical prediction (Eq. 4.4). The results are presented in Table 4.1. We can estimate the number of modes that a ground-truth state occupied. The purity is lower than the expectation, the error results mainly from a underestimation of $\mathcal{V}_C$. We attribute the error to two contributions: the influence of accidental coincidences and the lack of rare events originating from a long tail of the statistical distributions. We describe these influence in Appendix F.1. Here we infer that the estimation of the purity is inconclusive under the presence of those influences.

[4]The estimated deviation of $d$ with the model of accidental coincidences is lower than the expectation with the statistics of intensity by 16-fold standard deviation.

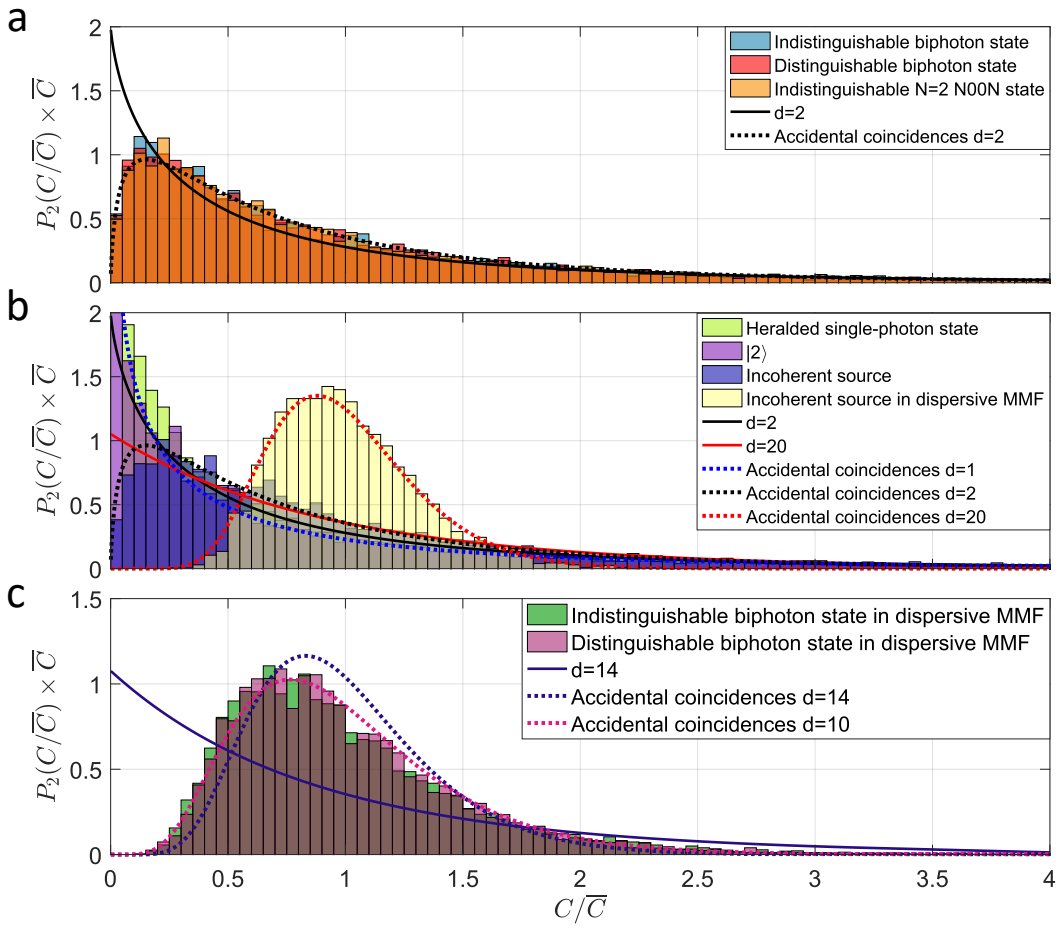


**Figure 4.7 – Probability density functions of two-fold coincidences** $P_2(C/\overline{C})$: (a) Indistinguishable biphoton state (blue), distinguishable biphoton state (red), and N=2 N00N state (orange) have the same distribution with $d = 2$. (b) Heralded single-photon state (light green) and two-photon state (magenta) have the same distribution. Ever though the two-fold coincidences of single-photon state result solely from the accidental coincidence $d = 1$, the distribution is identical to the distribution of genuine coincidence at $d = 1$ for two-photon state. Incoherent source (dark blue) in a 55-cm MMF and incoherent source (light yellow) in a 25-m MMF have different distributions with $d = 2$ and $d = 20$, respectively. (c) Indistinguishable (green) and distinguishable (light magenta) biphoton states in dispersive 25-m MMF have the same distribution that diverges from the PDF of expected accidental coincidences for $d \approx 14$ ($d_{\text{Indis}} = 14.7, d_{\text{Dis}} = 13.8$) predicted from the visibility of intensity speckle. The lines indicate distributions of two-fold coincidences for a pure maximally-entangled biphoton state (Eq. 4.3). The dashed lines indicate distributions of accidental coincidences (Eq. 4.10).

**Table 4.1** – Purity and dimensionality of monochromatic biphoton states.

| State | $\mathcal{V}_I$ | $\mathcal{V}_C$ | $\mathcal{P}$ | $d$ |
|---|---|---|---|---|
| biphoton state ($\delta = 0$) | $0.46 \pm 0.02$ | 1.38 | $0.45 \pm 0.03$ | $2.16 \pm 0.09$ |
| biphoton state ($\delta > l_c$) | $0.50 \pm 0.02$ | 1.34 | $0.35 \pm 0.03$ | $2.02 \pm 0.07$ |
| Indistinguishable N=2 N00N state | $0.45 \pm 0.01$ | 1.27 | $0.38 \pm 0.02$ | $2.24 \pm 0.01$ |
| $\|2_V\rangle$ | $0.85 \pm 0.06$ | 2.39 | $0.69 \pm 0.12$ | $1.18 \pm 0.09$ |

### 4.3.2 Statistics of normalized second-order correlation

The statistical properties of normalized second-order correlation are analysed in this section. As shown in Fig. 4.8, the statistical distributions of different ground-truth states can be better identifiable, compared to that of two-fold coincidences presented in the previous section. The key reason is that the normalized second-order correlation $g^{(2)}$ filters out the effect of the fluctuation of intensities presented in two-fold coincidences.

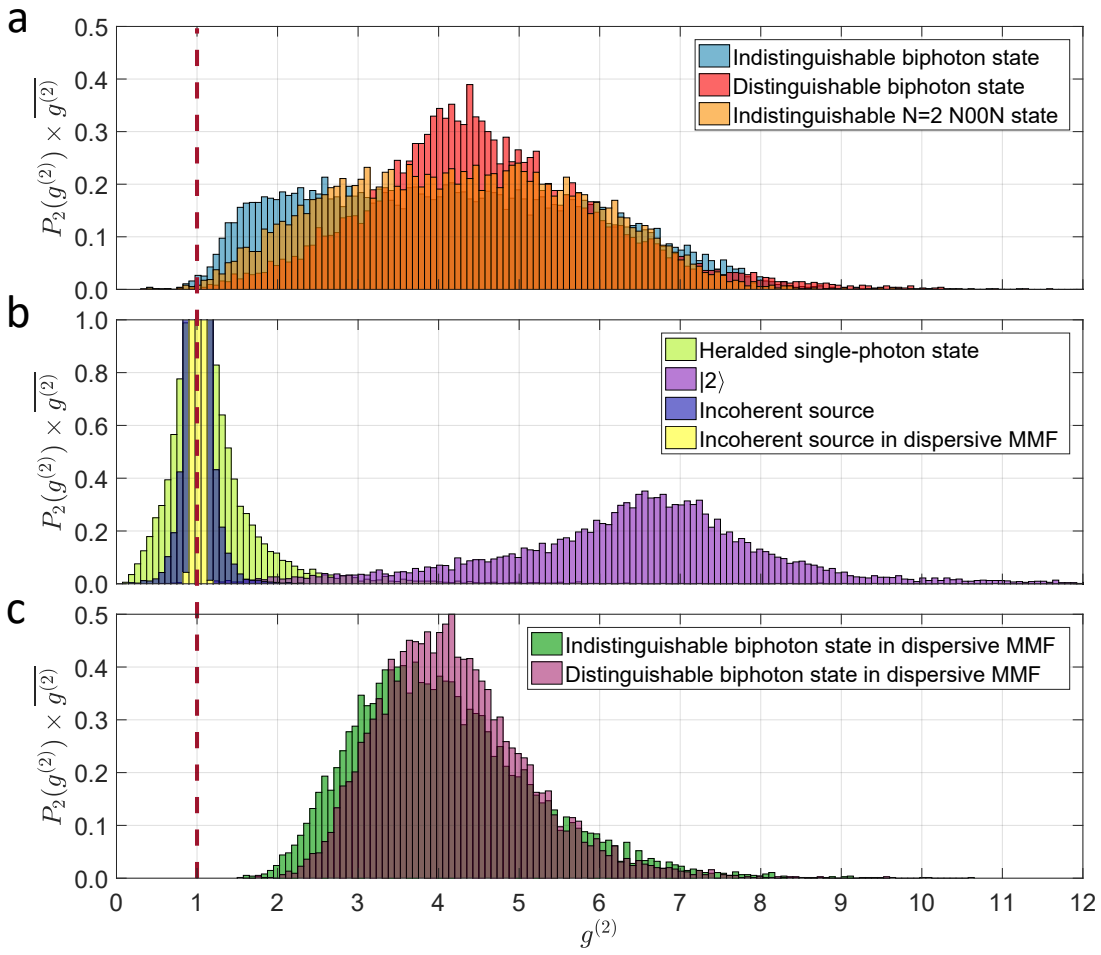


**Figure 4.8 – Probability density functions of normalized second-order correlation** $P_2(g^{(2)})$: (a) Distributions of indistinguishable biphoton state (blue), distinguishable biphoton state (red), and N=2 N00N state (orange) are different owing to the presence of quantum interference. (b) Distributions of heralded single-photon state (light green), incoherent source (dark blue) in a 55-cm long MMF, and incoherent source in a 25-m long MMF (light yellow) have the means at the accidental coincidence (the red dashed line, $g^{(2)} = 1$), while the two-photon Fock state $|2\rangle$ (magenta) has the highest mean of $g^{(2)}$. (c) Indistinguishable (green) and distinguishable (light magenta) biphoton states in dispersive 25-m MMF have different distributions, where the width of the indistinguishable case is wider than that of the distinguishable case. We expect that the contribution originates from quantum interference.

### On the effect of quantum interference

As presented in Fig. 4.8a, in the cases of indistinguishable biphoton state (light blue) and N=2 N00N state (orange), we observe a broader and flatter statistical distribution compared to the distinguishable case. This can be attributed to the effect of two-photon quantum interference that increases the variance of the distributions. Moreover, the variance of the normalized second-order correlation for the N=2 N00N state is lower than that for the indistinguishable biphoton state. We believe that this effect arises from the fact that the N00N state experiences dephasing effects since the N00N state is very sensitive to phase fluctuation that modulates faster than an integration time. Consequently, the second-ordered correlation detects only the root mean square response. To support this, we measure the visibility of normalized second-order correlation: $\mathcal{V}_{g^{(2)}} = \mathrm{Var}\left(g^{(2)}\right)/\overline{g^{(2)}}^2$. Then, we compare the ratio of the measured visibility of $g^{(2)}$ between the indistinguishable biphoton state and the N=2 N00N state as follows:

$$\frac{\mathcal{V}^{\mathrm{Indis}}_{g^{(2)}}}{\mathcal{V}^{\mathrm{N00N}}_{g^{(2)}}} = \frac{0.178}{0.127} = 1.402 \approx \sqrt{2}, \tag{4.11}$$

where $\mathcal{V}^{\mathrm{Indis}}_{g^{(2)}}$ is the visibility of $g^{(2)}$ for the indistinguishable biphoton state and $\mathcal{V}^{\mathrm{N00N}}_{g^{(2)}}$ is that of the N00N state with N=2. The ratio of $\sqrt{2}$ thus corresponds to the root mean square response of the measurement detecting a fast sinusoidal oscillation, which is linked to the oscillation of N00N-state interference (subsection 1.3.2). Accordingly, the statistical property of normalized second-order correlation can distinguish three types of biphoton states and can be used as a probe for the indistinguishability.

We further consider the heralded single-photon state (light green) and two incoherent states, one propagating through 55-cm long MMF (dark blue) and another propagating through 25-m long MMF (light yellow) as presented in Fig. 4.8b. The means of their two-fold coincidences are at the level of accidental coincidences because only classical correlation is present in the classical sources and the single-photon state. Moreover, the two-photon Fock state (magenta) can be distinguished from those classical states and the heralded single-photon state since it has the higher value of $g^{(2)}$. The measured visibilities of normalized second-order correlation of all states are reported in Table F.2.

### On the frequency-entangled biphoton states

As estimated by the visibility of intensity speckles, the number of modes that the frequency-entangled states occupied is approximately $d \approx 14$ (Fig. 4.6b and Table. F.2). This number corresponds to two modes inputs of different polarizations with approximately seven spectral modes for each input. The results infer that the biphoton states experience a dispersion of the fibre. In this situation, two-photon quantum interference of frequency-entangled states presents the dispersion cancellation effect owing to frequency entanglement [Steinberg et al., 1992b, Steinberg et al., 1992a]. The cancellation effect guarantees the robustness of quantum interference and increases the indistinguishability of the biphoton state.

As a result, we observe as shown in Fig. 4.8c that the statistical distribution of $g^{(2)}$ in the case of the indistinguishable biphoton state (green) is broadened, compared to the case of the distinguishable biphoton state (light magenta). The broadening of distribution follows a similar trend as for monochromatic indistinguishable biphoton state observed in

Fig. 4.8a. Accordingly, the $g^{(2)}$ seems to be a good indicator for probing the presence of quantum interference.

Lastly, we compare the measurement of $g^{(2)}/\overline{g^{(2)}}$ with the two-fold coincidences $C/\overline{C}$. We find that the measurements of normalized second-order correlation $g^{(2)}$ is correlated to the measurement of two-fold coincidences only in case of the frequency-entangled states as depicted in Fig. 4.9. The positive correlation between the two indicators hence supports the observation of the deviation presented in the statistical distribution of two-fold coincidences as shown in Fig. 4.7c.

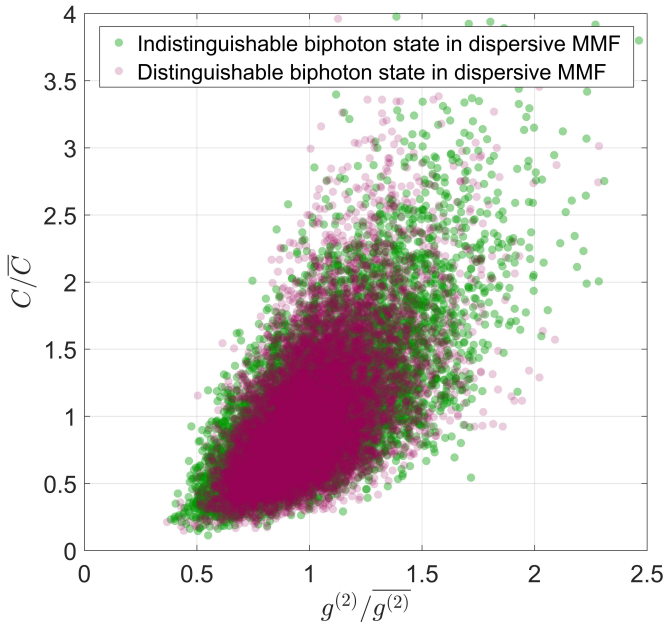


**Figure 4.9 – Correlation of measurements of two-fold coincidences $C/\overline{C}$ and normalized second-order correlation $g^{(2)}/\overline{g^{(2)}}$:** Each circle on the scatter plot displays one measurement of each realization of the optical mixer for indistinguishable biphoton state (green) and distinguishable biphoton state (light magenta).

### 4.3.3 State classification

Thanks to all of the information about a state that we can extract from the statistical properties of intensity speckle $P_1(I)$ and of normalized second-order correlation $P_2(g^{(2)})$, we can further classify an unknown state using both pieces of knowledge about the number of modes $d$ and the indistinguishability of a state. We propose that the visibility of the normalized second-order correlation, $\mathcal{V}_{g^{(2)}} = \mathrm{Var}\left(g^{(2)}\right)/\overline{g^{(2)}}^2$, is a good indicator of the latter. It can be used to obtain information about the degree of indistinguishability of a state, and it is thereby useful for state classification.

In order to classify a state using these statistical features, we further analyse all nine ground-truth states via the two indicators which are the visibility of speckle intensity ($\mathcal{V}_I$) and the visibility of normalized second-order correlation ($\mathcal{V}_{g^{(2)}}$). As shown in Fig. 4.10, each point represents the visibility that is estimated from 200 realizations of the optical mixer randomly sampled from the experimental datasets. The results show that both statistical features are highly independent and can classify a state having a different number of modes and degree of indistinguishably. The technique can also distinguish the indistinguishable (green) from the distinguishable (light magenta) frequency-entangled biphoton states.

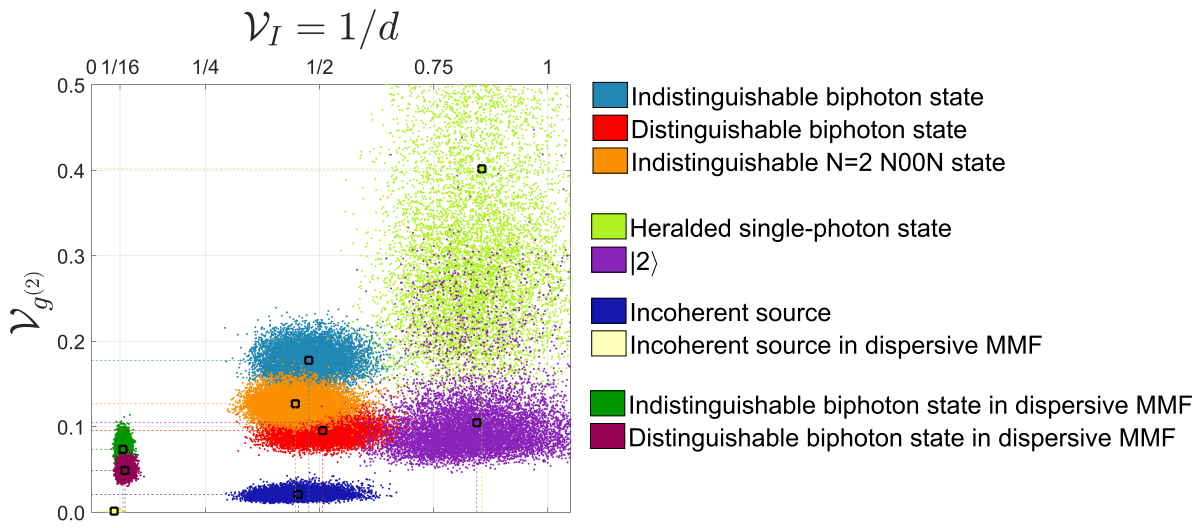


**Figure 4.10 – Feature plane for state classification**: The feature plane are plotted on the plane of the visibility of intensity ($\mathcal{V}_I$) and the visibility of normalised second-order correlation ($\mathcal{V}_{g^{(2)}}$).

## 4.4 | Summary and perspectives

In this chapter, we experimentally demonstrated the use of spatial light modulation in combination with the multimode fibre as a random projector for state classification. The state classifier is based on the statistical properties of generated speckles, both in intensity and in second-order correlations. The purity and dimensionality of arbitrary two-photon density matrix can be estimated using the visibilities of intensity speckle and two-fold coincidences speckle without performing state tomography *a priori*. Furthermore, we analysed the statistical properties of normalized second-order intensity correlation $g^{(2)}$ and experimentally showed that the degree of indistinguishability could be extracted from the visibility of $g^{(2)}$ and thereby provides useful information for further classifying states.

We plan to work on the theoretical prediction of a statistical distribution of normalized second-order intensity correlation. Statistical property of different classes of states such as a large number of single-photon states (boson sampling), high photon-number Fock state, squeezed states, multi-party entangled states are also appealing for further study. Furthermore, it is also interesting to study the statistical properties of higher-order correlations.

Apart from statistical properties considered here thanks to the complex mixing of the MMF, our optical platform does also provide the feature of reprogrammable linear optical network $\mathcal{L}$. Combination of both techniques can be applied to characterize a state further in more adaptive manners. Our perspective is to use a certification protocol to estimate a property of the state, e.g., purity and dimensionality, before doing tomography on the state based on those measured postulations.

# General conclusions and outlook

Complex mixing of modes, at first sight, is useless. Worse, it is usually regarded as a problem in optical communication with multimode fibre. In this dissertation, we have demonstrated, in contrast, the usefulness of mode mixing: an optical mixer, here a multimode fibre, is a useful device that allows us to harness isotropic mixing of information.

We have explored the property of a MMF for designing an alternative architecture of reprogrammable linear optical networks thanks to the use of wavefront control via a spatial light modulator. This optical design is a top-down approach where a reprogrammable small-dimensional photonic circuit is embedded in a high-dimensional transmission matrix of the multimode fibre. The concept of such reprogrammable linear optical networks is related to a general idea of *inverse-photonic design*, where one explores a large space of parameters to design an optical device.

We have experimentally demonstrated the programmability of the optical platform through control two-photon interferences in various interferometers across path-polarization degrees of freedom. The results of two-photon interference are used in the certification task of indistinguishability based on the zero-transmission law [Tichy et al., 2010]. High values of measured two-photon visibility, low loss close to the theoretical limit, and high fidelity of implemented optical networks demonstrate the reliability of the platform, which paves a route towards several quantum applications. The scalability of programmable optical networks is key. Fidelity of implemented large optical networks can be kept constant as the dimension of an optical mixer and the degree of wavefront control are linearly scaled together with the dimension of optical networks. Our platform, therefore, provides an efficient alternative to integrated circuits for quantum information processing.

Owing to the capability to implement arbitrary linear transformation, we have explored our programmable optical networks to study a non-unitary evolution of a biphoton state. In chapter 2, we observed two-photon interference with photon anti-coalescence in all input-output combinations. We further studied related phenomena in chapter 3, where non-linearity of two-photon absorption on a lossy beamsplitter and the simulation of coherent absorption effect have been demonstrated. We showed the control of lossy beamsplitters and therefore, the manipulation of the probability of two-photon survival. We anticipate these results pave an alternative route to implement quantum information processing protocols.

In addition to the requirement of random unitary linear networks to benchmark the computational complexity of the boson sampling problem, a complex mixing itself is also useful in many computational tasks [Mahoney, 2010, Collins and Nechita, 2016]. Speckles of high-order correlations, e.g., an outcome probability of the boson sampling problem, speckle of a high-dimensional entangled state, are of great interest for our understanding of quantum interference phenomenon. We explored how our optical mixer, a combination of SLM and MMF, can be exploited for studying statistical properties of nonclassical speckles that can be generated from various states of light. Part of the information about

an unknown input state can be extracted from statistical properties of speckles, e.g., state purity, dimensionality, and indistinguishability. We experimentally demonstrated the measurement of those parameters. Furthermore, we showed that the first two statistical moments of normalized second-order correlation, i.e., the visibility, can be used to extract the degree of indistinguishability. Together, all indicators of indistinguishability, dimensionality, and purity can be applied to further classify unknown input states. This includes the ability to measure the degree of indistinguishability of frequency-entangled states. Their statistical feature survives disordered-ensemble average and the effect of dispersion in a long fibre.

In conclusion, we have experimentally demonstrated the use of complex mixing of optical modes for quantum information processing in two particular ways: (1) reprogrammable linear optical networks and (2) speckle-based measurement (random projection) for state classification. We anticipate that the experimental results presented in the dissertation will ease the concerns about optical losses and complexity in wavefront control of high dimension which are typically considered to be the main drawback in quantum optics experiments. Therefore, it paves the way for further studies in many aspects, especially as a new optical platform for modern quantum optical experiments and photonic quantum information processing.

Our outlook for further investigations and technological developments are as follows:

- **Towards a large array of coincidence detection**: As shown in subsection 2.4.4, we have classically demonstrated the scalability of optical networks. A detector array of coincidence counts, e.g., single-photon avalanche diode (SPAD) array [Bruschini et al., 2019], intensified charge-coupled device (ICCD) [Peřina et al., 2012, Fickler et al., 2013], or electron multiplying charge-coupled device (EMCCD) [Reichert et al., 2018, Defienne et al., 2018b] will effectively allow us using the optical platform for implementing an optical network of higher dimension. Alternatively, photonic lanterns [Leon-Saval et al., 2010, Velázquez-Benítez et al., 2018] can also be used for coupling outputs to many single-photon detectors with high detection efficiency. We note that we tested the detection of HOM interference on the EMCCD camera. Currently, we are in the process of installing a SPAD array on the setup. Technological developments towards this direction are ongoing.

- **Towards control of more photonic degrees of freedom**: Wavefront control of light transports through a multimode fibre has classically demonstrated for beam engineering [Čižmár and Dholakia, 2012, Plöschner et al., 2015a] and pulse transportation [Morales-Delgado et al., 2015a, Xiong et al., 2019, Mounaix and Carpenter, 2019]. It is fundamentally interesting to understand quantum transports in traverse spatial degree of freedom and temporal-spectral degree of freedom. This know-how can be applied not only to implement optical networks on those photonic degrees of freedom but also to unscramble light for applications in optical quantum communications.

- **Boson sampling problem with multimode fibre**: Multimode fibres provide not only a large-dimension (a few hundreds to thousand) of mode mixing but also a lossless platform for boson sampling problem. The experimental challenge is the integration of many single-photon sources and detectors on the platform.

- **Entanglement as a resource**: High-dimensional and many-body entangled states are of great interests in fundamental physics and for applications in quantum in-

formation, communication, and computing. Generation and manipulation of those states on our platform are naturally easy and very promising.

- **Generalized programmable inverse photonic designs**: *Inverse photonic design* [Molesky et al., 2018] nowadays exploits large optical parameters to implement a specific intended optical element. Generalized optimal design of programmable optical networks is an interesting research question to be considered.
- **Adaptive quantum algorithm**: Implementation of many quantum algorithms will become possible as the scalability of a platform grows (including sources, optical network, and detectors). The goal is to demonstrate hybrid quantum-classical algorithms, e.g., quantum simulations, optimization and classification problems. One of the interesting aspects is to theoretically study and experimentally perform a randomized-based algorithm [Mahoney, 2010] in the quantum domain. An interesting perspective could be the demonstration of a noisy intermediate-scale quantum computer (NISQ) in the near future.

# Appendices

# A

# Experimental details of SPDC source

The frequency-degenerate photon pairs are generated from a type-II spontaneous parametric down-conversion (SPDC) source (Fig. A.1), using the periodically polled potassium titanyl phosphate crystal (ppKTP, Raicol Crystal) with the thermoelectric control (TEC) [Emanueli and Arie, 2003]. The dimension of crystal is $1 \times 2 \times 9.1$ mm$^3$ and its periodicity is of 10 $\mu$m. There are two pump lasers which can be selected to pump the ppKTP crystal on the optical setup. The first is the 40-mW single-longitudinal mode laser (DLproHP, Toptica). The second is the external-cavity didode laser with home-made grating-stabilization in the Littrow's configuration. The second laser has multiple-longitudinal modes. One of the blue lasers is used to pump the crystal in a configuration that generates a single spatial-mode photon pairs [Ljunggren and Tengner, 2005, Van Exter et al., 2006, Fedrizzi et al., 2007, Bennink, 2010, Grice et al., 2011, Da Cunha Pereira et al., 2013, Dixon et al., 2014]. The remaining laser light is blocked by a longpass filter (BLP01-664R, Semrock) and 10-nm bandpass spectral filter (FBH810-10, Thorlab). The photon pairs are separated by a polarizing beamsplitter (PBS). The indistinguishability of photon pairs is controlled by a temporal delay $\delta$. The photon pairs are then prepared in the same horizontal polarization, and collected with polarization-maintaining single-mode fibres (P1-780PMAR-2, Thorlab), which are then connected to the experimental platform. The indistinguishability of the photon-pair is characterized using a fibre-based beamsplitter (OZ Optics). The single photon counting module (SPCM-AQ4C, Excelitas) and the coincidence logic circuit (Spartan®-6 FPGA, Xilinx) are used for the detection of photoncounts and coincidences. A coincidence window is set at 2.5 ns.

In the case of pumping with the DLproHP laser, the collection of two-fold coincidence counts $C$ of our SPDC source is $C \sim 5 \times 10^5$ pair/s and the best biphoton coupling efficiency that we have achieved is $\eta = C/\sqrt{I_H I_V} \sim 0.2$, where $I_i$ is a photoncount. The visibility of the two-photon interference of the source is $0.95 \pm 0.03$ with a correction for an unbalanced beam splitter and the expected accidental coincidences (Fig. A.2). All experimental results reported in this dissertation uses the DLproHP laser for pumping.

In the case of pumping with the multiple-longitudinal mode laser, we observed the degradation of two-photon visibility. A similar result was reported in [Lee et al., 2015].

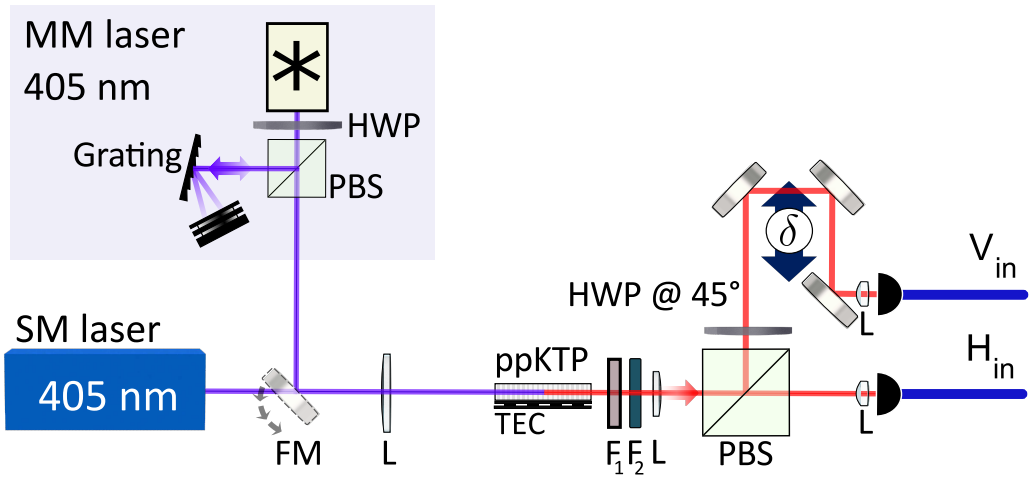


**Figure A.1 – Spontaneous parametric down-conversion source (SPDC)**: Two lasers, which are multiple-longitudinal mode laser (MM) and single-longitudinal mode (SM), can be selected to pump the ppKTP non-linear crystal. The MM laser is locked with the Littrow's configuration. The temperature of the crystal is controlled with the thermo-electric control (TEC) to generate frequency-degenerate photon pairs (approximately 30°C to 33°C depending on a central wavelength of the pump laser). L: lenses, $F_1$: longpass spectral filter (BLP01-664R, Semrock), $F_2$: bandpass spectral filter (FBH810-10, Thorlab), HWP: half-wave plate, PBS: polarizing beamsplitter, FM: flip mirror.

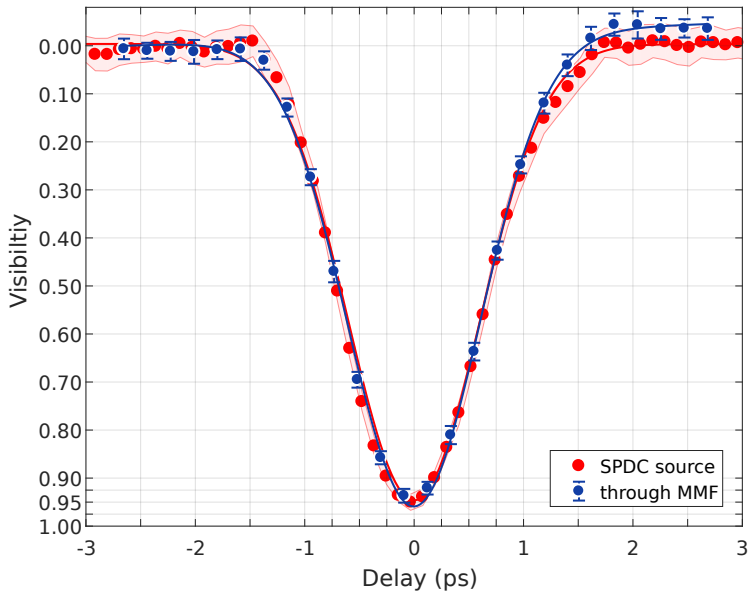


**Figure A.2 – Hong-Ou-Mandel interference**: The SPDC source is pumped with the single-longitudinal mode laser. (red circles) HOM interference of the SPDC source is measured with the fibre-based beamsplitter. (blue circles) HOM interference of the SPDC source is measured after propagating through the programmed linear optical networks with the 55-cm multimode fibre. The results in the case of propagating through the multimode fibre is obtained from all HOM dip cases in Figure 2.16.

# B | Mode mixing of multimode fibre

## B.1 | Modes of graded-index multimode fibres

Graded-index multimode fibre (MMF) is a cylindrical waveguide which has the refractive index profile described by

$$n_1^2(r) = n_1^2\left(1 - \frac{r^2}{b^2}\right), \tag{B.1}$$

where $r$ is radial coordinate defined from the optical axis ($r = 0$) of the fibre to the cladding ($r = D/2$), $n_1$ is the maximum refractive index on the optical axis, and $b = D/\sqrt{(8\Delta)}$ is a scaling parameter; $\Delta = (n_1^2 - n_0^2)/(2n_1^2)$ is known as the refractive index contrast where $n_0$ is the refractive index of cladding. The refractive index profile are displayed in Fig. B.1. The discontinuity of the refractive index at the cladding affects very high-order propagating modes. Considering scalar Helmholtz equation on the cylindrical coordinates $(r, \varphi, z)$ for a straight graded-index waveguide on the $z$ axis, we obtain a scalar mode basis [Snitzer, 1961, Snyder and Love, 1984],

$$\psi_{l,m}(r,\varphi,z) = \sqrt{\frac{\alpha}{2\pi}\frac{2m!}{(m+|l|)!}}\exp\left(-\frac{\alpha r^2}{2}\right) \times \left(\alpha r^2\right)^{|l|/2} L_m^{|l|}\left(\alpha r^2\right) e^{il\varphi} e^{i\beta_{lm}z}, \tag{B.2}$$

where $L_m^{|l|}$ is the associated Laguerre polynomials with $m$ index of radial modes ($m \in \mathbb{N}_0$) and $l$ index of orbital angular momentum ($l \in \mathbb{Z}$), $\alpha = kn_1/b$, and $k = 2\pi/\lambda$ is the wavenumber with wavelength $\lambda$. The propagation constants for each mode $(l, m)$ reads,

$$\beta_{l,m} = \sqrt{k^2 n_1^2 - 2\alpha(|l| + 2m + 1)}. \tag{B.3}$$

Considering the Helmholtz equation under the weak guidance approximation: $\Delta \approx (n_1 - n_0)/n_1$ and $\Delta \to 0$, the propagation constants can be written as

$$\beta_{l,m} \approx kn_1 - \frac{|l| + 2m + 1}{b}. \tag{B.4}$$

The mode basis is defined on the spatial transverse modes known as linear polarized (LP) modes. The polarizations of propagation modes are degenerated. The number of propagating modes $n$ can be approximately determined by the V parameter as follow,

$$n = \frac{V^2}{4}, \tag{B.5}$$

where $V = \frac{kD}{2}\sqrt{n_1^2 - n_0^2} = \frac{kD}{2}\mathrm{NA}$ with the numerical aperture NA. The basis set of propagating modes of MMF is depicted in Fig. B.1.

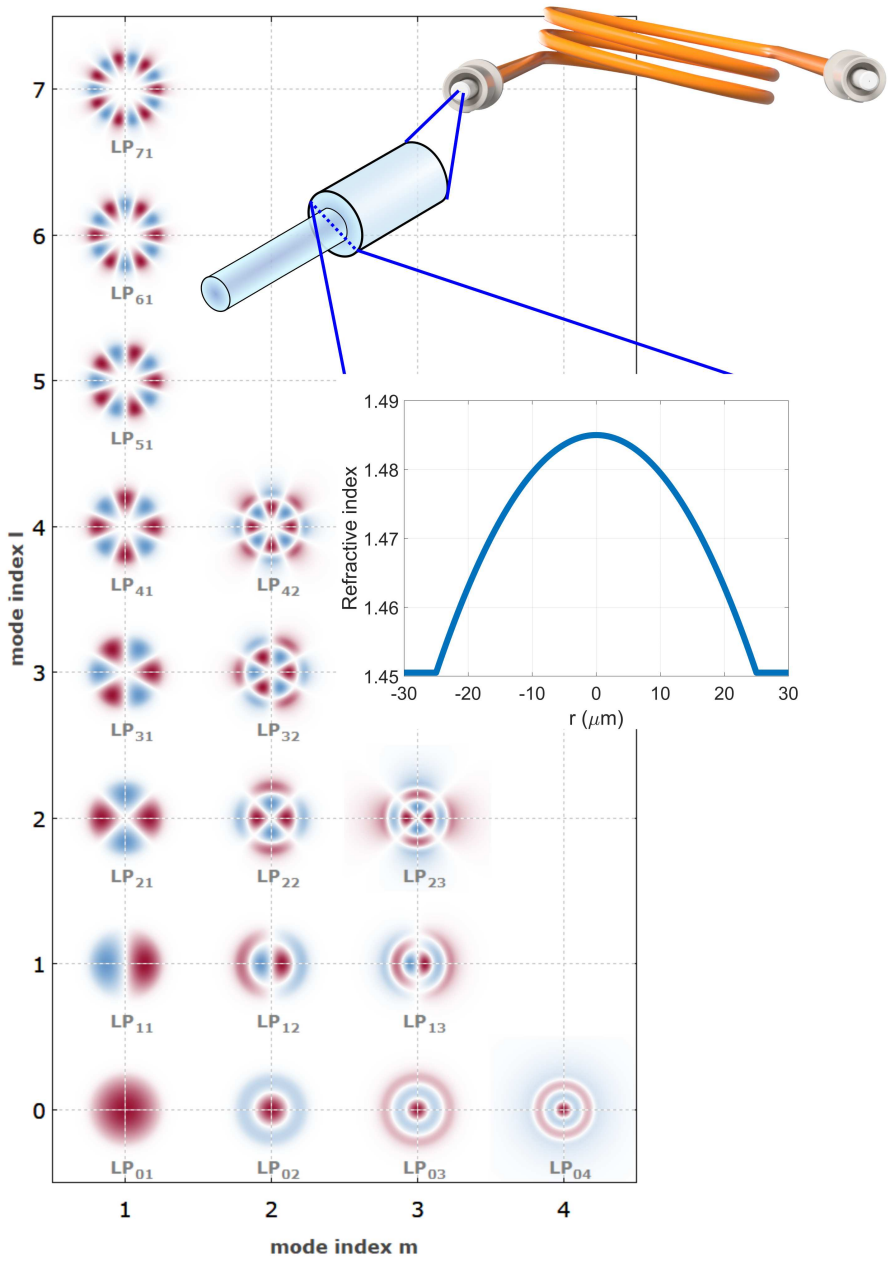


**Figure B.1 – Multimode fibre and its linear polarized (LP) mode basis**: The LP mode basis is adapted from https://www.rp-photonics.com/multimode_fibers.html

## B.2 | On transmission matrix of multimode fibres

D. E. B Flaes and co-workers have recently shown that the multimode fibre used here (Thorlabs, GIF50C) has a refractive index profile that deviates from a perfect parabola, thus presenting mode coupling between propagation-invariant modes [Boonzajer Flaes et al., 2018]. As a consequence, the speckle appearing after propagation along the MMF results both from the phase delays between modes of the fibre and from the mode coupling due to imperfections of the refractive index profile along the propagation axis. The TM of the MMF, which describes a linear relation between input and output fields of the MMF, is thus expected to comprise significant mixing across modes, irrespective of the basis being used. This implies that any targeted output mode can be excited by injecting combinations of many spatial and polarization input modes. An outcome optical field is also expected to produce a fully developed speckle. We provide the statistical distribution of phase obtained from elements of the measured TM as shown in Fig. B.2. The result is consistent with the distribution in Eq. 2.3.

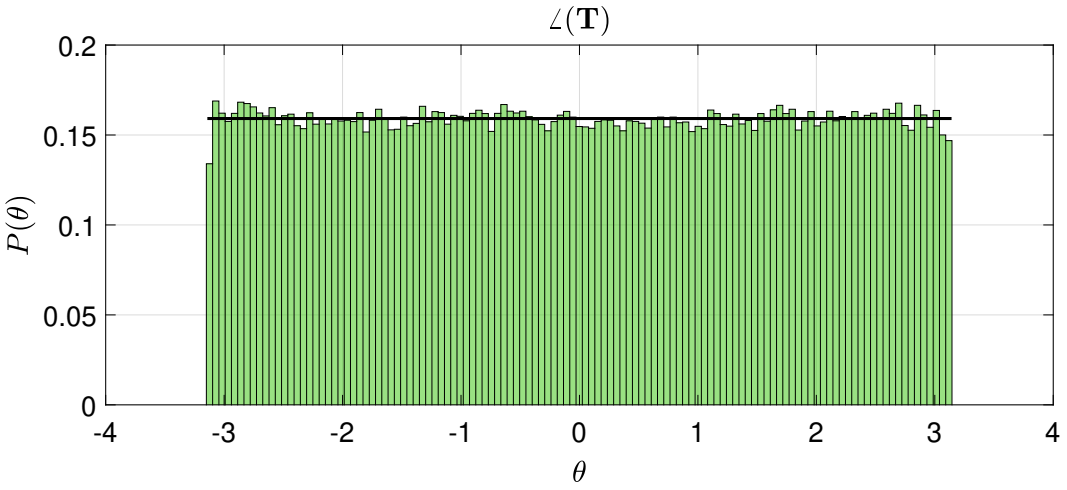


**Figure B.2** – Probability density function of the phase $\theta$: The result is obtained from the measured TM of the 55-cm MMF and is consistent with Eq. 2.3.

To further show the mixing property of the MMF, we experimentally study the probability distribution of transmission eigenvalues $\tau$ of measured transmission matrix $\mathbf{T}$. The transmission eigenvalues $\tau$ are extracted by means of a singular value decomposition of $\mathbf{T}^{\dagger}\mathbf{T}$ [Popoff et al., 2011]. First, to show the polarization mixing, we study the probability distribution of transmission eigenvalues $\tau$ for the part of the full measured transmission matrix $\mathbf{T}$ corresponding to each input-output polarization channel ($\mathrm{H_{out}H_{in}}$, $\mathrm{H_{out}V_{in}}$, $\mathrm{V_{out}H_{in}}$, $\mathrm{V_{out}V_{in}}$). We observe a similar distribution for all polarization pairs (Fig. B.3a). Second, the overall experimental probability distribution of transmission eigenvalues $\tau$ has been investigated (Fig. B.3b). To the best of our knowledge, there are only a few theoretical models proposed to explain a multimode fibre under a mode coupling [Ho and Kahn, 2011b, Chiarawongse et al., 2018, Li et al., 2019b]. We have found our experimental distribution of transmission eigenvalues can potentially be described by a model based on a random-matrix theory recently proposed in [Chiarawongse et al., 2018]. The model takes the mode-dependent loss into account and is based on the free probability theory and the Filtered Random Matrix ensemble [Goetschy and Stone, 2013].

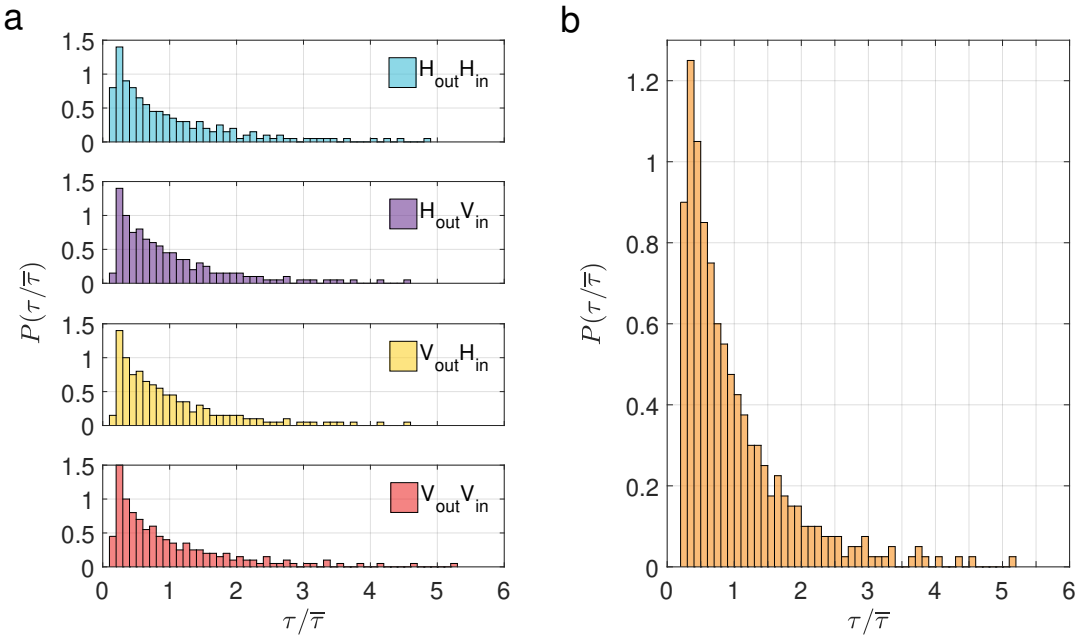


**Figure B.3** – (a) Probability distribution of transmission eigenvalues $p(\tau/\overline{\tau})$ for each polarization channel ($H_{out}H_{in}$, $H_{out}V_{in}$, $V_{out}H_{in}$, $V_{out}V_{in}$) (b) Probability distribution of overall transmission eigenvalues $p(\tau/\overline{\tau})$.

The complex mixing property of our fibre is also verified by checking that it is possible to focus light on any spatial and polarization state of the output plane (within the fibre core) with high efficiency, while keeping a low unstructured background (data not shown). We note that we will experience a negligible loss in transmission through the multimode fibre only when we couple light to high-order propagation modes where the corresponding optical field is close to the cladding of the fibre.

# C | Correlations of speckle patterns

## C.1 | Bimodal distribution

In this section, we introduce the experimental observations related to the bimodal distribution of transmission eigenvalues introduced in Sec. 2.1.1.

In optics, one year after the first achievement on a control light transport through a diffusive medium [Vellekoop and Mosk, 2007] (see Sec. 2.1.3 for the introduction of controlling light transport through complex medium), Ivo Vellekoop and Allard Mosk experimentally demonstrated the redistribution of the input flux to open channels of a diffusive slab, as shown in Fig. C.1a, resulting in an increase of the total transmission by means of maximizing the intensity on one targeted speckle grain, noted as $j_0$ [Vellekoop and Mosk, 2008]. The result infers that the achievement of perfect control of the input state $\Psi_{\text{in}}^{+}|_i = t_{j_0 i}^{*}, \forall i = 1, \ldots, n$ will provide the universal enhancement of total transmission of $2/3$ averaged over the target speckle. The value of $2/3$ is directly related to the decrease in electronic shot noise as predicted by the DMPK model [Beenakker, 2018, Rotter and Gigan, 2017] with the same underlying contribution from the bimodal distribution. The enhanced total transmission in optics comes from a higher probability of transporting light through open channels.

The probability of transporting light is proportional to $\tau^2$. While the fluctuation in the total transmitted current of electrons (fermionic fields) follows the binomial statistics: $\int_0^1 P(\tau)\tau(1-\tau)d\tau$. The second term of the latter, which corresponds to the reduction from the shot noise, is also proportional to $\tau^2$. Thus both effects identically result from the contribution of open channels. In other words, the maximally-transmitted intensity pattern as shown in Fig. C.1a (orange line) is promoted predominantly from open channels.

The experimental result in Fig. C.1a also implies the requirement of a complete and perfect wavefront control of all $n$ input modes of a disordered slab. The number of controlled modes can grow up from $\sim 10^4$ in [Vellekoop and Mosk, 2008] to $10^6$ and more easily for a thick medium. Several experiments have been later demonstrated on mastering the control and study of the effect of open channels on transmission properties in different aspects [Choi et al., 2011, Kim et al., 2013, Sarma et al., 2016]. For instance, by optimizing the total transmission through a diffusive medium directly (Fig. C.1b), both enhancement and suppression of the total transmission were achieved [Popoff et al., 2014] indicating the ability to modulate the total transmission. While optimizing, the modulation of total reflection was also monitored. The result demonstrates the anti-correlation between total transmission and total reflection because of the conservation of total flux. In a case of measuring partial square TM, the maximum transmission eigenvalue of the MP distribution (the value of 4 in Fig. 2.2) was measured by sending the corresponding eigenstate to the system [Kim et al., 2012]. Towards acquiring a complete

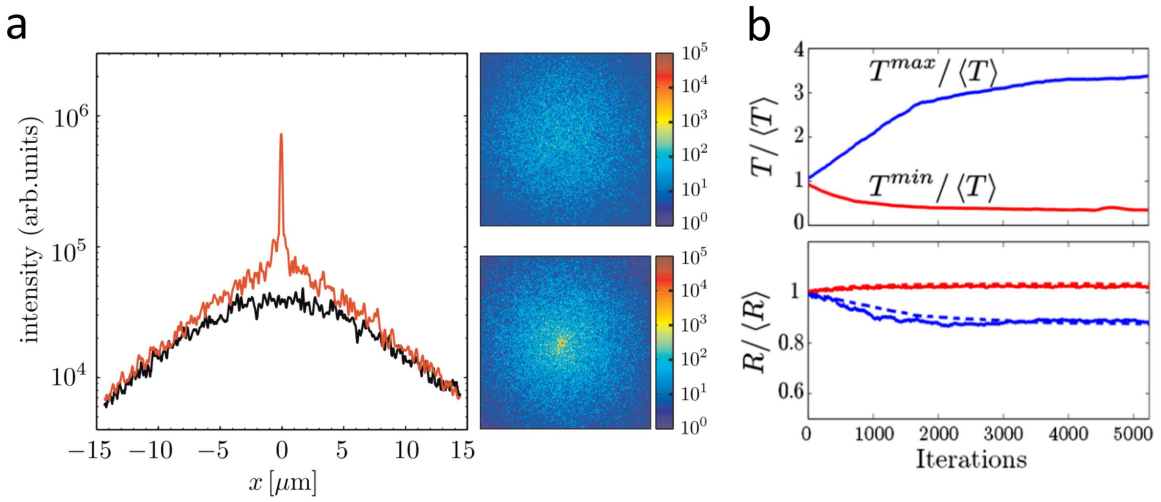


**Figure C.1 – Modulation of total transmissions**: (a) Right panel: Speckle behind a diffusive slab generated from a random incident wavefront (top) and generated from the optimized wavefront (bottom). The intensity at the targeted speckle is a factor $746\pm28$ enhanced from the background. Left panel: Intensity profile, integrated over y-direction: The optimized wavefront (red) has a peak and the random wavefront (black) lacks the peak. Adapted from [Beenakker, 2018] (b) Optimization of total transmissions: Measured transmission (top panel) and reflection (bottom panel) as function of the step number of optimization (Iterations). The maximization (blue) and minimization (red) of total transmission. Adapted from [Popoff et al., 2014].

TM, the violation from MP distribution have been reported and modelled [Yu et al., 2013, Akbulut et al., 2016b]. The observation of the bimodal distribution in optics has not been reported so far.

## C.2 | Correlations of speckle patterns

In addition to the bimodal distribution of transmission eigenvalues and its influence on the transmission properties, correlations can also be presented in speckle patterns. In particular, we want to focus on correlations between a transmission coefficient $T_{ij} = |t_{ij}|^2$ from $j$ input to $i$ output and that of another $i'$-to-$j'$ trajectory. Our goal is to introduce an overview of these correlations since they may have an influence on our programmable optical network. Let us consider a diffusive slab of the length $L$ as a model of scattering object, before discussing the model of diffusive waveguide and a multimode fibre later on. The input and output spaces of wave fields are defined on continuous angular variables described by a direction of $i$ and $j$ beams (plane waves) scattering from the slab[1]. The angular correlation function is expressed as

$$\mathsf{C}_{iji'j'} = \frac{\overline{\delta T_{ij}\delta T_{i'j'}}}{\overline{T_{ij}}\;\overline{T_{i'j'}}}, \tag{C.1}$$

[1]Note that the concept of correlation function can also be applied to describe correlations in time-frequency or other photonic degrees of freedom.

where $\delta T_{ij} = T_{ij} - \overline{T_{ij}}$, and $\bar{\cdot}$ is the average over disorder realizations[2]. An efficient way to determine the correlations is by means of so-called diagrammatic technique [Lee and Stone, 1985, Feng et al., 1988, Berkovits and Feng, 1994, van Rossum and Nieuwenhuizen, 1998, Dragoman and Dragoman, 2004, Montambaux, 2007, Akkermans and Montambaux, 2007]. It considers all possible paths $\mathcal{C}$ with a corresponding complex amplitude $E_{\mathcal{C}}$ linking a field from $i$ to $j$. Then, the correlation term $\overline{\delta T_{ij}\delta T_{i'j'}}$ involves a coherent sum over possibilities of products of four complex amplitudes of the propagating paths along $\mathcal{C}_1, \mathcal{C}_2, \mathcal{C}_3, \mathcal{C}_4$ as shown in Fig. C.2a. It can be expressed as

$$\sum_{\mathcal{C}_1,\mathcal{C}_2,\mathcal{C}_3,\mathcal{C}_4} \overline{E^{ij}_{\mathcal{C}_1} E^{*ij}_{\mathcal{C}_2} E^{i'j'}_{\mathcal{C}_3} E^{*i'j'}_{\mathcal{C}_4}}, \tag{C.2}$$

By keeping for all non-vanishing contributions to the correlation function, three main contributions in the diagrammatic expansion can be extracted [Feng et al., 1988],

$$\mathsf{C}_{iji'j'} = \mathsf{C}^{(1)}_{iji'j'} + \mathsf{C}^{(2)}_{iji'j'} + \mathsf{C}^{(3)}_{iji'j'} + \dots. \tag{C.3}$$

As presented in Fig. C.2b, the first term $\mathsf{C}^{(1)}$ involves two contributions, known as Diffusions[3], which are $\mathcal{C}_1 = \mathcal{C}_4$ and $\mathcal{C}_3 = \mathcal{C}_2$. They do not cross while propagating through the medium. The probability of crossing of two Diffusions, known as Hikami box [Akkermans and Montambaux, 2007][4], is typically proportional to $1/g$, where $g$ is the dimensionless conductance. Normally, $g$ is high, therefore, the contributions of $\mathsf{C}^{(2)} \propto 1/g$ and $\mathsf{C}^{(3)} \propto 1/g^2$, which have one and two crossing, respectively, are very small. We now discuss the correlations term by term.

### C.2.1 $\mathsf{C}^{(1)}$ correlation

$\mathsf{C}^{(1)}$ is known as the short-range correlation and results mainly in two effects. Firstly, for $i = i'$ and $j = j'$, this results in the size of speckle grain as depicted in Fig. 2.1a; it is known as the Rayleigh law: $\overline{\delta T_{ij}^2} = \overline{T_{ij}}^2$ which corresponds to the probability distribution of the intensity in Eq. 2.3c. Secondly, $\mathsf{C}^{(1)}_{iji'j'}$ predicts that a small change of property, traditionally a transverse momentum $q$, of an incoming mode from $j$ to $j'$ leads to the same change of the outgoing field: $\Delta q = q_i - q'_i = q_j - q'_j$. This is known as a *memory effect* [Feng et al., 1988, Freund et al., 1988]: by changing the direction of the incoming beam, the whole speckle pattern in all output modes is moved by the same amount. This effect is obvious in a situation with a single-scattering object where a large angular change of the incoming beam is possible. In the diffusive regime, the critical angle is of the order of $\Delta\theta \lesssim \lambda/(4L)$, where $\lambda$ is a wavelength [Feng et al., 1988]. This effect has been applied in many imaging techniques [Freund, 1990, Vellekoop and Aegerter, 2010, Bertolotti et al., 2012, Katz et al., 2014]. Especially for biological tissues which have a strong forward scattering, the angular memory effect range may be extended by more than an order of magnitude compared to the case of isotropic scattering [Schott et al., 2015]. The

[2]The ergodicity of a random process infers that the average over different realizations can be interchangeable with the average over an entire system at one specific setting.

[3]Diffusion is referred to the interference contribution from a pair having an identical path [Akkermans and Montambaux, 2007].

[4]The crossing (Hikami box) is referred to a possibility to permutes complex amplitudes of paths resulting in a new pairing of paths [Akkermans and Montambaux, 2007].

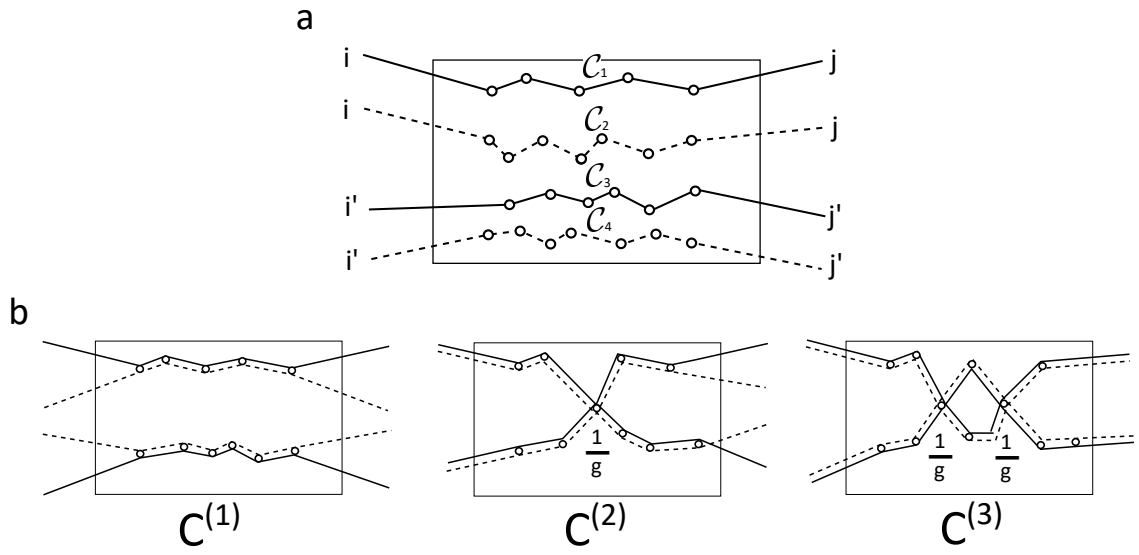


**Figure C.2 – Correlations of speckle patterns**: (a) Schematic representation of the product of four complex amplitudes of the propagating paths $\mathcal{C}$, represented by line and dashed line for amplitudes $E$ and complex conjugate of amplitudes $E^*$, respectively. (b) The contributions of each correlation term: $\mathsf{C}^{(1)}$ results in short-range speckle fluctuations (left panel), $\mathsf{C}^{(2)}$ results in long-range correlation (middle panel), and $\mathsf{C}^{(3)}$ results in universal conductance fluctuations (right panel).

complementary shift-to-shift memory effect [Judkewitz et al., 2015] and the generalized version on both angular and transitional memory effect [Osnabrugge et al., 2017] may also be present due to a high directionality of the scattered light. Light transmitted through open channels of a wide diffusive slab also shows a preservation of directionality [Yılmaz et al., 2019b]. Consequently, this increases the angular memory-effect range [Yılmaz et al., 2019a].

### C.2.2 $\mathsf{C}^{(2)}$ correlation

$\mathsf{C}^{(2)}$ involves one crossing leading to long-range correlations which is unique to the diffusive regime. The correlation is written as

$$\mathsf{C}^{(2)}_{iji'j'} = \frac{1}{g}\left[F_2(\Delta q_i L) + F_2(\Delta q_j L)\right], \quad F_2(x) = \frac{1}{\sinh^2 x}\left(\frac{\sinh 2x}{2x} - 1\right), \tag{C.4}$$

where $\Delta q_i = q_i - q_i'$ and $\Delta q_j = q_j - q_j'$ and $q$ is the transverse momentum of the light beams [Akkermans and Montambaux, 2007]. The contributions of $\mathsf{C}^{(2)}$ have a smaller effect $\propto 1/g$ and decreases algebraically with $F_2$ function and only vanishes if both $\Delta q$ of input and output are large. In general, the long-range contribution $\mathsf{C}^{(2)}$ is related to the violation from the Marčhenko-Pastur distribution, such as the presence of the bimodal distribution. It can be used to control of energy flux flowing through a diffusive slab onto a large targeted area [Popoff et al., 2014, Ojambati et al., 2016, Hsu et al., 2017, Yılmaz et al., 2019b]. For example, as shown in Fig. C.1a, the maximally-transmitted intensity pattern presents the enhancement largely surrounding the targeted focus which is the signature of the long-range correlation [Vellekoop and Mosk, 2008]. Furthermore, the long-range anti-correlation has been also presented between reflected and transmitted

speckle patterns [Fayard et al., 2015, Fayard et al., 2017, Starshynov et al., 2018] and has been applied recently to obtain an image of an object hidden behind a diffusive slab by using only the reflected light [Paniagua-Diaz et al., 2019b].

### C.2.3 $\mathsf{C}^{(3)}$ correlation

$\mathsf{C}^{(3)}$ is known as an infinite-range correlation and presents a universal contribution to the total correlation: $\mathsf{C}^{(3)} = 2/(15g^2)$, which is independent of the mean free path, and the geometry of scattering object in the diffusive regime [Akkermans and Montambaux, 2007]. The contribution physically leads to the universal conductance fluctuations[5] in the electron transport [Lee and Stone, 1985]. The $\mathsf{C}^{(3)}$ has also been observed in optics [Scheffold and Maret, 1998].

For the model of disordered waveguide, the transverse momentum $q$ are quantized into transverse modes. The correlation function: $\mathsf{C} = \mathsf{C}^{(1)} + \mathsf{C}^{(2)} + \mathsf{C}^{(3)}$ becomes [Mello et al., 1988b, Mello and Stone, 1991],

$$\mathsf{C}_{iji'j'} = \delta_{ii'}\delta_{jj'} + \frac{2}{3g}(\delta_{ii'} + \delta_{jj'}) + \frac{2}{15g^2}, \tag{C.5}$$

which presents the same structure as found by [Feng et al., 1988]. The first term expresses again the Rayleigh law governing the Gaussian statistics approximation which indicates uncorrelated modes. Whereas, the second term describes correlations between modes and is used to explain the universal value of 2/3 for enhancing of the averaged total transmission due to the presence of open channels [Beenakker, 2018]. The last term shows uniform correlation and is responsible for universal conductance fluctuations. Note that $\mathsf{C}^{(2)}$ and $\mathsf{C}^{(3)}$ presented above are only valid in the diffusive regime, the evolution of $\mathsf{C}^{(2)}$ and $\mathsf{C}^{(3)}$ from the ballistic to the diffusive regime was predicted by the DMPK model [García-Martín et al., 2002].

### C.2.4 Weak correlations

We now consider the correlations existing owing to the presence of reciprocity (time-reversal symmetry) using the circular orthogonal ensemble ($\beta = 1$)[6]. The DMPK model is subject to the correction term presented in Eq. C.6 leading to the reduction of the transmission averaged over different realizations of disordered configuration [Akkermans and Montambaux, 2007] as follows:

$$\begin{aligned} \overline{T} = \overline{\mathbf{T}^\dagger \mathbf{T}} &= \frac{n\ell^\star}{L} + \frac{\beta - 2}{3\beta} + O(1/n) \approx g, \\ \mathrm{Var}(T) &= \frac{2}{15\beta} + O(1/n). \end{aligned} \tag{C.6}$$

Moreover, one can notice that the conductance fluctuation $\mathrm{Var}(T)$ equals to $g^2\mathsf{C}^{(3)}$. This is decreased two-fold when the time-reversal symmetry is broken. The correction term is known as *weak localisation* because it corresponds to the reduction of the total transmission from the prediction of Ohm's law. Weak localisation is named as a relative effect

[5] The variance of the conductance $G = \sum_{ij} T_{ij}$ has a universal value $\mathrm{Var}(G) = g^2\mathsf{C}^{(3)} = 2/15$ [Lee and Stone, 1985]

[6] The circular unitary ensemble considered in Equation 2.5 has $\beta = 2$.

by reference to Anderson strong localisation. Owing to the conservation of energy, the weak localisation also contributes to the enhancement of energy in the reflection, i.e, coherent enhanced backscattering effect [Akkermans and Maynard, 1985, Akkermans et al., 1986] which can be observed both in electronics and optics [Akkermans and Montambaux, 2007]. In the diagrammatic approach, the correlation can be interpreted as the presence of time-reversed path pairs that always interfere constructively [Hastings et al., 1994].

## C.3 | Correlations in multimode fibres

In a multimode fibre, memory effects were also demonstrated in radial and azimuthal degrees of freedom in analogy to the angular memory effect discussed previously in subsection C.2.1. For the azimuthal degree, it has been shown that rotating an input state around the propagation axis of the optical fibre also leads to a rotation of an output pattern with the same amount of rotation [Amitonova et al., 2015, Rosen et al., 2015]. Owing to the cylindrical symmetry of the fibre, the rotational range of the memory effects is theoretically a full circle and the experimental results reported a maximum value of 100° for the 12-cm long step-index fibre (Thorlabs, FG050UGA) [Amitonova et al., 2015] and $\sim 10°$ for the 15-cm long bent graded-index fibre (Thorlabs, GIF50C) [Rosen et al., 2015]. The limitation is attributed to small imperfections in the fibre core geometry, small amounts of fibre bending or scattering from inhomogeneities and the imperfect control of an input [Amitonova et al., 2015].

For the radical modes, the memory effect was demonstrated indirectly [Čižmár and Dholakia, 2012]. As discussed in subsection 2.1.2, a multimode fibre presents strong mixing only in the mode group within the same radial mode index $m$. This means that when one sends a partial plane wave with a given $k$ wavevector through the MMF, it gets mixed mainly on the angular degrees but not on the radial thus generating a narrow cone of speckles with the same transverse angle of incidence at the far-field output. This kind of preservation indicates the existence of a memory effect in the radial degrees of freedom. The radial correlation range corresponds to the width of the output cone of the speckles. By using this fact, information of any radial curvature of the initial wavefront can be transferred to the output, for instance, using a defocus phase pattern to axially shift an output pattern [Čižmár and Dholakia, 2012]. Recently, the presence of long-range correlations of the multimode fibre in the spatio-temporal domain was discovered and applied for pulse delivery [Xiong et al., 2019].

# D | Statistical prediction of scalability for linear optical networks

In this appendix, we provide the theoretical analysis to support the performance and scalability of our experiment for programming a linear optical network.

## D.1 | Statistical properties of time-reversal operator

Let us consider a rectangular random matrix $\mathbf{T}$ of dimension $k \times d$. The matrix $\mathbf{T}$ physically represents the sub-part of transmission matrix linking the $d$ input modes to the $k$ target output modes of interest, where $d = n/m$ in the experiment. We note that $m$ is the number of input ports and $k$ is that of output ports of the associated optical network and $n$ is the number of propagation modes of the MMF.

In this model, the elements of $\mathbf{T}$ are sampled from i.i.d complex Gaussian random variables with $\mathrm{E}\left[t_{ip}t_{iq}^*\right] = \frac{1}{d}\delta_{pq}$. We are interested in the statistical properties of the time-reversal operator, a.k.a. Wishart matrix, $\mathbf{W} = \mathbf{T}\mathbf{T}^\dagger$. This matrix plays an important role in our optical network implementation since it maps the desired linear transformation to the implemented one as in Eq. 2.17. The elements of $\mathbf{W}$ are given by

$$w_{ij} = \sum_{q=1}^{d} t_{iq}t_{jq}^*, \tag{D.1}$$

where $t_{ij}$ is the element of $\mathbf{T}$ at position $(i, j)$. The expectation of coefficients $w_{ij}$ is determined by

$$\begin{aligned} \mathrm{E}\left[w_{ij}\right] &= \sum_{q=1}^{d} \mathrm{E}\left[t_{iq}t_{jq}^*\right] \\ &= \begin{cases} 0 & ,\text{if } i \neq j \\ \sum_{q=1}^{d} \mathrm{E}\left[|t_{iq}|^2\right] = 1 & ,\text{if } i = j \end{cases} \end{aligned} \tag{D.2}$$

So that, $\mathrm{E}\left[w_{ij}\right] = \delta_{ij}$, which means that for one physical realization of $\mathbf{T}$, we can estimate $\mathbf{T}\mathbf{T}^\dagger \approx \mathbb{1}$ to the first statistical moment.

Next we consider the variance of coefficients $w_{ij}$, defined as

$$\mathrm{Var}\left[w_{ij}\right] = \mathrm{E}\left[|w_{ij}|^2\right] - |\mathrm{E}\left[w_{ij}\right]|^2. \tag{D.3}$$

And using the moment theorem, $\mathrm{E}\left[|w_{ij}|^2\right]$ is expressed as,

$$\begin{aligned}\mathrm{E}\left[|w_{ij}|^2\right] &= \sum_{p=1}^{d}\sum_{q=1}^{d}\mathrm{E}\left[t_{ip}t_{jp}^{*}t_{iq}^{*}t_{jq}\right] \\ &= \underbrace{\sum_{p=1}^{d}\sum_{q=1}^{d}\mathrm{E}\left[t_{ip}t_{jp}^{*}\right]\mathrm{E}\left[t_{iq}^{*}t_{jq}\right]}_{|\mathrm{E}[w_{ij}]|^2} + \underbrace{\sum_{p=1}^{d}\sum_{q=1}^{d}\mathrm{E}\left[t_{ip}t_{iq}^{*}\right]\mathrm{E}\left[t_{jp}^{*}t_{jq}\right]}_{\mathrm{Var}[w_{ij}]}.\end{aligned} \tag{D.4}$$

We use that fact that $\mathrm{E}\left[t_{ip}t_{iq}^{*}\right] = \frac{1}{d}\delta_{pq}$ to determine $\mathrm{Var}\left[w_{ij}\right]$,

$$\mathrm{Var}\left[w_{ij}\right] = \frac{1}{d^2}\sum_{p=1}^{d}\sum_{q=1}^{d}\delta_{pq} = \frac{1}{d}. \tag{D.5}$$

This indicates that the elements of $\mathbf{W}$ fluctuate around the expectation $\delta_{ij}$ with the standard deviation $1/\sqrt{d}$. For one physical realization of $\mathbf{T}$, one can estimate $w_{ij} \approx \delta_{ij} + \mathcal{O}(1/\sqrt{d})$ to the second statistical moment. The corresponding matrix representation is,

$$\mathbf{T}\mathbf{T}^{\dagger} \approx \mathbb{1} + \frac{1}{\sqrt{d}}\mathbf{H}, \tag{D.6}$$

where $\mathbf{H}$ is a complex Hermitian noise matrix in which the fluctuation of coefficients is normalized. Substituting $d = n/m$ in Eq. D.6, we obtain,

$$\mathbf{T}^{(p)}\mathbf{T}^{(p)\dagger} = \mathbb{1} + \sqrt{\frac{m}{n}}\mathbf{H}, \tag{D.7}$$

In the subsection 2.4.1, $\mathbf{T}$ denotes $\mathbf{T}^{(p)}$ where $(p)$ is a label for a given $p$-th input port of an optical network. The Eq. D.7 is the origin of Eq. 2.18. We note that we omit the terms originating from higher-order statistical moments.

## D.2 | Distance between a desired linear transformation and implemented one

In this section, we prove that the distance between the desired linear transformation $\mathcal{L}$ and implemented linear transformation $\tilde{\mathcal{L}}$ scales as $\mathcal{O}\left(\sqrt{\frac{mk}{n}}\right)$ (see subsection 2.4.1). Let define the distance between $\mathcal{L}$ and $\tilde{\mathcal{L}}$, $\|\mathcal{L} - \tilde{\mathcal{L}}\|_s$, where $\|\cdot\|_s$ is defined as $\|A\| \equiv \sum_{i=1}^{k}\sum_{j=1}^{m}|a_{ij}|_s/(mk)$, where $s$ denotes the $\ell_s$-norm. We are interested in considering the statistical average of the element-wise distance, $\left|l_{ij} - \tilde{l}_{ij}\right|_s$, over a number of input and output ports of an optical network. We consider an element of the implemented linear transformation $\tilde{l}_{ij}$, which is related to an element of the desired linear transformation $l_{ij}$ by,

$$\tilde{l}_{ij} = \sum_{p=1}^{k} w_{ip}l_{pj}. \tag{D.8}$$

Using the estimation form of $w_{ip}$ from the section D.1, we obtain

$$\tilde{l}_{ij} = \sum_{p=1}^{k} \left( \delta_{ip} + \sqrt{\frac{m}{n}} H_{ip} \right) l_{pj}. \tag{D.9}$$

Considering the $\ell_2$-norm distance between a desired linear transformation and the effective implemented one, we have

$$\left| l_{ij} - \tilde{l}_{ij} \right|^2 = \frac{m}{n} \left| \sum_{p=1}^{k} H_{ip} l_{pj} \right|^2. \tag{D.10}$$

Now we determine the statistical properties of $\left| l_{ij} - \tilde{l}_{ij} \right|^2$. The expectation is determined by

$$\mathrm{E}\left[ \left| l_{ij} - \tilde{l}_{ij} \right|^2 \right] = \frac{m}{n} \mathrm{E}\left[ \left| \sum_{p=1}^{k} H_{ip} l_{pj} \right|^2 \right]. \tag{D.11}$$

Then,

$$\begin{aligned} \mathrm{E}\left[ \left| \sum_{p=1}^{k} H_{ip} l_{pj} \right|^2 \right] &= \mathrm{Var}\left[ \sum_{p=1}^{k} H_{ip} l_{pj} \right] + \left| \mathrm{E}\left[ \sum_{p=1}^{k} H_{ip} l_{pj} \right] \right|^2 \\ &= \sum_{p=1}^{k} \mathrm{Var}\left[ H_{ip} l_{pj} \right] + 2 \sum_{1 \le p < q \le k} \mathrm{Cov}\left[ H_{ip} l_{pj}, H_{iq} l_{qj} \right] + \left| \sum_{p=1}^{k} \mathrm{E}\left[ H_{ip} l_{pj} \right] \right|^2 \end{aligned} \tag{D.12}$$

First, we consider that $H_{ip}$ and $l_{pj}$ are two independent random variables. Thus, $H_{ip} l_{pj}$ are independent variables, so that the middle term is neglected and the equation can be rewritten as

$$\begin{aligned} \mathrm{E}\left[ \left| \sum_{p=1}^{k} H_{ip} l_{pj} \right|^2 \right] &= k \, \mathrm{Var}\left[ H_{ip} l_{pj} \right] + k^2 \left( \mathrm{E}\left[ H_{ip} l_{pj} \right] \right)^2 \\ &= k \left( \mathrm{E}\left[ H_{ip} \right]^2 \mathrm{Var}\left[ l_{pj} \right] + \mathrm{E}\left[ l_{pj} \right]^2 \mathrm{Var}\left[ H_{ip} \right] + \mathrm{Var}\left[ H_{ip} \right] \mathrm{Var}\left[ l_{pj} \right] \right) \\ &\quad + k^2 \left( \mathrm{E}\left[ H_{ip} \right] \mathrm{E}\left[ l_{pj} \right] \right)^2 \end{aligned} \tag{D.13}$$

Using the fact from the previous section that $\mathrm{E}\left[H_{ip}\right]=0$ and $\mathrm{Var}\left[H_{ip}\right]=1$, the equation is reduced to

$$\begin{aligned} \mathrm{E}\left[ \left| \sum_{p=1}^{k} H_{ip} l_{pj} \right|^2 \right] &= k \left( \mathrm{E}\left[ l_{pj} \right]^2 + \mathrm{Var}\left[ l_{pj} \right] \right) \\ &\approx \mathcal{O}(k) \end{aligned} \tag{D.14}$$

Thus, we can estimate the normalised $\ell_2$-norm,

$$\| \mathcal{L} - \tilde{\mathcal{L}} \|_2 = \sqrt{\mathrm{E}\left[ \left| l_{ij} - \tilde{l}_{ij} \right|^2 \right]} \approx \mathcal{O}\left( \sqrt{\frac{mk}{n}} \right). \tag{D.15}$$

This indicates the scalability of our implementation of an optical network as discussed in subsection 2.4.3.

Alternatively, we can calculate the distance with $\ell_1$-norm,

$$\left|l_{ij} - \tilde{l}_{ij}\right| = \sqrt{\frac{m}{n}}\left|\sum_{p=1}^{k} H_{ip} l_{pj}\right|. \tag{D.16}$$

Then we determine the statistical properties of $\left|l_{ij} - \tilde{l}_{ij}\right|$. The expectation is

$$\mathrm{E}\left[\left|l_{ij} - \tilde{l}_{ij}\right|\right] = \sqrt{\frac{m}{n}}\,\mathrm{E}\left[\left|\sum_{p=1}^{k} H_{ip} l_{pj}\right|\right]. \tag{D.17}$$

We assume here that $H_{ip}l_{pj}$ are the i.i.d. complex Gaussian random variable. The expectation is

$$\begin{aligned}\mathrm{E}\left[\left|\sum_{p=1}^{k} H_{ip} l_{pj}\right|\right] &= \sqrt{\mathrm{Var}\left[\sum_{p=1}^{k} H_{ip} l_{pj}\right]}\sqrt{\frac{2}{\pi}} \\ &= \sqrt{k\,\mathrm{Var}\left[H_{ip}l_{pj}\right]}\sqrt{\frac{2}{\pi}}\end{aligned} \tag{D.18}$$

Using the fact that $\mathrm{Var}\left[H_{ip}l_{pj}\right] = \left(\mathrm{E}\left[l_{pj}\right]^2 + \mathrm{Var}\left[l_{pj}\right]\right)$, we obtain

$$\begin{aligned}\mathrm{E}\left[\left|\sum_{p=1}^{k} H_{ip} l_{pj}\right|\right] &= \sqrt{k\left(\mathrm{E}\left[l_{pj}\right]^2 + \mathrm{Var}\left[l_{pj}\right]\right)}\sqrt{\frac{2}{\pi}} \\ &\approx \mathcal{O}\left(\sqrt{k}\right)\end{aligned} \tag{D.19}$$

So that,

$$\|\mathcal{L} - \tilde{\mathcal{L}}\|_1 = \mathrm{E}\left[\left|l_{ij} - \tilde{l}_{ij}\right|\right] \approx \mathcal{O}\left(\sqrt{\frac{mk}{n}}\right). \tag{D.20}$$

By substituting the distance in either $\ell_1$-norm or $\ell_2$-norm into the definition of $\mathcal{F}$, we finally obtain,

$$\mathcal{F}(\tilde{\mathcal{L}}, \mathcal{L}) = 1 - \mathcal{O}\left(\sqrt{\frac{mk}{n}}\right), \tag{D.21}$$

as described in subsection 2.4.1.

# E

# Bell states on a lossy beamsplitter

In this appendix, we consider theoretically the evolution of Bell states through a non-polarizing lossy beamsplitter. First, we define a set of Bell states,

$$\left|\Phi^{\pm}\right\rangle = \frac{1}{\sqrt{2}}(|1_{H1}\rangle\,|1_{H2}\rangle \pm |1_{V1}\rangle\,|1_{V2}\rangle) \tag{E.1a}$$

$$\left|\Psi^{\pm}\right\rangle = \frac{1}{\sqrt{2}}(|1_{H1}\rangle\,|1_{V2}\rangle \pm |1_{V1}\rangle\,|1_{H2}\rangle). \tag{E.1b}$$

And, we define a non-polarizing lossy beamsplitter (LBS) as

$$\mathrm{LBS} \equiv \frac{1}{2}\begin{array}{c} \begin{matrix} H1 & H2 & V1 & V2 \end{matrix} \\ \begin{bmatrix} 1 & -1 & 0 & 0 \\ -1 & 1 & 0 & 0 \\ 0 & 0 & 1 & -1 \\ 0 & 0 & -1 & 1 \end{bmatrix} \end{array} \begin{matrix} H1 \\ H2 \\ V1 \\ V2 \end{matrix} \tag{E.2}$$

In the following, we are going to simplify the presentation of the calculation by omitting the noise operators $\hat{F}_i$ from the evolution. In fact, the noise operators are added to the evolution of a state through the LBS in order to satisfy the commutation relations and the unitarity.

Firstly, we consider the evolution of $|\Phi^{\pm}\rangle$ through the LBS,

$$\begin{aligned} \mathrm{LBS}\left(\left|\Phi^{\pm}\right\rangle\right) &= \frac{1}{4\sqrt{2}}\left[(\hat{a}^{\dagger}_{H1} - \hat{a}^{\dagger}_{H2})(-\hat{a}^{\dagger}_{H1} + \hat{a}^{\dagger}_{H2}) \pm (\hat{a}^{\dagger}_{V1} - \hat{a}^{\dagger}_{V2})(-\hat{a}^{\dagger}_{V1} + \hat{a}^{\dagger}_{V2})\right]|0\rangle \\ &= \frac{1}{4\sqrt{2}}\left[-\hat{a}^{\dagger 2}_{H1} + 2\hat{a}^{\dagger}_{H1}\hat{a}^{\dagger}_{H2} - \hat{a}^{\dagger 2}_{H2} \mp \hat{a}^{\dagger 2}_{V1} \pm 2\hat{a}^{\dagger}_{V1}\hat{a}^{\dagger}_{V2} \mp \hat{a}^{\dagger 2}_{V2}\right]|0\rangle \\ &= \frac{1}{2}\left[\underbrace{-\frac{1}{2}\left(|2_{H1}\rangle + |2_{H2}\rangle \pm |2_{V1}\rangle \pm |2_{V2}\rangle\right)}_{\text{analogy to unitary evolution}}\right] + \frac{1}{2}\left|\Phi^{\pm}\right\rangle \end{aligned} \tag{E.3}$$

This shows that $|\Phi^{\pm}\rangle$ evolves to the superposition of the two contributions. The first term is in analogy to the unitary evolution of the state $|\Phi^{\pm}\rangle$ through a non-polarizing beamsplitter which occurs with a probability of 1/4. The second term is that the state $|\Phi^{\pm}\rangle$ evolves to itself with a probability of 1/4. If none of the above cases occurs, the half of the chance, the Bell states get lost from the LBS.

Next, we consider the evolution of $|\Psi^{\pm}\rangle$ through the LBS,

$$\begin{aligned}\mathrm{LBS}\left(\left|\Psi^{\pm}\right\rangle\right) &= \frac{1}{4\sqrt{2}}\left[(\hat{a}^{\dagger}_{H1}-\hat{a}^{\dagger}_{H2})(-\hat{a}^{\dagger}_{V1}+\hat{a}^{\dagger}_{V2}) \pm (\hat{a}^{\dagger}_{V1}-\hat{a}^{\dagger}_{V2})(-\hat{a}^{\dagger}_{H1}+\hat{a}^{\dagger}_{H2})\right]|0\rangle \\ &= \frac{1}{4\sqrt{2}}[-\hat{a}^{\dagger}_{H1}\hat{a}^{\dagger}_{V1}+\hat{a}^{\dagger}_{H2}\hat{a}^{\dagger}_{V1}+\hat{a}^{\dagger}_{H1}\hat{a}^{\dagger}_{V2}-\hat{a}^{\dagger}_{H2}\hat{a}^{\dagger}_{V2} \\ &\qquad \mp \hat{a}^{\dagger}_{V1}\hat{a}^{\dagger}_{H1} \pm \hat{a}^{\dagger}_{V2}\hat{a}^{\dagger}_{H1} \pm \hat{a}^{\dagger}_{V1}\hat{a}^{\dagger}_{H2} \mp \hat{a}^{\dagger}_{V2}\hat{a}^{\dagger}_{H2}]\,|0\rangle\,.\end{aligned} \tag{E.4}$$

In the case of $|\Psi^{+}\rangle$, it reads,

$$\begin{aligned}\mathrm{LBS}\left(\left|\Psi^{+}\right\rangle\right) &= \frac{1}{2\sqrt{2}}\left[-\hat{a}^{\dagger}_{H1}\hat{a}^{\dagger}_{V1}+\hat{a}^{\dagger}_{V1}\hat{a}^{\dagger}_{H2}+\hat{a}^{\dagger}_{H1}\hat{a}^{\dagger}_{V2}-\hat{a}^{\dagger}_{H2}\hat{a}^{\dagger}_{V2}\right] \\ &= \frac{1}{2}\left[\underbrace{-\frac{1}{\sqrt{2}}\left(|1_{H1}\rangle\,|1_{V1}\rangle+|1_{H2}\rangle\,|1_{V2}\rangle\right)}_{\text{analogy to unitary evolution}}\right]+\frac{1}{2}\left|\Psi^{+}\right\rangle.\end{aligned} \tag{E.5}$$

Hence, $|\Psi^{+}\rangle$ evolves to the superposition of the terms. The first is in analogy with the unitary evolution of $|\Psi^{+}\rangle$ through a non-polarizing beamsplitter which with a probability of 1/4. The second term is similar to the case of $|\Phi^{\pm}\rangle$, the $|\Psi^{+}\rangle$ state evolves to itself with a probability of 1/4. Otherwise, the Bell state gets lost.

And, in the case of $|\Psi^{-}\rangle$, it reads,

$$\mathrm{LBS}\left(\left|\Psi^{-}\right\rangle\right) = 0. \tag{E.6}$$

Therefore, we show that the evolution of singlet Bell state $|\Psi^{-}\rangle$ through the lossy non-polarizing beamsplitter gets completely lost. This is the manifestation of the coherent perfect absorption in the quantum regime.

# F

# Statistical data for state classifier

In this appendix, we provide additional experimental details and data for chapter 4. The experimental setting and status of each ground-truth states are presented in Table F.1.

**Table F.1** – Experimental parameters and status of ground-truth light sources. $\mathcal{N}$ is the number of realizations of the experiment. $V_{\text{before(after)}}$ is a visibility of two-photon interference before and after performing an experiment. $T$ is an integration time of detector for one realization.

| State | $T$ (s) | $\mathcal{N}$ | $V_{\text{before}}$ | $V_{\text{after}}$ | $\Delta\lambda$ (nm) |
|---|---|---|---|---|---|
| **Monochromatic case** | | | | | |
| Biphoton state ($\delta = 0$) | 15 | 10000 | 0.95 | 0.94 | 1.54 |
| Biphoton state ($\delta > l_c$) | 15 | 10000 | 0.94 | 0.74 | 1.53 |
| N=2 N00N state | 15 | 10000 | 0.98 | 0.98 | 1.65 |
| $\|2_V\rangle$ | 15 | 10000 | 0.98 | 0.82 | 1.53 |
| Single-photon state $\|1_V\rangle$ | 15 | 10000 | 0.98 | 0.98 | 1.54 |
| **Polychromatic case** | | | | | |
| Biphoton state ($\delta = 0$) | 15 | 10000 | 0.94 | 0.73 | 1.60 |
| Biphoton state ($\delta > l_c$) | 15 | 10000 | 0.82 | 0.92 | 1.52 |
| Incoherent dispersion source | 15 | 4004 | - | - | 2.35 |
| **Classical case** | | | | | |
| Incoherent source ($d = 2$) | 5 | 10000 | - | - | 2.35 |
| Coherent source ($d = 1$) | 5 | 10000 | - | - | 2.35 |

Furthermore, we tested the influence of noise due to a short integration time $T$ on the statistical distributions in the case of monochromatic biphoton state. We found that all statistical distributions for 15, 120, and 240 s have the same profiles.

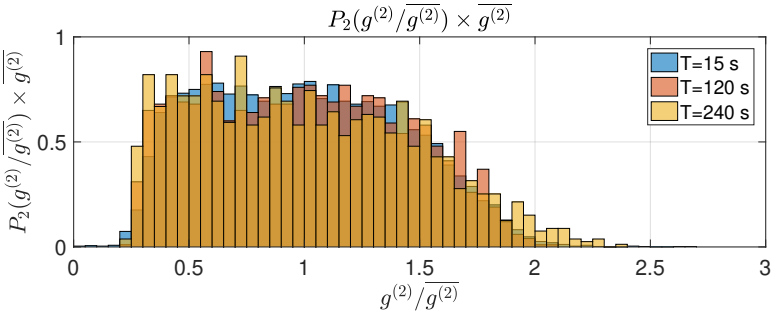


**Figure F.1 – Probability density functions of normalized second-order correlation**: for indistinguishable monochromatic biphoton state at different integration times $T$. The distributions present a broaden and flatten features compared to the distinguishable case presented in Fig. 4.6c. For $T$=15 s, the PDF is also plotted in Fig. 4.6c

## F.1 | Estimation of the purity

The measured visibilities of intensity $\mathcal{V}_I$, two-fold coincidences $\mathcal{V}_C$, and normalized second-order correlation $\mathcal{V}_{g^{(2)}}$ and the estimated purity $\mathcal{P}$ and dimensionality $d$ of ground-truth states are presented in Table F.2.

**Table F.2** – Visibilities and estimated properties of ground-truth states.

| State | $\mathcal{V}_I$ | $\mathcal{V}_C$ | $\mathcal{P}$ | $d$ | $\mathcal{V}_{g^{(2)}}$ |
|---|---|---|---|---|---|
| **Monochromatic case** | | | | | |
| Biphoton state ($\delta = 0$) | $0.46 \pm 0.02$ | 1.38 | $0.45 \pm 0.03$ | $2.16 \pm 0.09$ | 0.178 |
| Biphoton state ($\delta > l_c$) | $0.50 \pm 0.02$ | 1.34 | $0.35 \pm 0.03$ | $2.02 \pm 0.07$ | 0.096 |
| N=2 N00N state | $0.45 \pm 0.01$ | 1.27 | $0.38 \pm 0.02$ | $2.24 \pm 0.01$ | 0.127 |
| $\|2_V\rangle$ | $0.85 \pm 0.06$ | 2.39 | $0.69 \pm 0.12$ | $1.18 \pm 0.09$ | 0.105 |
| Single-photon state $\|1_V\rangle$ | $0.90 \pm 0.08$ | 1.65 | - | $1.1 \pm 0.1$ | 0.402 |
| **Polychromatic case** | | | | | |
| Biphoton state ($\delta = 0$) | $0.068 \pm 0.002$ | 0.26 | $0.120 \pm 0.003$ | $14.7 \pm 0.3$ | 0.074 |
| Biphoton state ($\delta > l_c$) | $0.073 \pm 0.002$ | 0.22 | $0.078 \pm 0.004$ | $13.8 \pm 0.4$ | 0.049 |
| Incoherent dispersion source | $0.048 \pm 0.003$ | 0.03 | - | $20 \pm 1$ | 0.001 |
| **Classical case** | | | | | |
| Incoherent source ($d = 2$) | $0.044 \pm 0.02$ | 1.14 | - | $2.3 \pm 0.1$ | 0.02 |
| Coherent source ($d = 1$) | $0.83 \pm 0.03$ | 2.39 | - | $1.21 \pm 0.05$ | 0.05 |

The estimations of purity of ground-truth states are lower than the expected values of one. This mainly is because of the underestimation of $\mathcal{V}_C$. We attribute the error to two contributions:

1. The first is the influence of accidental coincidences since it modifies the distribution of two-fold coincidences resulting in an incorrect expectation of $\mathcal{V}_C$. In the case of $d$=1, the estimation of $\mathcal{V}_C$ from the distribution of accidental coincidences (Eq. 4.10) is 1.25, which for example is close to the experimental value reported for N00N state. In the case of $d$=2 for the two-photon Fock state $|2\rangle$, the distributions of two-fold coincidences and accidental coincidences are identical. Both distributions estimate $\mathcal{V}_C = 3$, while experimentally we obtained 2.39 which is the same as the coherent

state $d = 1$. Therefore, the influence of accidental coincidences does not completely explain the error in the estimation of purity.

2. The second contribution is due to the lack of rare events originating from a long tail of the statistical distributions. We estimate the visibility of two-fold coincidences using the statistical distribution with the cut-off at $C/\overline{C} = 6$. We find $\mathcal{V}_C = 1.39$ for $d = 2$ which is close to the experimental estimation for monochromatic biphoton states. The value from the cut-off distribution is still far from the expected value of 2 for the pure state. For $d$=1, we find the same contribution. The visibility of two-fold coincidences is estimated to be $\mathcal{V}_C = 2.38$ using the calculation from the statistical distribution with the cut-off at $C/\overline{C} = 12$. The value is close to the experimental values reported for the two-photon Fock state $|2\rangle$ and the coherent state.

In conclusion, those contributions potentially explain the origin of the error. We, therefore, demonstrated the limitation of using the statistical distributions of two-fold coincidences at a low value of $d$ in the presence of accidental coincidences.

## F.2 | Statistical distributions

We provide the statistical distributions of intensity speckles for all ground-truth states in Fig. F.2. The same distributions are also observed for the intensity on the second detection $I_2$ (data are not shown).

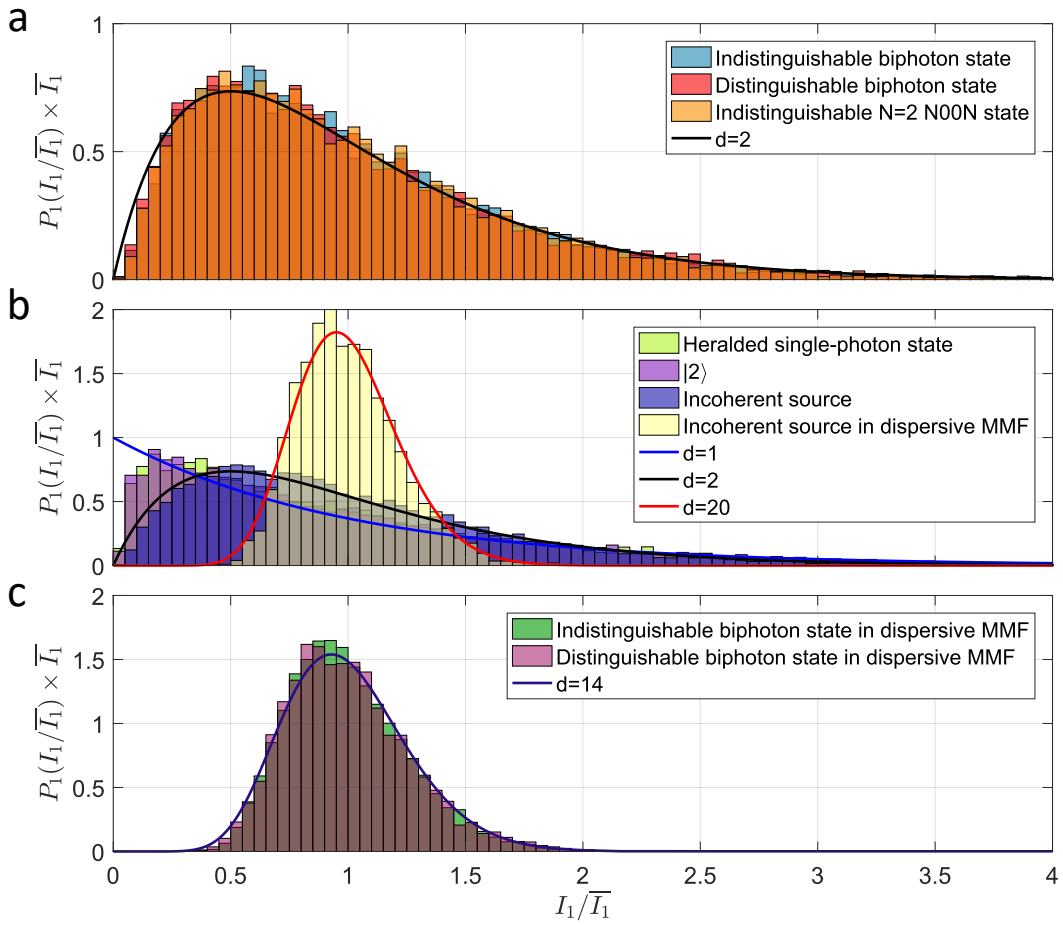


**Figure F.2 – Probability density functions of intensity**: (a) Indistinguishable biphoton state (blue), distinguishable biphoton state (red), N=2 N00N state (orange) have the same distribution with $d = 2$. (b) Heralded single-photon state (light green), two-photon state (magenta) have the same exponential decay $d = 1$. Incoherent source (dark blue) in a 55-cm MMF and incoherent source (light yellow) in a 25-m MMF have different distributions with $d = 2$ and $d = 20$. (c) Indistinguishable (green) and distinguishable (light magenta) biphoton states in dispersive 25-m MMF have the same distribution $d \approx 14$ $(d = 14.7, d = 13.8)$. Information from the statistical distribution of intensity provides only a number of modes $d$ that light occupied.

We provide the statistical distributions of two-fold coincidences speckles corrected for the expected accidental coincidences in Fig. F.3. The expected accidental coincidences are subtracted from measured two-fold coincidences. We note that classical states and the single-photon state do not result in true two-fold coincidences, thus the results are not shown in Fig. F.3. The measured distributions are still described well by the distribution of accidental coincidences in the cases of $d = 1$ and $d = 2$.

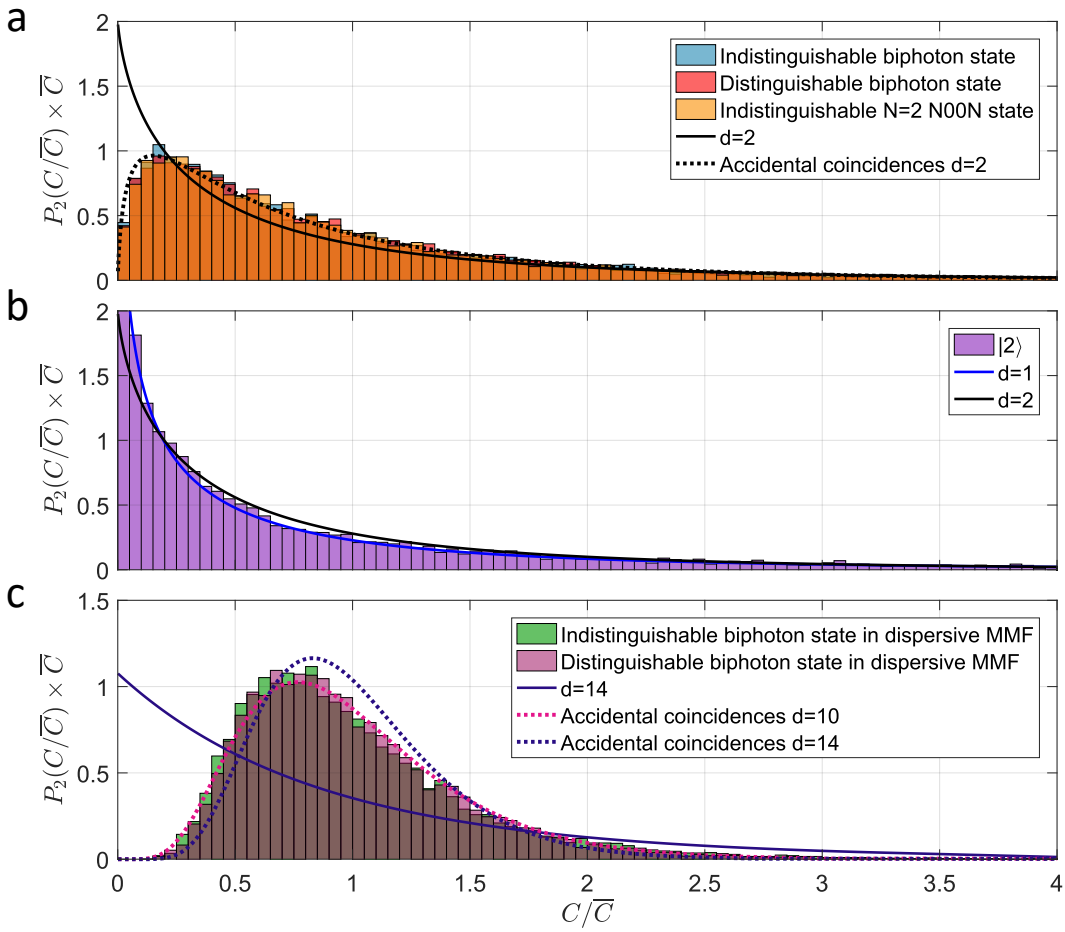


**Figure F.3 – Probability density functions of two-fold coincidences corrected for accidental coincidences**: (a) Indistinguishable biphoton state (blue), distinguishable biphoton state (red), N=2 N00N state (orange) have the same distribution with $d = 2$. (b) Two-photon state (magenta) have a decay profile $d = 1$. (c) Indistinguishable (green) and distinguishable (light magenta) biphoton states in dispersive 25-m MMF have the same distribution that diverge from the PDF of expected accidental coincidences $d \approx 14$ ($d_{\text{Indis}} = 14.7, d_{\text{Dis}} = 13.8$). The lines indicate distributions of two-fold coincidences for a pure maximally-entangled biphoton state (Eq. 4.3). The dashed lines indicate distributions of accidental coincidences (Eq. 4.10).

# Abstract

High-speed data transfer through optical fibres using spatial multiplexing is practically limited by modal crosstalk. Instead of considering this modal crosstalk as a limitation, we here harness its mode mixing to process quantum optical information. We implement a programmable linear optical network based on the concept of inverse photonic design exploiting the technology of wavefront shaping. We demonstrate manipulation of two-photon quantum interference on various linear networks across both spatial and polarization degrees of freedom. In particular, we experimentally show the *zero-transmission law* in Fourier and Sylvester interferometers, which are used to certificate the degree of indistinguishability of an input state. Moreover, thanks to the ability to implement a non-unitary network, we observe the photon anti-coalescence effect in all output configurations, as well as the realization of a tunable coherent absorption experiment. Therefore, we demonstrate the reconfigurability, accuracy, and scalability of the implemented linear optical networks for quantum information processing. Furthermore, we study the statistical properties of one- and two-photon speckles generated from various ground-truth states after propagating through a multimode fibre. These statistical properties of speckles can be used to extract information about the dimensionality, purity, and indistinguishability of an unknown input state of light, therefore allowing for state classification. Our results highlight the potential of complex media combined with wavefront shaping for quantum information processing.

**Keywords:** quantum optics, statistical optics, multimode fibre, multiple light scattering, wavefront shaping, spatial light modulator, linear optical network, zero-transmission law, coherent absorption, two-photon speckle.

# Résumé

Le transport à haut débit de données à travers des fibres optiques grâce au multiplexage spatial est en pratique limité par la diaphonie modale. Au lieu de considérer ce couplage modal comme une limitation, nous exploitons ici ce mélange de modes comme une ressource. Nous mettons en œuvre un réseau optique linéaire programmable basé sur le concept de design photonique inverse, exploitant les techniques de mise en forme du front d'onde. Nous démontrons la manipulation d'interférences quantiques à deux photons sur divers réseaux linéaires, comprenant des degrés de liberté spatiaux et de polarisations. En particulier, nous vérifions expérimentalement la « zero transmission law » dans des interféromètres de Fourier et de Sylvester, permettant de quantifier le degré d'indiscernabilité d'un état d'entrée. De plus, grâce à la possibilité de mettre en œuvre un réseau non unitaire, nous mettons en évidence l'anti-coalescence de photons dans toutes les configurations de sortie, et réalisons une expérience d'absorption cohérente. Nous démontrons ainsi l'aspect reconfigurable de l'implémentation de tels réseaux optiques linéaires dans des fibres multimodes. De plus, nous étudions les propriétés statistiques du speckle à un et à deux photons générés à partir de divers états d'entrée, après propagation dans une fibre multimode. Ces propriétés statistiques du speckle peuvent être utilisées pour extraire des informations sur la dimensionnalité, la pureté et l'indiscernabilité d'un état quantique inconnu, permettant ainsi leur classification. Ce travail met en évidence le potentiel du contrôle de front d'onde en milieux complexes pour le traitement quantique de l'information.

**Mots-clés:** optique quantique, optique statistique, fibres multimodes, diffusion multiple de la lumière, contrôle de front d'onde, réseau optique linéaire, absorption cohérente, speckle à deux photons

# Acknowledgements

Countless supports and inspirations from many people and nature have incubated me to this point of completing the PhD degree. First and foremost, I cannot thank you enough, my family, for taking good care of me. I am so thankful all of my teachers, especially, Surasak Arunrat, Pronpana Samairath and Pasong Rangsing, for always showing me how cool science can explain phenomena. I acknowledge IPST and NSTDA for financial supports that I have obtained since the early state of my study under their DPST and JSTP science-oriented education programmes. I thank my teachers during my undergraduate study, especially my supervisor, Chittanon Buranachai, for teaching me how amazing light and biological systems are. I acknowledge the MONABIOPHOT Erasmus Mundus Master programme and my teachers around Europe for showing me the world of optics and photonics from various aspects.

During my PhD, I would like to deeply thank all both past and current members of Gigan's lab namely Mickael Mounaix, Baptiste Blochet, Tom Sperber, Andrés de los Ríos Sommer, Antoine Boniface, Jonathan Dong, Louisiane Devaud, Julien Guilbert, Lei Zhu, Ming Xin, Thomas Juffman, Claudio Moretti, Hilton Barbosa De Aguiar, Awoke Negash, Ivan Gusachenko, Pauline Boucher, Mushegh Rafayelyan, Bernhard Rauer, Michal Dabrowski, Lorenzo Valzania, Fernado Soldevila Torres and interns. I really enjoyed such a great lab environment over the past three years. Numerous jokes, conversations and discussions with full of foods and drinks we had always fulfilled my daily life colourful. I would particularly like to thank Claudio and Hilton, who always teach and help me with technical works in the lab. I thank my colleagues, Luca Innocenti, Alessandro Ferraro, Mauro Paternostro for fruitful theoretical discussions and I thank Hugo Defienne and Thomas Juffman for their advice and experimental discussions. Also, I thank Berengere Argence and Jakob Reichel's lab, Torben Pöpplau, for helping and letting me borrow equipment. Furthermore, I thank all LKB members, LKB lab's secretariat, IT, electronic and mechanic people for their supports, in particular, thanks to Audrey for a lot of administrative works she did. Thank you to all of my friends, for sharing our life experiences and always keep supporting me. I gratefully acknowledge financial support from Franco-Thai Scholarship.

I am grateful to Christine Silberhorn, François Marquier, Riccardo Sapienza, Mattia Walschaers, Eleni Diamanti for being my committees. And, I thank Michal Dąbrowski and Pauline Boucher for their careful proof-reading my dissertation.

Finally, I would like to deeply express my appreciation to my supervisor, Sylvain Gigan for his passion, enthusiasm, expertise, and patience. I am grateful for all of his advice, supports and the opportunity to study and do research in his lab. I have learnt a lot not only scientific knowledge but also professional skills.

Thank you very much,

# Bibliography


[Aaronson, 2011] Aaronson, S. (2011). A linear-optical proof that the permanent is #P-hard. *Proceedings of the Royal Society A: Mathematical, Physical and Engineering Sciences*, 467(2136):3393–3405. (Cited on page 32.)

[Aaronson and Arkhipov, 2011] Aaronson, S. and Arkhipov, A. (2011). The computational complexity of linear optics. In *Proceedings of the 43rd annual ACM symposium on Theory of computing - STOC '11*, number 0844626, page 333, New York, New York, USA. ACM Press. (Cited on pages 32, 33, 34, and 101.)

[Abouraddy et al., 2002] Abouraddy, A. F., Nasr, M. B., Saleh, B. E. A., Sergienko, A. V., and Teich, M. C. (2002). Quantum optical coherence tomography with dispersion cancellation. *Phys. Rev. A*, 65(5):53817. (Cited on page 15.)

[Abraham and Lyons, 2010] Abraham, D. A. and Lyons, A. P. (2010). Reliable methods for estimating the K-distribution shape parameter. *IEEE Journal of Oceanic Engineering*, 35(2):288–302. (Cited on page 99.)

[Adcock et al., 2019] Adcock, J. C., Vigliar, C., Santagati, R., Silverstone, J. W., and Thompson, M. G. (2019). Programmable four-photon graph states on a silicon chip. *Nature Communications*, 10(1):3528. (Cited on page 28.)

[Agarwal, 2012] Agarwal, G. S. (2012). *Quantum Optics*. Cambridge University Press, Cambridge. (Cited on pages 8 and 10.)

[Agrawal, 2016] Agrawal, G. P. (2016). Optical Communication: Its History and Recent Progress. In *Optics in Our Time*, pages 177–199. Springer International Publishing, Cham. (Cited on pages 2 and 44.)

[Agresti et al., 2019] Agresti, I., Viggianiello, N., Flamini, F., Spagnolo, N., Crespi, A., Osellame, R., Wiebe, N., and Sciarrino, F. (2019). Pattern Recognition Techniques for Boson Sampling Validation. *Physical Review X*, 9(1):011013. (Cited on page 101.)

[Aiello and Woerdman, 2004] Aiello, A. and Woerdman, J. P. (2004). Intrinsic entanglement degradation by multimode detection. *Physical Review A*, 70(2):1–12. (Cited on page 97.)

[Aisawa et al., 1991] Aisawa, S., Noguchi, K., and Matsumoto, T. (1991). Remote image classification through multimode optical fiber using a neural network. *Optics Letters*, 16(9):645. (Cited on page 50.)

[Akbulut et al., 2016a] Akbulut, D., Strudley, T., Bertolotti, J., Bakkers, E. P. A. M., Lagendijk, A., Muskens, O. L., Vos, W. L., and Mosk, A. P. (2016a). Optical transmission matrix as a probe of the photonic strength. *Physical Review A*, 94(4):043817. (Cited on page 41.)

[Akbulut et al., 2016b] Akbulut, D., Strudley, T., Bertolotti, J., Bakkers, E. P. A. M., Lagendijk, A., Muskens, O. L., Vos, W. L., and Mosk, A. P. (2016b). Optical transmis-

sion matrix as a probe of the photonic strength. *Physical Review A*, 94(4):1–8. (Cited on page 126.)

[Akemann et al., 2018] Akemann, G., Baik, J., and Francesco, P. D. (2018). *The Oxford Handbook of Random Matrix Theory*. Oxford University Press. (Cited on page 39.)

[Akkermans and Maynard, 1985] Akkermans, E. and Maynard, R. (1985). Weak localization of waves. *Journal de Physique Lettres*, 46(22):1045–1053. (Cited on page 130.)

[Akkermans and Montambaux, 2007] Akkermans, E. and Montambaux, G. (2007). *Mesoscopic Physics of Electrons and Photons*. Cambridge University Press, Cambridge. (Cited on pages 127, 128, 129, and 130.)

[Akkermans et al., 1986] Akkermans, E., Wolf, P. E., and Maynard, R. (1986). Coherent backscattering of light by disordered media: Analysis of the peak line shape. *Physical Review Letters*, 56(14):1471–1474. (Cited on page 130.)

[Altuzarra et al., 2017] Altuzarra, C., Vezzoli, S., Valente, J., Gao, W., Soci, C., Faccio, D., and Couteau, C. (2017). Coherent Perfect Absorption in Metamaterials with Entangled Photons. *ACS Photonics*, 4(9):2124–2128. (Cited on page 86.)

[Amitonova et al., 2015] Amitonova, L. V., Mosk, A. P., and Pinkse, P. W. H. (2015). The rotational memory effect of a multimode fiber. *Optics Express*, 23(16):20569. (Cited on page 130.)

[Andreoli et al., 2015] Andreoli, D., Volpe, G., Popoff, S., Katz, O., Grésillon, S., and Gigan, S. (2015). Deterministic control of broadband light through a multiply scattering medium via the multispectral transmission matrix. *Scientific Reports*, 5(1):10347. (Cited on pages 48 and 49.)

[Andrews and Phillips, 2005] Andrews, L. C. and Phillips, R. L. (2005). *Laser Beam Propagation through Random Media*. SPIE, 1000 20th Street, Bellingham, WA 98227-0010 USA. (Cited on page 98.)

[Ang et al., 2016] Ang, J. I. W., Onneau, D. A. B., Illa, M. A. V., Ilverstone, J. O. W. S., Antagati, R. A. S., Iki, S. H. M., Amashita, T. A. R. O. Y., Ujiwara, M. I. F., Asaki, M. A. S., Erai, H. I. T., Anner, M. I. G. T., Atarajan, C. H. M. N., Adfield, R. O. H. H., Rien, J. E. L. O. B., Wang, J., Bonneau, D., Villa, M., Silverstone, J. W., Santagati, R., Miki, S., Yamashita, T., Fujiwara, M., Sasaki, M., Terai, H., Tanner, M. G., Natarajan, C. M., Hadfield, R. H., O'Brien, J. L., and Thompson, M. G. (2016). Chip-to-chip quantum photonic interconnect by path-polarization interconversion. *Optica*, 3(4):407. (Cited on page 32.)

[Annoni et al., 2017] Annoni, A., Guglielmi, E., Carminati, M., Ferrari, G., Sampietro, M., Miller, D. A., Melloni, A., and Morichetti, F. (2017). Unscrambling light—automatically undoing strong mixing between modes. *Light: Science & Applications*, 6(12):e17110. (Cited on page 20.)

[Arecchi et al., 2011] Arecchi, F. T., Bortolozzo, U., Montina, A., and Residori, S. (2011). Granularity and Inhomogeneity Are the Joint Generators of Optical Rogue Waves. *Physical Review Letters*, 106(15):153901. (Cited on page 98.)

[Arkhipov and Kuperberg, 2012] Arkhipov, A. and Kuperberg, G. (2012). The bosonic birthday paradox. In *Proceedings of the Freedman Fest*, volume 18, pages 1–7. (Cited on page 34.)

[Arute et al., 2019] Arute, F., Arya, K., Babbush, R., Bacon, D., Bardin, J. C., Barends, R., Biswas, R., Boixo, S., Brandao, F. G. S. L., Buell, D. A., Burkett, B., Chen, Y., Chen, Z., Chiaro, B., Collins, R., Courtney, W., Dunsworth, A., Farhi, E., Foxen, B., Fowler, A., Gidney, C., Giustina, M., Graff, R., Guerin, K., Habegger, S., Harrigan, M. P., Hartmann, M. J., Ho, A., Hoffmann, M., Huang, T., Humble, T. S., Isakov, S. V., Jeffrey, E., Jiang, Z., Kafri, D., Kechedzhi, K., Kelly, J., Klimov, P. V., Knysh, S., Korotkov, A., Kostritsa, F., Landhuis, D., Lindmark, M., Lucero, E., Lyakh, D., Mandrà, S., McClean, J. R., McEwen, M., Megrant, A., Mi, X., Michielsen, K., Mohseni, M., Mutus, J., Naaman, O., Neeley, M., Neill, C., Niu, M. Y., Ostby, E., Petukhov, A., Platt, J. C., Quintana, C., Rieffel, E. G., Roushan, P., Rubin, N. C., Sank, D., Satzinger, K. J., Smelyanskiy, V., Sung, K. J., Trevithick, M. D., Vainsencher, A., Villalonga, B., White, T., Yao, Z. J., Yeh, P., Zalcman, A., Neven, H., and Martinis, J. M. (2019). Quantum supremacy using a programmable superconducting processor. *Nature*, 574(7779):505–510. (Cited on pages 2 and 32.)

[Aspuru-Guzik and Walther, 2012] Aspuru-Guzik, A. and Walther, P. (2012). Photonic quantum simulators. *Nature Physics*, 8(4):285–291. (Cited on page 31.)

[Aubry and Derode, 2010] Aubry, A. and Derode, A. (2010). Singular value distribution of the propagation matrix in random scattering media. *Waves in Random and Complex Media*, 20(3):333–363. (Cited on page 69.)

[Bachor and Ralph, 2004] Bachor, H. and Ralph, T. C., editors (2004). *A Guide to Experiments in Quantum Optics*. Wiley. (Cited on page 8.)

[Bandilla, 1989] Bandilla, A. (1989). The influence of phase-destroying and absorption processes on squeezing. *Journal of Modern Optics*, 36(4):435–443. (Cited on page 78.)

[Barak and Ben-Aryeh, 2007] Barak, R. and Ben-Aryeh, Y. (2007). Quantum fast Fourier transform and quantum computation by linear optics. *Journal of the Optical Society of America B*, 24(2):231. (Cited on page 60.)

[Baranger and Mello, 1994] Baranger, H. U. and Mello, P. A. (1994). Mesoscopic transport through chaotic cavities: A random S -matrix theory approach. *Physical Review Letters*, 73(1):142–145. (Cited on page 41.)

[Baranov et al., 2017] Baranov, D. G., Krasnok, A., Shegai, T., Alù, A., and Chong, Y. (2017). Coherent perfect absorbers: linear control of light with light. *Nature Reviews Materials*, 2(12):17064. (Cited on pages 84, 85, and 92.)

[Barnett and Radmore, 2002] Barnett, S. and Radmore, P. (2002). *Methods in Theoretical Quantum Optics*. Oxford University Press. (Cited on page 80.)

[Barnett et al., 1996] Barnett, S. M., Gilson, C. R., Huttner, B., and Imoto, N. (1996). Field Commutation Relations in Optical Cavities. *Physical Review Letters*, 77(9):1739–1742. (Cited on page 79.)

[Barnett et al., 1998] Barnett, S. M., Jeffers, J., Gatti, A., and Loudon, R. (1998). Quantum optics of lossy beam splitters. *Physical Review A*, 57(3):2134–2145. (Cited on pages 60, 78, 79, 80, 82, 83, 84, 86, 87, and 92.)

[Barrett et al., 2019] Barrett, T. D., Rubenok, A., Stuart, D., Barter, O., Holleczek, A., Dilley, J., Nisbet-Jones, P. B. R., Poulios, K., Marshall, G. D., O'Brien, J. L., Politi, A., Matthews, J. C. F., and Kuhn, A. (2019). Multimode interferometry for entangling

atoms in quantum networks. *Quantum Science and Technology*, 4(2):025008. (Cited on page 45.)

[Basden et al., 2003] Basden, A. G., Haniff, C. A., and Mackay, C. D. (2003). Photon counting strategies with low-light-level CCDs. *Monthly Notices of the Royal Astronomical Society*, 345(3):985–991. (Cited on page 73.)

[Bauters et al., 2011] Bauters, J. F., Heck, M. J. R., John, D., Dai, D., Tien, M.-C., Barton, J. S., Leinse, A., Heideman, R. G., Blumenthal, D. J., and Bowers, J. E. (2011). Ultra-low-loss high-aspect-ratio $Si_3N_4$ waveguides. *Optics Express*, 19(4):3163. (Cited on page 26.)

[Beenakker, 1997] Beenakker, C. W. J. (1997). Random-matrix theory of quantum transport. *Reviews of Modern Physics*, 69(3):731–808. (Cited on pages 39 and 43.)

[Beenakker, 1998] Beenakker, C. W. J. (1998). Thermal radiation and amplified spontaneous emission from a random medium. *Physical Review Letters*, 81(9):4. (Cited on page 97.)

[Beenakker, 2018] Beenakker, C. W. J. (2018). *Classical and quantum optics*, volume 1. Oxford University Press. (Cited on pages 38, 42, 43, 97, 125, 126, and 129.)

[Beenakker and Patra, 1999] Beenakker, C. W. J. and Patra, M. (1999). Photon shot noise. *Modern Physics Letters B*, 13(11):337–347. (Cited on page 97.)

[Beenakker et al., 2009] Beenakker, C. W. J., Venderbos, J. W. F., and Van Exter, M. P. (2009). Two-Photon speckle as a probe of Multi-Dimensional entanglement. *Physical Review Letters*, 102(19):1–5. (Cited on pages 97, 98, 99, and 105.)

[Bennink, 2010] Bennink, R. S. (2010). Optimal collinear Gaussian beams for spontaneous parametric down-conversion. *Physical Review A*, 81(5):1–10. (Cited on page 119.)

[Bentivegna et al., 2015] Bentivegna, M., Spagnolo, N., Vitelli, C., Flamini, F., Viggianiello, N., Latmiral, L., Mataloni, P., Brod, D. J., Galvão, E. F., Crespi, A., Ramponi, R., Osellame, R., and Sciarrino, F. (2015). Experimental scattershot boson sampling. *Science Advances*, 1(3):e1400255. (Cited on page 34.)

[Berdagué and Facq, 1982] Berdagué, S. and Facq, P. (1982). Mode division multiplexing in optical fibers. *Applied Optics*, 21(11):1950. (Cited on page 44.)

[Berkovits and Feng, 1994] Berkovits, R. and Feng, S. (1994). Correlations in coherent multiple scattering. *Physics Reports*, 238(3):135–172. (Cited on page 127.)

[Bertolotti et al., 2012] Bertolotti, J., van Putten, E. G., Blum, C., Lagendijk, A., Vos, W. L., and Mosk, A. P. (2012). Non-invasive imaging through opaque scattering layers. *Nature*, 491(7423):232–234. (Cited on page 127.)

[Bianchi and Di Leonardo, 2012] Bianchi, S. and Di Leonardo, R. (2012). A multi-mode fiber probe for holographic micromanipulation and microscopy. *Lab on a Chip*, 12(3):635–639. (Cited on page 50.)

[Blow et al., 1990] Blow, K. J., Loudon, R., Phoenix, S. J. D., and Shepherd, T. J. (1990). Continuum fields in quantum optics. *Physical Review A*, 42(7):4102–4114. (Cited on page 79.)

[Bogdanov et al., 2017] Bogdanov, S., Shalaginov, M. Y., Boltasseva, A., and Shalaev, V. M. (2017). Material platforms for integrated quantum photonics. *Optical Materials Express*, 7(1):111. (Cited on page 25.)

[Bolduc et al., 2017] Bolduc, E., Faccio, D., and Leach, J. (2017). Acquisition of multiple photon pairs with an EMCCD camera. *Journal of Optics*, 19(5):054006. (Cited on page 73.)

[Boniface et al., 2017] Boniface, A., Mounaix, M., Blochet, B., Piestun, R., and Gigan, S. (2017). Transmission-matrix-based point-spread-function engineering through a complex medium. *Optica*, 4(1):54. (Cited on pages 48 and 49.)

[Bonneau et al., 2012] Bonneau, D., Engin, E., Ohira, K., Suzuki, N., Yoshida, H., Iizuka, N., Ezaki, M., Natarajan, C. M., Tanner, M. G., Hadfield, R. H., Dorenbos, S. N., Zwiller, V., O'Brien, J. L., and Thompson, M. G. (2012). Quantum interference and manipulation of entanglement in silicon wire waveguide quantum circuits. *New Journal of Physics*, 14(4):045003. (Cited on page 45.)

[Boonzajer Flaes et al., 2018] Boonzajer Flaes, D. E., Stopka, J., Turtaev, S., de Boer, J. F., Tyc, T., and Čižmár, T. (2018). Robustness of Light-Transport Processes to Bending Deformations in Graded-Index Multimode Waveguides. *Physical Review Letters*, 120(23):233901. (Cited on pages 44, 45, 50, and 123.)

[Borhani et al., 2018] Borhani, N., Kakkava, E., Moser, C., and Psaltis, D. (2018). Learning to see through multimode fibers. *Optica*, 5(8):960. (Cited on page 50.)

[Boyd, 2008] Boyd, R. W. (2008). The Nonlinear Optical Susceptibility. In *Nonlinear Optics*, pages 1–67. Elsevier. (Cited on page 8.)

[Brandt et al., 2019] Brandt, F., Hiekkamäki, M., Bouchard, F., Huber, M., and Fickler, R. (2019). High-dimensional quantum gates using full-field spatial modes of photons. pages 1–27. (Cited on page 29.)

[Brod et al., 2019] Brod, D. J., Galvão, E. F., Crespi, A., Osellame, R., and Spagnolo, N. (2019). Photonic implementation of boson sampling: a review. *Advanced Photonics*, 1(03):1. (Cited on pages 32 and 101.)

[Bromberg et al., 2009] Bromberg, Y., Lahini, Y., Morandotti, R., and Silberberg, Y. (2009). Quantum and classical correlations in waveguide lattices. *Physical Review Letters*, 102(25):1–4. (Cited on page 97.)

[Bromberg et al., 2019] Bromberg, Y., Redding, B., Popoff, S. M., Zhao, N., Li, G., and Cao, H. (2019). Remote key establishment by random mode mixing in multimode fibers and optical reciprocity. *Optical Engineering*, 58(01):1. (Cited on page 47.)

[Broome et al., 2013] Broome, M. A., Fedrizzi, A., Rahimi-Keshari, S., Dove, J., Aaronson, S., Ralph, T. C., and White, A. G. (2013). Photonic Boson Sampling in a Tunable Circuit. *Science*, 339(6121):794–798. (Cited on page 31.)

[Brouwer, 1971] Brouwer, P. (1971). *On the Random-matrix theory of quantum transport*. PhD thesis, University of Leiden. (Cited on page 39.)

[Bruce et al., 2019] Bruce, G. D., O'Donnell, L., Chen, M., and Dholakia, K. (2019). Overcoming the speckle correlation limit to achieve a fiber wavemeter with attometer resolution. *Optics Letters*, 44(6):1367. (Cited on page 48.)

[Bruck et al., 2016] Bruck, R., Vynck, K., Lalanne, P., Mills, B., Thomson, D. J., Mashanovich, G. Z., Reed, G. T., and Muskens, O. L. (2016). All-optical spatial light modulator for reconfigurable silicon photonic circuits. *Optica*, 3(4):396. (Cited on page 46.)

[Bruschini et al., 2019] Bruschini, C., Homulle, H., Antolovic, I. M., Burri, S., and Charbon, E. (2019). Single-photon avalanche diode imagers in biophotonics: review and outlook. *Light: Science & Applications*, 8(1):87. (Cited on pages 73 and 114.)

[Bunandar et al., 2018] Bunandar, D., Lentine, A., Lee, C., Cai, H., Long, C. M., Boynton, N., Martinez, N., Derose, C., Chen, C., Grein, M., Trotter, D., Starbuck, A., Pomerene, A., Hamilton, S., Wong, F. N., Camacho, R., Davids, P., Urayama, J., and Englund, D. (2018). Metropolitan Quantum Key Distribution with Silicon Photonics. *Physical Review X*, 8(2):21009. (Cited on page 32.)

[Burgwal et al., 2017] Burgwal, R., Clements, W. R., Smith, D. H., Gates, J. C., Kolthammer, W. S., Renema, J. J., and Walmsley, I. A. (2017). Using an imperfect photonic network to implement random unitaries. *Optics Express*, 25(23):28236. (Cited on page 27.)

[Campbell and Meyer, 2009] Campbell, S. L. and Meyer, C. D. (2009). *Generalized Inverses of Linear Transformations*. Society for Industrial and Applied Mathematics. (Cited on page 73.)

[Campos et al., 1990] Campos, R. A., Saleh, B. E. A., and Teich, M. C. (1990). Fourth-order interference of joint single-photon wave packets in lossless optical systems. *Physical Review A*, 42(7):4127–4137. (Cited on page 16.)

[Candé et al., 2014] Candé, M., Goetschy, A., and Skipetrov, S. E. (2014). Transmission of quantum entanglement through a random medium. *EPL (Europhysics Letters)*, 107(5):54004. (Cited on page 97.)

[Candé and Skipetrov, 2013] Candé, M. and Skipetrov, S. E. (2013). Quantum versus classical effects in two-photon speckle patterns. *Physical Review A*, 87(1):1–11. (Cited on page 97.)

[Candes and Tao, 2006] Candes, E. J. and Tao, T. (2006). Near-Optimal Signal Recovery From Random Projections: Universal Encoding Strategies? *IEEE Transactions on Information Theory*, 52(12):5406–5425. (Cited on page 47.)

[Cao and Wiersig, 2015] Cao, H. and Wiersig, J. (2015). Dielectric microcavities: Model systems for wave chaos and non-Hermitian physics. *Reviews of Modern Physics*, 87(1):61–111. (Cited on page 46.)

[Capmany et al., 2016] Capmany, J., Gasulla, I., and Pérez, D. (2016). Microwave photonics: The programmable processor. *Nature Photonics*, 10(1):6–8. (Cited on page 20.)

[Caramazza et al., 2019] Caramazza, P., Moran, O., Murray-Smith, R., and Faccio, D. (2019). Transmission of natural scene images through a multimode fibre. *Nature Communications*, 10(1):2029. (Cited on pages 50 and 55.)

[Caravaca-Aguirre et al., 2013] Caravaca-Aguirre, A. M., Niv, E., Conkey, D. B., and Piestun, R. (2013). Real-time resilient focusing through a bending multimode fiber. *Optics Express*, 21(10):12881. (Cited on page 50.)

[Caravaca-Aguirre and Piestun, 2017] Caravaca-Aguirre, A. M. and Piestun, R. (2017). Single multimode fiber endoscope. *Optics Express*, 25(3):1656. (Cited on page 50.)

[Carolan et al., 2015] Carolan, J., Harrold, C., Sparrow, C., Martin-Lopez, E., Russell, N. J., Silverstone, J. W., Shadbolt, P. J., Matsuda, N., Oguma, M., Itoh, M., Marshall, G. D., Thompson, M. G., Matthews, J. C. F., Hashimoto, T., O'Brien, J. L., and Laing, A. (2015). Universal linear optics. *Science*, 349(6249):711–716. (Cited on pages 25, 26, 27, 32, 45, and 60.)

[Carolan et al., 2014] Carolan, J., Meinecke, J. D., Shadbolt, P. J., Russell, N. J., Ismail, N., Wörhoff, K., Rudolph, T., Thompson, M. G., O'Brien, J. L., Matthews, J. C., and Laing, A. (2014). On the experimental verification of quantum complexity in linear optics. *Nature Photonics*, 8(8):621–626. (Cited on page 32.)

[Carpenter et al., 2014] Carpenter, J., Eggleton, B. J., and Schröder, J. (2014). 110X110 Optical Mode Transfer Matrix Inversion. *Optics Express*, 22(1):96. (Cited on pages 44 and 70.)

[Ceccarelli et al., 2019] Ceccarelli, F., Atzeni, S., Prencipe, A., Farinaro, R., and Osellame, R. (2019). Thermal Phase Shifters for Femtosecond Laser Written Photonic Integrated Circuits. *Journal of Lightwave Technology*, 37(17):4275–4281. (Cited on page 27.)

[Chen et al., 2017] Chen, S., Zhou, X., Mi, C., Liu, Z., Luo, H., and Wen, S. (2017). Dielectric metasurfaces for quantum weak measurements. *Applied Physics Letters*, 110(16):161115. (Cited on page 29.)

[Chen et al., 2018] Chen, Y., Gao, J., Jiao, Z.-Q., Sun, K., Shen, W.-G., Qiao, L.-F., Tang, H., Lin, X.-F., and Jin, X.-M. (2018). Mapping Twisted Light into and out of a Photonic Chip. *Physical Review Letters*, 121(23):233602. (Cited on page 28.)

[Cherroret and Buchleitner, 2011] Cherroret, N. and Buchleitner, A. (2011). Entanglement and Thouless times from coincidence measurements across disordered media. *Physical Review A*, 83(3):033827. (Cited on page 97.)

[Chiarawongse et al., 2018] Chiarawongse, P., Li, H., Xiong, W., Hsu, C. W., Cao, H., and Kottos, T. (2018). Statistical description of transport in multimode fibers with mode-dependent loss. *New Journal of Physics*, 20(11):113028. (Cited on pages 44, 70, and 123.)

[Choi et al., 2011] Choi, W., Mosk, A. P., Park, Q.-H., and Choi, W. (2011). Transmission eigenchannels in a disordered medium. *Physical Review B*, 83(13):134207. (Cited on page 125.)

[Choi et al., 2013] Choi, Y., Hillman, T. R., Choi, W., Lue, N., Dasari, R. R., So, P. T. C., Choi, W., and Yaqoob, Z. (2013). Measurement of the Time-Resolved Reflection Matrix for Enhancing Light Energy Delivery into a Scattering Medium. *Physical Review Letters*, 111(24):243901. (Cited on page 48.)

[Choi et al., 2012] Choi, Y., Yoon, C., Kim, M., Yang, T. D., Fang-Yen, C., Dasari, R. R., Lee, K. J., and Choi, W. (2012). Scanner-free and wide-field endoscopic imaging by using a single multimode optical fiber. *Physical Review Letters*, 109(20):1–5. (Cited on pages 2 and 50.)

[Chong et al., 2010] Chong, Y. D., Ge, L., Cao, H., and Stone, A. D. (2010). Coherent perfect absorbers: Time-reversed lasers. *Physical Review Letters*, 105(5):1–4. (Cited on pages 84, 85, and 86.)

[Chong and Stone, 2011] Chong, Y. D. and Stone, A. D. (2011). Hidden Black: Coherent Enhancement of Absorption in Strongly Scattering Media. *Physical Review Letters*, 107(16):163901. (Cited on page 85.)

[Chrapkiewicz et al., 2014] Chrapkiewicz, R., Wasilewski, W., and Banaszek, K. (2014). High-fidelity spatially resolved multiphoton counting for quantum imaging applications. *Optics Letters*, 39(17):5090. (Cited on page 73.)

[Chung et al., 2019] Chung, S., Nakai, M., and Hashemi, H. (2019). Low-power thermo-optic silicon modulator for large-scale photonic integrated systems. *Optics Express*, 27(9):13430. (Cited on page 27.)

[Ciampini et al., 2016] Ciampini, M. A., Orieux, A., Paesani, S., Sciarrino, F., Corrielli, G., Crespi, A., Ramponi, R., Osellame, R., and Mataloni, P. (2016). Path-polarization hyperentangled and cluster states of photons on a chip. *Light: Science $ Applications*, 5(4):e16064–e16064. (Cited on page 32.)

[Čižmár and Dholakia, 2011] Čižmár, T. and Dholakia, K. (2011). Shaping the light transmission through a multimode optical fibre: complex transformation analysis and applications in biophotonics. *Optics Express*, 19(20):18871. (Cited on pages 44, 50, 55, 58, 70, and 72.)

[Čižmár and Dholakia, 2012] Čižmár, T. and Dholakia, K. (2012). Exploiting multimode waveguides for pure fibre-based imaging. *Nature Communications*, 3(1):1027. (Cited on pages 2, 48, 50, 114, and 130.)

[Clements et al., 2016] Clements, W. R., Humphreys, P. C., Metcalf, B. J., Kolthammer, W. S., and Walmsley, I. A. (2016). Optimal design for universal multiport interferometers. *Optica*, 3(12):1460–1465. (Cited on pages 21, 23, 24, 71, and 92.)

[Collins and Nechita, 2016] Collins, B. and Nechita, I. (2016). Random matrix techniques in quantum information theory. *Journal of Mathematical Physics*, 57(1):015215. (Cited on page 113.)

[Cooley and Tukey, 1965] Cooley, J. W. and Tukey, J. W. (1965). An Algorithm for the Machine Calculation of Complex Fourier Series. *Mathematics of Computation*, 19(90):297. (Cited on page 60.)

[Couillet and Debbah, 2011] Couillet, R. and Debbah, M. (2011). *Random matrix methods for wireless communications*. Cambridge University Press. (Cited on page 40.)

[Crespi, 2015] Crespi, A. (2015). Suppression laws for multiparticle interference in Sylvester interferometers. *Physical Review A*, 91(1):1–8. (Cited on page 62.)

[Crespi et al., 2013a] Crespi, A., Osellame, R., Ramponi, R., Brod, D. J., Galvão, E. F., Spagnolo, N., Vitelli, C., Maiorino, E., Mataloni, P., and Sciarrino, F. (2013a). Integrated multimode interferometers with arbitrary designs for photonic boson sampling. *Nature Photonics*, 7(7):545–549. (Cited on page 31.)

[Crespi et al., 2013b] Crespi, A., Osellame, R., Ramponi, R., Giovannetti, V., Fazio, R., Sansoni, L., De Nicola, F., Sciarrino, F., and Mataloni, P. (2013b). Anderson lo-

calization of entangled photons in an integrated quantum walk. *Nature Photonics*, 7(4):322–328. (Cited on page 31.)

[Crespi et al., 2011] Crespi, A., Ramponi, R., Osellame, R., Sansoni, L., Bongioanni, I., Sciarrino, F., Vallone, G., and Mataloni, P. (2011). Integrated photonic quantum gates for polarization qubits. *Nature Communications*, 2(1):566. (Cited on page 31.)

[Da Cunha Pereira et al., 2013] Da Cunha Pereira, M., Becerra, F. E., Glebov, B. L., Fan, J., Nam, S. W., and Migdall, A. (2013). Demonstrating highly symmetric single-mode, single-photon heralding efficiency in spontaneous parametric downconversion. *Optics letters*, 38(10):1609–11. (Cited on page 119.)

[D'Ambrosio et al., 2019] D'Ambrosio, V., Carvacho, G., Agresti, I., Marrucci, L., and Sciarrino, F. (2019). Tunable Two-Photon Quantum Interference of Structured Light. *Physical Review Letters*, 122(1):3–4. (Cited on page 15.)

[Davanco et al., 2017] Davanco, M., Liu, J., Sapienza, L., Zhang, C.-Z., De Miranda Cardoso, J. V., Verma, V., Mirin, R., Nam, S. W., Liu, L., and Srinivasan, K. (2017). Heterogeneous integration for on-chip quantum photonic circuits with single quantum dot devices. *Nature Communications*, 8(1):889. (Cited on page 28.)

[Defienne, 2015] Defienne, H. (2015). *Quantum walks of photons in disordered media*. PhD thesis, UPMC. (Cited on pages 51 and 58.)

[Defienne et al., 2014] Defienne, H., Barbieri, M., Chalopin, B., Chatel, B., Walmsley, I. a., Smith, B. J., and Gigan, S. (2014). Nonclassical light manipulation in a multiple-scattering medium. *Optics Letters*, 39(21):6090. (Cited on page 51.)

[Defienne et al., 2016] Defienne, H., Barbieri, M., Walmsley, I. A., Smith, B. J., and Gigan, S. (2016). Two-photon quantum walk in a multimode fiber. *Science Advances*, 2(1):e1501054. (Cited on pages 51, 52, and 83.)

[Defienne et al., 2018a] Defienne, H., Reichert, M., and Fleischer, J. W. (2018a). Adaptive Quantum Optics with Spatially Entangled Photon Pairs. *Physical Review Letters*, 121(23):233601. (Cited on page 52.)

[Defienne et al., 2018b] Defienne, H., Reichert, M., and Fleischer, J. W. (2018b). General Model of Photon-Pair Detection with an Image Sensor. *Physical Review Letters*, 120(20):203604. (Cited on pages 73 and 114.)

[del Hougne and Lerosey, 2018] del Hougne, P. and Lerosey, G. (2018). Leveraging Chaos for Wave-Based Analog Computation: Demonstration with Indoor Wireless Communication Signals. *Physical Review X*, 8(4):1–20. (Cited on page 52.)

[Derode et al., 2001] Derode, A., Tourin, A., and Fink, M. (2001). Random multiple scattering of ultrasound. II. Is time reversal a self-averaging process? *Physical Review E*, 64(3):036606. (Cited on pages 69 and 72.)

[Descloux et al., 2016] Descloux, A., Amitonova, L. V., and Pinkse, P. W. H. (2016). Aberrations of the point spread function of a multimode fiber due to partial mode excitation. *Optics Express*, 24(16):18501. (Cited on page 50.)

[Deutsch, 1985] Deutsch, D. (1985). Quantum Theory, the Church-Turing Principle and the Universal Quantum Computer. *Proceedings of the Royal Society A: Mathematical, Physical and Engineering Sciences*, 400(1818):97–117. (Cited on page 1.)

[Dhand et al., 2016] Dhand, I., Khalid, A., Lu, H., and Sanders, B. C. (2016). Accurate and precise characterization of linear optical interferometers. *Journal of Optics*, 18(3):035204. (Cited on page 55.)

[Di Leonardo and Bianchi, 2011] Di Leonardo, R. and Bianchi, S. (2011). Hologram transmission through multi-mode optical fibers. *Optics Express*, 19(1):247. (Cited on pages 44 and 50.)

[Di Lorenzo Pires et al., 2012] Di Lorenzo Pires, H., Woudenberg, J., and Van Exter, M. P. (2012). Statistical properties of two-photon speckles. *Physical Review A*, 85(3):1–5. (Cited on pages 99 and 100.)

[Dittel et al., 2018a] Dittel, C., Dufour, G., Walschaers, M., Weihs, G., Buchleitner, A., and Keil, R. (2018a). Totally Destructive Interference for Permutation-Symmetric Many-Particle States. *Physical Review Letters*, 120(24):240404. (Cited on page 60.)

[Dittel et al., 2018b] Dittel, C., Dufour, G., Walschaers, M., Weihs, G., Buchleitner, A., and Keil, R. (2018b). Totally destructive interference for permutation-symmetric many-particle states. *Physical Review A*, 97(6):1–14. (Cited on page 60.)

[DiVincenzo, 1995] DiVincenzo, D. P. (1995). Two-bit gates are universal for quantum computation. *Physical Review A*, 51(2):1015–1022. (Cited on page 17.)

[DiVincenzo, 2000] DiVincenzo, D. P. (2000). The Physical Implementation of Quantum Computation. *Fortschritte der Physik*, 48(9-11):771–783. (Cited on page 17.)

[Dixon et al., 2014] Dixon, P. B., Rosenberg, D., Stelmakh, V., Grein, M. E., Bennink, R. S., Dauler, E. A., Kerman, A. J., Molnar, R. J., and Wong, F. N. C. (2014). Heralding efficiency and correlated-mode coupling of near-IR fiber-coupled photon pairs. *Physical Review A*, 90(4):043804. (Cited on page 119.)

[Donoho, 2006] Donoho, D. (2006). Compressed sensing. *IEEE Transactions on Information Theory*, 52(4):1289–1306. (Cited on page 47.)

[Dorokhov, 1982] Dorokhov, O. (1982). Transmission coefficient and the localization length of an electron in N bound disordered chains. *Soviet Journal of Experimental and Theoretical Physics Letters*, 36(7):318. (Cited on page 41.)

[Dorokhov, 1984] Dorokhov, O. (1984). On the coexistence of localized and extended electronic states in the metallic phase. *Solid State Communications*, 51(6):381–384. (Cited on page 42.)

[Doya et al., 2002] Doya, V., Legrand, O., Mortessagne, F., and Miniatura, C. (2002). Speckle statistics in a chaotic multimode fiber. *Physical Review E*, 65(5):056223. (Cited on page 46.)

[Dragoman and Dragoman, 2004] Dragoman, D. and Dragoman, M. (2004). *Quantum-Classical Analogies*. The Frontiers Collection. Springer Berlin Heidelberg, Berlin, Heidelberg. (Cited on pages 41 and 127.)

[Drémeau et al., 2015] Drémeau, A., Liutkus, A., Martina, D., Katz, O., Schülke, C., Krzakala, F., Gigan, S., and Daudet, L. (2015). Reference-less measurement of the transmission matrix of a highly scattering material using a DMD and phase retrieval techniques. *Optics express*, 23(9):11898–911. (Cited on pages 55 and 72.)

[Dutta Gupta, 2007] Dutta Gupta, S. (2007). Strong-interaction—mediated critical coupling at two distinct frequencies. *Optics Letters*, 32(11):1483. (Cited on page 84.)

[Dyakonov et al., 2018] Dyakonov, I. V., Pogorelov, I. A., Bobrov, I. B., Kalinkin, A. A., Straupe, S. S., Kulik, S. P., Dyakonov, P. V., and Evlashin, S. A. (2018). Reconfigurable Photonics on a Glass Chip. *Physical Review Applied*, 10(4):044048. (Cited on page 26.)

[Dyson, 1962a] Dyson, F. J. (1962a). Statistical theory of the energy levels of complex systems. I. *Journal of Mathematical Physics*, 3(1):140–156. (Cited on page 40.)

[Dyson, 1962b] Dyson, F. J. (1962b). The Threefold Way. Algebraic Structure of Symmetry Groups and Ensembles in Quantum Mechanics. *Journal of Mathematical Physics*, 3(6):1199–1215. (Cited on page 40.)

[Edgar et al., 2012] Edgar, M. P., Tasca, D. S., Izdebski, F., Warburton, R. E., Leach, J., Agnew, M., Buller, G. S., Boyd, R. W., and Padgett, M. J. (2012). Imaging high-dimensional spatial entanglement with a camera. *Nature Communications*, 3(1):984. (Cited on page 73.)

[Ellis et al., 2018] Ellis, D. J., Bennett, A. J., Dangel, C., Lee, J. P., Griffiths, J. P., Mitchell, T. A., Paraiso, T. K., Spencer, P., Ritchie, D. A., and Shields, A. J. (2018). Independent indistinguishable quantum light sources on a reconfigurable photonic integrated circuit. *Applied Physics Letters*, 112(21). (Cited on page 28.)

[Emanueli and Arie, 2003] Emanueli, S. and Arie, A. (2003). Temperature-Dependent Dispersion Equations for KTiOPO4 and KTiOAsO4. *Applied Optics*, 42(33):6661. (Cited on page 119.)

[Esat Kondakci et al., 2016] Esat Kondakci, H., Szameit, A., Abouraddy, A. F., Christodoulides, D. N., and Saleh, B. E. A. (2016). Sub-thermal to super-thermal light statistics from a disordered lattice via deterministic control of excitation symmetry. *Optica*, 3(5):477. (Cited on page 97.)

[Fan et al., 2019] Fan, P., Zhao, T., and Su, L. (2019). Deep learning the high variability and randomness inside multimode fibers. *Optics Express*, 27(15):20241. (Cited on page 50.)

[Fang et al., 2015] Fang, X., MacDonald, K. F., and Zheludev, N. I. (2015). Controlling light with light using coherent metadevices: all-optical transistor, summator and invertor. *Light: Science & Applications*, 4(5):e292–e292. (Cited on pages 86 and 92.)

[Farahi et al., 2013] Farahi, S., Ziegler, D., Papadopoulos, I. N., Psaltis, D., and Moser, C. (2013). Dynamic bending compensation while focusing through a multimode fiber. *Optics Express*, 21(19):22504. (Cited on page 50.)

[Fayard et al., 2015] Fayard, N., Cazé, A., Pierrat, R., and Carminati, R. (2015). Intensity correlations between reflected and transmitted speckle patterns. *Physical Review A*, 92(3):033827. (Cited on page 129.)

[Fayard et al., 2017] Fayard, N., Goetschy, A., Pierrat, R., and Carminati, R. (2017). Mutual information between reflected and transmitted speckle images. *Physical Review Letters*, 120(7):73901. (Cited on page 129.)

[Fearn and Loudon, 1989] Fearn, H. and Loudon, R. (1989). Theory of two-photon interference. *Journal of the Optical Society of America B*, 6(5):917. (Cited on pages 14 and 80.)

[Fedrizzi et al., 2007] Fedrizzi, A., Herbst, T., Poppe, A., Jennewein, T., and Zeilinger, A. (2007). A wavelength-tunable fiber-coupled source of narrowband entangled photons. *Optics Express*, 15(23):15377. (Cited on page 119.)

[Feng et al., 2019] Feng, L.-T., Zhang, M., Xiong, X., Chen, Y., Wu, H., Li, M., Guo, G.-P., Guo, G.-C., Dai, D.-X., and Ren, X.-F. (2019). On-chip transverse-mode entangled photon pair source. *npj Quantum Information*, 5(1):2. (Cited on page 28.)

[Feng et al., 2016] Feng, L.-T., Zhang, M., Zhou, Z.-Y., Li, M., Xiong, X., Yu, L., Shi, B.-S., Guo, G.-P., Dai, D.-X., Ren, X.-F., and Guo, G.-C. (2016). On-chip coherent conversion of photonic quantum entanglement between different degrees of freedom. *Nature Communications*, 7(1):11985. (Cited on page 28.)

[Feng et al., 1988] Feng, S., Kane, C., Lee, P. A., and Stone, A. D. (1988). Correlations and Fluctuations of Coherent Wave Transmission through Disordered Media. *Physical Review Letters*, 61(7):834–837. (Cited on pages 127 and 129.)

[Fickler et al., 2020] Fickler, R., Bouchard, F., Giese, E., Grillo, V., Leuchs, G., and Karimi, E. (2020). Full-field mode sorter using two optimized phase transformations for high-dimensional quantum cryptography. *Journal of Optics*, 22(2):024001. (Cited on page 29.)

[Fickler et al., 2017] Fickler, R., Ginoya, M., and Boyd, R. W. (2017). Custom-tailored spatial mode sorting by controlled random scattering. *Physical Review B*, 95(16):161108. (Cited on pages 48 and 49.)

[Fickler et al., 2013] Fickler, R., Krenn, M., Lapkiewicz, R., Ramelow, S., and Zeilinger, A. (2013). Real-Time Imaging of Quantum Entanglement. *Scientific Reports*, 3(1):1914. (Cited on pages 73 and 114.)

[Flamini et al., 2015] Flamini, F., Magrini, L., Rab, A. S., Spagnolo, N., D'Ambrosio, V., Mataloni, P., Sciarrino, F., Zandrini, T., Crespi, A., Ramponi, R., and Osellame, R. (2015). Thermally reconfigurable quantum photonic circuits at telecom wavelength by femtosecond laser micromachining. *Light: Science & Applications*, 4(11):1–7. (Cited on page 27.)

[Flamini et al., 2019] Flamini, F., Spagnolo, N., and Sciarrino, F. (2019). Photonic quantum information processing: a review. *Reports on Progress in Physics*, 82(1):016001. (Cited on pages 25, 31, and 35.)

[Florentin et al., 2018] Florentin, R., Kermene, V., Desfarges-Berthelemot, A., and Barthelemy, A. (2018). Fast Transmission Matrix Measurement of a Multimode Optical Fiber With Common Path Reference. *IEEE Photonics Journal*, 10(5):1–6. (Cited on page 55.)

[Fontaine et al., 2017] Fontaine, N. K., Ryf, R., Chen, H., Neilson, D., and Carpenter, J. (2017). Design of High Order Mode-Multiplexers using Multiplane Light Conversion. In *2017 European Conference on Optical Communication (ECOC)*, volume 2017-Septe, pages 1–3. IEEE. (Cited on page 29.)

[Fontaine et al., 2019] Fontaine, N. K., Ryf, R., Chen, H., Neilson, D. T., Kim, K., and Carpenter, J. (2019). Laguerre-Gaussian mode sorter. *Nature Communications*, 10(1):1865. (Cited on pages 29 and 30.)

[Fontaine et al., 2018] Fontaine, N. K., Ryf, R., Chen, H., Wittek, S., Li, J., Alvarado, J. C., Lopez, J. E. A., Cappuzzo, M., Kopf, R., Tate, A., Safar, H., Bolle, C., Neilson, D. T., Burrows, E., Kim, K., Sillard, P., Achten, F., Bigot, M., Amezcua-Correa, A., Correa, R. A., Du, J., He, Z., and Carpenter, J. (2018). Packaged 45-Mode Multiplexers for a 50-$\mu$m Graded Index Fiber. In *2018 European Conference on Optical Communication (ECOC)*, volume 2018-Septe, pages 1–3. IEEE. (Cited on page 44.)

[Forbes et al., 2016] Forbes, A., Dudley, A., and McLaren, M. (2016). Creation and detection of optical modes with spatial light modulators. *Advances in Optics and Photonics*, 8(2):200–227. (Cited on page 29.)

[Freund, 1990] Freund, I. (1990). Looking through walls and around corners. *Physica A: Statistical Mechanics and its Applications*, 168(1):49–65. (Cited on page 127.)

[Freund et al., 1988] Freund, I., Rosenbluh, M., and Feng, S. (1988). Memory Effects in Propagation of Optical Waves through Disordered Media. *Physical Review Letters*, 61(20):2328–2331. (Cited on page 127.)

[Fridman et al., 2012] Fridman, M., Suchowski, H., Nixon, M., Friesem, A. A., and Davidson, N. (2012). Modal dynamics in multimode fibers. *Journal of the Optical Society of America A*, 29(4):541. (Cited on page 45.)

[García-Martín et al., 2002] García-Martín, A., Scheffold, F., Nieto-Vesperinas, M., and Sáenz, J. J. (2002). Finite-Size Effects on Intensity Correlations in Random Media. *Physical Review Letters*, 88(14):143901. (Cited on page 129.)

[García-Patrón et al., 2019] García-Patrón, R., Renema, J. J., and Shchesnovich, V. (2019). Simulating boson sampling in lossy architectures. *Quantum*, 3:169. (Cited on page 78.)

[Gérardin et al., 2014] Gérardin, B., Laurent, J., Derode, A., Prada, C., and Aubry, A. (2014). Full transmission and reflection of waves propagating through a maze of disorder. *Physical Review Letters*, 113(17):1–5. (Cited on page 42.)

[Giordani et al., 2018] Giordani, T., Flamini, F., Pompili, M., Viggianiello, N., Spagnolo, N., Crespi, A., Osellame, R., Wiebe, N., Walschaers, M., Buchleitner, A., and Sciarrino, F. (2018). Experimental statistical signature of many-body quantum interference. *Nature Photonics*, 12(3):173–178. (Cited on page 101.)

[Glauber, 1963a] Glauber, R. J. (1963a). Coherent and Incoherent States of the Radiation Field. *Physical Review*, 131(6):2766–2788. (Cited on page 7.)

[Glauber, 1963b] Glauber, R. J. (1963b). The Quantum Theory of Optical Coherence. *Physical Review*, 130(6):2529–2539. (Cited on pages 8 and 12.)

[Gloge, 1971] Gloge, D. (1971). Weakly Guiding Fibers. *Applied Optics*, 10(10):2252–2258. (Cited on page 43.)

[Gmachl, 2010] Gmachl, C. F. (2010). Suckers for light. *Nature*, 467(7311):37–39. (Cited on page 84.)

[Goetschy and Stone, 2013] Goetschy, A. and Stone, A. D. (2013). Filtering Random Matrices: The Effect of Incomplete Channel Control in Multiple Scattering. *Physical Review Letters*, 111(6):063901. (Cited on pages 44 and 123.)

[Goodman, 2005a] Goodman, J. W. (2005a). *Introduction to Fourier Optics*. (Cited on page 46.)

[Goodman, 2005b] Goodman, J. W. (2005b). *Speckle phenomena in optics: theory and applications*. Roberts and Company Publishers. (Cited on pages 38, 39, and 96.)

[Goorden et al., 2014] Goorden, S. A., Horstmann, M., Mosk, A. P., Škorić, B., and Pinkse, P. W. H. (2014). Quantum-secure authentication of a physical unclonable key. *Optica*, 1(6):421. (Cited on page 47.)

[Gordon et al., 2019] Gordon, G. S. D., Gataric, M., Ramos, A. G. C. P., Mouthaan, R., Williams, C., Yoon, J., Wilkinson, T. D., and Bohndiek, S. E. (2019). Characterising optical fibre transmission matrices using metasurface reflector stacks for lensless imaging without distal access. (Cited on page 50.)

[Gottesman and Chuang, 1999] Gottesman, D. and Chuang, I. L. (1999). Demonstrating the viability of universal quantum computation using teleportation and single-qubit operations. *Nature*, 402(6760):390–393. (Cited on page 18.)

[Gräfe et al., 2016] Gräfe, M., Heilmann, R., Lebugle, M., Guzman-Silva, D., Perez-Leija, A., and Szameit, A. (2016). Integrated photonic quantum walks. *Journal of Optics*, 18(10):103002. (Cited on page 31.)

[Grice et al., 2011] Grice, W. P., Bennink, R. S., Goodman, D. S., and Ryan, A. T. (2011). Spatial entanglement and optimal single-mode coupling. *Physical Review A*, 83(2):023810. (Cited on page 119.)

[Grice et al., 2001] Grice, W. P., U'Ren, A. B., and Walmsley, I. A. (2001). Eliminating frequency and space-time correlations in multiphoton states. *Physical Review A*, 64(6):1–7. (Cited on page 12.)

[Grice and Walmsley, 1997] Grice, W. P. and Walmsley, I. A. (1997). Spectral information and distinguishability in type-II down-conversion with a broadband pump. *Physical Review A*, 56(2):1627–1634. (Cited on page 12.)

[Gruner and Welsch, 1996] Gruner, T. and Welsch, D.-G. (1996). Quantum-optical input-output relations for dispersive and lossy multilayer dielectric plates. *Physical Review A*, 54(2):1661–1677. (Cited on page 78.)

[Gu et al., 2015] Gu, R. Y., Mahalati, R. N., and Kahn, J. M. (2015). Design of flexible multi-mode fiber endoscope. *Optics Express*, 23(21):26905. (Cited on page 50.)

[Gusachenko et al., 2017] Gusachenko, I., Chen, M., and Dholakia, K. (2017). Raman imaging through a single multimode fibre. *Optics Express*, 25(12):13782. (Cited on page 50.)

[Hamilton et al., 2017] Hamilton, C. S., Kruse, R., Sansoni, L., Barkhofen, S., Silberhorn, C., and Jex, I. (2017). Gaussian Boson Sampling. *Physical Review Letters*, 119(17):170501. (Cited on page 34.)

[Han et al., 2015] Han, S., Seok, T. J., Quack, N., Yoo, B.-W., and Wu, M. C. (2015). Large-scale silicon photonic switches with movable directional couplers. *Optica*, 2(4):370. (Cited on page 27.)

[Hardal and Wubs, 2019] Hardal, A. Ü. C. and Wubs, M. (2019). Quantum coherent absorption of squeezed light. *Optica*, 6(2):181. (Cited on page 86.)

[Harris et al., 2018] Harris, N. C., Carolan, J., Bunandar, D., Prabhu, M., Hochberg, M., Baehr-Jones, T., Fanto, M. L., Smith, A. M., Tison, C. C., Alsing, P. M., and Englund, D. (2018). Linear programmable nanophotonic processors. *Optica*, 5(12):1623. (Cited on pages 25, 27, 31, 35, and 45.)

[Harris et al., 2014] Harris, N. C., Ma, Y., Mower, J., Baehr-Jones, T., Englund, D., Hochberg, M., and Galland, C. (2014). Efficient, compact and low loss thermo-optic phase shifter in silicon. *Optics Express*, 22(9):10487. (Cited on page 27.)

[Harris et al., 2017] Harris, N. C., Steinbrecher, G. R., Prabhu, M., Lahini, Y., Mower, J., Bunandar, D., Chen, C., Wong, F. N. C., Baehr-Jones, T., Hochberg, M., Lloyd, S., and Englund, D. (2017). Quantum transport simulations in a programmable nanophotonic processor. *Nature Photonics*, 11(7):447–452. (Cited on pages 26, 27, and 32.)

[Hastings et al., 1994] Hastings, M. B., Stone, A. D., and Baranger, H. U. (1994). Inequivalence of weak localization and coherent backscattering. *Physical Review B*, 50(12):8230–8244. (Cited on page 130.)

[He et al., 2007] He, B., Bergou, J. A., and Wang, Z. (2007). Implementation of quantum operations on single-photon qudits. *Physical Review A*, 76(4):1–4. (Cited on page 24.)

[Heeres et al., 2013] Heeres, R. W., Kouwenhoven, L. P., and Zwiller, V. (2013). Quantum interference in plasmonic circuits. *Nature Nanotechnology*, 8(10):719–722. (Cited on page 15.)

[Ho and Kahn, 2011a] Ho, K.-p. and Kahn, J. M. (2011a). Mode-dependent loss and gain: statistics and effect on mode-division multiplexing. *Optics Express*, 19(17):16612. (Cited on page 44.)

[Ho and Kahn, 2011b] Ho, K.-P. and Kahn, J. M. (2011b). Statistics of Group Delays in Multimode Fiber With Strong Mode Coupling. *Journal of Lightwave Technology*, 29(21):3119–3128. (Cited on pages 44 and 123.)

[Ho and Kahn, 2013] Ho, K.-P. and Kahn, J. M. (2013). Mode Coupling and its Impact on Spatially Multiplexed Systems. In *Optical Fiber Telecommunications*, pages 491–568. Elsevier, sixth edit edition. (Cited on page 44.)

[Hofer and Brasselet, 2019] Hofer, M. and Brasselet, S. (2019). Manipulating the transmission matrix of scattering media for nonlinear imaging beyond the memory effect. *Optics Letters*, 44(9):2137. (Cited on pages 58 and 72.)

[Hong et al., 1987] Hong, C. K., Ou, Z. Y., and Mandel, L. (1987). Measurement of subpicosecond time intervals between two photons by interference. *Physical Review Letters*, 59(18):2044–2046. (Cited on pages 14, 51, 62, 81, and 86.)

[Horstmeyer et al., 2013] Horstmeyer, R., Judkewitz, B., Vellekoop, I. M., Assawaworrarit, S., and Yang, C. (2013). Physical key-protected one-time pad. *Scientific Reports*, 3(1):3543. (Cited on page 47.)

[Horstmeyer et al., 2015] Horstmeyer, R., Ruan, H., and Yang, C. (2015). Guidestar-assisted wavefront-shaping methods for focusing light into biological tissue. *Nature Photonics*, 9(9):563–571. (Cited on page 46.)

[Hsu et al., 2017] Hsu, C. W., Liew, S. F., Goetschy, A., Cao, H., and Douglas Stone, A. (2017). Correlation-enhanced control of wave focusing in disordered media. *Nature Physics*, 13(5):497–502. (Cited on page 128.)

[Huang and Agarwal, 2014] Huang, S. and Agarwal, G. S. (2014). Coherent perfect absorption of path entangled single photons. *Optics Express*, 22(17):20936. (Cited on page 86.)

[Huisman, 2013] Huisman, S. (2013). *Light Control with Ordered and Disordered Nanophotonic Media*. PhD thesis, University of Twente. (Cited on page 70.)

[Huisman et al., 2014a] Huisman, S. R., Huisman, T. J., Goorden, S. A., Mosk, A. P., and Pinkse, P. W. H. (2014a). Programming balanced optical beam splitters in white paint. *Optics Express*, 22(7):8320. (Cited on pages 52 and 78.)

[Huisman et al., 2015] Huisman, S. R., Huisman, T. J., Wolterink, T. A. W., Mosk, A. P., and Pinkse, P. W. H. (2015). Programmable multiport optical circuits in opaque scattering materials. *Optics Express*, 23(3):3102. (Cited on pages 48, 52, and 55.)

[Huisman et al., 2014b] Huisman, T. J., Huisman, S. R., Mosk, A. P., and Pinkse, P. W. H. (2014b). Controlling single-photon Fock-state propagation through opaque scattering media. *Applied Physics B: Lasers and Optics*, 116(3):603–607. (Cited on pages 50 and 51.)

[Humphreys et al., 2013] Humphreys, P. C., Metcalf, B. J., Spring, J. B., Moore, M., Jin, X.-M., Barbieri, M., Kolthammer, W. S., and Walmsley, I. A. (2013). Linear Optical Quantum Computing in a Single Spatial Mode. *Physical Review Letters*, 111(15):150501. (Cited on page 27.)

[Humphreys et al., 2014] Humphreys, P. C., Metcalf, B. J., Spring, J. B., Moore, M., Salter, P. S., Booth, M. J., Steven Kolthammer, W., and Walmsley, I. A. (2014). Strain-optic active control for quantum integrated photonics. *Optics Express*, 22(18):21719. (Cited on page 27.)

[Huttner and Barnett, 1992] Huttner, B. and Barnett, S. M. (1992). Quantization of the electromagnetic field in dielectrics. *Physical Review A*, 46(7):4306–4322. (Cited on page 79.)

[Imany et al., 2019] Imany, P., Jaramillo-Villegas, J. A., Alshaykh, M. S., Lukens, J. M., Odele, O. D., Moore, A. J., Leaird, D. E., Qi, M., and Weiner, A. M. (2019). High-dimensional optical quantum logic in large operational spaces. *npj Quantum Information*, 5(1):59. (Cited on page 27.)

[Imry, 1986] Imry, Y. (1986). Active Transmission Channels and Universal Conductance Fluctuations. *Europhysics Letters (EPL)*, 1(5):249–256. (Cited on page 42.)

[Jachura and Chrapkiewicz, 2015] Jachura, M. and Chrapkiewicz, R. (2015). Shot-by-shot imaging of Hong–Ou–Mandel interference with an intensified sCMOS camera. *Optics Letters*, 40(7):1540. (Cited on page 73.)

[Jacques et al., 2019] Jacques, M., Samani, A., El-Fiky, E., Patel, D., Xing, Z., and Plant, D. V. (2019). Optimization of thermo-optic phase-shifter design and mitigation of thermal crosstalk on the SOI platform. *Optics Express*, 27(8):10456. (Cited on page 27.)

[Jalabert et al., 1994] Jalabert, R. A., Pichard, J.-L., and Beenakker, C. W. J. (1994). Universal Quantum Signatures of Chaos in Ballistic Transport. *Europhysics Letters (EPL)*, 27(4):255–260. (Cited on page 41.)

[Janik and Nowak, 2003] Janik, R. A. and Nowak, M. A. (2003). Wishart and anti-Wishart random matrices. *Journal of Physics A: Mathematical and General*, 36(12 SPEC. ISS.):3629–3637. (Cited on page 40.)

[Jeffers, 2000] Jeffers, J. (2000). Interference and the lossless lossy beam splitter. *Journal of Modern Optics*, 47(11):1819–1824. (Cited on pages 86, 87, and 92.)

[Jeffers, 2019] Jeffers, J. (2019). Nonlocal Coherent Perfect Absorption. *Physical Review Letters*, 123(14):143602. (Cited on page 86.)

[Jon Cartwright, 2007] Jon Cartwright (2007). Opaque lens focuses light – Physics World. (Cited on page 47.)

[Joseph et al., 2015] Joseph, S. K., Sabuco, J., Chew, L. Y., and Sanjuán, M. A. F. (2015). Effect of geometry on the classical entanglement in a chaotic optical fiber. *Optics Express*, 23(25):32191. (Cited on page 46.)

[Jost et al., 1998] Jost, B., Sergienko, A., Abouraddy, A., Saleh, B., and Teich, M. (1998). Spatial correlations of spontaneously down-converted photon pairs detected with a single-photon-sensitive CCD camera. *Optics Express*, 3(2):81. (Cited on page 73.)

[Judkewitz et al., 2015] Judkewitz, B., Horstmeyer, R., Vellekoop, I. M., Papadopoulos, I. N., and Yang, C. (2015). Translation correlations in anisotropically scattering media. *Nature Physics*, 11(June):1–6. (Cited on page 128.)

[Kang et al., 2015] Kang, S., Jeong, S., Choi, W., Ko, H., Yang, T. D., Joo, J. H., Lee, J.-S., Lim, Y.-S., Park, Q.-H., and Choi, W. (2015). Imaging deep within a scattering medium using collective accumulation of single-scattered waves. *Nature Photonics*, 9(4):253–258. (Cited on page 48.)

[Karimi et al., 2014a] Karimi, E., Boyd, R. W., De La Hoz, P., de Guise, H., Řeháček, J., Hradil, Z., Aiello, A., Leuchs, G., and Sánchez-Soto, L. L. (2014a). Radial quantum number of Laguerre-Gauss modes. *Physical Review A*, 89(6):063813. (Cited on page 29.)

[Karimi et al., 2014b] Karimi, E., Giovannini, D., Bolduc, E., Bent, N., Miatto, F. M., Padgett, M. J., and Boyd, R. W. (2014b). Exploring the quantum nature of the radial degree of freedom of a photon via Hong-Ou-Mandel interference. *Physical Review A*, 89(1):013829. (Cited on page 15.)

[Katz et al., 2014] Katz, O., Small, E., Guan, Y., Silberberg, Y., Heidmann, P., Fink, M., and Gigan, S. (2014). Non-invasive real-time imaging through scattering layers and around corners via speckle correlations. *Nature Photonics*, 8(10):784–790. (Cited on page 127.)

[Kaufman et al., 2018] Kaufman, A. M., Tichy, M. C., Mintert, F., Rey, A. M., and Regal, C. A. (2018). The Hong–Ou–Mandel Effect With Atoms. pages 377–427. (Cited on page 15.)

[Kelley and Kleiner, 1964] Kelley, P. L. and Kleiner, W. H. (1964). Theory of Electromagnetic Field Measurement and Photoelectron Counting. *Physical Review*, 136(2A):A316–A334. (Cited on page 80.)

[Kiesewetter, 2010] Kiesewetter, D. V. (2010). Polarisation characteristics of light from multimode optical fibres. *Quantum Electronics*, 40(6):519–524. (Cited on page 45.)

[Kim et al., 2013] Kim, M., Choi, W., Yoon, C., Kim, G. H., and Choi, W. (2013). Relation between transmission eigenchannels and single-channel optimizing modes in a disordered medium. *Optics Letters*, 38(16):2994. (Cited on page 125.)

[Kim et al., 2012] Kim, M., Choi, Y., Yoon, C., Choi, W., Kim, J., Park, Q. H., and Choi, W. (2012). Maximal energy transport through disordered media with the implementation of transmission eigenchannels. *Nature Photonics*, 6(9):581–585. (Cited on page 125.)

[Kim and Grice, 2003] Kim, Y.-H. and Grice, W. P. (2003). Observation of correlated-photon statistics using a single detector. *Physical Review A*, 67(6):065802. (Cited on page 14.)

[Kiršanskė et al., 2017] Kiršanskė, G., Thyrrestrup, H., Daveau, R. S., Dreeßen, C. L., Pregnolato, T., Midolo, L., Tighineanu, P., Javadi, A., Stobbe, S., Schott, R., Ludwig, A., Wieck, A. D., Park, S. I., Song, J. D., Kuhlmann, A. V., Söllner, I., Löbl, M. C., Warburton, R. J., and Lodahl, P. (2017). Indistinguishable and efficient single photons from a quantum dot in a planar nanobeam waveguide. *Physical Review B*, 96(16):165306. (Cited on page 28.)

[Knill et al., 2001] Knill, E., La, R., Milburn, G. J., Laflamme, R., and Milburn, G. J. (2001). A scheme for efficient quantum computation with linear optics. *Nature*, 409(6816):46–52. (Cited on page 18.)

[Knill et al., 2002] Knill, E., Laflamme, R., Ashikhmin, A., Barnum, H., Viola, L., and Zurek, W. H. (2002). Introduction to Quantum Error Correction. In *Quantum Computation: A Grand Mathematical Challenge for the Twenty-First Century and the Millennium*, pages 221–235. Proceedings of Symposia in Applied Mathematics. (Cited on page 17.)

[Kok et al., 2007] Kok, P., Munro, W. J., Nemoto, K., Ralph, T. C., Dowling, J. P., and Milburn, G. J. (2007). Linear optical quantum computing with photonic qubits. *Reviews of Modern Physics*, 79(1):135–174. (Cited on pages 2, 18, 78, and 92.)

[Kondakci et al., 2017] Kondakci, H. E., Szameit, A., Abouraddy, A. F., Christodoulides, D. N., and Saleh, B. E. A. (2017). Interferometric control of the photon-number distribution. *APL Photonics*, 2(7):071301. (Cited on page 97.)

[Korneev et al., 2018] Korneev, A., Kovalyuk, V., An, P., Golikov, A., Zubkova, E., Goltsman, G., Ferrari, S., Kahl, O., and Pernice, W. (2018). Superconducting Single-Photon Detectors for Integrated Nanophotonics Circuits. *2017 16th International Superconductive Electronics Conference, ISEC 2017*, 2018-Janua:1–3. (Cited on page 28.)

[Krenn et al., 2017] Krenn, M., Malik, M., Erhard, M., Zeilinger, A., Soc, A., and Krenn, M. (2017). Orbital angular momentum of photons and the entanglement of Laguerre – Gaussian modes Subject Areas : Authors for correspondence :. *Philosophical Transac-*

*tions of the Royal Society A: Mathematical, Physical and Engineering Sciences*. (Cited on page 29.)

[Kruse et al., 2019] Kruse, R., Hamilton, C. S., Sansoni, L., Barkhofen, S., Silberhorn, C., and Jex, I. (2019). Detailed study of Gaussian boson sampling. *Physical Review A*, 100(3):032326. (Cited on page 34.)

[Kues et al., 2016] Kues, M., Morandotti, R., Moss, D. J., Bromberg, Y., Caspani, L., Chu, S. T., Roztocki, P., Little, B. E., Wetzel, B., Reimer, C., Grazioso, F., and Johnston, T. (2016). Generation of multiphoton entangled quantum states by means of integrated frequency combs. *Science*, 351(6278):1176–1180. (Cited on page 27.)

[Kues et al., 2017] Kues, M., Reimer, C., Roztocki, P., Romero Cortés, L., Sciara, S., Wetzel, B., Zhang, Y., Cino, A., Chu, S. T., Little, B. E., Moss, D. J., Caspani, L., Azaña, J., and Morandotti, R. (2017). On-chip generation of high-dimensional entangled quantum states and their coherent control. *Nature Publishing Group*, 546(7660):622–626. (Cited on page 27.)

[Kuznetsov et al., 2016] Kuznetsov, A. I., Miroshnichenko, A. E., Brongersma, M. L., Kivshar, Y. S., and Luk'yanchuk, B. (2016). Optically resonant dielectric nanostructures. *Science*, 354(6314):aag2472. (Cited on page 29.)

[Labroille et al., 2014] Labroille, G., Denolle, B., Jian, P., Genevaux, P., Treps, N., Morizur, J.-F. F., Genevaux, P., and Treps, N. (2014). Efficient and mode selective spatial mode multiplexer based on multi-plane light conversion. *Optics Express*, 22(13):15599. (Cited on page 29.)

[Lahini et al., 2010] Lahini, Y., Bromberg, Y., Christodoulides, D. N., and Silberberg, Y. (2010). Quantum correlations in two-particle Anderson localization. *Physical Review Letters*, 105(16):1–4. (Cited on page 97.)

[Laing and O'Brien, 2012] Laing, A. and O'Brien, J. L. (2012). Super-stable tomography of any linear optical device. (Cited on page 56.)

[Lang et al., 2013] Lang, C., Eichler, C., Steffen, L., Fink, J. M., Woolley, M. J., Blais, A., and Wallraff, A. (2013). Correlations, indistinguishability and entanglement in Hong-Ou-Mandel experiments at microwave frequencies. *Nature Physics*, 9(6):345–348. (Cited on page 15.)

[Lanyon et al., 2009] Lanyon, B. P., Barbieri, M., Almeida, M. P., Jennewein, T., Ralph, T. C., Resch, K. J., Pryde, G. J., O'Brien, J. L., Gilchrist, A., and White, A. G. (2009). Simplifying quantum logic using higher-dimensional Hilbert spaces. *Nature Physics*, 5(2):134–140. (Cited on page 27.)

[Lee et al., 2015] Lee, H. J., Kim, H., Lee, S. M., and Moon, H. S. (2015). Indistinguishability of photon pair in a periodically poled KTiOPO4. *Applied Physics B*, 121(4):541–547. (Cited on page 119.)

[Lee and Stone, 1985] Lee, P. A. and Stone, A. D. (1985). Universal conductance fluctuations in metals. *Physical Review Letters*, 55(15):1622–1625. (Cited on pages 127 and 129.)

[Lenzini et al., 2018] Lenzini, F., Janousek, J., Thearle, O., Villa, M., Haylock, B., Kasture, S., Cui, L., Phan, H.-P., Dao, D. V., Yonezawa, H., Lam, P. K., Huntington, E. H., and Lobino, M. (2018). Integrated photonic platform for quantum information with continuous variables. *Science Advances*, 4(12):eaat9331. (Cited on page 28.)

[Leon-Saval et al., 2010] Leon-Saval, S. G., Argyros, A., and Bland-Hawthorn, J. (2010). Photonic lanterns: a study of light propagation in multimode to single-mode converters. *Optics Express*, 18(8):8430. (Cited on page 114.)

[Li et al., 2019a] Li, D., Yao, Y., and Li, M. (2019a). Statistical distribution of quantum correlation induced by multiple scattering in the disordered medium. *Optics Communications*, 446:106–112. (Cited on page 97.)

[Li et al., 2017] Li, H., Suwunnarat, S., Fleischmann, R., Schanz, H., and Kottos, T. (2017). Random Matrix Theory Approach to Chaotic Coherent Perfect Absorbers. *Physical Review Letters*, 118(4):1–6. (Cited on page 85.)

[Li et al., 2011] Li, H. W., Przeslak, S., Niskanen, A. O., Matthews, J. C. F., Politi, A., Shadbolt, P., Laing, A., Lobino, M., Thompson, M. G., and O'Brien, J. L. (2011). Reconfigurable controlled two-qubit operation on a quantum photonic chip. *New Journal of Physics*, 13(11):115009. (Cited on page 31.)

[Li et al., 2019b] Li, Y., Cohen, D., and Kottos, T. (2019b). Coherent Wave Propagation in Multimode Systems with Correlated Noise. *Physical Review Letters*, 122(15):153903. (Cited on pages 44 and 123.)

[Li et al., 2018] Li, Y., Xue, Y., and Tian, L. (2018). Deep speckle correlation: a deep learning approach toward scalable imaging through scattering media. *Optica*, 5(10):1181. (Cited on page 50.)

[Liew et al., 2016] Liew, S. F., Popoff, S. M., Sheehan, S. W., Goetschy, A., Schmuttenmaer, C. A., Stone, A. D., and Cao, H. (2016). Coherent Control of Photocurrent in a Strongly Scattering Photoelectrochemical System. *ACS Photonics*, 3(3):449–455. (Cited on pages 85 and 86.)

[Lifante, 2003] Lifante, G. (2003). *Integrated Photonics: Fundamentals*. John Wiley & Sons, Ltd, Chichester, UK. (Cited on page 45.)

[Liutkus et al., 2014] Liutkus, A., Martina, D., Popoff, S., Chardon, G., Katz, O., Lerosey, G., Gigan, S., Daudet, L., and Carron, I. (2014). Imaging With Nature: Compressive Imaging Using a Multiply Scattering Medium. *Scientific Reports*, 4(1):5552. (Cited on page 47.)

[Ljunggren and Tengner, 2005] Ljunggren, D. and Tengner, M. (2005). Optimal focusing for maximal collection of entangled narrow-band photon pairs into single-mode fibers. *Physical Review A*, 72(6):1–17. (Cited on page 119.)

[Lodahl, 2006a] Lodahl, P. (2006a). Quantum correlations induced by multiple scattering of quadrature squeezed light. *Optics Express*, 14(15):6919. (Cited on page 97.)

[Lodahl, 2006b] Lodahl, P. (2006b). Quantum noise frequency correlations of multiply scattered light. *Optics Letters*, 31(1):110. (Cited on page 97.)

[Lodahl and Lagendijk, 2005] Lodahl, P. and Lagendijk, A. (2005). Transport of Quantum Noise through Random Media. *Physical Review Letters*, 94(15):153905. (Cited on page 97.)

[Lodahl et al., 2015] Lodahl, P., Mahmoodian, S., and Stobbe, S. (2015). Interfacing single photons and single quantum dots with photonic nanostructures. (Cited on page 28.)

[Lodahl et al., 2005] Lodahl, P., Mosk, A. P., and Lagendijk, A. (2005). Spatial quantum correlations in multiple scattered light. *Physical Review Letters*, 95(17):1–4. (Cited on pages 97 and 99.)

[Lopes et al., 2015] Lopes, R., Imanaliev, A., Aspect, A., Cheneau, M., Boiron, D., and Westbrook, C. I. (2015). Atomic Hong-Ou-Mandel experiment. *Nature*, 520(7545):66–68. (Cited on page 15.)

[Loterie et al., 2015] Loterie, D., Farahi, S., Papadopoulos, I., Goy, A., Psaltis, D., and Moser, C. (2015). Digital confocal microscopy through a multimode fiber. *Optics Express*, 23(18):23845. (Cited on page 50.)

[Loudon, 1980] Loudon, R. (1980). Non-classical effects in the statistical properties of light. *Reports on Progress in Physics*, 43(7):913–949. (Cited on page 12.)

[Lu et al., 2019] Lu, X., Li, Q., Westly, D. A., Moille, G., Singh, A., Anant, V., and Srinivasan, K. (2019). Chip-integrated visible–telecom entangled photon pair source for quantum communication. *Nature Physics*, 15(4):373–381. (Cited on page 28.)

[Lund et al., 2014] Lund, A. P., Laing, A., Rahimi-Keshari, S., Rudolph, T., O'Brien, J. L., and Ralph, T. C. (2014). Boson Sampling from a Gaussian State. *Physical Review Letters*, 113(10):100502. (Cited on page 34.)

[Luo et al., 2019] Luo, K.-H., Brauner, S., Eigner, C., Sharapova, P. R., Ricken, R., Meier, T., Herrmann, H., and Silberhorn, C. (2019). Nonlinear integrated quantum electro-optic circuits. *Science Advances*, 5(1):eaat1451. (Cited on page 28.)

[Lyons et al., 2018] Lyons, A., Knee, G. C., Bolduc, E., Roger, T., Leach, J., Gauger, E. M., and Faccio, D. (2018). Attosecond-resolution Hong-Ou-Mandel interferometry. *Science Advances*, 4(5):eaap9416. (Cited on page 15.)

[Lyons et al., 2019] Lyons, A., Oren, D., Roger, T., Savinov, V., Valente, J., Vezzoli, S., Zheludev, N. I., Segev, M., and Faccio, D. (2019). Coherent metamaterial absorption of two-photon states with 40efficiency. *Physical Review A*, 99(1):011801. (Cited on pages 88 and 89.)

[Mahalati et al., 2012] Mahalati, R. N., Askarov, D., Wilde, J. P., and Kahn, J. M. (2012). Adaptive control of input field to achieve desired output intensity profile in multimode fiber with random mode coupling. *Optics Express*, 20(13):14321. (Cited on page 50.)

[Mahalati et al., 2013] Mahalati, R. N., Gu, R. Y., and Kahn, J. M. (2013). Resolution limits for imaging through multi-mode fiber. *Optics express*, 21(2):1656–68. (Cited on page 50.)

[Mahoney, 2010] Mahoney, M. W. (2010). Randomized Algorithms for Matrices and Data. *Foundations and Trends® in Machine Learning*, 3(2):123–224. (Cited on pages 101, 113, and 115.)

[Mandel, 1983] Mandel, L. (1983). Photon interference and correlation effects produced by independent quantum sources. *Physical Review A*, 28(2):929–943. (Cited on page 15.)

[Mandel and Wolf, 1995] Mandel, L. and Wolf, E. (1995). *Optical coherence and quantum optics*. Cambridge University Press, Cambridge. (Cited on pages 6, 7, 8, and 12.)

[Marčenko and Pastur, 1967] Marčenko, V. A. and Pastur, L. A. (1967). Distribution of Eigenvalues for Some Sets of Random Matrices. *Mathematics of the USSR-Sbornik*, 1(4):457–483. (Cited on page 40.)

[Marcuse, 1991] Marcuse, D. (1991). *Theory of Dielectric Optical Waveguides*. Elsevier. (Cited on page 44.)

[Marshall et al., 2009] Marshall, G. D., Politi, A., Matthews, J. C. F., Dekker, P., Ams, M., Withford, M. J., and O'Brien, J. L. (2009). Laser written waveguide photonic quantum circuits. *Optics Express*, 17(15):12546. (Cited on page 31.)

[Marusarz and Sayeh, 2001] Marusarz, R. K. and Sayeh, M. R. (2001). Neural network-based multimode fiber-optic information transmission. *Applied Optics*, 40(2):219. (Cited on page 50.)

[Masada et al., 2015] Masada, G., Miyata, K., Politi, A., Hashimoto, T., O'Brien, J. L., and Furusawa, A. (2015). Continuous-variable entanglement on a chip. *Nature Photonics*, 9(5):316–319. (Cited on page 32.)

[Matloob and Loudon, 1996] Matloob, R. and Loudon, R. (1996). Electromagnetic field quantization in absorbing dielectrics. II. *Physical Review A*, 53(6):4567–4582. (Cited on page 79.)

[Matloob et al., 1995] Matloob, R., Loudon, R., Barnett, S. M., and Jeffers, J. (1995). Electromagnetic field quantization in absorbing dielectrics. *Physical Review A*, 52(6):4823–4838. (Cited on page 79.)

[Matthès et al., 2019] Matthès, M. W., del Hougne, P., de Rosny, J., Lerosey, G., and Popoff, S. M. (2019). Optical complex media as universal reconfigurable linear operators. *Optica*, 6(4):465. (Cited on pages 52, 53, and 55.)

[Matthews et al., 2011] Matthews, J. C. F., Politi, A., Bonneau, D., and O'Brien, J. L. (2011). Heralding two-photon and four-photon path entanglement on a chip. *Physical Review Letters*, 107(16):1–5. (Cited on page 31.)

[Matthews et al., 2009] Matthews, J. C. F., Politi, A., Stefanov, A., and O'Brien, J. L. (2009). Manipulation of multiphoton entanglement in waveguide quantum circuits. *Nature Photonics*, 3(6):346–350. (Cited on pages 25, 27, and 31.)

[McCabe et al., 2011] McCabe, D. J., Tajalli, A., Austin, D. R., Bondareff, P., Walmsley, I. a., Gigan, S., and Chatel, B. (2011). Spatio-temporal focusing of an ultrafast pulse through a multiply scattering medium. *Nature Communications*, 2(1):447. (Cited on pages 48 and 49.)

[McMichael et al., 1987] McMichael, I., Yeh, P., and Beckwith, P. (1987). Correction of polarization and modal scrambling in multimode fibers by phase conjugation. *Optics Letters*, 12(7):507. (Cited on page 45.)

[Mello et al., 1988a] Mello, P., Pereyra, P., and Kumar, N. (1988a). Macroscopic approach to multichannel disordered conductors. *Annals of Physics*, 181(2):290–317. (Cited on page 41.)

[Mello et al., 1988b] Mello, P. A., Akkermans, E., and Shapiro, B. (1988b). Macroscopic Approach to Correlations in the Electronic Transmission and Reflection from Disordered Conductors. *Physical Review Letters*, 61(4):459–462. (Cited on page 129.)

[Mello and Stone, 1991] Mello, P. A. and Stone, A. D. (1991). Maximum-entropy model for quantum-mechanical interference effects in metallic conductors. *Physical Review B*, 44(8):3559–3576. (Cited on page 129.)

[Metcalf et al., 2014] Metcalf, B. J., Spring, J. B., Humphreys, P. C., Thomas-Peter, N., Barbieri, M., Kolthammer, W. S., Jin, X.-m., Langford, N. K., Kundys, D., Gates, J. C., Smith, B. J., Smith, P. G. R., and Walmsley, I. A. (2014). Quantum teleportation on a photonic chip. *Nature Photonics*, 8(10):770–774. (Cited on page 31.)

[Metcalf et al., 2013] Metcalf, B. J., Thomas-Peter, N., Spring, J. B., Kundys, D., Broome, M. a., Humphreys, P. C., Jin, X.-M., Barbieri, M., Steven Kolthammer, W., Gates, J. C., Smith, B. J., Langford, N. K., Smith, P. G., and Walmsley, I. a. (2013). Multiphoton quantum interference in a multiport integrated photonic device. *Nature Communications*, 4(1):1356. (Cited on pages 25 and 31.)

[Meyer-Scott et al., 2017] Meyer-Scott, E., Montaut, N., Tiedau, J., Sansoni, L., Herrmann, H., Bartley, T. J., and Silberhorn, C. (2017). Limits on the heralding efficiencies and spectral purities of spectrally filtered single photons from photon-pair sources. *Physical Review A*, 95(6):061803. (Cited on page 12.)

[Mezzadri, 2006] Mezzadri, F. (2006). How to generate random matrices from the classical compact groups. (Cited on page 69.)

[Mickelson and Eriksrud, 1983] Mickelson, A. R. and Eriksrud, M. (1983). Mode-dependent attenuation in optical fibers. *Journal of the Optical Society of America*, 73(10):1282. (Cited on page 44.)

[Milanizadeh et al., 2019] Milanizadeh, M., Aguiar, D., Melloni, A., and Morichetti, F. (2019). Canceling Thermal Cross-Talk Effects in Photonic Integrated Circuits. *Journal of Lightwave Technology*, 37(4):1325–1332. (Cited on page 27.)

[Milburn, 1989] Milburn, G. J. (1989). Quantum optical Fredkin gate. *Physical Review Letters*, 62(18):2124–2127. (Cited on page 17.)

[Miller, 2013a] Miller, D. A. B. (2013a). How complicated must an optical component be? *Journal of the Optical Society of America A*, 30(2):238. (Cited on page 92.)

[Miller, 2013b] Miller, D. A. B. (2013b). Self-configuring universal linear optical component [Invited]. *Photonics Research*, 1(1):1. (Cited on pages 24, 71, and 92.)

[Miller, 2015a] Miller, D. A. B. (2015a). Perfect optics with imperfect components. *Optica*, 2(8):747. (Cited on page 27.)

[Miller, 2015b] Miller, D. A. B. (2015b). Sorting out light. *Science*, 347(6229):1423–1424. (Cited on page 20.)

[Minzioni et al., 2019] Minzioni, P., Lacava, C., Tanabe, T., Dong, J., Hu, X., Csaba, G., Porod, W., Singh, G., Willner, A. E., Almaiman, A., Torres-Company, V., Schröder, J., Peacock, A. C., Strain, M. J., Parmigiani, F., Contestabile, G., Marpaung, D., Liu, Z., Bowers, J. E., Chang, L., Fabbri, S., Ramos Vázquez, M., Bharadwaj, V., Eaton, S. M., Lodahl, P., Zhang, X., Eggleton, B. J., Munro, W. J., Nemoto, K., Morin, O., Laurat, J., and Nunn, J. (2019). Roadmap on all-optical processing. *Journal of Optics*, 21(6):063001. (Cited on page 25.)

[Mohanty et al., 2017] Mohanty, A., Zhang, M., Dutt, A., Ramelow, S., Nussenzveig, P., and Lipson, M. (2017). Quantum interference between transverse spatial waveguide modes. *Nature Communications*, 8(1):14010. (Cited on page 28.)

[Molesky et al., 2018] Molesky, S., Lin, Z., Piggott, A. Y., Jin, W., Vucković, J., and Rodriguez, A. W. (2018). Inverse design in nanophotonics. *Nature Photonics*, 12(11):659–670. (Cited on pages 28, 30, 35, and 115.)

[Montambaux, 2007] Montambaux, G. (2007). Coherence and Interactions in Diffusive Systems. In *Physics of Zero- and One-Dimensional Nanoscopic Systems*, pages 187–227. (Cited on page 127.)

[Morales-Delgado et al., 2015a] Morales-Delgado, E. E., Farahi, S., Papadopoulos, I. N., Psaltis, D., and Moser, C. (2015a). Delivery of focused short pulses through a multimode fiber. *Optics Express*, 23(7):9109. (Cited on pages 50 and 114.)

[Morales-Delgado et al., 2015b] Morales-Delgado, E. E., Psaltis, D., and Moser, C. (2015b). Two-photon imaging through a multimode fiber. *Optics Express*, 23(25):32158. (Cited on page 50.)

[Morizur et al., 2010] Morizur, J.-F., Nicholls, L., Jian, P., Armstrong, S., Treps, N., Hage, B., Hsu, M., Bowen, W., Janousek, J., and Bachor, H.-A. (2010). Programmable unitary spatial mode manipulation. *Journal of the Optical Society of America A*, 27(11):2524. (Cited on pages 29 and 35.)

[Mosk et al., 2012] Mosk, A. P., Lagendijk, A., Lerosey, G., and Fink, M. (2012). Controlling waves in space and time for imaging and focusing in complex media. *Nature Photonics*, 6(5):283–292. (Cited on page 47.)

[Mosley et al., 2008] Mosley, P. J., Lundeen, J. S., Smith, B. J., Wasylczyk, P., U'Ren, A. B., Silberhorn, C., and Walmsley, I. A. (2008). Heralded generation of ultrafast single photons in pure quantum states. *Physical Review Letters*, 100(13):1–4. (Cited on page 12.)

[Motes et al., 2015] Motes, K. R., Olson, J. P., Rabeaux, E. J., Dowling, J. P., Olson, S. J., and Rohde, P. P. (2015). Linear Optical Quantum Metrology with Single Photons: Exploiting Spontaneously Generated Entanglement to Beat the Shot-Noise Limit. *Physical Review Letters*, 114(17):1–10. (Cited on page 60.)

[Mounaix et al., 2016a] Mounaix, M., Andreoli, D., Defienne, H., Volpe, G., Katz, O., Grésillon, S., and Gigan, S. (2016a). Spatiotemporal Coherent Control of Light through a Multiple Scattering Medium with the Multispectral Transmission Matrix. *Physical Review Letters*, 116(25):253901. (Cited on page 48.)

[Mounaix and Carpenter, 2019] Mounaix, M. and Carpenter, J. (2019). Control of the temporal and polarization response of a multimode fiber. *Nature Communications*, 10(1):5085. (Cited on pages 50 and 114.)

[Mounaix et al., 2016b] Mounaix, M., Defienne, H., and Gigan, S. (2016b). Deterministic light focusing in space and time through multiple scattering media with a time-resolved transmission matrix approach. *Physical Review A*, 94(4):041802. (Cited on page 48.)

[Mower et al., 2015] Mower, J., Harris, N. C., Steinbrecher, G. R., Lahini, Y., and Englund, D. (2015). High-fidelity quantum state evolution in imperfect photonic integrated circuits. *Physical Review A*, 92(3):1–7. (Cited on page 27.)

[Myers and Laflamme, 2006] Myers, C. R. and Laflamme, R. (2006). Linear opties quantum computation: An overview. In *Proceedings of the International School of Physics "Enrico Fermi"*, volume 162, pages 45–93. (Cited on pages 17 and 18.)

[Nagata et al., 2007] Nagata, T., Okamoto, R., O'Brien, J. L., Sasaki, K., and Takeuchi, S. (2007). Beating the standard quantum limit with four-entangled photons. *Science*, 316(5825):726–729. (Cited on page 16.)

[Najafi et al., 2015] Najafi, F., Mower, J., Harris, N. C., Bellei, F., Dane, A., Lee, C., Hu, X., Kharel, P., Marsili, F., Assefa, S., Berggren, K. K., and Englund, D. (2015). On-chip detection of non-classical light by scalable integration of single-photon detectors. *Nature Communications*, 6(1):5873. (Cited on page 28.)

[N'Gom et al., 2018] N'Gom, M., Norris, T. B., Michielssen, E., and Nadakuditi, R. R. (2018). Mode control in a multimode fiber through acquiring its transmission matrix from a reference-less optical system. *Optics Letters*, 43(3):419. (Cited on page 55.)

[Nielsen, 2004] Nielsen, M. A. (2004). Optical Quantum Computation Using Cluster States. *Physical Review Letters*, 93(4):040503. (Cited on pages 15, 18, and 20.)

[Nielsen and Chuang, 2010] Nielsen, M. A. and Chuang, I. L. (2010). *Quantum Computation and Quantum Information*. Cambridge University Press, Cambridge. (Cited on pages 1, 17, 18, and 20.)

[Oberholzer et al., 2002] Oberholzer, S., Sukhorukov, E. V., and Schönenberger, C. (2002). Crossover between classical and quantum shot noise in chaotic cavities. *Nature*, 415(6873):765–767. (Cited on page 42.)

[O'Brien, 2007] O'Brien, J. L. (2007). Optical Quantum Computing. *Science*, 318(5856):1567–1570. (Cited on pages 19 and 20.)

[O'Brien et al., 2009] O'Brien, J. L., Furusawa, A., and Vučković, J. (2009). Photonic quantum technologies. *Nature Photonics*, 3(12):687–695. (Cited on pages 2 and 20.)

[Ohayon et al., 2018] Ohayon, S., Caravaca-Aguirre, A., Piestun, R., and DiCarlo, J. J. (2018). Minimally invasive multimode optical fiber microendoscope for deep brain fluorescence imaging. *Biomedical Optics Express*, 9(4):1492. (Cited on pages 2 and 50.)

[Ojambati et al., 2016] Ojambati, O. S., Hosmer-Quint, J. T., Gorter, K.-J., Mosk, A. P., and Vos, W. L. (2016). Controlling the intensity of light in large areas at the interfaces of a scattering medium. *Physical Review A*, 94(4):043834. (Cited on page 128.)

[Okamoto et al., 2011] Okamoto, R., O'Brien, J. L., Hofmann, H. F., and Takeuchi, S. (2011). Realization of a knill-laflamme-milburn controlled-NOT photonic quantum circuit combining effective optical nonlinearities. *Proceedings of the National Academy of Sciences of the United States of America*, 108(25):10067–10071. (Cited on page 31.)

[Olshansky, 1975] Olshansky, R. (1975). Mode Coupling Effects in Graded-Index Optical Fibers. *Applied Optics*, 14(4):935. (Cited on page 44.)

[Orieux and Diamanti, 2016] Orieux, A. and Diamanti, E. (2016). Recent advances on integrated quantum communications. *Journal of Optics*, 18(8):083002. (Cited on page 31.)

[Osellame et al., 2012] Osellame, R., Cerullo, G., and Ramponi, R., editors (2012). *Femtosecond Laser Micromachining*, volume 123 of *Topics in Applied Physics*. Springer Berlin Heidelberg, Berlin, Heidelberg. (Cited on page 26.)

[Osnabrugge et al., 2017] Osnabrugge, G., Horstmeyer, R., Papadopoulos, I. N., Judkewitz, B., and Vellekoop, I. M. (2017). Generalized optical memory effect. *Optica*, 4(8):1–11. (Cited on page 128.)

[Oszmaniec and Brod, 2018] Oszmaniec, M. and Brod, D. J. (2018). Classical simulation of photonic linear optics with lost particles. *New Journal of Physics*, 20(9):092002. (Cited on page 78.)

[Ott, 2012] Ott, J. R. (2012). *Quantum Optical Multiple Scattering*. PhD thesis, Technical University of Denmark. (Cited on page 97.)

[Ott et al., 2010] Ott, J. R., Mortensen, N. A., and Lodahl, P. (2010). Quantum Interference and Entanglement Induced by Multiple Scattering of Light. *Physical Review Letters*, 105(9):090501. (Cited on page 97.)

[Ou, 1988] Ou, Z. Y. (1988). Quantum theory of fourth-order interference. *Physical Review A*, 37(5):1607–1619. (Cited on page 15.)

[Ou, 2007] Ou, Z. Y. (2007). Multi-Photon Interference and Temporal Distinguishability of Photons. *International Journal of Modern Physics B*, 21(30):5033–5058. (Cited on page 12.)

[Paesani et al., 2019] Paesani, S., Ding, Y., Santagati, R., Chakhmakhchyan, L., Vigliar, C., Rottwitt, K., Oxenløwe, L. K., Wang, J., Thompson, M. G., and Laing, A. (2019). Generation and sampling of quantum states of light in a silicon chip. *Nature Physics*, 15(9):925–929. (Cited on page 28.)

[Paesani et al., 2017] Paesani, S., Gentile, A. A., Santagati, R., Wang, J., Wiebe, N., Tew, D. P., O'Brien, J. L., and Thompson, M. G. (2017). Experimental Bayesian Quantum Phase Estimation on a Silicon Photonic Chip. *Physical Review Letters*, 118(10):1–6. (Cited on page 32.)

[Pai et al., 2018] Pai, S., Bartlett, B., Solgaard, O., and Miller, D. A. B. (2018). Matrix optimization on universal unitary photonic devices. *Physical Review Applied*, 10(1):1. (Cited on pages 27 and 33.)

[Pan et al., 2012] Pan, J. W., Chen, Z. B., Lu, C. Y., Weinfurter, H., Zeilinger, A., and Zukowski, M. (2012). Multiphoton entanglement and interferometry. *Reviews of Modern Physics*, 84(2). (Cited on pages 12 and 16.)

[Paniagua-Diaz et al., 2019a] Paniagua-Diaz, A. M., Starshynov, I., Fayard, N., Goetschy, A., Pierrat, R., Carminati, R., and Bertolotti, J. (2019a). Blind ghost imaging. *Optica*, 6(4):460. (Cited on pages 29 and 30.)

[Paniagua-Diaz et al., 2019b] Paniagua-Diaz, A. M., Starshynov, I., Fayard, N., Goetschy, A., Pierrat, R., Carminati, R., and Bertolotti, J. (2019b). Blind ghost imaging. *Optica*, 6(4):460. (Cited on page 129.)

[Papadopoulos et al., 2012] Papadopoulos, I. N., Farahi, S., Moser, C., and Psaltis, D. (2012). Focusing and scanning light through a multimode optical fiber using digital phase conjugation. *Optics Express*, 20(10):10583. (Cited on page 50.)

[Papadopoulos et al., 2013] Papadopoulos, I. N., Farahi, S., Moser, C., and Psaltis, D. (2013). High-resolution, lensless endoscope based on digital scanning through a multimode optical fiber. *Biomedical Optics Express*, 4(2):260. (Cited on page 50.)

[Papaioannou et al., 2016a] Papaioannou, M., Plum, E., Valente, J., Rogers, E. T., and Zheludev, N. I. (2016a). Two-dimensional control of light with light on metasurfaces. *Light: Science & Applications*, 5(4):e16070–e16070. (Cited on pages 86 and 92.)

[Papaioannou et al., 2016b] Papaioannou, M., Plum, E., Valente, J., Rogers, E. T. F., and Zheludev, N. I. (2016b). All-optical multichannel logic based on coherent perfect absorption in a plasmonic metamaterial. *APL Photonics*, 1(9):090801. (Cited on pages 86 and 92.)

[Pappu et al., 2002] Pappu, R., Recht, B., Taylor, J., and Gershenfeld, N. (2002). Physical one-way functions. *Science*, 297(5589):2026–2030. (Cited on page 47.)

[Patra, 2000] Patra, M. (2000). *On Quantum Optics of Random Media*. PhD thesis, Leiden University. (Cited on page 97.)

[Patra and Beenakker, 2000] Patra, M. and Beenakker, C. W. (2000). Propagation of squeezed radiation through amplifying or absorbing random media. *Physical Review A*, 61(6):8. (Cited on pages 78 and 97.)

[Paudel et al., 2013] Paudel, H. P., Stockbridge, C., Mertz, J., Bifano, T., and Corporation, B. M. (2013). Focusing polychromatic light through strongly scattering media. *Optics express*, 21(14):17299–308. (Cited on page 48.)

[Peeters et al., 2010] Peeters, W. H., Moerman, J. J. D., and van Exter, M. P. (2010). Observation of Two-Photon Speckle Patterns. *Physical Review Letters*, 104(17):173601. (Cited on pages 99 and 100.)

[Peřina et al., 2012] Peřina, J., Hamar, M., Michálek, V., and Haderka, O. (2012). Photon-number distributions of twin beams generated in spontaneous parametric down-conversion and measured by an intensified CCD camera. *Physical Review A*, 85(2):023816. (Cited on pages 73 and 114.)

[Pendry et al., 1990] Pendry, J., MacKinnon, A., and Pretre, A. (1990). Maximal fluctuations — A new phenomenon in disordered systems. *Physica A: Statistical Mechanics and its Applications*, 168(1):400–407. (Cited on page 42.)

[Pernice et al., 2012] Pernice, W., Schuck, C., Minaeva, O., Li, M., Goltsman, G., Sergienko, A., and Tang, H. (2012). High-speed and high-efficiency travelling wave single-photon detectors embedded in nanophotonic circuits. *Nature Communications*, 3(1):1325. (Cited on page 28.)

[Peruzzo et al., 2011] Peruzzo, A., Laing, A., Politi, A., Rudolph, T., and O'Brien, J. L. (2011). Multimode quantum interference of photons in multiport integrated devices. *Nature Communications*, 2(1):224. (Cited on page 45.)

[Peruzzo et al., 2010] Peruzzo, A., Lobino, M., Matthews, J. C. F., Matsuda, N., Poulios, K., Zhou, X. Q. X.-Q. X.-q., Lahini, Y., Ismail, N., Wörhoff, K., Bromberg, Y., Silberberg, Y., Thompson, M. G., Obrien, J. L., W, K., Politi, A., Poulios, K., Zhou, X. Q. X.-Q. X.-q., Lahini, Y., Ismail, N., Wörhoff, K., Bromberg, Y., Silberberg, Y., Thompson, M. G., Obrien, J. L., Worhoff, K., Bromberg, Y., Silberberg, Y., Thompson, M. G., and Obrien, J. L. (2010). Quantum Walks of Correlated Photons. *Science*, 329(5998):1500–1503. (Cited on page 31.)

[Peruzzo et al., 2014] Peruzzo, A., McClean, J., Shadbolt, P., Yung, M.-H., Zhou, X.-Q., Love, P. J., Aspuru-Guzik, A., and O'Brien, J. L. (2014). A variational eigenvalue

solver on a photonic quantum processor. *Nature Communications*, 5(1):4213. (Cited on page 32.)

[Peruzzo et al., 2012] Peruzzo, A., Shadbolt, P., Brunner, N., Popescu, S., and O'Brien, J. L. (2012). A Quantum Delayed-Choice Experiment. *Science*, 338(6107):634–637. (Cited on page 31.)

[Phillips et al., 2019] Phillips, D. S., Walschaers, M., Renema, J. J., Walmsley, I. A., Treps, N., and Sperling, J. (2019). Benchmarking of Gaussian boson sampling using two-point correlators. *Physical Review A*, 99(2):023836. (Cited on page 101.)

[Pichler et al., 2019] Pichler, K., Kühmayer, M., Böhm, J., Brandstötter, A., Ambichl, P., Kuhl, U., and Rotter, S. (2019). Random anti-lasing through coherent perfect absorption in a disordered medium. *Nature*, 567(7748):351–355. (Cited on page 85.)

[Piggott et al., 2015] Piggott, A. Y., Lu, J., Lagoudakis, K. G., Petykiewicz, J., Babinec, T. M., and Vučković, J. (2015). Inverse design and demonstration of a compact and broadband on-chip wavelength demultiplexer. *Nature Photonics*, 9(6):374–377. (Cited on page 29.)

[Plick and Krenn, 2015] Plick, W. N. and Krenn, M. (2015). Physical meaning of the radial index of Laguerre-Gauss beams. *Physical Review A*, 92(6):063841. (Cited on page 29.)

[Plöschner and Čižmár, 2015] Plöschner, M. and Čižmár, T. (2015). Compact multimode fiber beam-shaping system based on GPU accelerated digital holography. *Optics Letters*, 40(2):197. (Cited on page 50.)

[Plöschner et al., 2015a] Plöschner, M., Kollárová, V., Dostál, Z., Nylk, J., Barton-Owen, T., Ferrier, D. E. K., Chmelík, R., Dholakia, K., and Čižmár, T. (2015a). Multimode fibre: Light-sheet microscopy at the tip of a needle. *Scientific Reports*, 5(August):18050. (Cited on pages 50 and 114.)

[Plöschner et al., 2014] Plöschner, M., Straka, B., Dholakia, K., and Čižmár, T. (2014). GPU accelerated toolbox for real-time beam-shaping in multimode fibres. *Optics Express*, 22(3):2933. (Cited on page 50.)

[Plöschner et al., 2015b] Plöschner, M., Tyc, T., and Čižmár, T. (2015b). Seeing through chaos in multimode fibres. *Nature Photonics*, 9(8):529–535. (Cited on pages 44, 45, 50, 72, and 73.)

[Poem et al., 2012] Poem, E., Gilead, Y., and Silberberg, Y. (2012). Two-Photon Path-Entangled States in Multimode Waveguides. *Physical Review Letters*, 108(15):153602. (Cited on page 45.)

[Politi et al., 2008] Politi, A., Cryan, M. J., Rarity, J. G., Yu, S., and O'Brien, J. L. (2008). Silica-on-Silicon Waveguide Quantum Circuits. *Science*, 320(5876):646–649. (Cited on page 31.)

[Politi et al., 2009a] Politi, A., Matthews, J., Thompson, M., and O'Brien, J. (2009a). Integrated Quantum Photonics. *IEEE Journal of Selected Topics in Quantum Electronics*, 15(6):1673–1684. (Cited on page 26.)

[Politi et al., 2009b] Politi, A., Matthews, J. C. F., and O'Brien, J. L. (2009b). Shor's Quantum Factoring Algorithm on a Photonic Chip. *Science*, 325(5945):1221–1221. (Cited on page 31.)

[Poot and Tang, 2014] Poot, M. and Tang, H. X. (2014). Broadband nanoelectromechanical phase shifting of light on a chip. *Applied Physics Letters*, 104(6):061101. (Cited on page 27.)

[Popoff et al., 2010a] Popoff, S., Lerosey, G., Fink, M., Boccara, A. C., and Gigan, S. (2010a). Image transmission through an opaque material. *Nature Communications*, 1(1):81. (Cited on pages 72 and 73.)

[Popoff et al., 2014] Popoff, S. M., Goetschy, A., Liew, S. F., Stone, A. D., and Cao, H. (2014). Coherent control of total transmission of light through disordered media. *Physical Review Letters*, 112(13):1–5. (Cited on pages 125, 126, and 128.)

[Popoff et al., 2010b] Popoff, S. M., Lerosey, G., Carminati, R., Fink, M., Boccara, A. C., and Gigan, S. (2010b). Measuring the transmission matrix in optics: An approach to the study and control of light propagation in disordered media. *Physical Review Letters*, 104(10):1–4. (Cited on pages 40, 46, 48, 51, 55, 56, and 69.)

[Popoff et al., 2011] Popoff, S. M., Lerosey, G., Fink, M., Boccara, A. C., and Gigan, S. (2011). Controlling light through optical disordered media: transmission matrix approach. *New Journal of Physics*, 13(12):123021. (Cited on pages 40 and 123.)

[Poulios et al., 2013] Poulios, K., Fry, D., Politi, A., Ismail, N., Wörhoff, K., O'Brien, J. L., and Thompson, M. G. (2013). Two-photon quantum interference in integrated multi-mode interference devices. *Optics Express*, 21(20):23401. (Cited on page 45.)

[Prada and Fink, 1994] Prada, C. and Fink, M. (1994). Eigenmodes of the time reversal operator: A solution to selective focusing in multiple-target media. *Wave Motion*, 20(2):151–163. (Cited on page 40.)

[Puentes et al., 2007] Puentes, G., Aiello, A., Voigt, D., and Woerdman, J. P. (2007). Entangled mixed-state generation by twin-photon scattering. *Physical Review A*, 75(3):1–5. (Cited on pages 97 and 99.)

[Qiang et al., 2018] Qiang, X., Zhou, X., Wang, J., Wilkes, C. M., Loke, T., O'Gara, S., Kling, L., Marshall, G. D., Santagati, R., Ralph, T. C., Wang, J. B., O'Brien, J. L., Thompson, M. G., and Matthews, J. C. F. (2018). Large-scale silicon quantum photonics implementing arbitrary two-qubit processing. *Nature Photonics*, 12(9):534–539. (Cited on page 32.)

[Rahimi-Keshari et al., 2013] Rahimi-Keshari, S., Broome, M. A., Fickler, R., Fedrizzi, A., Ralph, T. C., and White, A. G. (2013). Direct characterization of linear-optical networks. *Optics Express*, 21(11):13450. (Cited on page 55.)

[Rahmani et al., 2018] Rahmani, B., Loterie, D., Konstantinou, G., Psaltis, D., and Moser, C. (2018). Multimode optical fiber transmission with a deep learning network. *Light: Science & Applications*, 7(1):69. (Cited on page 50.)

[Rarity et al., 1990] Rarity, J. G., Tapster, P. R., Jakeman, E., Larchuk, T., Campos, R. A., Teich, M. C., and Saleh, B. E. A. (1990). Two-photon interference in a Mach-Zehnder interferometer. *Physical Review Letters*, 65(11):1348–1351. (Cited on page 16.)

[Rarity et al., 2005] Rarity, J. G., Tapster, P. R., and Loudon, R. (2005). Non-classical interference between independent sources. *J. Opt. B: Quantum Semiclass. Opt.*, 7:6. (Cited on page 15.)

[Raussendorf and Briegel, 2001] Raussendorf, R. and Briegel, H. J. (2001). A One-Way Quantum Computer. *Physical Review Letters*, 86(22):5188–5191. (Cited on pages 18 and 20.)

[Raussendorf et al., 2003] Raussendorf, R., Browne, D. E., and Briegel, H. J. (2003). Measurement-based quantum computation on cluster states. *Physical Review A*, 68(2):32. (Cited on pages 18 and 20.)

[Reck et al., 1994] Reck, M., Zeilinger, A., Bernstein, H. J., and Bertani, P. (1994). Experimental realization of any discrete unitary operator. *Physical Review Letters*, 73(1):58–61. (Cited on pages 20, 21, 71, and 92.)

[Redding and Cao, 2012] Redding, B. and Cao, H. (2012). Using a multimode fiber as a high-resolution, low-loss spectrometer. *Optics Letters*, 37(16):3384. (Cited on page 48.)

[Réfrégier, 2004] Réfrégier, P. (2004). *Noise Theory and Application to Physics*. Advanced Texts in Physics. Springer New York, New York, NY. (Cited on pages 96 and 98.)

[Reichert et al., 2018] Reichert, M., Defienne, H., and Fleischer, J. W. (2018). Massively Parallel Coincidence Counting of High-Dimensional Entangled States. *Scientific Reports*, 8(1):7925. (Cited on pages 73 and 114.)

[Richardson et al., 2013] Richardson, D. J., Fini, J. M., and Nelson, L. E. (2013). Space-division multiplexing in optical fibres. *Nature Photonics*, 7(5):354–362. (Cited on pages 2 and 44.)

[Roger et al., 2016] Roger, T., Restuccia, S., Lyons, A., Giovannini, D., Romero, J., Jeffers, J., Padgett, M., and Faccio, D. (2016). Coherent Absorption of N00N States. *Physical Review Letters*, 117(2):1–5. (Cited on pages 88 and 89.)

[Roger et al., 2015] Roger, T., Vezzoli, S., Bolduc, E., Valente, J., Heitz, J. J. F., Jeffers, J., Soci, C., Leach, J., Couteau, C., Zheludev, N. I., and Faccio, D. (2015). Coherent perfect absorption in deeply subwavelength films in the single-photon regime. *Nature Communications*, 6(1):7031. (Cited on page 86.)

[Rohde and Ralph, 2012] Rohde, P. P. and Ralph, T. C. (2012). Error tolerance of the boson-sampling model for linear optics quantum computing. *Physical Review A*, 85(2):1–5. (Cited on page 78.)

[Rosen et al., 2015] Rosen, S., Gilboa, D., Katz, O., and Silberberg, Y. (2015). Focusing and Scanning through Flexible Multimode Fibers without Access to the Distal End. pages 1–8. (Cited on pages 50 and 130.)

[Rotter and Gigan, 2017] Rotter, S. and Gigan, S. (2017). Light fields in complex media: Mesoscopic scattering meets wave control. *Reviews of Modern Physics*, 89(1):015005. (Cited on pages 2, 39, 41, 42, 43, 47, 58, 70, and 125.)

[Rowe, 1999] Rowe, H. E. (1999). *Electromagnetic Propagation in Multi-Mode Random Media*. John Wiley & Sons, Inc., New York, USA. (Cited on page 44.)

[Rudolph, 2017] Rudolph, T. (2017). Why I am optimistic about the silicon-photonic route to quantum computing. *APL Photonics*, 2(3):030901. (Cited on pages 18 and 78.)

[Russell et al., 2017] Russell, N. J., Chakhmakhchyan, L., O'Brien, J. L., and Laing, A. (2017). Direct dialling of Haar random unitary matrices. *New Journal of Physics*, 19(3). (Cited on page 33.)

[Sakamaki et al., 2007] Sakamaki, Y., Saida, T., Hashimoto, T., and Takahashi, H. (2007). New Optical Waveguide Design Based on Wavefront Matching Method. *Journal of Lightwave Technology*, 25(11):3511–3518. (Cited on page 29.)

[Sansoni et al., 2017] Sansoni, L., Luo, K. H., Eigner, C., Ricken, R., Quiring, V., Herrmann, H., and Silberhorn, C. (2017). A two-channel, spectrally degenerate polarization entangled source on chip. *npj Quantum Information*, 3(1):1–5. (Cited on page 28.)

[Sansoni et al., 2010] Sansoni, L., Sciarrino, F., Vallone, G., Mataloni, P., Crespi, A., Ramponi, R., and Osellame, R. (2010). Polarization entangled state measurement on a chip. *Physical Review Letters*, 105(20):200503. (Cited on pages 26 and 31.)

[Santagati et al., 2017] Santagati, R., Silverstone, J. W., Strain, M. J., Sorel, M., Miki, S., Yamashita, T., Fujiwara, M., Sasaki, M., Terai, H., Tanner, M. G., Natarajan, C. M., Hadfield, R. H., O'Brien, J. L., and Thompson, M. G. (2017). Silicon photonic processor of two-qubit entangling quantum logic. *Journal of Optics*, 19(11):114006. (Cited on page 32.)

[Santagati et al., 2018] Santagati, R., Wang, J., Gentile, A. A., Paesani, S., Wiebe, N., McClean, J. R., Morley-Short, S., Shadbolt, P. J., Bonneau, D., Silverstone, J. W., Tew, D. P., Zhou, X., O'Brien, J. L., and Thompson, M. G. (2018). Witnessing eigenstates for quantum simulation of Hamiltonian spectra. *Science Advances*, 4(1):eaap9646. (Cited on page 32.)

[Sarma et al., 2016] Sarma, R., Yamilov, A. G., Petrenko, S., Bromberg, Y., and Cao, H. (2016). Control of Energy Density inside a Disordered Medium by Coupling to Open or Closed Channels. *Physical Review Letters*, 117(8):086803. (Cited on page 125.)

[Sarmiento-Merenguel et al., 2015] Sarmiento-Merenguel, J. D., Halir, R., Le Roux, X., Alonso-Ramos, C., Vivien, L., Cheben, P., Durán-Valdeiglesias, E., Molina-Fernández, I., Marris-Morini, D., Xu, D.-X., Schmid, J. H., Janz, S., and Ortega-Moñux, A. (2015). Demonstration of integrated polarization control with a 40 dB range in extinction ratio. *Optica*, 2(12):1019. (Cited on page 28.)

[Schaeff et al., 2015] Schaeff, C., Polster, R., Huber, M., Ramelow, S., and Zeilinger, A. (2015). Experimental access to higher-dimensional entangled quantum systems using integrated optics. *Optica*, 2(6):523. (Cited on page 32.)

[Scheffold and Maret, 1998] Scheffold, F. and Maret, G. (1998). Universal Conductance Fluctuations of Light. *Physical Review Letters*, 81(26):5800–5803. (Cited on page 129.)

[Schneeloch and Howell, 2015] Schneeloch, J. and Howell, J. C. (2015). Introduction to the Transverse Spatial Correlations in Spontaneous Parametric Down-Conversion through the Biphoton Birth Zone. *Journal of Optics*, 18(5):0. (Cited on page 9.)

[Schott et al., 2015] Schott, S., Bertolotti, J., Léger, J.-F., Bourdieu, L., and Gigan, S. (2015). Characterization of the angular memory effect of scattered light in biological tissues. *Optics Express*, 23(10):13505. (Cited on page 127.)

[Schuck et al., 2016a] Schuck, C., Guo, X., Fan, L., Ma, X., Poot, M., and Tang, H. X. (2016a). Quantum interference in heterogeneous superconducting-photonic circuits on a silicon chip. *Nature Communications*, 7(1):10352. (Cited on page 28.)

[Schuck et al., 2016b] Schuck, C., Guo, X., Fan, L., Ma, X., Poot, M., and Tang, H. X. (2016b). Quantum interference in heterogeneous superconducting-photonic circuits on a silicon chip. *Nature Communications*, 7(1):10352. (Cited on pages 60 and 67.)

[Shadbolt et al., 2012a] Shadbolt, P., Vértesi, T., Liang, Y.-C., Branciard, C., Brunner, N., and O'Brien, J. L. (2012a). Guaranteed violation of a Bell inequality without aligned reference frames or calibrated devices. *Scientific Reports*, 2:1–7. (Cited on page 31.)

[Shadbolt et al., 2012b] Shadbolt, P. J., Verde, M. R., Peruzzo, A., Politi, A., Laing, A., Lobino, M., Matthews, J. C. F., Thompson, M. G., O'Brien, J. L., Lobino, M., Matthews, J. C. F., Thompson, M. G., and O'Brien, J. L. (2012b). Generating, manipulating and measuring entanglement and mixture with a reconfigurable photonic circuit. *Nature Photonics*, 6(1):45–49. (Cited on page 31.)

[Shemirani, 2010] Shemirani, M. B. (2010). *Modeling and Compensation of Modal Dispersion in Graded-Index Multimode Fiber*. PhD thesis, Stanford University. (Cited on page 44.)

[Shemirani and Kahn, 2009] Shemirani, M. B. and Kahn, J. M. (2009). Higher-order modal dispersion in graded-index multimode fiber. *Journal of Lightwave Technology*, 27(23):5461–5468. (Cited on page 44.)

[Shemirani et al., 2009] Shemirani, M. B., Mao, W., Panicker, R. A., and Kahn, J. M. (2009). Principal Modes in Graded-Index Multimode Fiber in Presence of Spatial- and Polarization-Mode Coupling. *Journal of Lightwave Technology*, 27(10):1248–1261. (Cited on pages 44 and 45.)

[Shen et al., 2015] Shen, B., Wang, P., Polson, R., and Menon, R. (2015). An integrated-nanophotonics polarization beamsplitter with $2.4 \times 2.4\ \mu m^2$ footprint. *Nature Photonics*, 9(6):378–382. (Cited on page 29.)

[Shen et al., 2017] Shen, Y., Harris, N. C., Skirlo, S., Prabhu, M., Baehr-Jones, T., Hochberg, M., Sun, X., Zhao, S., Larochelle, H., Englund, D., and Soljačić, M. (2017). Deep learning with coherent nanophotonic circuits. *Nature Photonics*, 11(7):441–446. (Cited on page 20.)

[Shih et al., 1994] Shih, Y. H., Sergienko, A. V., Rubin, M. H., Kiess, T. E., and Alley, C. O. (1994). Two-photon interference in a standard Mach-Zehnder interferometer. *Physical Review A*, 49(5):4243–4246. (Cited on page 16.)

[Shor, 1997] Shor, P. W. (1997). Polynomial-Time Algorithms for Prime Factorization and Discrete Logarithms on a Quantum Computer. *SIAM Journal on Computing*, 26(5):1484–1509. (Cited on pages 1 and 60.)

[Sibson et al., 2017a] Sibson, P., Erven, C., Godfrey, M., Miki, S., Yamashita, T., Fujiwara, M., Sasaki, M., Terai, H., Tanner, M. G., Natarajan, C. M., Hadfield, R. H., O'Brien, J. L., and Thompson, M. G. (2017a). Chip-based quantum key distribution. *Nature Communications*, 8(1):13984. (Cited on page 32.)

[Sibson et al., 2017b] Sibson, P., Kennard, J. E., Stanisic, S., Erven, C., O'Brien, J. L., and Thompson, M. G. (2017b). Integrated silicon photonics for high-speed quantum key distribution. *Optica*, 4(2):172. (Cited on page 32.)

[Sillard et al., 2016] Sillard, P., Molin, D., Bigot-Astruc, M., Amezcua-Correa, A., de Jongh, K., and Achten, F. (2016). 50 $\mu$m Multimode Fibers for Mode Division Multiplexing. *Journal of Lightwave Technology*, 34(8):1672–1677. (Cited on page 44.)

[Silverstone et al., 2016] Silverstone, J. W., Bonneau, D., O'Brien, J. L., and Thompson, M. G. (2016). Silicon Quantum Photonics. *IEEE Journal of Selected Topics in Quantum Electronics*, 22(6):390–402. (Cited on pages 26 and 28.)

[Sivankutty et al., 2016] Sivankutty, S., Andresen, E. R., Cossart, R., Bouwmans, G., Monneret, S., and Rigneault, H. (2016). Ultra-thin rigid endoscope: two-photon imaging through a graded-index multi-mode fiber. *Optics Express*, 24(2):825. (Cited on page 50.)

[Skipetrov, 2003] Skipetrov, S. E. (2003). Information transfer through disordered media by diffuse waves. *Physical Review E*, 67(3):036621. (Cited on page 47.)

[Skipetrov, 2007] Skipetrov, S. E. (2007). Quantum theory of dynamic multiple light scattering in fluctuating disordered media. *Physical Review A*, 75(5):1–5. (Cited on page 97.)

[Slussarenko and Pryde, 2019] Slussarenko, S. and Pryde, G. J. (2019). Photonic quantum information processing: A concise review. *Applied Physics Reviews*, 6(4):041303. (Cited on page 25.)

[Small et al., 2012a] Small, E., Katz, O., Guan, Y., and Silberberg, Y. (2012a). Spectral control of broadband light through random media by wavefront shaping. *Optics Letters*, 37(22):4663. (Cited on pages 48 and 49.)

[Small et al., 2012b] Small, E., Katz, O., Guan, Y., and Silberberg, Y. (2012b). Spectral control of broadband light through random media by wavefront shaping. *Optics Letters*, 37(16):3429. (Cited on page 48.)

[Smith et al., 2009] Smith, B. J., Kundys, D., Thomas-Peter, N., Smith, P. G. R., and Walmsley, I. A. (2009). Phase-controlled integrated photonic quantum circuits. *Optics Express*, 17(16):13516—-13525. (Cited on pages 25, 27, and 31.)

[Smolka et al., 2009] Smolka, S., Huck, A., Andersen, U. L., Lagendijk, A., and Lodahl, P. (2009). Observation of Spatial Quantum Correlations Induced by Multiple Scattering of Nonclassical Light. *Physical Review Letters*, 102(19):193901. (Cited on pages 97 and 99.)

[Smolka et al., 2012] Smolka, S., Huck, A., Andersen, U. L., Lagendijk, A., and Lodahl, P. (2012). Erratum: Observation of Spatial Quantum Correlations Induced by Multiple Scattering of Nonclassical Light [Phys. Rev. Lett. 102 , 193901 (2009)]. *Physical Review Letters*, 109(25):259904. (Cited on page 97.)

[Smolka et al., 2011] Smolka, S., Muskens, O. L., Lagendijk, A., and Lodahl, P. (2011). Angle-resolved photon-coincidence measurements in a multiple-scattering medium. *Physical Review A*, 83(4):043819. (Cited on page 97.)

[Snitzer, 1961] Snitzer, E. (1961). Cylindrical Dielectric Waveguide Modes*. *Journal of the Optical Society of America*, 51(5):491. (Cited on pages 43 and 121.)

[Snyder and Love, 1984] Snyder, A. W. and Love, J. D. (1984). *Optical Waveguide Theory*. Springer US, Boston, MA. (Cited on pages 43 and 121.)

[Soldano and Pennings, 1995] Soldano, L. B. and Pennings, E. C. (1995). Optical Multi-Mode Interference Devices Based on Self-Imaging: Principles and Applications. *Journal of Lightwave Technology*, 13(4):615–627. (Cited on page 45.)

[Spagnolo et al., 2012] Spagnolo, N., Aparo, L., Vitelli, C., Crespi, A., Ramponi, R., Osellame, R., Mataloni, P., and Sciarrino, F. (2012). Quantum interferometry with three-dimensional geometry. *Scientific Reports*, 2(1):862. (Cited on page 31.)

[Spagnolo et al., 2017] Spagnolo, N., Maiorino, E., Vitelli, C., Bentivegna, M., Crespi, A., Ramponi, R., Mataloni, P., Osellame, R., and Sciarrino, F. (2017). Learning an unknown transformation via a genetic approach. *Scientific Reports*, 7(1):1–7. (Cited on page 55.)

[Spagnolo et al., 2014] Spagnolo, N., Vitelli, C., Bentivegna, M., Brod, D. J., Crespi, A., Flamini, F., Giacomini, S., Milani, G., Ramponi, R., Mataloni, P., Osellame, R., Galvão, E. F., and Sciarrino, F. (2014). Experimental validation of photonic boson sampling. *Nature Photonics*, 8(8):615–620. (Cited on pages 32 and 101.)

[Sparrow et al., 2018] Sparrow, C., Martín-López, E., Maraviglia, N., Neville, A., Harrold, C., Carolan, J., Joglekar, Y. N., Hashimoto, T., Matsuda, N., O'Brien, J. L., Tew, D. P., Laing, A., O'Brien, J. L., Tew, D. P., and Laing, A. (2018). Simulating the vibrational quantum dynamics of molecules using photonics. *Nature*, 557(7707):660–667. (Cited on page 32.)

[Sprengers et al., 2011] Sprengers, J. P., Gaggero, A., Sahin, D., Jahanmirinejad, S., Frucci, G., Mattioli, F., Leoni, R., Beetz, J., Lermer, M., Kamp, M., Höfling, S., Sanjines, R., and Fiore, A. (2011). Waveguide superconducting single-photon detectors for integrated quantum photonic circuits. *Applied Physics Letters*, 99(18):181110. (Cited on page 28.)

[Spring et al., 2013a] Spring, J. B., Metcalf, B. J., Humphreys, P. C., Kolthammer, W. S., Jin, X.-M., Barbieri, M., Datta, A., Thomas-Peter, N., Langford, N. K., Kundys, D., Gates, J. C., Smith, B. J., Smith, P. G. R., and Walmsley, I. A. (2013a). Boson sampling on a photonic chip. *Science*, 339(6121):798–801. (Cited on page 31.)

[Spring et al., 2013b] Spring, J. B., Salter, P. S., Metcalf, B. J., Humphreys, P. C., Moore, M., Thomas-Peter, N., Barbieri, M., Jin, X.-M., Langford, N. K., Kolthammer, W. S., Booth, M. J., and Walmsley, I. A. (2013b). On-chip low loss heralded source of pure single photons. *Optics Express*, 21(11):13522. (Cited on page 28.)

[Starshynov et al., 2016] Starshynov, I., Bertolotti, J., and Anders, J. (2016). Quantum correlation of light scattered by disordered media. *Optics Express*, 24(5):4662. (Cited on page 97.)

[Starshynov et al., 2018] Starshynov, I., Paniagua-Diaz, A. M., Fayard, N., Goetschy, A., Pierrat, R., Carminati, R., and Bertolotti, J. (2018). Non-Gaussian Correlations between Reflected and Transmitted Intensity Patterns Emerging from Opaque Disordered Media. *Physical Review X*, 8(2):021041. (Cited on page 129.)

[Stav et al., 2018] Stav, T., Faerman, A., Maguid, E., Oren, D., Kleiner, V., Hasman, E., and Segev, M. (2018). Quantum entanglement of the spin and orbital angular

momentum of photons using metamaterials. *Science*, 361(6407):1101–1104. (Cited on page 29.)

[Steinberg et al., 1992a] Steinberg, A. M., Kwiat, P. G., and Chiao, R. Y. (1992a). Dispersion cancellation and high-resolution time measurements in a fourth-order optical interferometer. *Physical Review A*, 45(9):6659–6665. (Cited on page 108.)

[Steinberg et al., 1992b] Steinberg, A. M., Kwiat, P. G., and Chiao, R. Y. (1992b). Dispersion cancellation in a measurement of the single-photon propagation velocity in glass. *Physical Review Letters*, 68(16):2421–2424. (Cited on page 108.)

[Su et al., 2019] Su, D., Dhand, I., Helt, L. G., Vernon, Z., and Brádler, K. (2019). Hybrid spatiotemporal architectures for universal linear optics. *Physical Review A*, 99(6):062301. (Cited on page 27.)

[Su et al., 2017] Su, Z.-E., Li, Y., Rohde, P. P., Huang, H.-L., Wang, X.-L., Li, L., Liu, N.-L., Dowling, J. P., Lu, C.-Y., and Pan, J.-W. (2017). Multiphoton Interference in Quantum Fourier Transform Circuits and Applications to Quantum Metrology. *Physical Review Letters*, 119(8):080502. (Cited on page 60.)

[Taballione et al., 2019] Taballione, C., Wolterink, T. A. W., Lugani, J., Eckstein, A., Bell, B. A., Grootjans, R., Visscher, I., Geskus, D., Roeloffzen, C. G. H., Renema, J. J., Walmsley, I. A., Pinkse, P. W. H., and Boller, K.-J. (2019). 8x8 reconfigurable quantum photonic processor based on silicon nitride waveguides. *Optics Express*, 27(19):26842. (Cited on pages 27, 28, and 83.)

[Takagi et al., 2017] Takagi, R., Horisaki, R., and Tanida, J. (2017). Object recognition through a multi-mode fiber. *Optical Review*, 24(2):117–120. (Cited on page 50.)

[Takeda and Furusawa, 2019] Takeda, S. and Furusawa, A. (2019). Toward large-scale fault-tolerant universal photonic quantum computing. *APL Photonics*, 4(6):060902. (Cited on pages 18 and 27.)

[Takenaka et al., 2018] Takenaka, M., Han, J. H., Park, J. K., Boeuf, F., Fujikata, J., Takahashi, S., and Takagi, S. (2018). High-efficiency, low-loss optical phase modulator based on III-V/Si Hybrid MOS capacitor. In *2018 Optical Fiber Communications Conference and Exposition, OFC 2018 - Proceedings*, pages 1–3. OSA. (Cited on page 27.)

[Tang et al., 2017] Tang, R., Tanemura, T., and Nakano, Y. (2017). Integrated Reconfigurable Unitary Optical Mode Converter using MMI Couplers. *IEEE Photonics Technology Letters*, 1135(c):1–1. (Cited on pages 20 and 29.)

[Tanter et al., 2000] Tanter, M., Thomas, J.-l., and Fink, M. (2000). Time reversal and the inverse filter. *The Journal of the Acoustical Society of America*, 108(1):223–234. (Cited on page 72.)

[Tao, 2012] Tao, T. (2012). *Topics in Random Matrix Theory*, volume 132 of *Graduate Studies in Mathematics*. American Mathematical Society, Providence, Rhode Island. (Cited on page 39.)

[Tao et al., 2015] Tao, X., Bodington, D., Reinig, M., and Kubby, J. (2015). High-speed scanning interferometric focusing by fast measurement of binary transmission matrix for channel demixing. *Optics Express*, 23(11):14168. (Cited on page 72.)

[Tasca et al., 2013] Tasca, D. S., Edgar, M. P., Izdebski, F., Buller, G. S., and Padgett, M. J. (2013). Optimizing the use of detector arrays for measuring intensity correlations of photon pairs. *Physical Review A*, 88(1):013816. (Cited on page 73.)

[Tichy, 2014] Tichy, M. C. (2014). Interference of identical particles from entanglement to boson-sampling. *Journal of Physics B: Atomic, Molecular and Optical Physics*, 47(10):103001. (Cited on pages 33 and 60.)

[Tichy et al., 2010] Tichy, M. C., Tiersch, M., De Melo, F., Mintert, F., and Buchleitner, A. (2010). Zero-transmission law for multiport beam splitters. *Physical Review Letters*, 104(22):1–4. (Cited on pages 14, 67, 101, and 113.)

[Tillmann et al., 2013] Tillmann, M., Dakić, B., Heilmann, R., Nolte, S., Szameit, A., and Walther, P. (2013). Experimental boson sampling. *Nature Photonics*, 7(7):540–544. (Cited on page 31.)

[Tillmann et al., 2016] Tillmann, M., Schmidt, C., and Walther, P. (2016). On unitary reconstruction of linear optical networks. *Journal of Optics*, 18(11):114002. (Cited on page 71.)

[Timurdogan et al., 2017] Timurdogan, E., Poulton, C. V., Byrd, M. J., and Watts, M. R. (2017). Electric field-induced second-order nonlinear optical effects in silicon waveguides. *Nature Photonics*, 11(3):200–206. (Cited on page 27.)

[Tischler et al., 2018] Tischler, N., Rockstuhl, C., and Słowik, K. (2018). Quantum Optical Realization of Arbitrary Linear Transformations Allowing for Loss and Gain. *Physical Review X*, 8(2):1–13. (Cited on pages 24 and 71.)

[Tripathi et al., 2012] Tripathi, S., Paxman, R., Bifano, T., and Toussaint, K. C. (2012). Vector transmission matrix for the polarization behavior of light propagation in highly scattering media. *Optics Express*, 20(14):16067. (Cited on page 48.)

[Tripathi and Toussaint, 2014] Tripathi, S. and Toussaint, K. C. (2014). Harnessing randomness to control the polarization of light transmitted through highly scattering media. *Optics Express*, 22(4):4412. (Cited on page 48.)

[Tulino and Verdú, 2004] Tulino, A. M. and Verdú, S. (2004). Random Matrix Theory and Wireless Communications. *Foundations and Trends$^{TM}$ in Communications and Information Theory*, 1(1):1–182. (Cited on page 40.)

[Turpin et al., 2018] Turpin, A., Vishniakou, I., and Seelig, J. d. (2018). Light scattering control in transmission and reflection with neural networks. *Optics Express*, 26(23):30911. (Cited on page 50.)

[Turtaev et al., 2018] Turtaev, S., Leite, I. T., Altwegg-Boussac, T., Pakan, J. M. P., Rochefort, N. L., and Čižmár, T. (2018). High-fidelity multimode fibre-based endoscopy for deep brain in vivo imaging. *Light: Science & Applications*, 7(1):92. (Cited on pages 2 and 50.)

[Turtaev et al., 2017] Turtaev, S., Leite, I. T., Mitchell, K. J., Padgett, M. J., Phillips, D. B., and Čižmár, T. (2017). Comparison of nematic liquid-crystal and DMD based spatial light modulation in complex photonics. *Optics Express*, 25(24):29874. (Cited on page 72.)

[Tyson, 1991] Tyson, R. K. (1991). *Principles of Adaptive Optics*. Elsevier. (Cited on page 46.)

[Uppu et al., 2016] Uppu, R., Wolterink, T. A. W., Tentrup, T. B. H., and Pinkse, P. W. H. (2016). Quantum optics of lossy asymmetric beam splitters. *Optics Express*, 24(15):16440. (Cited on page 78.)

[Urbina et al., 2016] Urbina, J. D., Kuipers, J., Matsumoto, S., Hummel, Q., and Richter, K. (2016). Multiparticle Correlations in Mesoscopic Scattering: Boson Sampling, Birthday Paradox, and Hong-Ou-Mandel Profiles. *Physical Review Letters*, 116(10):1–6. (Cited on page 34.)

[Valiant, 1979] Valiant, L. G. (1979). The complexity of computing the permanent. *Theoretical Computer Science*, 8(2):189–201. (Cited on page 34.)

[van Enk and Beenakker, 2012] van Enk, S. J. and Beenakker, C. W. J. (2012). Measuring $\mathrm{Tr}\rho^n$ on Single Copies of $\rho$ Using Random Measurements. *Physical Review Letters*, 108(11):110503. (Cited on page 98.)

[Van Exter et al., 2006] Van Exter, M. P., Aiello, A., Oemrawsingh, S. S., Nienhuis, G., and Woerdman, J. P. (2006). Effect of spatial filtering on the Schmidt decomposition of entangled photons. *Physical Review A*, 74(1):2–5. (Cited on page 119.)

[Van Exter et al., 2012] Van Exter, M. P., Woudenberg, J., Di Lorenzo Pires, H., and Peeters, W. H. (2012). Bosonic, fermionic, and anyonic symmetry in two-photon random scattering. *Physical Review A*, 85(3):1–5. (Cited on page 99.)

[van Lint et al., 2001] van Lint, J. H., van Lint, Wilson, R. M., and Wilson, R. M. (2001). *A Course in Combinatorics*. Cambridge University Press. (Cited on page 34.)

[van Niekerk et al., 2019] van Niekerk, M., Steidle, J. A., Howland, G. A., Fanto, M. L., Soures, N., Zohora, F. T., Kudithipudi, D., and Preble, S. (2019). Approximating large scale arbitrary unitaries with integrated multimode interferometers. In Hayduk, M., Frey, M. R., Donkor, E., Lomonaco, S. J., and Myers, J. M., editors, *Quantum Information Science, Sensing, and Computation XI*, number May, page 20. SPIE. (Cited on page 46.)

[van Rossum and Nieuwenhuizen, 1998] van Rossum, M. C. W. and Nieuwenhuizen, T. M. (1998). Multiple scattering of classical waves: from microscopy to mesoscopy and diffusion. *Reviews of Modern Physics*, 71(1):86. (Cited on page 127.)

[Van Velsen and Beenakker, 2004] Van Velsen, J. L. and Beenakker, C. W. J. (2004). Transition from pure-state to mixed-state entanglement by random scattering. *Physical Review A*, 70(3):1–6. (Cited on page 97.)

[Vasquez-Lopez et al., 2018] Vasquez-Lopez, S. A., Turcotte, R., Koren, V., Plöschner, M., Padamsey, Z., Booth, M. J., Čižmár, T., and Emptage, N. J. (2018). Subcellular spatial resolution achieved for deep-brain imaging in vivo using a minimally invasive multimode fiber. *Light: Science & Applications*, 7(1):110. (Cited on pages 2 and 50.)

[Velázquez-Benítez et al., 2018] Velázquez-Benítez, A. M., Antonio-López, J. E., Alvarado-Zacarías, J. C., Fontaine, N. K., Ryf, R., Chen, H., Hernández-Cordero, J., Sillard, P., Okonkwo, C., Leon-Saval, S. G., and Amezcua-Correa, R. (2018). Scaling photonic lanterns for space-division multiplexing. *Scientific Reports*, 8(1):8897. (Cited on page 114.)

[Vellekoop, 2015] Vellekoop, I. M. (2015). Feedback-based wavefront shaping. *Optics Express*, 23(9):12189. (Cited on pages 46 and 72.)

[Vellekoop and Aegerter, 2010] Vellekoop, I. M. and Aegerter, C. M. (2010). Scattered light fluorescence microscopy: imaging through turbid layers. *Optics Letters*, 35(8):1245. (Cited on page 127.)

[Vellekoop et al., 2010] Vellekoop, I. M., Lagendijk, A., and Mosk, A. P. (2010). Exploiting disorder for perfect focusing. *Nature Photonics*, 4(5):320–322. (Cited on page 47.)

[Vellekoop and Mosk, 2007] Vellekoop, I. M. and Mosk, A. P. (2007). Focusing coherent light through opaque strongly scattering media. *Optics Letters*, 32(16):2309. (Cited on pages 46, 48, 49, 50, 72, and 125.)

[Vellekoop and Mosk, 2008] Vellekoop, I. M. and Mosk, A. P. (2008). Universal optimal transmission of light through disordered materials. *Physical Review Letters*, 101(12):1–4. (Cited on pages 47, 125, and 128.)

[Vest et al., 2017] Vest, B., Dheur, M.-c. M.-C. M. C., Devaux, É., Baron, A., Rousseau, E., Hugonin, J.-P. J.-p. P., Greffet, J.-j. J.-J. J. J., Messin, G., Marquier, F., Devaux, E., Baron, A., Rousseau, E., Hugonin, J.-P. J.-p. P., Greffet, J.-j. J.-J. J. J., Messin, G., and Marquier, F. (2017). Anti-coalescence of bosons on a lossy beam splitter. *Science*, 356(6345):1373–1376. (Cited on page 83.)

[Vest et al., 2018] Vest, B., Shlesinger, I., Dheur, M.-c., Devaux, É., Greffet, J.-j., Messin, G., and Marquier, F. (2018). Plasmonic interferences of two-particle N00N states. *New Journal of Physics*, 20(5):053050. (Cited on pages 88 and 89.)

[Viggianiello et al., 2018] Viggianiello, N., Flamini, F., Innocenti, L., Cozzolino, D., Bentivegna, M., Spagnolo, N. N., Crespi, A., Brod, D. J., Galvao, E. F., Osellame, R., Sciarrino, F., Galvão, E. F., Osellame, R., and Sciarrino, F. (2018). Experimental generalized quantum suppression law in Sylvester interferometers. *New Journal of Physics*, 20(3):033017. (Cited on pages 60, 62, and 67.)

[Walschaers et al., 2016a] Walschaers, M., Kuipers, J., and Buchleitner, A. (2016a). From many-particle interference to correlation spectroscopy. *Physical Review A*, 94(2):020104. (Cited on page 101.)

[Walschaers et al., 2016b] Walschaers, M., Kuipers, J., Urbina, J. D., Mayer, K., Tichy, M. C., Richter, K., and Buchleitner, A. (2016b). Statistical benchmark for boson sampling. *New Journal of Physics*, 18(3):032001. (Cited on pages 101 and 105.)

[Wan et al., 2011] Wan, W., Chong, Y., Ge, L., Noh, H., Stone, A. D., and Cao, H. (2011). Time-reversed lasing and interferometric control of absorption. *Science*, 331(6019):889–892. (Cited on page 84.)

[Wang et al., 2017a] Wang, H., He, Y.-M., Li, Y.-H., Su, Z.-E., Li, B., Huang, H.-L., Ding, X., Chen, M.-C., Liu, C., Qin, J., Li, J.-P., He, Y.-M., Schneider, C., Kamp, M., Peng, C.-Z., Höfling, S., Lu, C.-Y., and Pan, J.-W. (2017a). High-efficiency multiphoton boson sampling. *Nature Photonics*, 11(6):361–365. (Cited on page 34.)

[Wang et al., 2018a] Wang, H., Li, W., Jiang, X., Li, Y.-H. H., Ding, X., Chen, M.-C. C., Liu, C., Peng, C.-Z. Z., Schneider, C., Kamp, M., Zhang, W.-J. J., Li, H., Wang, Z., Dowling, J. P., He, Y.-M. M., Li, Y.-H. H., Ding, X., Chen, M.-C. C., Qin, J., Peng, C.-Z. Z., Schneider, C., Kamp, M., Zhang, W.-J. J., Li, H., You, L.-X. X., Wang,

Z., Dowling, J. P., Höfling, S., Lu, C.-Y. Y., Pan, J.-W. W., Liu, C., Peng, C.-Z. Z., Schneider, C., Kamp, M., Zhang, W.-J. J., Li, H., Wang, Z., Dowling, J. P., He, Y.-M. M., Li, Y.-H. H., Ding, X., Chen, M.-C. C., Qin, J., Peng, C.-Z. Z., Schneider, C., Kamp, M., Zhang, W.-J. J., Li, H., You, L.-X. X., Wang, Z., Dowling, J. P., Höfling, S., Lu, C.-Y. Y., and Pan, J.-W. W. (2018a). Toward Scalable Boson Sampling with Photon Loss. *Physical Review Letters*, 120(23):4–11. (Cited on pages 34 and 78.)

[Wang et al., 2019a] Wang, H., Qin, J., Ding, X., Chen, M.-C., Chen, S., You, X., He, Y.-M., Jiang, X., You, L., Wang, Z., Schneider, C., Renema, J. J., Höfling, S., Lu, C.-Y., and Pan, J.-W. (2019a). Boson Sampling with 20 Input Photons and a 60-Mode Interferometer in a $10^{14}$ -Dimensional Hilbert Space. *Physical Review Letters*, 123(25):250503. (Cited on page 34.)

[Wang et al., 2018b] Wang, J., Paesani, S., Ding, Y., Santagati, R., Skrzypczyk, P., Salavrakos, A., Tura, J., Augusiak, R., Mančinska, L., Bacco, D., Bonneau, D., Silverstone, J. W., Gong, Q., Acín, A., Rottwitt, K., Oxenløwe, L. K., O'Brien, J. L., Laing, A., and Thompson, M. G. (2018b). Multidimensional quantum entanglement with large-scale integrated optics. *Science*, 360(6386):285–291. (Cited on pages 27, 28, and 32.)

[Wang et al., 2019b] Wang, J., Sciarrino, F., Laing, A., and Thompson, M. G. (2019b). Integrated photonic quantum technologies. *Nature Photonics*. (Cited on pages 2, 31, and 35.)

[Wang et al., 2017b] Wang, Y., Potoček, V., Barnett, S. M., and Feng, X. (2017b). Programmable holographic technique for implementing unitary and nonunitary transformations. *Physical Review A*, 95(3):033827. (Cited on page 29.)

[Weihs et al., 1996] Weihs, G., Reck, M., Weinfurter, H., and Zeilinger, A. (1996). Two-photon interference in optical fiber multiports. *Physical Review A*, 54(1):893–897. (Cited on page 45.)

[Wiersma et al., 1997] Wiersma, D. S., Bartolini, P., Lagendijk, A., and Righini, R. (1997). Localization of light in a disordered medium. *Nature*, 390(6661):671–673. (Cited on page 41.)

[Wigner, 1951] Wigner, E. P. (1951). On the statistical distribution of the widths and spacings of nuclear resonance levels. *Mathematical Proceedings of the Cambridge Philosophical Society*, 47(4):790–798. (Cited on page 39.)

[Wishart, 1928] Wishart, J. (1928). The Generalised Product Moment Distribution in Samples from a Normal Multivariate Population. *Biometrika*, 20A(1/2):32. (Cited on pages 39 and 40.)

[Wolterink et al., 2015] Wolterink, T. A. W., Uppu, R., Ctistis, G., Vos, W. L., Boller, K. J., and Pinkse, P. W. H. (2015). Programmable two-photon quantum interference in $10^3$ channels in opaque scattering media. *Physical Review A*, 93(5):053817. (Cited on pages 51, 52, and 83.)

[Wu et al., 2019] Wu, P. C., Pala, R. A., Kafaie Shirmanesh, G., Cheng, W.-H., Sokhoyan, R., Grajower, M., Alam, M. Z., Lee, D., and Atwater, H. A. (2019). Dynamic beam steering with all-dielectric electro-optic III–V multiple-quantum-well metasurfaces. *Nature Communications*, 10(1):3654. (Cited on page 29.)

[Xiong et al., 2015] Xiong, C., Zhang, X., Mahendra, A., He, J., Choi, D.-Y., Chae, C. J., Marpaung, D., Leinse, A., Heideman, R. G., Hoekman, M., Roeloffzen, C. G. H., Oldenbeuving, R. M., van Dijk, P. W. L., Taddei, C., Leong, P. H. W., and Eggleton, B. J. (2015). Compact and reconfigurable silicon nitride time-bin entanglement circuit. *Optica*, 2(8):724. (Cited on page 28.)

[Xiong et al., 2018] Xiong, W., Hsu, C. W., Bromberg, Y., Antonio-Lopez, J. E., Amezcua Correa, R., and Cao, H. (2018). Complete polarization control in multimode fibers with polarization and mode coupling. *Light: Science & Applications*, 7(1):54. (Cited on pages 45, 48, and 50.)

[Xiong et al., 2019] Xiong, W., Hsu, C. W., and Cao, H. (2019). Long-range spatio-temporal correlations in multimode fibers for pulse delivery. *Nature Communications*, 10(1):2973. (Cited on pages 114 and 130.)

[Xomalis et al., 2018] Xomalis, A., Demirtzioglou, I., Plum, E., Jung, Y., Nalla, V., Lacava, C., MacDonald, K. F., Petropoulos, P., Richardson, D. J., and Zheludev, N. I. (2018). Fibre-optic metadevice for all-optical signal modulation based on coherent absorption. *Nature Communications*, 9(1):182. (Cited on pages 86 and 92.)

[Xu et al., 2014] Xu, Q., Chen, L., Wood, M. G., Sun, P., and Reano, R. M. (2014). Electrically tunable optical polarization rotation on a silicon chip using Berry's phase. *Nature Communications*, 5(1):5337. (Cited on pages 27 and 28.)

[Yamaguchi and Zhang, 1997] Yamaguchi, I. and Zhang, T. (1997). Phase-shifting digital holography. *Optics Letters*, 22(16):1268. (Cited on page 56.)

[Yılmaz et al., 2019a] Yılmaz, H., Hsu, C. W., Goetschy, A., Bittner, S., Rotter, S., Yamilov, A., and Cao, H. (2019a). Angular Memory Effect of Transmission Eigenchannels. *Physical Review Letters*, 123(20):203901. (Cited on page 128.)

[Yılmaz et al., 2019b] Yılmaz, H., Hsu, C. W., Yamilov, A., and Cao, H. (2019b). Transverse localization of transmission eigenchannels. *Nature Photonics*, 13(5):352–358. (Cited on page 128.)

[Yu et al., 2013] Yu, H., Hillman, T. R., Choi, W., Lee, J. O., Feld, M. S., Dasari, R. R., and Park, Y. (2013). Measuring large optical transmission matrices of disordered media. *Physical Review Letters*, 111(15):1–5. (Cited on page 126.)

[Zhang et al., 2012] Zhang, J., MacDonald, K. F., and Zheludev, N. I. (2012). Controlling light-with-light without nonlinearity. *Light: Science & Applications*, 1(7):e18–e18. (Cited on pages 86 and 92.)

[Zhang et al., 2016] Zhang, Y., Prabhakar, S., Rosales-Guzmán, C., Roux, F. S., Karimi, E., and Forbes, A. (2016). Hong-Ou-Mandel interference of entangled Hermite-Gauss modes. *Physical Review A*, 94(3):033855. (Cited on page 15.)

[Zhao et al., 2019] Zhao, P., Li, S., Feng, X., Barnett, S. M., Zhang, W., Cui, K., Liu, F., and Huang, Y. (2019). Universal linear optical operations on discrete phase-coherent spatial modes with a fixed and non-cascaded setup. *Journal of Optics*, 21(10):104003. (Cited on page 29.)

[Zhong et al., 2018] Zhong, H.-s., Li, Y., Li, W., Peng, L.-c., Su, Z.-e., Hu, Y., He, Y.-m., Ding, X., Zhang, W., Li, H., Zhang, L., Wang, Z., You, L., Wang, X.-l., Jiang, X.,

Li, L., Chen, Y.-a., Liu, N.-l., Lu, C.-y., and Pan, J.-w. (2018). 12-Photon Entanglement and Scalable Scattershot Boson Sampling with Optimal Entangled-Photon Pairs from Parametric Down-Conversion. *Physical Review Letters*, 121(25):250505. (Cited on page 34.)

[Zhou et al., 2018] Zhou, J., Wu, J., and Hu, Q. (2018). Tunable arbitrary unitary transformer based on multiple sections of multicore fibers with phase control. *Optics Express*, 26(3):3020. (Cited on pages 20 and 29.)

[Zhuang et al., 2015] Zhuang, L., Roeloffzen, C. G. H., Hoekman, M., Boller, K.-J., and Lowery, A. J. (2015). Programmable photonic signal processor chip for radiofrequency applications. *Optica*, 2(10):854. (Cited on page 20.)

[Życzkowski and Kuś, 1994] Życzkowski, K. and Kuś, M. (1994). Random unitary matrices. *Journal of Physics A: Mathematical and General*, 27(12):4235–4245. (Cited on page 33.)